Universidad de Castilla-La Mancha

PhD Thesis

Control and Navigation of Unmanned Aerial Vehicles Based on Computer Vision for Assistance Robotics

by

Lidia María Belmonte Moreno

Supervisors:
Dr. Rafael Morales Herrera
Dr. Antonio Fernández-Caballero

Albacete, 2019

UNIVERSIDAD DE CASTILLA-LA MANCHA

Tesis Doctoral:
Control y navegación de vehículos aéreos no tripulados basado en visión artificial para robótica asistencial

Doctoranda:
Lidia María Belmonte Moreno

Directores:
Dr. Rafael Morales Herrera y Dr. Antonio Fernández Caballero

Tesis financiada por el Ministerio de Educación, Cultura y Deporte mediante la ayuda de Formación de Profesorado Universitario (FPU014/05283)

A mis directores de tesis.
A mis padres, hermano y familia.
A mi llalla y mi tata.

Declaration

This dissertation is the result of my own work and does not include any outcome of work done in collaboration except where it has been specially indicated in the text. It has not been previously submitted, partially or totally, to any university or institution for any degree, diploma or other qualification.

Moreover, I hereby declare to be one of the main authors of every work used in this thesis by compendium of publications, including the following ones which have been published in journals with impact factor:

- L.M. Belmonte; R. Morales; A. Fernández-Caballero; J.A. Somolinos. "A Tandem Active Disturbance Rejection Control for a Laboratory Helicopter with Variable Speed Rotors". *IEEE Transactions on Industrial Electronics*, 63(10), 6395–6406. IEEE, 2016. DOI:10.1109/TIE.2016.2587238. IF: 7.168, Q1 (1/60 Automation & Control Systems, 12/262 Engineering, Electrical & Electronic, 1/58 Instruments & Instrumentation).
- L.M. Belmonte; R. Morales; A. Fernández-Caballero; J.A. Somolinos. "Robust Decentralized Nonlinear Control for a Twin Rotor MIMO System". *Sensors*, 16(8), article 1160. MDPI, 2016. DOI:10.3390/s16081160. IF: 2.677, Q1 (10/58 Instruments & Instrumentation).
- A. Fernández-Caballero; L.M. Belmonte; R. Morales; J.A. Somolinos. "Generalized Proportional Integral Control for an Unmanned Quadrotor System". *International Journal of Advanced Robotic Systems*, 12(85), 1–14. InTech, 2015. DOI:10.5772/60833. IF: 0.615, Q4 (19/25 Robotics).

Albacete, May 2019

Signed: Lidia María Belmonte Moreno

Summary

Control and Navigation of Unmanned Aerial Vehicles Based on Computer Vision for Assistance Robotics

Unmanned aerial vehicles (UAVs), commonly known as drones, have gained great popularity in recent years. Given their characteristics, they can be used to access remote or difficult-to-reach points without requiring the intervention of an onboard operator. In this sense, technological advances are directing towards totally autonomous UAVs, i.e., those aircraft that can perform a complete flight, from take-off to landing, without being controlled or supervised by an operator on the ground. This doctoral dissertation is framed in this area of autonomous UAVs.

The research focuses on the development of control algorithms and navigation solutions for autonomous UAVs based on computer vision. The final objective is their use in assistance robotics, mainly for home care of dependents or elderly persons. These people require assistance to perform daily tasks and, in many cases, they are forced to leave their homes to receive care in specialized centers. However, this situation is not usually their preference. This, together with the problems they suffer, leads to a loss of quality of life. To counteract this situation, it is essential to increase the autonomy of these people, and for that, technology should play a fundamental role.

At this point, unmanned aerial vehicles represent a new model of assistant flying robots. This thesis proposes the use of UAVs equipped with cameras to monitor the dependent's activities. This way, the information grabbed is processed to determine the person's state and the assistance required at each time. The aim is that dependent people live at their home as long as they wish, receiving the necessary attention. Bringing such UAV assistants into real homes is, however, a complex goal in which multiple challenges need to be addressed. Both human and technical factors must be considered. In this sense, this doctoral thesis contributes by addressing three main topics: (a) the use of computer vision in the navigation and flight control of autonomous UAVs, (b) the development of new robust control algorithms and navigation solutions for different models of UAV, and finally, (c) the study of the feasibility of computer-vision based UAVs as assistants of dependent people both indoor (at home) and outdoor environments.

Resumen

Control y navegación de vehículos aéreos no tripulados basado en visión artificial para robótica asistencial

Los vehículos aéreos no tripulados (unmanned aerial vehicles, UAVs), comúnmente conocidos como drones, han ganado gran popularidad en los últimos años. Dadas sus características, pueden utilizarse para acceder a puntos remotos o de difícil acceso sin la intervención de un operador a bordo. En este sentido, el avance tecnológico se dirige hacia los UAVs totalmente autónomos, es decir, aquellas aeronaves que pueden realizar un vuelo completo, desde el despegue hasta el aterrizaje, sin ser controladas o supervisadas por un operador en tierra. En esta área de UAVs autónomos se enmarca esta tesis doctoral.

La investigación se centra en el desarrollo de algoritmos de control y soluciones de navegación para UAVs autónomos basados en visión artificial. El objetivo final es su uso en robótica asistencial, principalmente para la atención domiciliaria de personas dependientes o ancianos. Estas personas requieren asistencia para realizar las tareas diarias y, en muchos casos, se ven obligadas a abandonar sus hogares para recibir atención en centros especializados. Sin embargo, esta situación no suele ser su preferencia. Esto, junto con los problemas que sufren, lleva a una pérdida de calidad de vida. Para contrarrestar esta situación, es esencial aumentar la autonomía de estas personas, y para eso, la tecnología debe jugar un papel fundamental.

En este punto, los vehículos aéreos no tripulados representan un nuevo modelo de robots voladores asistentes. Esta tesis propone el uso de UAVs equipados con cámaras para monitorizar la actividad de los dependientes. De esta manera, la información obtenida puede procesarse para determinar el estado de la persona y la asistencia requerida en cada momento. El objetivo es que las personas dependientes puedan vivir en el hogar, siempre que lo deseen, recibiendo la atención necesaria. Llevar a dichos UAVs asistentes a hogares reales es, sin embargo, un objetivo complejo en el que deben abordarse múltiples desafíos. Tanto los factores humanos como los técnicos deben ser considerados. En este sentido, esta tesis doctoral contribuye abordando tres temas principales: (a) el uso de la visión artificial en la navegación y el control de vuelo de los UAV autónomos, (b) el desarrollo de nuevos algoritmos de control robustos y soluciones de navegación para diferentes modelos de UAV, y finalmente,(c) el estudio de la viabilidad de los UAVs basados en visión artificial como asistentes de personas dependientes tanto en interiores (en casa) como en exteriores.

Abbreviations

AAL	Ambient Assisted Living
AAR	autonomous aerial refueling
ADRC	active disturbance rejection control
AT	assistive technology
AUAV	autonomous unmanned aerial vehicle
DoF	degrees of freedom
FWMAV	flapping-wing miniature air vehicle
GPI	generalized proportional integral
HILS	hardware-in-the-loop simulation
IBVS	image-based visual servoing
IF	impact factor
IILS	image-in-loop simulation
JCR	Journal Citation Reports
LQR	linear quadratic regulator
MQTT	Message Queue Telemetry Transport
PBVS	position-based visual servoing
PID	proportional-integral-derivative
QoL	quality of life
RQ	research question
SAA	sense-and-avoid
SLAM	simultaneous localization and mapping
TRMS	Twin Rotor MIMO System
UAS	unmanned aircraft system
UAV	unmanned aerial vehicle
VR	virtual reality
VTOL	vertical take-off and landing
WHO	World Health Organization

Contents

List of Figures

CHAPTER 1

Introduction

This chapter presents the fundamental aspects of this doctoral thesis submitted in the form of a compendium of publications. Section 1.1 summaries the current context and the need to bet on technology as a means to facilitate care for the persons in a dependency situation. Ambient assisted living and robotics provide remarkable solutions in this respect. Section 1.2 describes the hypotheses or initial considerations and the objectives of the research on vision-based unmanned aerial vehicles (UAVs) for assistance purposes. Section 1.3 presents the methodology and work plan divided into three thematic blocks according to the partial goals; computer vision in UAVs, control algorithms for UAVs, and the proposal of UAVs to assist dependent persons. To conclude this introductory chapter, Section 1.4 details the structure of this thesis.

1.1 Justification

1.1.1 Overview

In recent decades, socio-economic development in most regions has been marked by a reduction in birth rates and a substantial increase in life expectancy. This situation has produced major demographic changes in the population, increasing the number and proportion of elderly people [33]. Public health must provide effective responses to the challenges that this new situation poses. It is essential to foster policies that promote the well-being of older people, provide favorable environments, and adapt health systems to meet the needs associated with people's increased longevity. The fundamental objective to achieve is that this increase in longevity be accompanied by an enhancement in health status.

In this regard, the World Health Organization (WHO) has been developing and promoting a new framework to improve the **quality of life** (QoL) of older people. QoL is a broad-ranging concept on the individual perception of the position in life within the personal context and goals [34]. Physical health, psychological state, personal beliefs, social relationships and the relationship to the environment's salient features are key points in that perception. In 2002, WHO published the document *Active Ageing: A Policy Framework* [31], which defines **active ageing** as 'the process of optimizing opportunities for health, participation and security in order to enhance quality of life as people age". It identifies different types of factors involved in this process, such as economic, personal, social and physical environment, and highlights the importance of health, both for older people and for the positive impact of their participation in society.

On the other hand, the previous report presents policies for health systems to promote healthy aging. Among them, the following factors should be highlighted: (a) preventing and reducing excessive burden of disabilities and diseases, (b) reducing risk factors and increasing the factors that protect health, (c) developing accessible and adapted social and health services, and (d) providing training to caregivers. However, this study fails in detailing the systematic changes that are really necessary to address the challenges of this new demographic and social situation. The above is reflected in the document *World Report on Ageing and Health* [32], elaborated in 2015 by WHO. The study highlights a lack of adaptation of health systems to the needs of older people, a lack of adequate and sustainable models of long-term care, the obstacles of physical and social environments, as well as a lack of incentives for health and participation. In order to reverse this situation, a new concept of old age and transformative approaches are needed to improve the state of health, and quality of life in general, throughout the course of life.

To this end, WHO proposes strategies associated with **healthy aging**. This term refers to the process of developing and maintaining the functional ability that enables well-being in older age. Functional ability encompasses: (a) intrinsic ability, a combination of a person's physical and mental abilities, (b) the relevant characteristics of the environment, and (c) the interactions between the individual and these characteristics. For its part, well-being brings together all the physical, mental and social factors that affect all spheres of life. Issues such as happiness, satisfaction, and fulfillment are considered at this point. In this model of healthy aging, a remarkable concept is that of **resilience**. This refers to maintaining or improving the level of functional ability in the face of adversity. Resistance, recovery or adaptation are fundamental to achieve this. It is, therefore, a question of favoring the quality of life so that older people continue to do what they want and value, without being limited by their loss of capacities.

Figure 1.1, extracted from the above-mentioned report on aging and health, represents the three stages that are generally distinguished in people's intrinsic capacity throughout their lives. These stages are not defined by chronological age, do not have the same duration in all individuals, and may be disturbed by an accident and/or a serious illness. However, the graph reflects the usual development marked by a first stage of high capacity, an intermediate stage of diminished capacity, and, finally, the phase of significant loss of capacity.

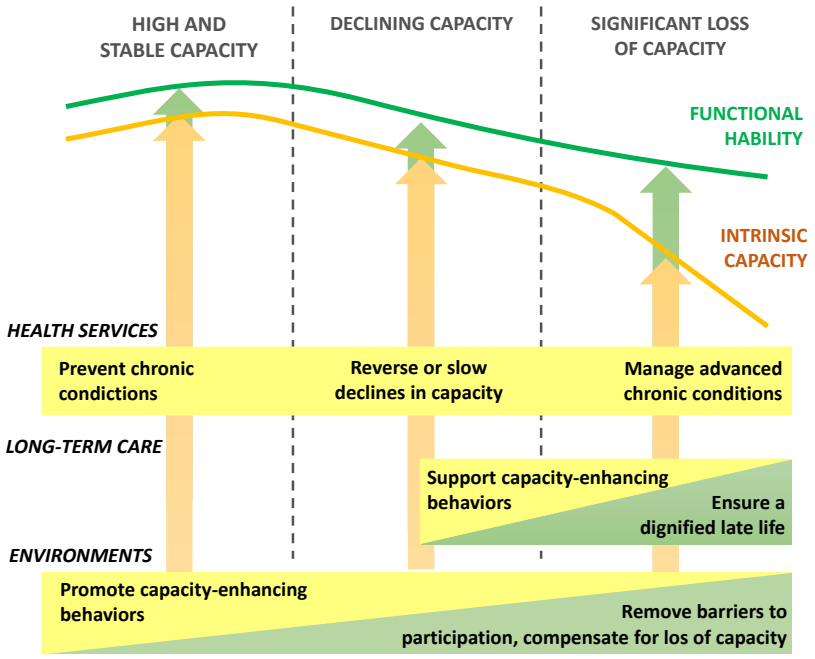

Figure 1.1: A public-health framework for healthy aging: opportunities for public-health action across the life course [32]

The necessary health strategies differ for each of these phases. (i) Fostering and maintaining the high level of capacity for as long as possible is fundamental in the first phase. The environment should encourage healthy behaviors that help to achieve this goal. (ii) In the second phase, the goal is to reduce the effects that different conditions may cause. This requires systems that contribute to halting, moderating or even reversing capacity impairment, and improving or promoting functional ability through adapted environments and coping strategies. (iii) Finally, in the third stage, it is necessary to focus efforts on long-term care so that people with significant capacity loss, or at risk of this loss, maintain a level of functional ability consistent with their basic rights, fundamental freedoms and human dignity.

WHO considers different key issues for developing healthy aging. Among these, we must highlight the person-centered approach and aging in place. The first considers the need to design solutions that are safe, effective and adapted to the preferences of the people for whom they are intended. On the other hand, the second concept, detailed below, is fundamental in the context of this doctoral thesis. The **aging in place** encourages the permanence of people at their home (or community where they have lived), regardless of age or ability, so that they continue to live comfortably, independently and safely for as long as possible, and receive the necessary care [10, 14, 22]. This last point is fundamental. When people experience significant capacity impairment, they need help with everyday tasks. This situation of dependency (or care dependency) often entails the need to adapt homes, and even the need to leave them in order to receive the necessary care in specialized centers. Generally, this transfer decision is not voluntary, negatively affecting the patient's mood, and also inferring a reduction in his/her quality of life [7, 35].

To counteract this situation, in many cases, the family members of the dependent person must spend their time and effort to attend the needs of their family member. However, this situation produces a loss in the quality of life of the caregivers, who generally lack adequate training. So, it is not the most convenient solution [8, 9]. Furthermore, we must bear in mind that today's society is not only marked by the general aging of the population, but also by an increase in the number of people living alone. For these people, it is even more complicated to stay at their homes as their capacity decreases. It is in this context of dependent people, who generally live alone, where technology should provide new solutions that allow people to stay longer at their community, which provides them independence, a sense of connection and safety. Ambient assisted living and robotics are two key technologies.

1.1.2 Ambient Assisted Living and Assistance Robotics

Quality of Life (QoL) is the appreciation of well-being in daily human lives, including emotional, social and physical aspects [23, 27, 34]. To improve the QoL of persons who have chronic or degenerative limitations in motor and/or cognitive abilities, a broad range of services and devices has been developed in the last few years. These are encompassed in the concept of assistive technologies.

Assistive technology (AT) is a broad term that groups those systems and services related to the delivery of assistance [30]. These devices and services (i) help all persons with disabilities to improve their accessibility in all aspects of their life [15], (ii) maintain or improve an individual's functioning and independence to facilitate participation and to enhance overall well-being [28], (iii) reduces the need for formal health and support services, long-term care and the work of caregivers, (iv) they can also help prevent impairments and secondary health conditions. This way, AT aims to increase the quality of life, to reduce dependence on the caregiver and to decrease dependence on the long-term care system [3]. The range of products and services is huge and diverse. Here are included any item, piece of equipment, software program or product system that is used to increase, maintain or improve the functional capabilities of persons [1]. We can cite several examples like wheelchairs, prostheses, hearings aids, visual aids, and specialized computer software and hardware that increase mobility, hearing, vision, or communication capacities. AT can enable older people to continue to live at home and delay or prevent the need for long-term care [17]. Given the aging trend of the population, this is a research area of great interest. In this sense, and in a similar way to other technologies, the products and services designed to help dependents will be increasingly intelligent and autonomous.

As a result of the technological evolution in assistance devices, a new multidisciplinary field emerges aiming at exploiting information and communication technologies in personal health care and tele-health systems. Ambient Assisted Living (AAL) is the result of a progression from individual devices assisting with one task or activity of daily living to ambient systems in which the assistance or support completely encompasses the living area and the person [4]. This way, the AAL concept concerns products and services that

constitute intelligent environments in favor of elder people and those with special disabilities [21]. AAL systems integrate, among other, medical sensors, wireless sensors, actuator networks, computer hardware, computer networks, software applications, and databases, which are interconnected to exchange data and provide services in an ambient assisted environment [19]. Through the intelligent processing of such data, it is possible to extract useful information to control health, recognize human activity or detect potentially dangerous areas or situations at home. However, sometimes the deployment of all the technology in real homes that are not adapted for them is complicated. The need for a complete system maintenance must also be considered. In addition to this, there is also an additional problem to the traditional concept of sensors installed within the home, such as static cameras, the blind-zones which limit the ability to perceive the complete environment and the people to be assisted. To affront these problems, robotics can play a relevant role by means of mobile platforms [13].

Assistance robotics is one of the most relevant technologies to provide direct aid to elderly people or persons with disabilities. Several names can be found to refer to robotic devices for assistance purposes, namely assistive robot [16], personal assistant (robot) [6] or AAL robot [25]. Within these robots, mainly two classes are differentiated according to their purpose [5, 18]: rehabilitation robots and social robots. The first one groups those robotic solutions aimed to provide physical assistance. The second one encompasses service robots for supporting daily activities and monitoring tasks, and companion robots for social interaction. Personal assistant robots offer support and services in a broad range of scenarios [20]. Health monitoring, assessment and assistance is probably the most relevant in the context of this doctoral dissertation. An assistance robot continuously observes and monitors the activities of its user. This allows also to provide valuable data for a long-term assessment and to detect changes in behavior that might indicate a decline in the overall health state, e.g. reduced mobility. This way, in base of the information provided by the assistant robot, it is possible to determine the needs of the dependent person as a step towards improving his/her attention and quality of life.

1.2 Hypothesis and Objectives

The development of this doctoral thesis is constructed on the premise that unmanned aerial vehicles (UAVs) based on computer vision are a viable solution in applications devoted to assistance robotics. These aircraft, equipped with vision sensors, represent a new present and especially future model of personal assistants. The operation of personal assistants is mainly based on monitoring the activity of people to provide them help and support in day-to-day tasks. Different models of aid could be useful for different sectors of the population. However, the focus of this research is persons in situations of dependency, mainly elderly people.

Given the current demographic situation, the frequent number of people living alone at their homes, and the care needs of these people, a flying assistant robot represents an innovative technological solution to help reducing the effects of the intrinsic capacity decline

in the elderly. This thesis, therefore, falls within the scope of assisted living environments and responds to part of the strategies that the WHO considers essential to promote healthy aging and the improvement of quality of life, which are person-based approaches and aging in place.

In this context of assistance, it is essential to know the state of the person so that the system can provide effective solutions to different situations. In this respect, since the beginning of the thesis project, the recognition of emotions has been considered as one of the most appropriate tools for this task. The idea is to perform, in the future, the analysis and interpretation of emotions through a computer system based on artificial intelligence. This system will be responsible for analyzing the facial images that the assistant robot, in this case, a UAV, provides. In addition, this system could be expanded to consider other aspects such as the behavior of the person, so that the assistance provided to the dependent person is as appropriate and complete as possible. This computer system, which will make it possible to respond to the different situations or states of the assisted person, will form part of a future comprehensive system for the home care of dependent persons. The (long-term) objective is to contribute to improving the autonomy of these people so that they continue living at their homes for as long as they wish, receiving the necessary care.

For this ambitious future project, this thesis focuses on the control and navigation of autonomous UAVs as a means for monitoring the individual. The mission of the UAV will, therefore, be to monitor the person at home. This is, in an autonomous way, and from time to time, the UAV will carry out a flight for the supervision of the person. During this flight, the UAV will position itself in front of the face of the person in order to capture facial images that can be subsequently processed to determine the emotional state of the person and the assistance required in each case.

Therefore, **the main objective of the thesis is the control and navigation of small UAVs based on computer vision for future use as part of a comprehensive system of assistance for the improvement of the quality of life and care of dependent persons**. To address this broad topic of research, the following sub-objectives are defined:

- **Sub-objective 1: Study of the integration of computer vision in navigation and flight control in autonomous UAVs.**
  - Analysis of computer vision-based solutions for flight operations in UAVs.
  - Development of navigation solutions using computer vision algorithms to process and interpret information related to the flight environment and the UAV itself.
- **Sub-objective 2: Increase of the movement capacity and improvement of the stability of the UAV in relation to disturbances of different nature.**
  - Study of the dynamic behavior of different UAV models.
  - Development and validation of robust control schemes using numerical simulation tools and experimental platforms.

- **Sub-objective 3: Development of the proposal for UAVs as assistance system for the aid of dependent persons.**
  - Study of the technical and human aspects to be considered in the design of assistant UAVs.
  - Determination of the most suitable UAV model for use in domestic environments.
  - Definition of a development and validation tool based on virtual reality.
  - Development of the trajectory planner for the UAV in the monitoring tasks.

1.3 Methodology and Work Plan

The methodology and the work plan of this thesis have been organized into three main blocks according to the sub-objectives defined above. The main research tasks carried out and the means used are briefly described below.

1. SOLUTIONS BASED ON COMPUTER VISION FOR NAVIGATION AND FLIGHT CONTROL IN AUTONOMOUS UAVs.

   1.1. Systematic Mapping Study

   Performing a systematic mapping study to review, classify and structure papers on computer vision solutions for navigation and flight control operations in UAVs. This study has been approached both from a general perspective of autonomous air vehicles and from the point of view of UAVs taking the role of personal assistants. This way, it has been possible to draw conclusions regarding which flight operations based on computer vision are more relevant on the development of such flying assistant robots, as well the most appropriate features of the UAV, vision system and validation process for this research line.

   1.2. Navigation Solutions Using Computer Vision

   Use of computer vision algorithms for the identification and interpretation of the flight environment and the state of the UAV itself, based on the information contained in aerial images. In this sense, a visual navigation solution for indoors has been developed. This solution is based on the use of a depth camera on board the flying robot. Firstly, the mapping of the flight environment is addressed using the camera as a range sensor. Secondly, the position of the robot within the map of the environment is estimated by processing the images of the depth camera as if it were a gray-scale camera.

2. DEVELOPMENT AND VALIDATION OF CONTROL ALGORITHMS FOR UAVs

2.1. Design of Control Algorithms

Theoretical study of the dynamic model of different UAVs, and design of robust control algorithms. In this regard, a quadrotor system model, a novel flapping-wing air vehicle, and the laboratory helicopter Twin Rotor MIMO System (TRMS) have been the platforms studied. For each of them, non-linear robust control schemes were designed, which were later validated by simulations and/or experimental tests.

2.2. Simulation Tests

Validation of the previously designed control algorithms through numerical simulations using the MATLAB/Simulink® software tool. These trials have been used as a preliminary step to ensure the controller's performance prior to the lab experiments, as well as the future flight tests that will be conducted with unmanned aircraft.

2.3. Experimental Tests

Experimental validation of non-linear control schemes in the TRMS. Two have been the robust controllers validated experimentally in this laboratory platform. Both use a cascade scheme that is based on the independence of the electrical and mechanical model that represents the dynamic behavior of this system.

3. PROPOSAL OF VISION-BASED UAVs TO ASSIST DEPENDENT PERSONS

3.1. Study of the Proposal

Analysis of the technical and human challenges present in the development of autonomous UAVs based on computer vision as a means for care robotics. Definition of the most suitable characteristics of the UAV as a personal assistant.

3.2. Virtual Reality Environment

Development of a virtual reality platform for the simulation of the flight of the UAV in assistance robotics. Real-time integration of the dynamic simulation software, MATLAB/Simulink®, and the Unity 3D game engine (https://unity.com) using the Message Queue Telemetry Transport (MQTT) protocol.

3.3. Trajectory Planning

Development of the trajectory planner for the flight of the UAV in tasks of monitoring the person. Simulation tests using MATLAB/Simulink® and later the virtual reality platform once its development is complete.

1.4 Thesis Outline

The following lines describe the general structure of this doctoral thesis submitted in the form of a compendium of publications. To fulfill the requirements of this format, the articles will be presented in the results chapter, maintaining the publication format of the respective journals. Some other papers published in international books have also been included. In addition to the central chapter of results, this introductory chapter and the final chapter, which is dedicated to the closure of this dissertation, have been included to contextualize, summarize and complement the information included in the publications. Below, the contents of the three chapters that make this dissertation are detailed.

Chapter 1 addresses the general considerations of the thesis, justification of the research, definition of the hypothesis and objectives, description of the work plan, and thesis outline (present section). The main points are briefly summarized below.

- The current demographic situation is marked by the increase in the number and proportion of the elderly population and the consequent need for solutions that help mitigate the loss of intrinsic capacity associated with greater longevity. In this context, robotics should play a highlighted role for the aid and care of dependent persons, generally the elderly population, but also those other persons who require daily help or assistance for other reasons such as illnesses or accidents. The monitoring of the individual is essential to identify the state of the person and determine the assistance needed at any given time. In this sense, the doctoral thesis bets on UAVs as a promising model of assistant robot, whose main mission will be to carry out flights in the patient's environment for the supervision of his/her condition. The information collected will be sent to a future computer system that will analyze the images and determine the assistance response needed for each situation.

- The main objective of the thesis is the control and navigation of UAVs based on computer vision for assistance purposes. To address it, three sub-objectives which have also defined the three stages of the work plan have been proposed. The first two of a more general nature include the study on the integration of computer vision for autonomous navigation of the UAV and the development of robust control algorithms to improve its flight capacity and stability against perturbations of different nature. The third one focuses specifically on the concept of UAV as assistance robot for home care of dependent persons.

Chapter 2 presents the results of the doctoral thesis per compendium of publications. A total of nine articles have been included, of which four have been published in journals indexed in the Journal Citation Reports (JCR) and five have been published as book chapters. It should be noted that all the included publications are related to the research line on UAVs and/or their use for assistance robotics. This way, the chapter has been structured in four sections that group the works according to their main topic:

1. Control and Navigation of UAVs Based on Computer Vision

   Section 2.1 includes two papers related to computer vision in autonomous UAVs. Firstly, there is a systematic mapping study on vision-based solutions for navigation and flight control operations in UAVs, and secondly a visual navigation proposal based on the use of a depth camera on board a flying robot.

2. Simulation of Control Algorithms

   Section 2.2 groups a total of three papers that deal with the design of novel control algorithms for a quadrotor system, a flapping-wing UAV and the laboratory helicopter TRMS, respectively. These three control schemes have been validated by means of numerical simulations within the MATLAB/Simulink® environment.

3. Experimentation of Control Algorithms

   Section 2.3 contains two papers on nonlinear cascade-based controllers designed and validated experimentally with the TRMS platform. At this point, it is necessary to highlight the paper "A Tandem Active Disturbance Rejection Control for a Laboratory Helicopter with Variable Speed Rotors" published in the journal IEEE Transactions on Industrial Electronics, number one in two JCR categories, Automation & Control Systems, and Instruments & Instrumentation.

4. UAVs Based on Computer Vision for Assistance Robotics

   Section 2.4 encompasses two papers focused on the proposal of UAVs as assistants for dependent persons. The first deals with the matter from a more theoretical point of view, describing the main challenges in the design of the assistant UAVs and the proposed virtual reality platform, while the second deals with the trajectory planning of a quadrotor for the monitoring flight.

Chapter 3 is dedicated to the closure of this dissertation. Two sections constitute this chapter. Firstly, a broad discussion about the research carried out is presented. The text is divided again into the three main blocks according to the sub-objectives and work plan; computer vision in autonomous UAVs, development of robust control algorithms and the proposal of UAVs to assist dependent persons. The main contributions regarding each goal are detailed at this point. Secondly, the last section briefly deals with conclusions and future works. This way, a dissertation recap is provided, the ongoing research is described, and future directions to continue the research line in UAVs for assistance purposes are recommended.

CHAPTER 2

Results

This chapter presents the results published on the research carried out during the development of the doctoral thesis. The chapter is divided into four sections which group the works according to their topic. Section 2.1 is focused on the study of how computer vision is integrated as part of the navigation and flight control solutions for autonomous UAVs. Section 2.2 presents those works in which simulations of newly designed control algorithms have been performed for different unmanned aircraft models. Section 2.3 is focused on those research works that address the design of robust control algorithms and their experimentation in a laboratory platform whose dynamic behavior is similar to a real helicopter. Finally, Section 2.4 includes those articles focused on the proposal of vision-based autonomous UAVs taking the role of personal assistants, the ambitious research initiated with this doctoral thesis.

2.1 Control and Navigation of Unmanned Aerial Vehicles Based on Computer Vision

The main topic of the doctoral thesis is the control and navigation of UAVs based on computer vision with application in the field of assistance robotics. In this context, autonomous UAVs are required, i.e, those unmanned aircraft which are not controlled or supervised by an operator on the ground. The first research question is, therefore, how computer vision is used in autonomous UAVs.

Vision sensors, mainly cameras, capture information from the flight environment and the aircraft itself. This information is later processed by computer vision algorithms in order to obtain useful reference data that are integrated into the navigation and control systems of these aircraft. In this sense, a vast amount of works on vision-based solutions for different flight operations in autonomous UAVs have been published in the last few years. To analyze this previous research, a systematic mapping study has been performed.

A systematic mapping study is a method to review, classify and structure documents focused on a specific research topic. In this case, a total of 144 papers on vision-based solutions for navigation and/or flight control in autonomous UAVs were analyzed. The papers were classified according to four categories: (a) the task for which computer vision has been used, (b) the class of UAV for which the solution was designed or validated, (c) the features of the vision system employed, and finally, (d) the types of tests performed to validate the proposals. This study allowed not only to obtain a wide point of view on this topic, the vision-based solutions for autonomous UAVs, but also obtain conclusions on which operations our research should focus on, and what are the most suitable characteristics of the UAV and the vision system for their future use as personal assistants.

The systematic mapping study was the subject of the scientific publication presented in Subsection 2.1.1: "Computer Vision in Autonomous Unmanned Aerial Vehicles – A Systematic Mapping Study".

In the research line on computer vision techniques for UAVs, a visual navigation solution in home facilities was developed in the publication "Flying Depth Camera for Indoor Mapping and Localization", which is presented in Subsection 2.1.2. This proposal is based on the use of a depth camera with double functionality on board a flying robot. Firstly, the depth camera is utilized as a range sensor for mapping purpose. In this phase, the flight environment is represented as a collection of modular occupancy grids which are added to the map as far as the robot finds objects outside the existing grids. Secondly, the vision system is considered as a gray-scale camera to extract features which can be tracked in order to estimate the flying robot's position in the environment.

2.1.1 Computer Vision in Autonomous Unmanned Aerial Vehicles – A Systematic Mapping Study

Publication Data

ABSTRACT:
Personal assistant robots provide novel technological solutions in order to monitor people's activities, helping them in their daily lives. In this sense, unmanned aerial vehicles (UAVs) can also bring forward a present and future model of assistant robots. To develop aerial assistants, it is necessary to address the issue of autonomous navigation based on visual cues. Indeed, navigating autonomously is still a challenge in which computer vision technologies tend to play an outstanding role. Thus, the design of vision systems and algorithms for autonomous UAV navigation and flight control has become a prominent research field in the last few years. In this paper, a systematic mapping study is carried out in order to obtain a general view of this subject. The study provides an extensive analysis of papers that address computer vision as regards the following autonomous UAV vision-based tasks: (1) navigation, (2) control, (3) tracking or guidance, and, (4) sense-and-avoid. The works considered in the mapping study –a total of 144 papers from an initial set of 2,081– have been classified under the four categories above. Moreover, type of UAV, features of the vision systems employed and validation procedures are also analyzed. The results obtained make it possible to draw conclusions about the research focuses, which UAV platforms are mostly used in each category, which vision systems are most frequently employed, and which types of tests are usually performed to validate the proposed solutions. The results of this systematic mapping study demonstrate the scientific community's growing interest in the development of vision-based solutions for autonomous UAVs. Moreover, they will make it possible to study the feasibility and characteristics of future UAVs taking the role of personal assistants.

CITATION:
L.M. Belmonte; R. Morales; A. Fernández-Caballero; "Computer Vision in Autonomous Unmanned Aerial Vehicles – A Systematic Mapping Study". *Applied Sciences*, 9(15), article 3196. MDPI, 2019. ISSN 2076-3417. DOI:10.3390/app9153196.

© 2019 by the authors. Licensee MDPI, Basel, Switzerland. This article is an open access article distributed under the terms and conditions of the Creative Commons Attribution (CC BY) license (http://creativecommons.org/licenses/by/4.0/).

applied sciences

MDPI

Review

Computer Vision in Autonomous Unmanned Aerial Vehicles—A Systematic Mapping Study

Lidia María Belmonte [1,2], Rafael Morales [1,3] and Antonio Fernández-Caballero [1,2,*]

1 Escuela Técnica Superior de Ingenieros Industriales, Universidad de Castilla-La Mancha, 02071 Albacete, Spain
2 Departamento de Sistemas Informáticos, Universidad de Castilla-La Mancha, 02071 Albacete, Spain
3 Departamento de Ingeniería Eléctrica, Electrónica, Automática y Comunicaciones, Universidad de Castilla-La Mancha, 02071 Albacete, Spain
* Correspondence: Antonio.Fdez@uclm.es; Tel.: +34-967-599-200

Received: 29 May 2019; Accepted: 22 July 2019; Published: 5 August 2019

Abstract: Personal assistant robots provide novel technological solutions in order to monitor people's activities, helping them in their daily lives. In this sense, unmanned aerial vehicles (UAVs) can also bring forward a present and future model of assistant robots. To develop aerial assistants, it is necessary to address the issue of autonomous navigation based on visual cues. Indeed, navigating autonomously is still a challenge in which computer vision technologies tend to play an outstanding role. Thus, the design of vision systems and algorithms for autonomous UAV navigation and flight control has become a prominent research field in the last few years. In this paper, a systematic mapping study is carried out in order to obtain a general view of this subject. The study provides an extensive analysis of papers that address computer vision as regards the following autonomous UAV vision-based tasks: (1) navigation, (2) control, (3) tracking or guidance, and (4) sense-and-avoid. The works considered in the mapping study—a total of 144 papers from an initial set of 2081—have been classified under the four categories above. Moreover, type of UAV, features of the vision systems employed and validation procedures are also analyzed. The results obtained make it possible to draw conclusions about the research focuses, which UAV platforms are mostly used in each category, which vision systems are most frequently employed, and which types of tests are usually performed to validate the proposed solutions. The results of this systematic mapping study demonstrate the scientific community's growing interest in the development of vision-based solutions for autonomous UAVs. Moreover, they will make it possible to study the feasibility and characteristics of future UAVs taking the role of personal assistants.

Keywords: personal assistant robot; unmanned aerial vehicle; computer vision; systematic mapping study

1. Introduction

The use of unmanned aerial vehicles (UAVs) has significantly increased in recent years. These aircraft are mainly characterized by the fact that they allow access to remote places without the direct intervention of a human operator aboard. These places are generally difficult to access and/or have unfavorable conditions. UAVs' abilities are permitting their use in manifold applications, such as remote sensing, support in emergency situations, inspection of infrastructures, logistics systems, professional photography and video, and precision agriculture spray systems, among others [1]. An emerging domain is flying assistance robotics, where UAVs come through with a present and future model of fully autonomous personal monitoring capacities. Some examples are Aire, a self-flying robotic assistant for the home [2], Fleye, a personal flying robot [3], and CIMON and Astrobee, flying assistant robots in the space station [4,5].

Appl. Sci. **2019**, *9*, 3196

Personal assistant robots are principally based on monitoring people's activities in order to provide them help and support in daily activities. Our current research interest is framed in this field. One of our major objectives is to design an autonomous aerial vehicle to assist dependent people [6,7]. In this sense, it is necessary that a vision system captures images of the dependent person, which are analyzed in order to determine the assistance required at each moment. Therefore, it is necessary to address the problem of autonomous navigation in both indoor and outdoor environments. In other words, the UAV must perform flights in a completely autonomous manner. At this point, and given the need to have a vision system for monitoring the assisted person, both issues may be intertwined.

In this respect, a series of complex operations must still be solved in order to achieve fully autonomous UAVs. Full autonomous navigation means flying in an environment without even requiring the control of an operator on land. In this respect, it should be noted that a UAV requires sensors to (a) measure the aircraft's state, (b) sense the environment, (c) detect landmarks and targets (in tracking missions), and even (d) detect both static and dynamic obstacles, among others, if it is to fly autonomously. Moreover, it is necessary to integrate this information into a control system so as to ensure that the movement of the aircraft is accurate and safe.

Vision systems play an outstanding role as regards performing all these complex and interrelated tasks, since images captured by a vision camera contain a vast amount of data concerning the flight environment. This information is then extracted and analyzed by using computer vision algorithms to obtain useful information for navigation and flight control. As a result, the amount of works focused on the development of solutions based on computer vision for autonomous UAVs has grown notably in the last few years. We therefore present a systematic mapping of literature in order to summarize and analyze the research carried out on this topic.

A systematic mapping is a method that is employed to review, classify and structure documents focused on a specific research topic. Systematic mapping studies were initially used principally in the field of medical research, but they are now also being applied to other areas related to engineering and new technologies, such as web development [8], mobile devices [9], social-technical congruence [10], and unmanned aerial systems in smart cities [11]. With regard to the topic of computer vision systems in mobile robots, reviews and meta-analyses have been presented for both ground [12] and aerial vehicles [13–15]. However, a systematic mapping study that provides an objective procedure with which to identify the nature and extent of the research on this topic has not been conducted to date. This is, therefore, to the best of our knowledge, the first systematic mapping study focused on how computer vision is being used in autonomous flying robots. Its purpose is to provide a global view of those papers that introduce computer vision-based solutions for autonomous UAVs.

The paper is organized as follows. Section 2 describes the research method used, including the research questions and classification scheme. Section 3 presents the results obtained from the systematic mapping study. Finally, Section 4 provides the main findings of the study and Section 5 the most relevant conclusions.

2. Methods

A systematic mapping study "maps" a research area by classifying papers in order to identify which topics are well-studied and which need additional study. Therefore, a systematic mapping study aims to get an overview of a certain research area and how far it is covered in research by studying the research field by using methods from information retrieval and statistical analysis. The present systematic mapping study has been performed on the basis of guidelines provided by the Template for a Mapping Study Protocol [16]. Figure 1 illustrates the methodology used. It mainly consists of four steps: (1) the definition of the research questions in order to determine the search strategy, (2) performing the search to obtain an initial set of documents, (3) the screening of papers to select the most relevant ones, and (4) the classification and mapping process carried out in order to eventually obtain the results. The research questions, search strategy, inclusion and exclusion criteria, studies selection and classification scheme are detailed below.

Appl. Sci. **2019**, *9*, 3196

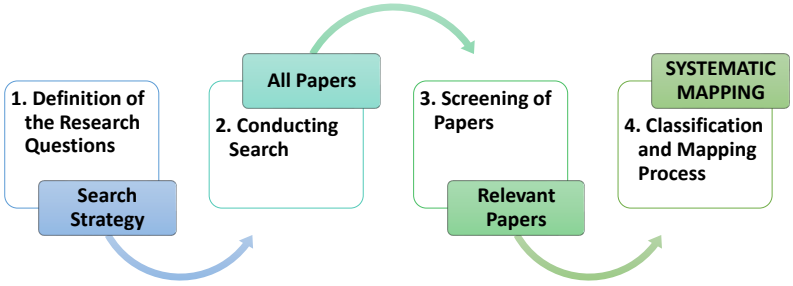

Figure 1. Systematic mapping process.

2.1. Research Questions

As stated before, the goal of this systematic mapping study is to provide an overview of the current research on the topic of computer vision in autonomous UAVs. This way, we will obtain a broad view of navigation and flight control operations in which computer vision is relevant. Consequently, it will be possible to address future in-depth studies for the development of autonomous aerial robots, and, particularly, assistant UAVs. This overall approach has led to the following research questions:

- *RQ1: How many papers have been published on computer vision in autonomous UAVs?*
  This first question aims to discover the number of works about the use of computer vision in autonomous UAVs that have been published and the forums in which these papers are most frequently published.
- *RQ2: How is computer vision used in autonomous UAVs?*
  The second question concerns the idea of grouping articles according to the type of operation for which computer vision is used. Four main categories related to navigation, stability and maneuver control, guidance or tracking, and obstacle detection and avoidance are considered. This enables us to know on what areas the research is principally focused, and allows us to carry out a more in-depth analysis of the remaining questions.
- *RQ3: What types of UAVs have been used in the proposed solutions?*
  One of the most determining aspects is to discover for what type of UAV platform each proposal has been designed and validated. This is precisely the goal of the third question. In addition, by considering the first classification on the use of vision, we can get an idea of which type of UAV is most frequently used in each operation.
- *RQ4: What are the characteristics of the vision systems?*
  The number, localization, and orientation of the cameras will be analyzed at this point in order to draw conclusions about the main features of the vision systems commonly used in each navigation and flight control area.
- *RQ5: What is the validation process for each proposed solution?*
  The last research question is related to the kind of tests carried out to validate the proposals; flight, experimental, and simulation trials, or a combination of them. The idea is to perform an analysis of the kind of tests most frequently performed for each main category considered.

2.2. Research Strategy

A search string was defined in order to automatically find articles that use computer vision technologies for the autonomous navigation and control of UAVs by using terms related to the two main concepts: *UAV* and *vision*. The search string was, therefore, composed of two parts. The first part contained words related to autonomous aircraft, while the second was defined by employing terms related to computer vision. Table 1 shows the definition of the search string, in which the Boolean OR was used to join terms and synonyms, and the Boolean AND was used to join the two main parts.

Table 1. Search string.

Concept	Alternative Terms and Synonyms	
UAV	*("unmanned aerial vehicle" OR "unmanned air vehicle" OR "unmanned aircraft systems" OR "UAV" OR "UAS" OR "autonomous aerial vehicles" OR "aerial robotics" OR "flying machines" OR "quadrotor" OR "quad-rotor" OR "quadcopter" OR "helicopter" OR "rotorcraft" OR "VTOL" OR ("vertical taking off" AND "landing"))*	AND
vision	*("vision" OR "image" OR "visual" OR "video" OR "artificial intelligence" OR "camera" OR "lidar")*	

2.3. Inclusion and Exclusion Criteria

Inclusion and exclusion criteria were formulated in close relation to our current research interests in aerial assistant robots. In this sense, we only focused on works concerning technological solutions and not on their acceptance. Thereby, only papers published in Engineering and Computer Science on autonomous vision-based navigation and flight control solutions for individual UAVs (not swarm or multi-UAVs) were considered. In this manner, inclusion and exclusion criteria were defined as follows:

- Inclusion criteria:
  - I1. Papers focused on computer vision for autonomous UAVs.
  - I2. Papers whose subject area is Engineering or Computer Science.
  - I3. Papers written in English.
  - I4. Papers published until 31 December 2017.
- Exclusion criteria:
  - E1. Review papers.
  - E2. Papers describing missions with multiple UAVs.
  - E3. Papers focused only on recording and/or enhancing aerial images.
  - E4. Papers focused on designing UAV simulators or hardware.
  - E5. Papers not focused on UAV navigation or flight control.

2.4. Selection of Studies

This section shows details of the results obtained during the process of selecting the papers (see Figure 2).

The Scopus database was selected with the objective of finding papers containing the words related to UAVs and vision defined by the search string (see Table 1) in their title, abstract or keywords. Additionally, some options of the Scopus search engine were used to limit the results to papers published in the areas of Engineering or Computer Science (I2), written in English (I3), and published until December 2017 (I4). The complete research string can be consulted in Figure 2.

The search took place in June 2018 and resulted in a total of 2081 papers. After collecting the papers, eight duplicated works were removed and the other 2073 articles were passed through a screening process composed of three filters. Firstly, a manual screening was carried out to analyze them. In this stage, we observed that many papers referred to vision systems in remotely controlled UAVs (not autonomous) or that the flight control system did not depend on visual information. In the kind of papers mainly focused on applications such as remote sensing, the vision system is not, therefore, used for the navigation and/or flight control of autonomous UAVs, signifying that inclusion criterion I1 was not completely met. An automatic filter (see details in Figure 2) was consequently applied to ensure the effectiveness of this criterion.

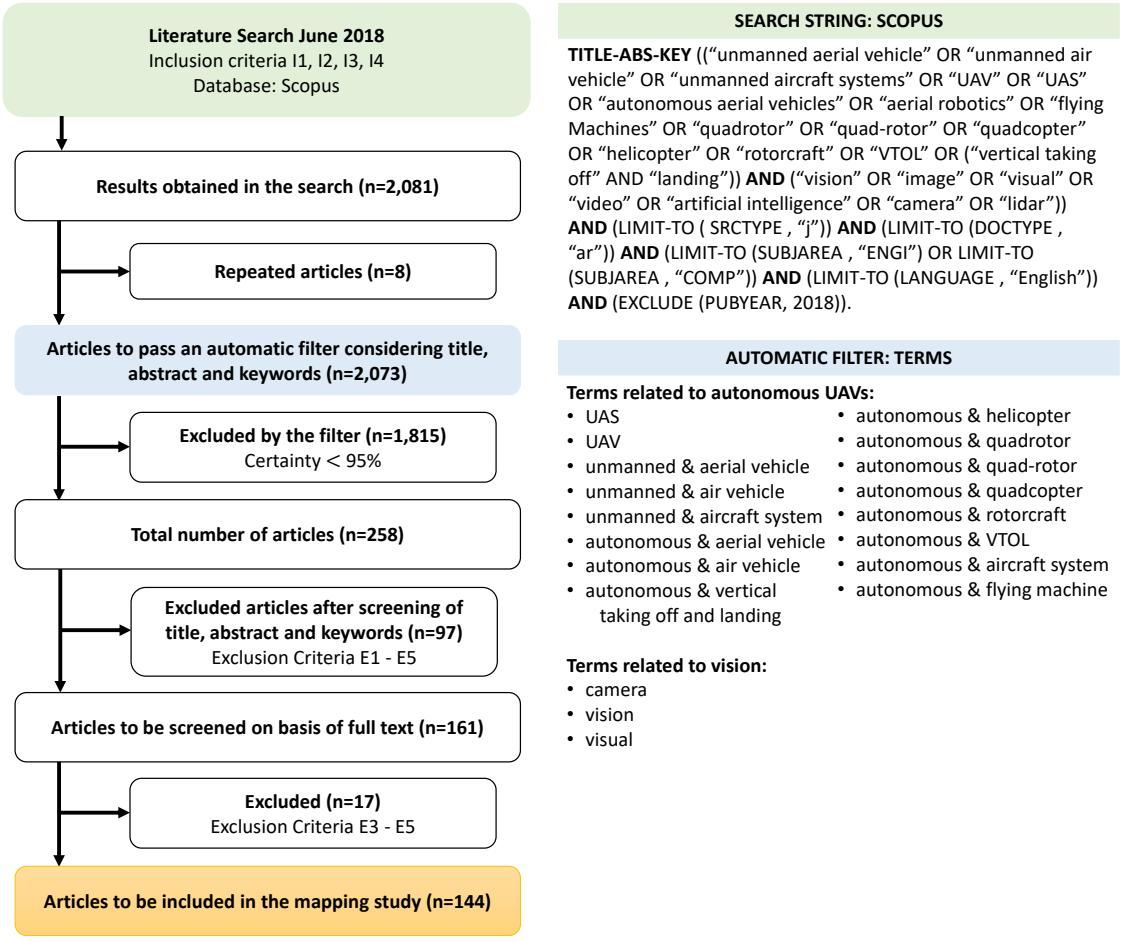

Figure 2. Systematic search consort diagram.

The idea was that papers that contained at least one term (or a pair of terms) on UAVs and at least one vision term in title, abstract and keywords, would attain a 100% certainty percentage. When the presence of these terms in any of these fields decreased, their percentage also decreased. After the application of the automatic filter—which excluded a total of 1815 articles whose certainty percentage was lower than 95—two filtering processes were manually performed.

During a first manual screening, each record retrieved from the automated filter was evaluated to decide whether or not it should be excluded by reading its title, abstract and keywords. As a result, 97 of the 258 remaining papers were excluded because their title, abstract or keywords met at least one of the exclusion criteria E1 to E5. After removing these papers, a last filter was applied using the same exclusion criteria but this time screening the full-text. In this step, after reading the complete text of the remaining 161 articles, 17 works were not included in the final selection owing to the fact that they satisfy at least one of the some exclusion criteria E3 to E5. After carrying out the selection process, a total of 144 articles were considered in order to carry out the systematic mapping study.

2.5. Classification

The papers were classified according to four properties that were used to answer the research questions (see Figure 3): the *Task* for which computer vision has been used, the *Class of UAV* for which the vision-based solution has been designed, the *Vision System* employed, and the *Validation Process* used to test the solution.

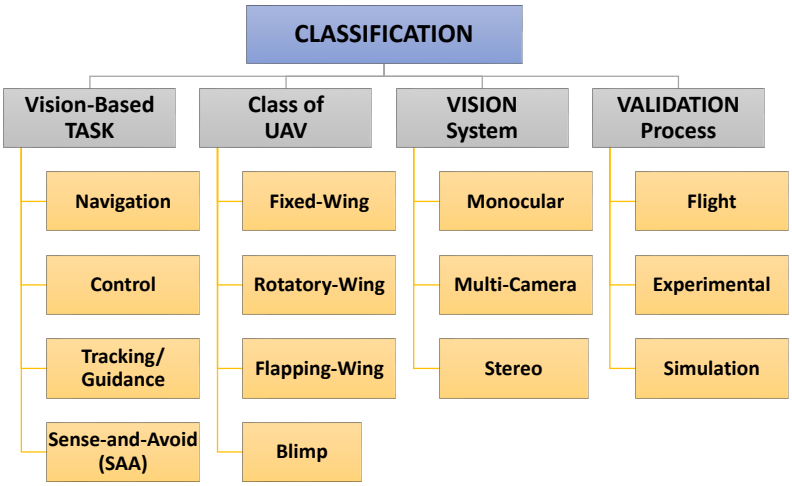

Figure 3. Classification scheme.

2.5.1. Vision-Based Task

With regard to RQ2 (*Use of Computer Vision*), each paper was classified in one of the following main categories:

- *Visual Navigation*: The navigation task includes determining the aircraft's position and orientation (e.g., [17–19]). Sensors are, therefore, required to measure the aircraft's state and to sense the flight environment. Here, the main feature when compared to those of other solutions is the use of a vision system as the main sensor, which may be complemented by other sensors (e.g., inertial measurement units, global positioning systems) in order to correct the visual estimation. Two examples are shown in Figure 4. These are a quadrotor using artificial visual markers to estimate its position in an indoor environment (see a.1), and a vision-based terrain referenced navigation approach, in which aerial images are compared with a digital terrain elevation database to estimate the UAV's position (see a.2).
- *Vision-Based Control*: The aircraft's position and orientation are controlled on the basis of the information captured by vision sensors and subsequently processed by computer vision algorithms (e.g., [20–22]). The vision-based control of UAVs began in the 1990s. Since then, several solutions have been proposed in order to address operations such as stabilization to maintain a constant altitude and/or a straight flight (see b.1), and maneuver control to guide a UAV so that it performs a specific and precise movement, such as positioning with respect to a visual mark (see b.2). When the information obtained by a vision system is integrated into the control loop directly, this is called *visual servoing*. In this case, the control law depends directly on the error signal obtained from visual information.
- *Vision-Based Tracking/Guidance*: In vision-based tracking or guidance, the UAV control system is designed to perform a flight based on relative navigation with respect to a target—usually in motion—or a flight path defined by a series of visual references or features (e.g., [23–25]). A vision-based system must, therefore, be able to detect the target or visual reference, estimate its position and determine the actions required to control the UAV's flight path. Two examples are presented in Figure 4. There is a mobile target tracking by a fixed-wing UAV (see c.1) and a quadrotor following a visual path defined by images of a previously known environment (see c.2).
- *Vision-Based Sense-and-Avoid (SAA)*: A completely autonomous navigation requires the ability to detect and avoid both static and dynamic obstacles. When these tasks are performed on the basis of the information captured and processed by a vision system, we refer to vision-based sense-and-avoid (e.g., [26–29]). The main objective is, therefore, to use one or more cameras to detect possible collisions with objects or even with other aircraft, and to determine the control

actions required to achieve a collision-free flight. Two examples of vision-based SAA operations are illustrated in Figure 4. We have a quadrotor detecting the approach to an obstacle in its flight path (see d.1), and a mapping-based autonomous flight of a quadrotor in a coal mine (see d.2).

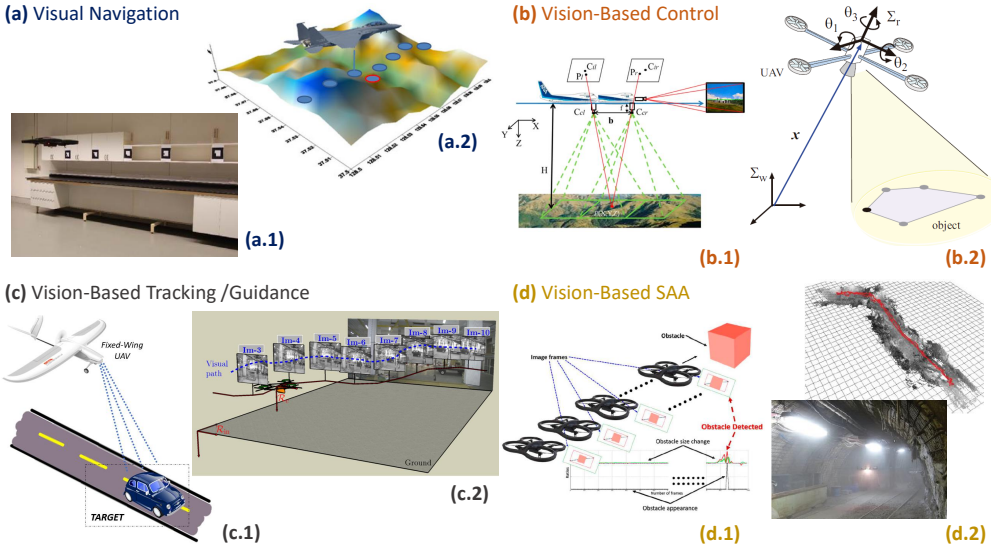

Figure 4. Examples of vision-based tasks. (**a**) visual navigation: **a.1** (reprinted from [19] under the terms of the Creative Commons Attribution License), **a.2** (reprinted by permission from Springer Nature: [30], Copyright 2012); (**b**) vision-based control: **b.1** (reprinted from [31] under the terms of the Creative Commons Attribution License), **b.2** (reprinted from [32] by permission from Taylor & Francis Ltd); (**c**) vision-based tracking/guidance: **c.1** (illustration of a target tracking mission, e.g. [33]), **c.2** (reprinted from [34], Copyright 2010, with permission from Elsevier); (**d**) vision-based sense-and-avoid: **d.1** (reprinted from [29] under the terms of the Creative Commons Attribution License), **d.2** (reprinted from [35] by permission from John Wiley and Sons).

2.5.2. Class of UAV

With regard to RQ3 (*UAV Platform*), each paper was classified into one of the following classes of UAV according to the aircraft's configuration [36,37]:

- *Fixed-Wing*: This aircraft consists basically of a rigid wing that has a predetermined airfoil, which makes flight possible by generating lift due to the UAV's forward airspeed. This airspeed is generated by the forward thrust produced usually by a propeller turned by an electric motor. It is mainly characterized by its high cruise speed and long endurance and is mostly used for long distance, long range and high altitude missions (e.g., [38–41]). Two models of fixed-wing UAVs are illustrated in Figure 5 (see a.1 and a.2).
- *Rotatory-Wing*: These aircraft have rotors composed of blades in constant motion, which produce the airflow required to generate lift. These flying machines, which are also called vertical take-off and landing (VTOL) rotorcraft, are normally used for missions that require hovering flight. They allow a heavier payload, easier take-off and landing, and better maneuvering than fixed-wing UAVs (e.g., [42–45]). The most common models are helicopters and quadrotors, a multi-rotor aircraft with four rotors that is widely used at present [46]. Figure 5 displays two such models, a helicopter (see b.1), and a quadrotor, also named quadcopter (see b.2).
- *Flapping-Wing*: This class of micro-UAV reproduces the flight of birds or insects [47–49]. It has an extremely low payload capability and low endurance owing to its reduced size. However, flapping-wing UAVs have low power consumption and can perform vertical take-offs and

landings. Despite these advantages, the difficulties related to their construction and set-up are still relevant today. Two designs of these novel aircraft are illustrated in Figure 5 (see c.1 and c.2).

- *Airship*: An airship or dirigible is a "lighter-than-air" aircraft that is steered and propelled through the air by using rudders and propellers or another thrust. These aerostatic aircraft stay aloft by filling a large cavity like a balloon with a lifting gas. Major types of airship are non-rigid (or blimps), semi-rigid and rigid. A blimp (technically a "pressure airship") is a powered, steerable, lighter-than-air vehicle whose shape is maintained by the pressure of gases within its envelope [50]. Since no energy is expended to lift this aircraft, the saving is used as a power source for displacement actuators, thus enabling long-duration flights. In addition, this air vehicle has the capability to work safely at low levels, close to people and buildings [51,52]. Figure 5 shows two examples of airship, namely, a blimp UAV (see d.1), and an innovative blimp UAV in spherical-shape (see d.2).

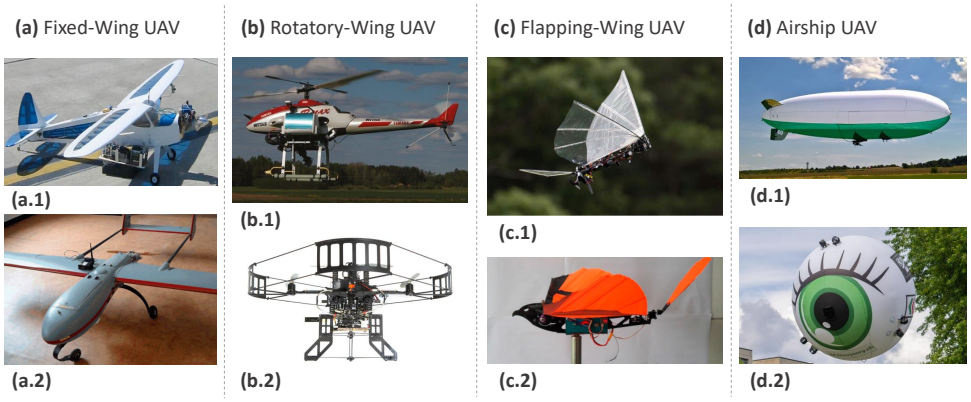

Figure 5. Classes of Unmanned Aerial Vehicles (UAVs): Examples of commercial and prototype aircraft. (**a**) fixed-wing UAV: **a.1** Sig rascal model (reprinted from [53] by permission from American Society of Civil Engineers), **a.2** fixed-wing platform (reprinted from [38] under the terms of the Creative Commons Attribution License); (**b**) rotatory-wing UAV: **b.1** Yamaha Rmax helicopter (reprinted from [54] under the terms of the Creative Commons Attribution License), **b.2** experimental platform based on an Ascending Technologies Pelican quadrotor (reprinted from [35] by permission from John Wiley and Sons); (**c**) flapping-wing UAV: **c.1** Robo Raven V (reprinted from [55] under the terms of the Creative Commons Attribution License), **c.2** Carbonsail Ornithopter kit (reprinted from [49] under the terms of the Creative Commons Attribution License); (**d**) airship: **d.1** Airship ACC – 15X developed by CS AERO (https://www.csaero.cz/en), **d.2** Skye drone developed by AEROTAIN (http://www.aerotain.com/).

2.5.3. Vision System

With regard to RQ4 (*Vision System*), each paper was first classified by considering the number of cameras as:

- *Monocular*: A vision system with just one camera is used as a vision-based solution (e.g., [56–59]). An example of a monocular system is displayed in Figure 6 (a.1).
- *Multi-camera*: A vision system with two or more cameras is employed in the proposed approach. Here, the cameras are separate or have different orientations (e.g., [60–62]). A multi-camera configuration is illustrated in Figure 6 (a.2).
- *Stereo*: A special and widely used case of a multi-camera system with two cameras in a stereo configuration (in the same localization and with the same orientation) or a stereo-camera (two vision sensors) is employed for the vision-based proposal (e.g., [63–66]). A stereo vision system is presented in Figure 6 (a.3).

Appl. Sci. **2019**, *9*, 3196 9 of 34

In addition to the number of cameras, their location either on board the UAV or on the ground, and the orientation of the system, that is, where the vision sensors look (in the direction of the flight, toward the ground, or toward the UAV itself), was also considered to complete the classification according to the vision system used. Figure 6 shows several configurations considering the location and orientation of the cameras (see b.1, b.2 and b.3).

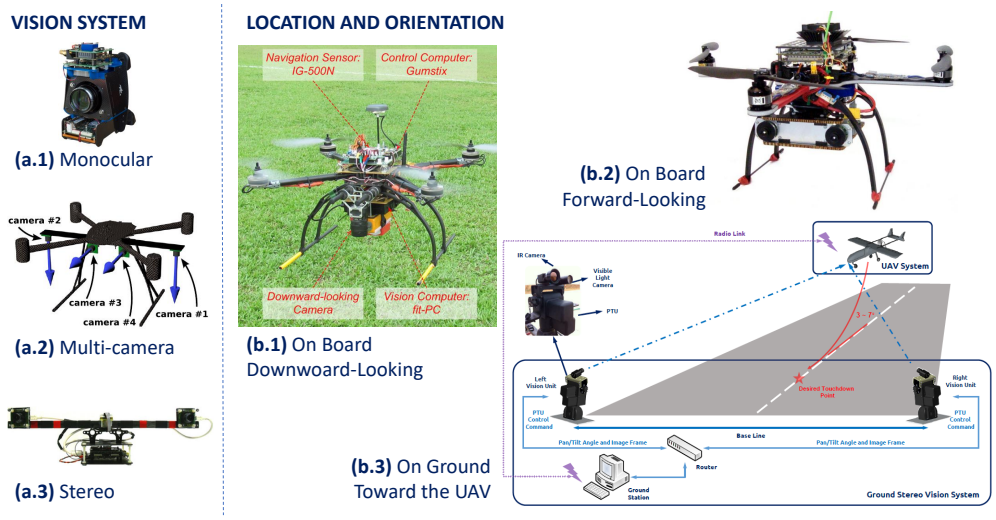

Figure 6. Classes of vision system and examples of configurations (location and orientation). (**a.1**) monocular (reprinted from [67] under the terms of the Creative Commons Attribution License); (**a.2**) multi-camera (reprinted by permission from Springer Nature: [68], Copyright 2014); (**a.3**) stereo (reprinted by permission from Springer Nature: [69], Copyright 2011); (**b.1**) on board camera pointing downward (reprinted by permission from Springer Nature:[18], Copyright 2015); (**b.2**) on board stereo camera pointing forward (reprinted by permission from Springer Nature: [70], Copyright 2013); (**b.3**) on ground stereo camera pointing toward the UAV (reprinted from [66] under the terms of the Creative Commons Attribution License.)

2.5.4. Type of Validation

With regard to RQ5 (*Validation Tests*), each paper was classified into one or more of the following types of trials (see Table 2):

- *Flight*: In this case, the proposed solution has been tested during a real flight of a UAV in outdoor and/or indoor environments (e.g., [68,71,72]). The UAV may sometimes be controlled by an operator (remotely or manually) during the flight.
- *Experimental* (e.g., [73–75]): Two kinds of experiments were considered: offline tests with which to validate the proposed solution by using data and images recorded on a previously performed flight, and lab tests in which the proposal is tested by using a laboratory platform that simulates the dynamic behavior of a real aircraft (for instance, Twin Rotor MIMO System [76–78]).
- *Simulation*: In this kind of trial, the proposed solution is validated by means of simulation tests, such as hardware-in-the-loop simulations (HILS), image-in-loop simulations (IILS), virtual reality environments, and numerical simulations. In all these cases, the main feature is that the flight of a model or virtual aircraft is simulated (e.g., [79–82]). With respect to the camera employed, it is a real device (physical), a virtual camera in a 3D environment or even a model that represents its behavior by providing theoretical measurements that would be obtained with computer vision.

Appl. Sci. **2019**, *9*, 3196

Table 2. Validation process. Features of the trials.

Validation Process	Aircraft	Camera	Environment	Flight
Flight	UAV	Physical	Indoor/Outdoor	Real-Time
Experimental				
Offline Tests	UAV	Physical	Indoor/Outdoor	Offline
Lab Tests	UAV/Platform	Physical	Lab	Limited
Simulation				
Hardware-in-the-Loop Simulation (HILS)	Virtual/Model	Physical	Virtual	Simulated
Image-in-Loop Simulation (IILS)	Virtual/Model	Physical	Indoor/Outdoor	Simulated
3D Virtual Reality	Virtual	Virtual	Virtual	Simulated
Numerical Simulation	Model	Model	Model	Simulated

3. Results

In this section, we respond to the five research questions described previously in accordance with the literature selected.

3.1. RQ1: How Many Papers Have Been Published on Computer Vision in Autonomous UAVs?

According to the classification and mapping process, a total of 144 papers have been published on computer vision for autonomous UAVs during the period studied (until December 2017). The annual trend of the papers is shown in Figure 7, which illustrates the evolution of the number of works focused on computer vision for the navigation and control of UAVs since 1999. Despite an initial slow growth in the early years, a boom started in 2007 when the amount of research began to grow remarkably. Since that year, the extension has been continuous and the number of papers published in recent years has been very significant, demonstrating that the subject matter of this review is of great interest to the scientific community.

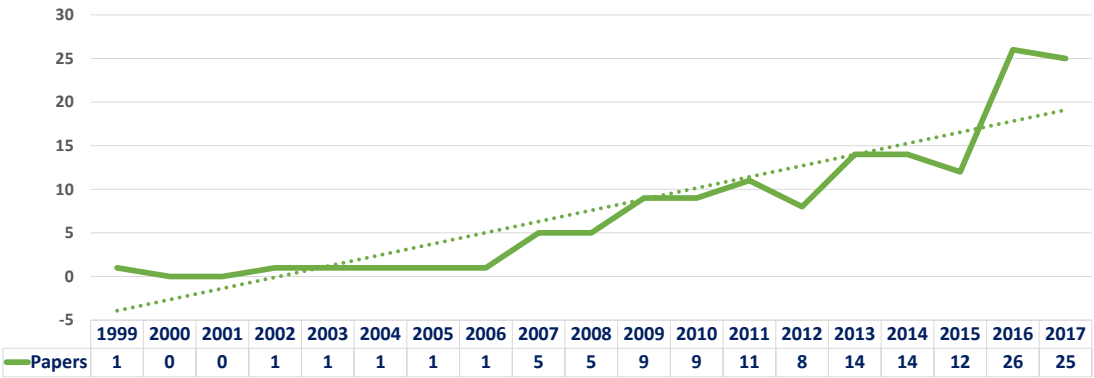

Figure 7. Annual trend of publications.

The 144 papers were published in 68 journals. As shown in Table 3, more than half of the papers originate from 13 top venues. Almost a third of the total works belong to the top five venues, which include five or more papers each. It is noteworthy that the Journal of Intelligent & Robotic Systems contains 23 papers (≈16% of the total). The full list of papers from the 68 journals can be consulted in Appendix A.

Table 3. List of the most popular publication venues.

Journal	N	%	Papers
Journal of Intelligent & Robotic Systems	**23**	15.97%	[18,20,27,30,40,51,68,69,71,73,83–95]
IEEE Transactions on Aerospace and Electronic Systems	**7**	4.86%	[28,96–101]
Sensors	**7**	4.86%	[17,29,31,66,72,102,103]
International Journal of Advanced Robotic Systems	**5**	3.47%	[38,64,104–106]
Journal of Guidance, Control, and Dynamics	**5**	3.47%	[33,39,107–109]
Autonomous Robots	**4**	2.78%	[58,110–112]
IEEE/ASME Transactions on Mechatronics	**4**	2.78%	[22,59,113,114]
Journal of Field Robotics	**4**	2.78%	[35,75,115,116]
Robotics and Autonomous Systems	**4**	2.78%	[117–120]
Canadian Aeronautics and Space Journal	**3**	2.08%	[121–123]
Control Engineering Practice	**3**	2.08%	[34,124,125]
IEEE Transactions on Industrial Electronics	**3**	2.08%	[44,126,127]
IEEE Transactions on Robotics	**3**	2.08%	[128–130]
Other 55 Journals	**69**	47.92%	[19,21,23–25,32,41–43,45,53,54,57,60–63,65, 74,80–82,131–177]

Considering the Journal Citation Reports (JCR), some conclusions can be drawn. According to data from year 2007, most of the 68 journals have a notable impact factor (IF) for categories such as 'Engineering, Aerospace', 'Robotics', 'Automation & Control Systems', 'Instruments & Instrumentations' and 'Computer Science, Artificial Intelligence'. Figure 8 represents the number of journals (and the papers published) within each JCR quartile. In this respect, 124 of 144 papers (over 86%) were published in indexed journals. These numbers make it possible to highlight the scientific relevance of the papers considered in this systematic mapping study. This also shows that the development of a fully autonomous UAV capable of flying without the control of a human operator is a challenging and multidisciplinary problem. This is a remarkable sign of the complexity involved in the development of solutions based on computer vision for UAV navigation and flight control.

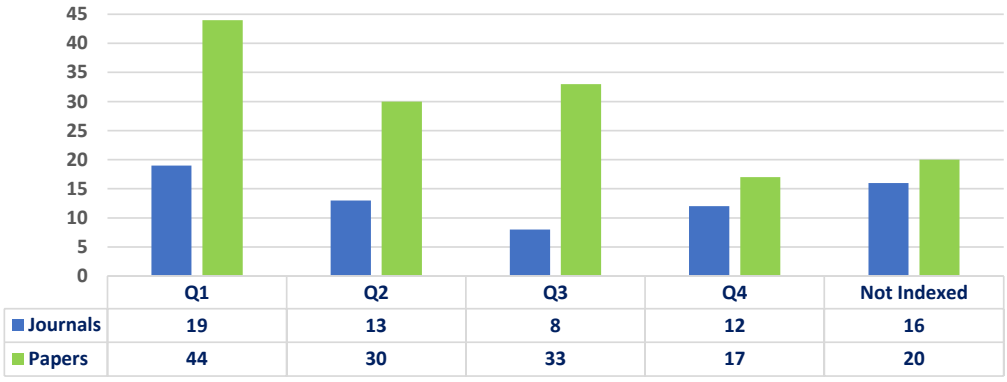

Figure 8. Quartile distribution of the number of journals and papers according to Journal Citation Reports (year 2017).

Appl. Sci. **2019**, *9*, 3196 12 of 34

3.2. RQ2: How Is Computer Vision Used in Autonomous UAVs?

Depending on the task for which computer vision has been employed, each paper has first been classified into four main categories: *1. Visual Navigation*, *2. Vision-Based Control*, *3. Vision-Based Tracking/Guidance* and *4. Vision-Based Sense-and-Avoid (SAA)*. It should be noted that solutions presented in more than one paper have been considered only once, and those papers that deal with different operations will be classified only according to the main task considered.

3.2.1. Distribution and Annual Trend per Category

The way in which the 144 papers are distributed in the four main categories is shown in Figure 9. The graph shows the number of papers in each main category and also details the classification that has been carried out considering the specific operation addressed. The results show that practically two of every three papers belong to the first two categories, 41 are focused on the design of visual solutions for UAV navigation (cat. 1) and 55 present control algorithms based on the information provided by a vision system (cat. 2) . The remaining papers are divided into the two other categories: 33 and 15 papers focus on developing solutions for the visual guidance of a UAV (cat. 3) and solutions to allow a UAV to detect and avoid obstacles during its flight (cat. 4) , respectively.

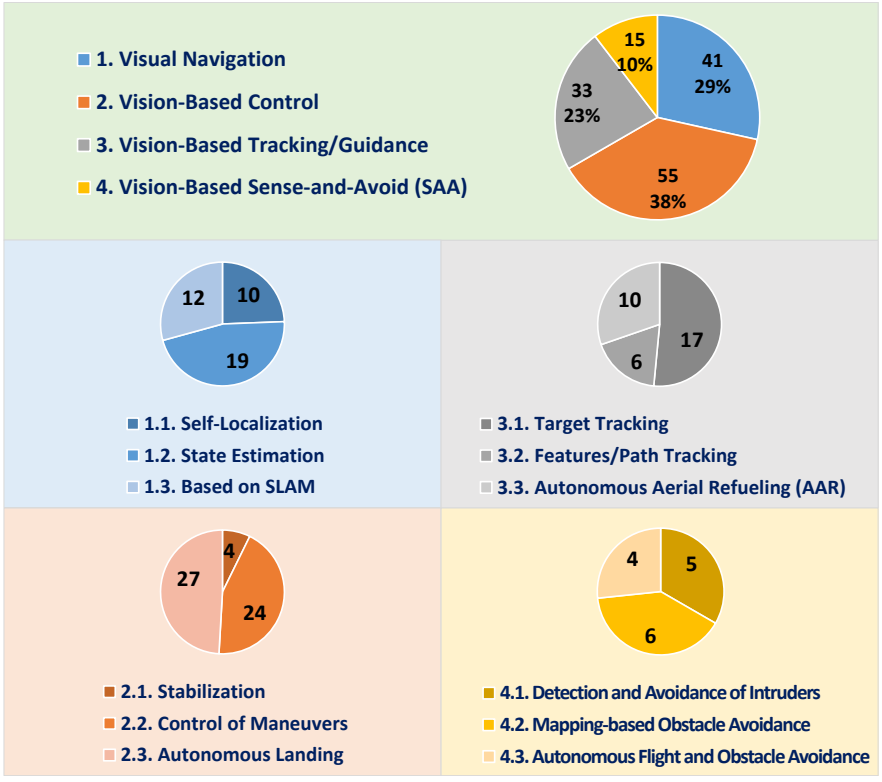

Figure 9. Category distribution over the database.

The number of works published annually within each main category can be consulted in Figure 10. In general, an upward trend that is remarkable for the second and third categories can be appreciated. When considering the publication year, we can highlight that the earlier works appertain to the two first categories, while papers presenting vision-based solutions for the guidance or detection and avoidance of obstacles are more recent. In our opinion, this is a clear consequence of the fact that navigation and control are basic (essential) tasks to be dealt with before confronting more complex tasks, such as objective/obstacle tracking and avoidance. Flying autonomously and safely requires the design of more complex and robust control systems. Another noteworthy fact is that, except in the

Appl. Sci. **2019**, *9*, 3196

first years (2000–2001), works on computer vision for UAVs have appeared annually, and, since 2013, the works have been distributed in the four categories. These data highlight the scientific community's current interest in the development of computer vision systems for different navigation and flight control operations.

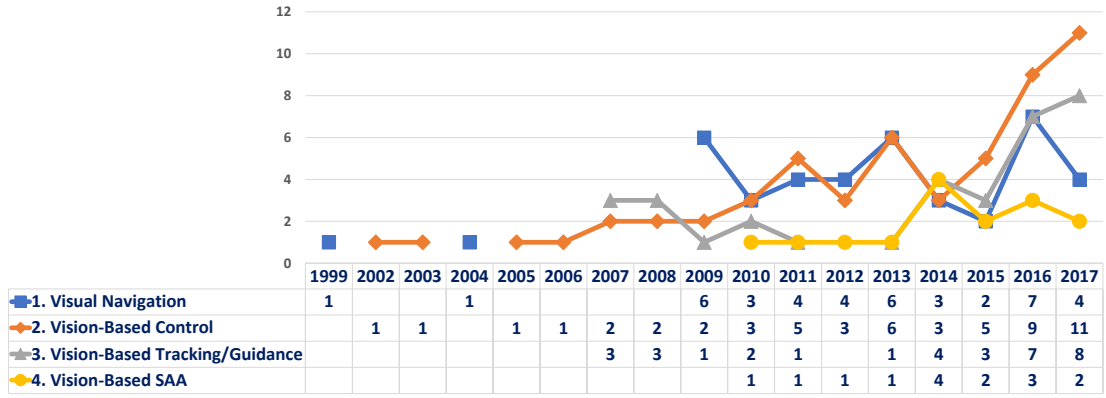

	1999	2002	2003	2004	2005	2006	2007	2008	2009	2010	2011	2012	2013	2014	2015	2016	2017
1. Visual Navigation	1			1					6	3	4	4	6	3	2	7	4
2. Vision-Based Control		1	1		1	1	2	2	2	3	5	3	6	3	5	9	11
3. Vision-Based Tracking/Guidance							3	3	1	2	1		1	4	3	7	8
4. Vision-Based SAA										1	1	1	1	4	2	3	2

Figure 10. Annual trend per category.

The data for the classification according to the specific operation can be consulted in Table 4. It shows the complete list of the 144 papers grouped into twelve subcategories (three for each main category). The operations considered and the results obtained are discussed below.

Table 4. List of papers per category.

Category	N	%	Papers
1. Visual Navigation			
1.1. Self-Localization	**10**	6.94%	[19,30,54,73,85,100,101,111,156,171]
1.2. State Estimation	**19**	13.19%	[18,65,69,93,95,105,108,110,112,117,119,120,133,136, 139,141,148,167,173]
1.3. Based on SLAM	**12**	8.33%	[17,51,68,84,86,126,146,159,160,164,175,176]
2. Vision-Based Control			
2.1. Stabilization	**4**	2.78%	[21,31,131,140]
2.2. Control of Maneuvers	**24**	16.67%	[22,32,44,45,60,61,72,87,88,97,99,109,114,115,128–130, 142,144,150,162,163,165,177]
2.3. Autonomous Landing	**27**	18.75%	[20,38,40,41,58,62,64,66,74,82,89,90,92,102–104,106, 107,113,116,118,123,125,134,135,152,170]
3. Vision-Based Tracking/Guidance			
3.1. Target Tracking	**17**	11.81%	[24,33,59,80,81,121,124,132,145,149,151,153–155,166, 168,169]
3.2. Features/Path Tracking	**6**	4.17%	[25,34,53,94,127,157]
3.3. Autonomous Aerial Refueling (AAR)	**10**	6.94%	[23,42,57,63,96,137,138,147,161,174]
4. Vision-Based Sense-and-Avoid (SAA)			
4.1. Detection and Avoidance of Intruders	**5**	3.47%	[27,39,43,75,98]
4.2. Mapping-based Obstacle Avoidance	**6**	4.17%	[28,35,71,91,122,158]
4.3. Autonomous Flight and Obstacle Avoidance	**4**	2.78%	[29,83,143,172]

3.2.2. Vision-Based Task

Category 1. Visual Navigation

Firstly, it should be kept in mind that the flight control of a UAV depends principally on knowing where the UAV is and where it wants to go. Knowledge of the aircraft's state is, therefore, essential. Therefore, it seems logical that navigation solutions have been the focus of much research carried out to date. The subcategories considered within the first category are: *1.1. Self-Localization* for those papers that use computer vision to determine the aircraft's position within the flight environment (19 papers); *1.2. State Estimation* for papers focused on solutions by which to compose the aircraft's state using visual information (based principally on visual odometry) (10 papers); and, *1.3. Based on SLAM* to classify vision-based solutions that simultaneously determine the aircraft's localization and build a map or model of the flight environment (12 papers). At this point, it is important to note that other sensors are frequently used to complement and correct the visual ones. The most common are global positioning systems (only for outdoors), inertial measurement units, and altimeters.

Unfortunately, this information is not clearly detailed in some papers analyzed, especially papers in which validation trials do not consist of real flights. For this reason, the study of complementary sensors had not been considered in this mapping study. However, it would be interesting to address this issue in future more in-depth reviews.

Category 2. Vision-Based Control

This is the category in which the greatest number of papers has been found. In addition, its tendency toward annual growth is highly notable. As mentioned above, vision-based control consists of determining the actions required to control the aircraft's position and orientation by using visual information as a reference. In this second category, the papers have been classified, according to their control purpose, into: *2.1. Stabilization* when visual information is integrated into the control system of the aircraft to stabilize its flight; principally using the skyline as a reference, or using algorithms for the detection and compensation of movement; *2.2. Control of Maneuvers* when the objective is to regulate the UAV's position in order to perform accurate movements such as positioning in relation to a visual landmark; and *2.3. Autonomous Landing* when the information provided by vision sensors is integrated into the landing control system (papers focused on the detection of the landing site and the consequent estimation of the aircraft's pose to assist in landing have also been considered here). The results show that stabilization is, without any doubt, the least frequent topic with only four papers, while both the control of maneuvers and landing (a specific type of maneuver) are the subcategories with a greater number of papers (24 and 27, respectively).

Visual Servoing

At this moment, it is important to introduce visual servoing [88], which means that the motion of a UAV (or a robot, in general) is controlled with respect to a visual target, defined by features or artificial landmarks. Visual information is directly integrated into the feedback control in this widely used control approach. Three main methods are considered [163]: (a) position-based visual servoing (PBVS), or 3D visual servoing, which involves the reconstruction of the target pose with respect to the camera, (b) image-based visual servoing (IBVS), or 2D visual servoing, which aims to control the dynamics of features directly in the image plane, and (c) hybrid visual servoing, or 2 1/2D visual servoing, which is based on combining visual features obtained directly from the image, and features expressed in the Euclidean space.

Of these three methods, the most commonly used is IBVS, in which the control action is directly determined from the error signal obtained by comparing the actual image captured by the camera and a reference image. This method has been used principally in maneuvers for rotatory-wing UAVs and in landing for fixed-wing UAVs. Furthermore, the visual servoing scheme is not only limited to operations classified under vision-based control. In fact, it has been widely used in target following missions

(generally in motion). This is one of the operations considered in the vision-based guidance/tracking category discussed below. In relation to visual servoing, motion capture systems like VICON are used as complementary sensors (see, for instance, articles [109,145]) that estimate the velocity of the UAV whilst the UAV looks toward the visual landmark. Unfortunately, motion capture systems are still limited to a specific small volume inside research labs [178].

Category 3: Vision-Based Tracking/Guidance

This way, continuing with the third category, the papers have been classified into the following groups: *3.1. Target Tracking* when the proposed solution is designed so that a UAV detects and follows a specific target (generally in motion); *3.2. Features/Path Tracking* for papers in which a UAV is visually guided to follow a path defined by images, or a UAV is guided through visual features that it must detect and follow, such as lines on a road; and, finally, *3.3. Autonomous Aerial Refueling (AAR)* which groups those papers in which one UAV follows another in order to solve the problem of autonomous resupply. It should be noted that some of the papers classified here address only the first stage of the problem, that is, the pose estimation between the two UAVs involved in the refueling process (tanker and receiver UAV). Of these subcategories, the most popular is target tracking with 17 papers, while in second place we find the AAR subcategory with 10 papers, and, finally, the tracking of routes or features with only six works.

Category 4: Vision-Based Sense-and-Avoid (SAA)

Lastly, the following subcategories have been considered for the fourth category: *4.1. Detection and Avoidance of Intruders* which includes solutions to avoid collisions with other aircraft, primarily through evasive maneuvers; *4.2. Mapping-Based Obstacle Avoidance* on the use of strategies to avoid obstacles based on a mapping process and subsequent obstacle-free path planning; and, finally, *4.3. Autonomous Flight and Obstacle Avoidance* in which autonomous navigation in complex environments has been addressed. In this last case, the UAV generally uses a strategy based on finding which path to follow in order to avoid colliding with obstacles (e.g., navigation between a row of trees in orchard). Based on the results obtained, the subcategory in which the highest number of papers has been published is related to mapping-based solutions, with six papers, followed very closely by avoiding other aircraft and autonomous flight, with five and four papers, respectively. All these operations are very close to the concept of fully autonomous UAVs, and it is, therefore, foreseeable that research will continue to focus on them in the near future.

3.3. RQ3: What Types of UAVs Have Been Used in the Proposed Solutions?

The papers have been grouped into *Fixed-Wing*, *Rotatory-Wing*, *Flapping-Wing* and *Airship*, according to the aircraft's configuration. Moreover, an additional *Not Specified* group has been considered in order to classify those papers that do not detail the class of UAV.

3.3.1. Distribution and Annual Trend per UAV Class

The UAV class distribution over the total of 144 papers is shown in Figure 11. This graph shows that, without any doubt, the most widely used UAV platform corresponds to the rotatory-wing class (102 papers, 71%), followed by 25% that represents the fixed-wing class (37 papers). Only one paper uses an airship UAV. Finally, three papers do not specify the type of UAV. The only class of UAV not present in the systematic mapping study is, therefore, flapping-wing aircraft. Consequently, there is an interesting gap on which future research should be focused. Moreover, considering the characteristics of flapping-wing UAVs, they could be very useful for indoor applications and/or approaches requiring a small aircraft.

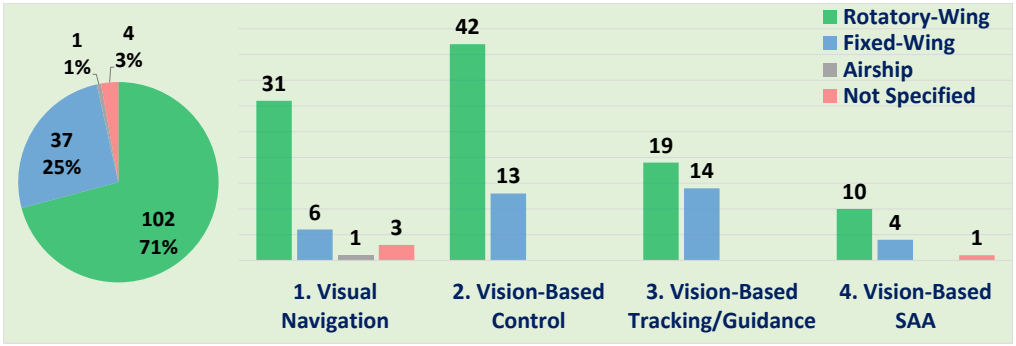

Figure 11. UAV class distribution over the database.

The above data are also endorsed when observing the annual trend considering the UAV class (see Figure 12). This graph presents the annual evolution of the number of works. The data again provide evidence of a greater use of rotatory-wing UAVs. Another noteworthy fact is that the use of rotary-wing aircraft has continued since 1999, also showing a clear trend of growth, which can be considered almost exponential in recent years. However, the other UAV classes have a discontinuous evolution over time. With the exception of fixed-wing UAVs, for which some evolution can be appreciated, no conclusions can be drawn for the remaining cases, given the small number of works.

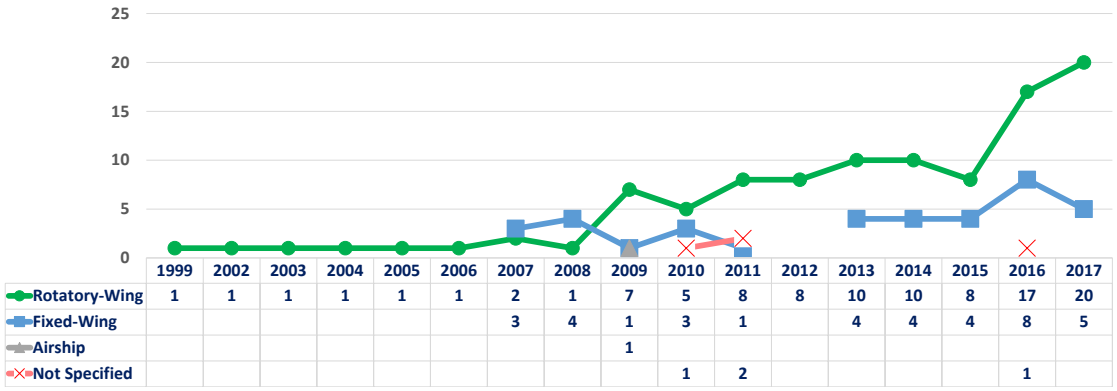

	1999	2002	2003	2004	2005	2006	2007	2008	2009	2010	2011	2012	2013	2014	2015	2016	2017
Rotatory-Wing	1	1	1	1	1	1	2	1	7	5	8	8	10	10	8	17	20
Fixed-Wing							3	4	1	3	1		4	4	4	8	5
Airship									1								
Not Specified										1	2					1	

Figure 12. Annual trend per UAV class.

3.3.2. Concerning the Vision-Based Task and Type of UAV

If we consider the first classification regarding the computer vision task in each paper, the distribution again shows that the most frequent type of UAV belongs to the rotatory-wing class. Rotary-wing UAVs are the majority in all categories, and more clearly for the first two focused on navigation and control. The papers that do not specify the type or employ a less frequent type of UAV belong to categories *1. Visual Navigation* and *4. Vision-Based Sense-and-Avoid (SAA)*. These papers are usually validated by means of tests using images obtained from databases or satellite maps. Furthermore, a more in-depth analysis has been performed considering the specific types of aircraft within each class. Figure 13 shows the UAV class distribution over the four categories detailing the type of UAV. This information is provided as "Class: Type of UAV"; for example, Rotatory-Wing: Helicopter. When the type of UAV is not available, only the name of its class is indicated.

Appl. Sci. **2019**, *9*, 3196

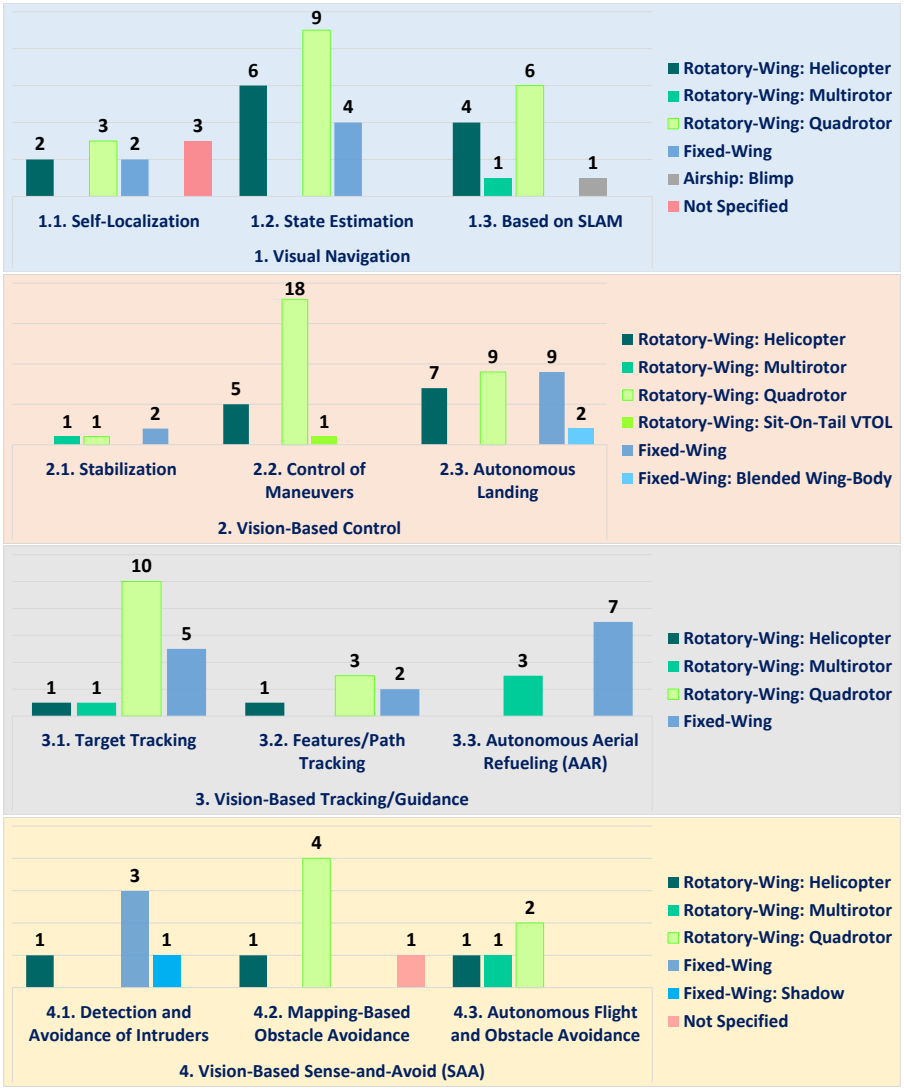

Figure 13. UAV class distribution over the categories.

Starting with the most common *Rotatory-Wing* class of UAV, the types of UAV found in the analysis are *Helicopter*, *Quadrotor*, *Multirotor* and *Sit-On-Tail VTOL*. Quadrotors are clearly the most widely used, higlighting 18 papers in the control of maneuvers subcategory. In this respect, quadcopters are vehicles with four rotors, relatively simple to control, with high maneuverability and the ability to hover. All this, together with the wide range of low-cost quadrotors on the market, has made a significant contribution to their clear predominance in the research developed to date. The second most frequent type of rotary vehicles are helicopters, distantly followed in third place by multirotors. A Sit-On-Tail VTOL aircraft, which is used in a paper on the control of maneuvers, is in the last position.

With respect to the second most common class, *Fixed-Wing*, we should point out that it is usual not to provide details of which model of fixed-wing aircraft has been used. In fact, only three papers provide this information. Two of them address the process of autonomous landing by using a *Blended Wing-Body* aircraft, whereas a *Shadow* model is used in one paper on the detection and avoidance of an intruder aircraft. Furthermore, the only UAV grouped in *Airship* is a *Blimp*, which is used in a paper concerning visual navigation based on SLAM.

An additional fact is that these graphs once again show the predominance of rotary-wing air vehicles over the fixed-wing category, not only as regards the number of articles, but also as regards the fact that this type of air vehicle is present in all the subcategories considered, while fixed-wing

air vehicles are used in only some of them. However, it should be highlighted that fixed-wing UAVs are more used in operations related to high-altitude flight and large distances due to the features of such airplanes. For instance, in the case of autonomous aerial refueling operations, whose purpose is, in effect, to increase flight autonomy (the ability to perform the complete flight without the need of making stops to refuel on the ground). Fixed-wing UAVs are also used frequently in stabilization of the UAV's flight regarding the skyline, and in detection and avoidance of other aircraft.

Finally, in order to conclude this extensive analysis of UAV platforms, the complete list of the 144 papers considered in this mapping study, classified according to the class of UAV and also detailing the type of aircraft, is shown in Table 5.

Table 5. List of papers per UAV class.

UAV Class	N	%	Papers
Rotatory-Wing: Helicopter	**29**	20.14%	[43,54,73,83,84,86,87,89,91,104–106,112,115–118,120,121, 127,141,142,144,148,152,163,170,175,176]
Rotatory-Wing: Multirotor	**7**	4.86%	[42,63,68,131,138,169,172]
Rotatory-Wing: Quadrotor	**65**	45.14%	[17–22,24,25,28,29,32,34,35,44,58–62,69,71,72,74,80–82,85, 88,92–95,97,99,102,107,109–111,114,119,122,126,128–130, 132,135,136,139,143,145,146,149–151,153,159,160,162,164, 165,168,173,177]
Rotatory-Wing: Sit-On-Tail VTOL	**1**	0.69%	[45]
Fixed-Wing	**34**	23.61%	[23,27,30,31,33,38,41,53,57,64–66,75,90,96,98,103,108,113, 123,124,133,134,137,140,147,154–157,161,166,167,174]
Fixed-Wing: Blended Wing-Body	**2**	1.39%	[40,125]
Fixed-Wing: Shadow	**1**	0.69%	[39]
Airship: Blimp	**1**	0.69%	[51]
Not Specified	**4**	2.78%	[100,101,158,171]

3.4. RQ4: What Are the Characteristics of the Vision System?

The 144 papers considered in this systematic mapping study have been classified with regard to the vision system in terms of the number of cameras as *Monocular* (1 camera), *Multi-camera (2)* (two cameras), *Multi-camera (4)* (four cameras), and, finally, a special type of multi-camera, *Stereo* (two vision sensors in a stereo configuration, i.e., at the same location and oriented toward a same point).

Concerning the vision systems, their location, that is, where they are installed, and also their orientation, that is, where they point to, has also been analyzed. Other concepts, such as the camera technology used and the images recorded (color or gray scale), have not been considered because this information is not always detailed in the papers analyzed. In addition, this question makes no sense in the case of those proposals that are validated using tests that do not require a physical camera device (see Table 2), such as virtual reality or numerical simulations. Moreover, more information on technical aspects of the vision systems are out the scope of a systematic mapping study. Nevertheless, we believe that a more in-depth analysis of the cameras would be interesting for future detailed reviews, particularly those focused on solutions validated during a UAV's real flight.

3.4.1. Distribution and Annual Trend per Vision System

The distribution of these types of vision systems as regards the database is shown in Figure 14, in which the predominance of monocular systems is clear, with a total of 116 papers representing 80% of the papers. Secondly, stereo systems are present in 20 papers, representing 14%. The remaining 6% is divided between multi-camera (2) and multi-camera (4) systems with 7 and 1 papers, respectively.

Appl. Sci. **2019**, *9*, 3196

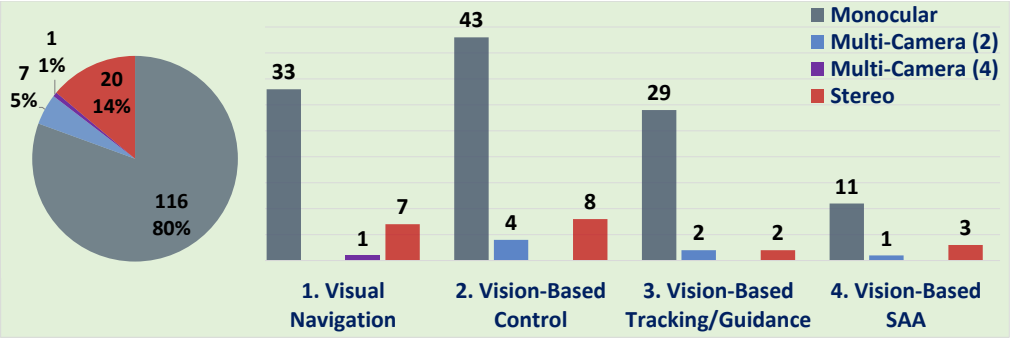

Figure 14. Vision system class distribution over the database.

Figure 15 shows the annual trend of papers considering the vision system employed. A clear predominance of monocular vision systems can be observed again. Moreover, the graph shows a remarkable growth trend for these monocular systems. In the case of stereo, the growth is not clear. However, some increase can be observed in the last few years' research (since 2014). This data may suggest that the lower use of stereo systems can be due to their later development. Regarding the rest of multi-camera configurations, it is not possible to draw relevant conclusions as a result of the reduced number of papers focused on these systems.

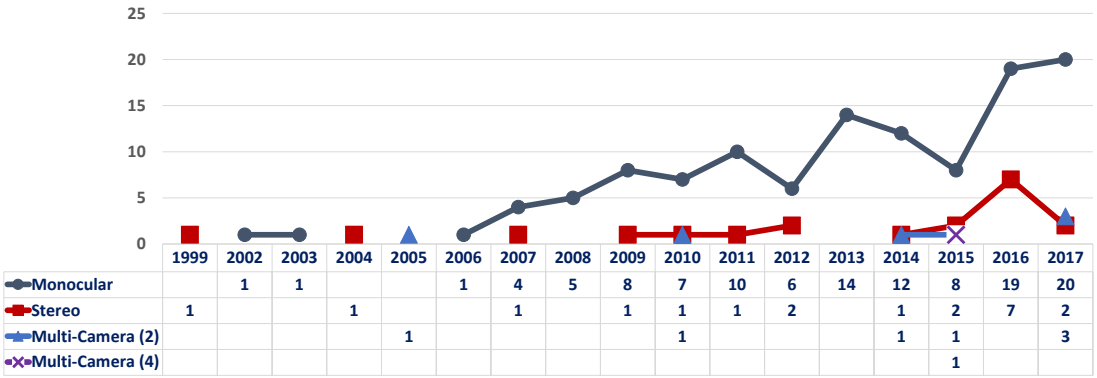

	1999	2002	2003	2004	2005	2006	2007	2008	2009	2010	2011	2012	2013	2014	2015	2016	2017
Monocular		1	1			1	4	5	8	7	10	6	14	12	8	19	20
Stereo	1			1			1		1	1	1	2		1	2	7	2
Multi-Camera (2)					1					1				1	1		3
Multi-Camera (4)															1		

Figure 15. Annual trend per vision system.

3.4.2. Concerning the Vision-Based Task, Localization, and Orientation

With regard to the influence of the computer vision task at hand, the predominant system is again the monocular one for all the categories, followed noticeably by the stereo system, which is present in all the categories. The case of multi-camera systems is different. In fact, a 2-camera system is used in tasks related to control, tracking and sense-and-avoidance (cat. 2, 3 and 4), and a 4-camera system is employed only for navigation (cat. 1). The remaining details concerning the vision system distribution in each main category are provided in Figure 16.

Table 6 presents the list of 144 papers grouped considering the number, localization, and orientation of the cameras. The location is *On Board* the UAV and *On Ground*, or a combination of both in multi-camera systems. With regard to the orientation, when the vision system is on board, the most frequent setups are pointing *Downward* (inclined towards the ground) and *Forward* (in the direction of flight). In the case of papers that address autonomous aerial refueling, a camera pointing to the other aircraft involved in the process has also been considered. Here, the system points to the UAV that acts as a receiver (*Toward the Receiver UAV*) or to the aircraft with the fuel tank (*To the Tanker UAV*). However, in the case of ground vision systems, their orientation is always directed *Toward the UAV*. Finally, in a few cases, the vision system's orientation is modified (shown as *Depending on the test*).

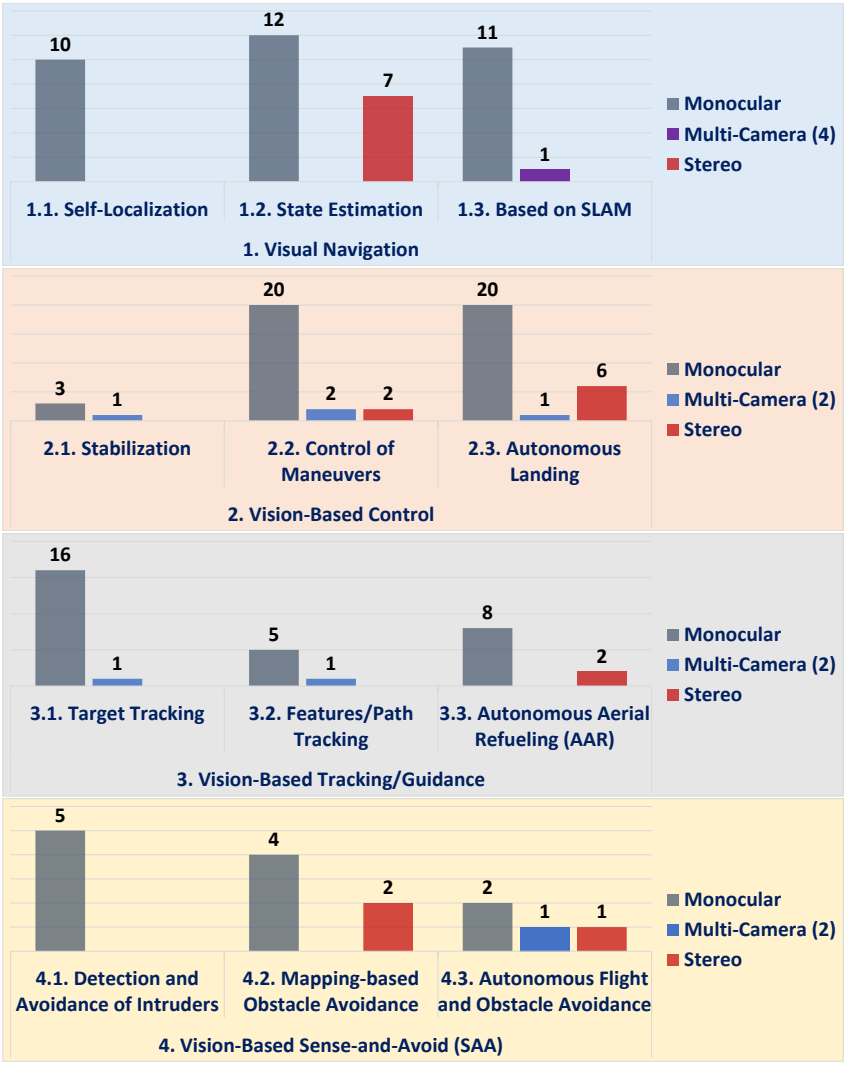

Figure 16. Vision system distribution over the categories.

Lastly, some conclusions are presented on the data related to the vision systems used. (a) The results show a predominance of on-board monocular systems. This is mainly owing to the lower complexity of computer vision algorithms, and also to the ease of installation of a single camera on a UAV, with a resulting decrease in the weight added to the aircraft. (b) With regard to camera orientation, this depends to a large extent on the task for which the proposal has been designed. Visual navigation systems generally use cameras pointing toward the ground (especially in geolocation systems). Such orientation is also necessary in missions involving the tracking of targets on the ground. (c) The orientation pointing in the direction of flight is mostly used in systems for the detection and avoidance of obstacles, and when the visual reference is placed in front of the UAV. In the particular case of aerial refueling, the camera, which is installed on board the UAV receptor or tanker, points in the direction of the other aircraft in order to measure the distance between both. (d) Multi-camera systems are also interesting solutions, especially stereo systems, which have been used in a good number of papers. In this case, these systems provide information of the depth, which is a clear advantage despite being more complex. (e) The stereo systems are usually installed aboard the UAV, but some solutions also use stereo systems installed on the ground, mainly to guide fixed-wing UAVs during their landing maneuvers. In this case, the orientation of the cameras is obviously towards the UAV itself.

Table 6. List of papers per vision system.

Vision System	Localization	Orientation	N	%	Papers
Monocular	On Board	Downward	80	55.56%	[17,18,20,22,24,25,30,32,33,40,51,53,54,58,59,72–74,80,81,84–86,88–95,97,99–102,104,105,107–109,111,114,116,118,119,121,125–131,133–136,144–146,149–152,154–157,160,166–171,173,175–177]
Monocular	On Board	Forward	26	18.06%	[19,21,27,39,41,43,45,71,75,83,98,113,115,120,122–124,140,143,148,153,158,159,162–164]
Monocular	On Board	Toward the Receiver UAV	1	0.69%	[57]
Monocular	On Board	Toward the Tanker UAV	7	4.86%	[23,96,137,138,147,161,174]
Monocular	On Board	Depending on the Test	1	0.69%	[142]
Monocular	On Ground	Toward the UAV	1	0.69%	[44]
Multi-Camera (2)	On Board	Forward & Downward	6	4.17%	[29,31,34,60,62,132]
Multi-Camera (2)	On Board & On Ground	Downward & Toward the UAV	1	0.69%	[61]
Multi-Camera (4)	On Board	Depending on the Test	1	0.69%	[68]
Stereo	On Board	Downward	8	5.56%	[65,82,106,110,112,117,139,141]
Stereo	On Board	Forward	5	3.47%	[28,35,69,87,172]
Stereo	On Board	Toward the Receiver UAV	2	1.39%	[42,63]
Stereo	On Ground	Toward the UAV	5	3.47%	[38,64,66,103,165]

3.5. RQ5: What Is the Validation Process for Each Proposed Solution?

Lastly, the processes employed to validate the proposed solutions described in the papers have been addressed. Figure 17 enables us to appreciate the different validation processes (*Flight*, *Experimental* and *Simulation*) and the number of papers that make use of them. The figure also shows the distribution over the four main categories regarding the navigation and flight control task performed. In this figure, please note that: (1) experimental and simulation tests have been indicated by means of the terms EXP and SIM, respectively, and (2) the symbol & indicates that the validation process is composed of different types of tests.

Upon observing the results, it is possible to state that the most widely used validation process is flight tests, with a total of 56 papers (39%). When considering the validation processes using flight and other types of simulation and/or experimentation trials, the percentage rises to more than 54%, which is really remarkable. On the contrary, a significant number of the papers (around 25%; 38 papers) use only simulation tests for validation, while another 27 papers (close to 20%) conduct experimental tests. In this respect, some proposals have been validated by means of offline tests, i.e., trials that employed flight data and images recorded during previous navigation. These tests, together with tests carried out in laboratories, have been considered as experimental tests, which are less relevant than flight tests. However, they are also necessary as a previous step to ensure the performance of a proposed solution.

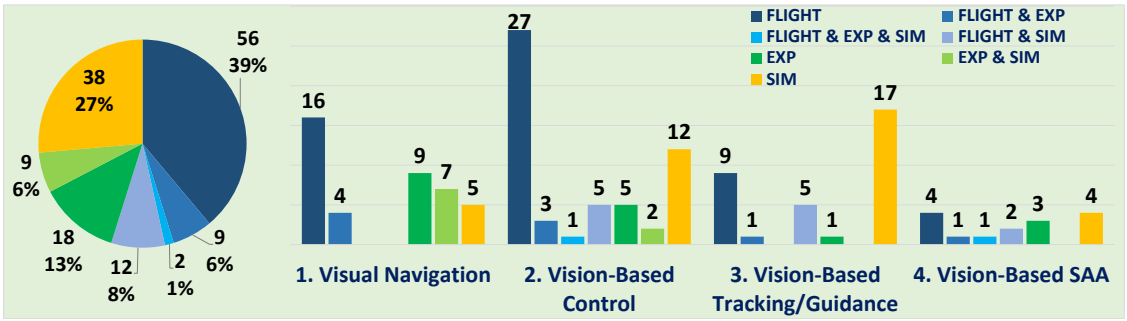

Figure 17. Validation process distribution over the database.

If we analyze the data considering the four main categories of operations, the flight is still predominant and stands out notably in the case of visual navigation and vision-based control. However, the weights of simulation tests are very important in some categories, especially in vision-based control and tracking/guidance. This way, an important number of papers used only simulations tests, which could be considered a negative point. However, not only numerical simulations (usually in visual

servoing approaches) but also new paradigms as interesting as virtual reality have been employed. We consider that the kind of technology that simulates complex tasks, such as aerial refueling that involves two aircraft, is one of the most promising areas for the development of improved UAVs. In this respect, it is possible to perform realistic simulations, which may be very useful to test and improve new control algorithms, without the need to acquire expensive aircraft.

The total of 144 papers, grouped according to their validation process, is shown in Figure 18. Three large circles have been drawn to represent the three types of tests, (*Flight*, *Experimental* and *Simulation*). The intersections of the circles represent those validation processes that are composed of several types of tests.

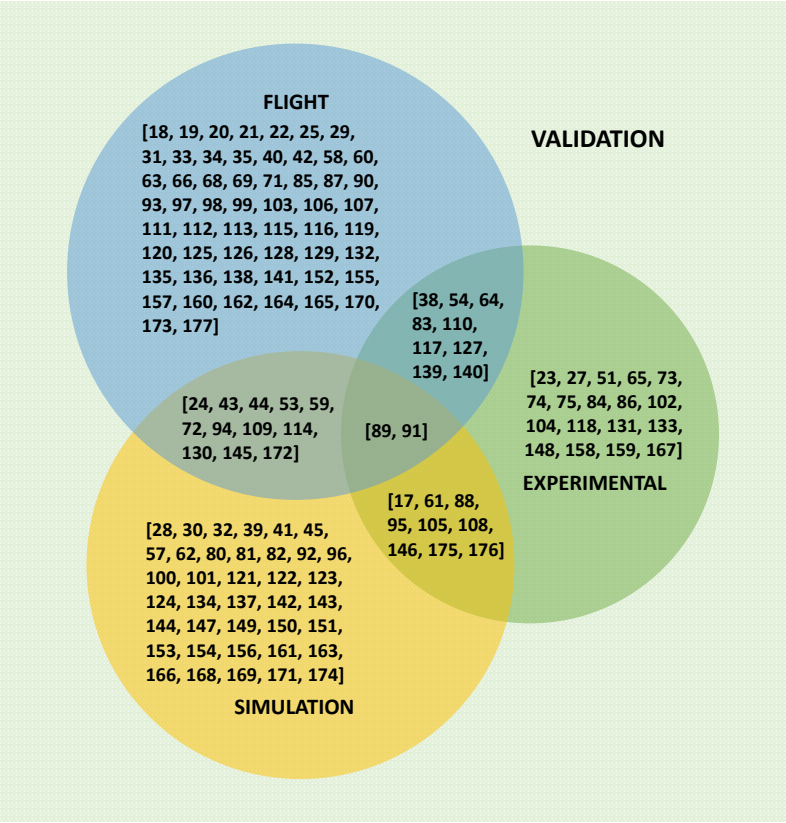

Figure 18. Papers per validation process.

In addition, in Figure 19, all papers that use flight for validation are classified into: *Outdoor* and *Indoor* flights. These two groups are again represented using circles, signifying that the intersection between both means flight tests in both indoor and outdoor environments (5 papers). The results show that outdoor flights are slightly more frequent than indoor ones.

Finally, in relation to precision or accuracy, it must be highlighted that the scarce information provided in the articles has been decisive not to include this parameter in this systematic mapping study. In fact, there is a very limited number of papers addressing this topic in detail. Most papers approach precision only from a qualitative point of view, not providing numerical values, or showing graphical figures difficult to measure and, consequently, to compare with other works. The several solutions presented a state that they are accurate, but they are difficult to analyze as they have been tested with distinct platforms, sensors, cameras. In this sense, the difference between flight, experimental, and simulation tests is also a disadvantage when comparing different solutions in a correct way. It should also be considered that the analyzed papers address a wide range of flight operations, whose objectives are very dissimilar, so that a comparison in precision could lead to confusion.

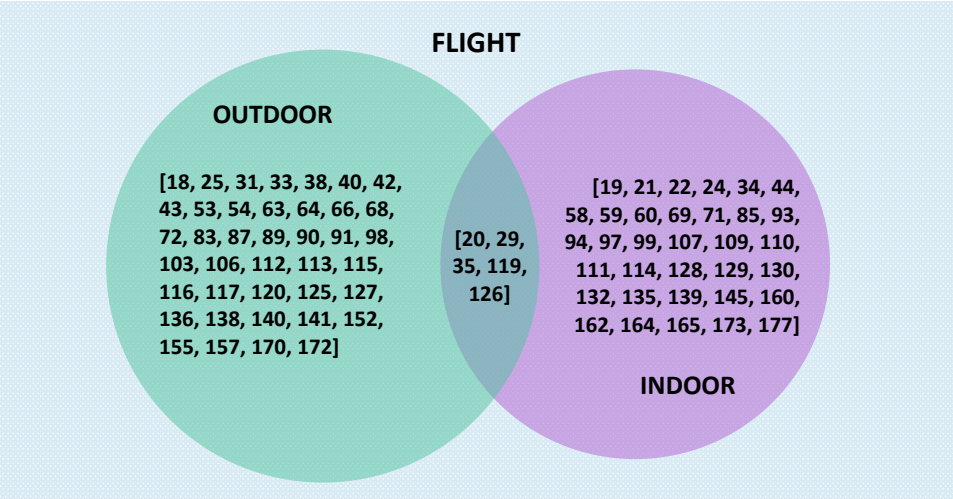

Figure 19. Papers per flight conditions.

4. Discussion

- *Number and Relevance of the Papers:*
  (i) The number of research works focused on the use of computer vision for autonomous aerial vehicles has not stopped growing in recent years, which confirms the scientific community's interest in this topic. (ii) More than 86% of the papers analyzed in this study were published in journals indexed in JCR in such outstanding areas as Aerospace Engineering, Robotics, Automation, and Artificial Intelligence.
- *Computer-Vision Tasks*
  (i) The vast majority of research analyzed propose only solutions to tackle some kind of task and not a complete solution for a fully autonomous vision-based UAV. This fact, which has allowed us to structure the results in different categories, can be considered as negative since the aerial vehicles described fail to perform completely autonomous flights in real environments. However, it is foreseeable that the presence of completely autonomous UAVs based on computer vision will be common in the coming years, considering the rapid development and the annual trend of this research field. (ii) In this sense, the focus of research is shifting from relatively simpler operations, such as location and stabilization, to more complex solutions which are closer to the concept of autonomous UAV, such as following moving targets or trajectories defined by visual references, as well as solutions for the detection and avoidance of both static and dynamic obstacles, so as to carry out a collision-free flight.
- *Type of UAV, Vision System and Validation Process*
  (i) The most widely used UAVs belong to the rotary-wing class. With regard to this type of aerial vehicle, which is principally characterized by the fact that they permit vertical take-off and landing, suspended flight, and greater maneuverability than fixed-wing vehicles, the number of papers presenting solutions specifically designed for or tested on them has not stopped growing in this century. Quadrotors and (to a lesser extent) helicopters are the most frequent vehicles within this class of UAV. (ii) The most widely used vision system is a single camera installed on board the UAV. This configuration is present in almost 80% percent of the works analyzed. Secondly, stereo systems have also been used in a significant number of cases. Again, the annual trend shows the predominance of mono-camera vision systems against multi-camera configurations. (iii) More than 54% of the works analyzed have included flight tests in their validation process. However, a non-negligible number (around 25%) have validated their proposals only through the use of simulation tests. Nevertheless, in this case, not only have numerical simulations been employed, but also virtual reality environments, in addition to hardware- and image-in-the-loop simulations.

After these general conclusions concerning the systematic mapping, we should state that we believe that the study carried out here is of great value since it has allowed the analysis of practically two decades of research. It should, therefore, be of great help to researchers who are starting to develop solutions for UAVs using computer vision, and for experts who wish to consult previously presented solutions. In addition, the classification structure introduced in this paper could be of great help for future reviews focused on the most recent years or certain types of operations, UAV classes, or validation processes carried out during real flights. These future studies may address technical issues in greater depth that are beyond the scope of a systematic mapping study.

Lastly, it is necessary to center the discussion in the concept of assistant aerial robots, our personal research interest which led to performing this systematic mapping study. This way, and considering the information we have analyzed performing this study, a series of conclusions have been drawn to focus our future developments. This, defines, therefore, our guidelines to advance in developing an autonomous UAV based on computer vision to assist dependent persons. In this sense, we summarize the main conclusions following:

- Our personal interest in assistant aerial robots requires us to focus future studies on vision-based target tracking and obstacle avoidance principally, so that the UAV follows the person in order to perform monitoring tasks, meeting the safety conditions to make it possible to use such assistant UAVs in real environments.
- We consider that quadrotors are the most suited for our purpose of developing aerial assistant robots for dependent people. The above-mentioned advantages regarding the rotatory-class are relevant reasons. In addition, the hovering ability and its relative simpler flight control make it possible to use these UAVs in dependents' complex indoor/outdoor environments for which the assistant will be designed.
- Initially, the best solution for our purpose is the use of a monocular system aboard the UAV. This solution is easier to install, allows us to reduce the payload for the UAV and the vision algorithms are simpler. However, we should not discard the use of a stereo system in the future, should we need accurate depth information. What does seem clear is the location of the vision system on board the UAV, which allows us to perform the tracking of the person in order to determine the action of assistance required at any given time.
- We consider that virtual reality will be essential in our development process of the new personal flying assistant. Virtual reality allows us to test the performance of the UAV in a realistic home indoor environment containing multiple obstacles, as well as outdoor environments. In addition, virtual simulation tools make it possible to carry out studies using immersive and semi-immersive technologies, such as virtual reality helmets. This way, it will be possible to validate the proposal of an assistant UAV in a safe environment and, at the same time, the user acceptance of such technology. After that, real flight tests in controlled conditions will be conducted before bringing these novel assistants to real lives.

5. Conclusions

This paper has presented the first systematic mapping study focused on the topic of computer vision in autonomous unmanned aerial vehicles. The objective has, therefore, been to analyze papers that introduce the development of solutions based on computer vision for navigation tasks and flight control in UAVs. After a search process that returned a total of 2081 papers, a screening process was applied that eventually allowed us to obtain 144 papers. In order to answer the research questions posed, the papers were analyzed and classified according to the task for which computer vision had been used, the UAV class for which the proposal had been designed or validated, the characteristics of the vision system installed, and the validation process used in each case.

Author Contributions: Conceptualization, L.M.B., R.M. and A.F.-C.; Methodology, A.F.-C.; Investigation, L.M.B., R.M. and A.F.-C.; Data Curation, R.M. and A.F.-C.; Writing-Original Draft Preparation, L.M.B.; Writing-Review & Editing, L.M.B., R.M. and A.F.-C.; Funding Acquisition, A.F.-C.

Funding: This work was partially supported by Spanish Ministerio de Ciencia, Innovación y Universidades, Agencia Estatal de Investigación (AEI)/European Regional Development Fund (FEDER, EU) under DPI2016-80894-R grant. Lidia María Belmonte holds a scholarship (FPU014/05283) from the Spanish Ministerio de Educación y Formación Profesional.

Conflicts of Interest: The authors declare no conflict of interest. The funders had no role in the design of the study; in the collection, analyses, or interpretation of data; in the writing of the manuscript, or in the decision to publish the results.

Abbreviations

The following abbreviations are used in this manuscript:

HILS	hardware-in-the-loop simulation
IBVS	image-based visual servoing
IF	impact factor
IILS	image-in-loop simulation
JCR	Journal Citation Reports
PBVS	position-based visual servoing
RQ	research question
SAA	sense-and-avoid
SLAM	simultaneous localization and mapping
UAS	unmanned aircraft system
UAV	unmanned aerial vehicle
VTOL	vertical take-off and landing

Appendix A. List of Journals and Papers Published

Journal	Papers
Journal of Intelligent & Robotic Systems	[18,20,27,30,40,51,68,69,71,73,83–95]
IEEE Transactions on Aerospace and Electronic Systems	[28,96–101]
Sensors	[17,29,31,66,72,102,103]
International Journal of Advanced Robotic Systems	[38,64,104–106]
Journal of Guidance, Control, and Dynamics	[33,39,107–109]
Autonomous Robots	[58,110–112]
IEEE/ASME Transactions on Mechatronics	[22,59,113,114]
Journal of Field Robotics	[35,75,115,116]
Robotics and Autonomous Systems	[117–120]
Canadian Aeronautics and Space Journal	[121–123]
Control Engineering Practice	[34,124,125]
IEEE Transactions on Industrial Electronics	[44,126,127]
IEEE Transactions on Robotics	[128–130]
Advanced Robotics	[24,32]
Aircraft Engineering and Aerospace Technology	[158,169]
Asian Journal of Control	[151,153]
Expert Systems with Applications	[74,143]
IEEE Transactions on Instrumentation and Measurement	[23,57]
IFAC-PapersOnLine	[146,172]
International Journal of Robotics Research	[61,65]
International Journal of Robust and Nonlinear Control	[45,142]
ISA Transactions	[80,150]
Journal of Aerospace Information Systems	[147,173]
Journal of Aerospace Engineering	[159,164]
Optik	[135,136]
Science China Information Sciences	[42,144]
Science China Technological Sciences	[41,63]
Advances in Mechanical Engineering	[160]
Aeronautical Journal	[137]
Aerospace Science and Technology	[62]
Automation in Construction	[163]
Aviation	[154]
Engineering Letters	[139]

Journal	Papers
Eurasip Journal on Advances in Signal Processing	[54]
IEEE Aerospace and Electronic Systems Magazine	[43]
IEEE Sensors Journal	[25]
IEEE Transactions on Circuits and Systems for Video Technology	[133]
IEEE Transactions on Control Systems Technology	[82]
IEEE Transactions on Robotics and Automation	[170]
IEEE Transactions on Systems, Man and Cybernetics Part C: Applications and Reviews	[161]
IEEE Transactions on Vehicular Technology	[140]
IEICE Electronics Express	[152]
IET Control Theory and Applications	[81]
Industrial Robot	[176]
International Journal of Aeronautical and Space Sciences	[155]
International Journal of Automation and Computing	[175]
International Journal of Control	[177]
International Journal of Control, Automation and Systems	[157]
International Journal of Distributed Sensor Networks	[132]
International Journal of High Performance Systems Architecture	[171]
International Journal of Imaging and Robotics	[168]
International Journal of Optomechatronics	[134]
International Journal of Robotics and Automation	[149]
International Journal on Electrical Engineering and Informatics	[166]
Journal of Infrastructure Systems	[53]
Journal of Robotic Systems	[141]
Journal of Robotics and Mechatronics	[165]
Journal of Vibration and Control	[167]
Machine Vision and Applications	[174]
Mobile Information Systems	[21]
Neurocomputing	[162]
Optical Engineering	[138]
Proceedings of the Institution of Mechanical Engineers, Part G: Journal of Aerospace Engineering	[156]
Robotica	[60]
Sensor Review	[148]
Transport and Telecommunication	[131]
Trends in Bioinformatics	[19]
Unmanned Systems	[145]

References

1. González-Jorge, H.; Martínez-Sánchez, J.; Bueno, M.; Arias, P. Unmanned Aerial Systems for Civil Applications: A Review. *Drones* **2017**, *1*, 2. [CrossRef]
2. Aire. A Self-Flying Robotic Assistant for the Home by Aevena Aire. Available online: https://esist.tech/2017/09/21/aire-a-self-flying-robotic-assistant-for-the-home-by-aevena-aire/ (accessed on 18 March 2019).
3. Fleye. Fleye—Your Personal Flying Robot. Available online: https://www.kickstarter.com/projects/gofleye/fleye-your-personal-flying-robot (accessed on 18 March 2019).
4. CIMON. Assisting Astronauts with Airbus Innovation. Available online: https://www.airbus.com/newsroom/stories/Assisting-astronauts-with-Airbus-innovation.html (accessed on 18 March 2019).
5. Bualat, M.G.; Smith, T.; Smith, E.E.; Fong, T.; Wheeler, D. Astrobee: A New Tool for ISS Operations. In Proceedings of the 15th International Conference on Space Operations. American Institute of Aeronautics and Astronautics, Marseille, France, 28 May–1 June 2018, doi:10.2514/6.2018-2517.
6. Belmonte, L.M.; Morales, R.; García, A.S.; Segura, E.; Novais, P.; Fernández-Caballero, A. Assisting Dependent People at Home through Autonomous Unmanned Aerial Vehicles. In Proceedings of the ISAmI 2019, Ávila, Spain, 26–28 June 2019.
7. Belmonte, L.M.; Morales, R.; García, A.S.; Segura, E.; Novais, P.; Fernández-Caballero, A. Trajectory Planning of a Quadrotor to Monitor Dependent People. In Proceedings of the IWINAC 2019, Almería, Spain, 3–7 June 2019.

8. Fernandez, A.; Insfran, E.; Abrahão, S. Usability evaluation methods for the web: A systematic mapping study. *Inf. Softw. Technol.* **2011**, *53*, 789–817. [CrossRef]
9. Roberto, R.; Lima, J.P.; Teichrieb, V. Tracking for mobile devices: A systematic mapping study. *Comput. Graph.* **2016**, *56*, 20–30. [CrossRef]
10. Sierra, J.M.; Vizcaíno, A.; Genero, M.; Piattini, M. A systematic mapping study about socio-technical congruence. *Inf. Softw. Technol.* **2018**, *94*, 111–129. [CrossRef]
11. Moguel, E.; Conejero, J.M.; Sánchez-Figueroa, F.; Hernández, J.; Preciado, J.C.; Rodríguez-Echeverría, R. Towards the Use of Unmanned Aerial Systems for Providing Sustainable Services in Smart Cities. *Sensors* **2017**, *18*, 64. [CrossRef] [PubMed]
12. Martinez-Gomez, J.; Fernández-Caballero, A.; Garcia-Varea, I.; Rodriguez, L.; Romero-Gonzalez, C. A Taxonomy of Vision Systems for Ground Mobile Robots. *Int. J. Adv. Robot. Syst.* **2014**, *11*, 111. [CrossRef]
13. Kanellakis, C.; Nikolakopoulos, G. Survey on Computer Vision for UAVs: Current Developments and Trends. *J. Intell. Robot. Syst.* **2017**, *87*, 141–168. [CrossRef]
14. Al-Kaff, A.; Martín, D.; García, F.; de la Escalera, A.; Armingol, J.M. Survey of computer vision algorithms and applications for unmanned aerial vehicles. *Expert Syst. Appl.* **2018**, *92*, 447–463. [CrossRef]
15. Lu, Y.; Xue, Z.; Xia, G.S.; Zhang, L. A survey on vision-based UAV navigation. *Geo-Spat. Inf. Sci.* **2018**, *21*, 21–32. [CrossRef]
16. RG, E. Template for a Mapping Study. Available online: https://community.dur.ac.uk/ebse/resources/templates/MappingStudyTemplate.pdf (accessed on 10 January 2018).
17. Munguía, R.; Urzua, S.; Bolea, Y.; Grau, A. Vision-based SLAM system for unmanned aerial vehicles. *Sensors* **2016**, *16*, 372. [CrossRef]
18. Zhao, S.; Lin, F.; Peng, K.; Dong, X.; Chen, B.M.; Lee, T.H. Vision-aided estimation of attitude, velocity, and inertial measurement bias for UAV stabilization. *J. Intell. Robot. Syst.* **2016**, *81*, 531–549. [CrossRef]
19. Seng, L.K.; Ovinis, M.; Nagarajan; Seulin, R.; Morel, O. Vision-based state estimation of an unmanned aerial vehicle. *Trends Bioinform.* **2016**, *10*, 11–19. [CrossRef]
20. Cocchioni, F.; Frontoni, E.; Ippoliti, G.; Longhi, S.; Mancini, A.; Zingaretti, P. Visual based landing for an unmanned quadrotor. *J. Intell. Robot. Syst.* **2016**, *84*, 511–528. [CrossRef]
21. Jeong, H.J.; Choi, J.D.; Ha, Y.G. Vision based displacement detection for stabilized UAV control on cloud server. *Mob. Inf. Syst.* **2016**, *2016*, 8937176. [CrossRef]
22. Xie, H.; Low, K.H.; He, Z. Adaptive visual servoing of unmanned aerial vehicles in GPS-denied environments. *IEEE/ASME Trans. Mechatron.* **2017**, *22*, 2554–2563. [CrossRef]
23. Yin, Y.; Wang, X.; Xu, D.; Liu, F.; Wang, Y.; Wu, W. Robust visual detection-learning-tracking framework for autonomous aerial refueling of UAVs. *IEEE Trans. Instrum. Meas.* **2016**, *65*, 510–521. [CrossRef]
24. Harik, E.H.C.; Guérin, F.; Guinand, F.; Brethé, J.F.; Pelvillain, H.; Parédé, J.Y. Fuzzy logic controller for predictive vision-based target tracking with an unmanned aerial vehicle. *Adv. Robot.* **2017**, *31*, 368–381. [CrossRef]
25. Liu, Y.; Wang, Q.; Zhuang, Y.; Hu, H. A novel trail detection and scene understanding framework for a quadrotor UAV with monocular vision. *IEEE Sens. J.* **2017**, *17*, 6778–6787. [CrossRef]
26. Wan, Y.; Tang, J.; Lao, S. Research on the collision avoidance algorithm for fixed-wing UAVs based on maneuver coordination and planned trajectories prediction. *Appl. Sci.* **2019**, *9*, 798. [CrossRef]
27. Fasano, G.; Accardo, D.; Tirri, A.E.; Moccia, A.; Lellis, E.D. Sky region obstacle detection and tracking for vision-based UAS sense and avoid. *J. Intell. Robot. Syst.* **2016**, *84*, 121–144. [CrossRef]
28. Park, J.; Kim, Y. Collision avoidance for quadrotor using stereo vision depth maps. *IEEE Trans. Aerosp. Electron. Syst.* **2015**, *51*, 3226–3241. [CrossRef]
29. Al-Kaff, A.; García, F.; Martín, D.; De La Escalera, A.; Armingol, J. Obstacle detection and avoidance system based on monocular camera and size expansion algorithm for UAVs. *Sensors* **2017**, *17*, 1061. [CrossRef] [PubMed]
30. Lee, D.; Kim, Y.; Bang, H. Vision-based terrain referenced navigation for unmanned aerial vehicles using homography relationship. *J. Intell. Robot. Syst.* **2013**, *69*, 489–497. [CrossRef]
31. Huang, K.L.; Chiu, C.C.; Chiu, S.Y.; Teng, Y.J.; Hao, S.S. Monocular vision system for fixed altitude flight of unmanned aerial vehicles. *Sensors* **2015**, *15*, 16848–16865. [CrossRef] [PubMed]
32. Ozawa, R.; Chaumette, F. Dynamic visual servoing with image moments for an unmanned aerial vehicle using a virtual spring approach. *Adv. Robot.* **2013**, *27*, 683–696. [CrossRef]

33. Dobrokhodov, V.N.; Kaminer, I.I.; Jones, K.D.; Ghabcheloo, R. Vision-based tracking and motion estimation for moving targets using unmanned air vehicles. *J. Guid. Control Dyn.* **2008**, *31*, 907–917. [CrossRef]
34. Courbon, J.; Mezouar, Y.; Guénard, N.; Martinet, P. Vision-based navigation of unmanned aerial vehicles. *Control Eng. Pract.* **2010**, *18*, 789–799. [CrossRef]
35. Schmid, K.; Lutz, P.; Tomić, T.; Mair, E.; Hirschmüller, H. Autonomous vision-based micro air vehicle for indoor and outdoor navigation. *J. Field Robot.* **2014**, *31*, 537–570. [CrossRef]
36. García Carrillo, L.R.; Dzul López, A.E.; Lozano, R.; Pégard, C. *Quad Rotorcraft Control*; Advances in Industrial Control; Springer: London, UK, 2013, doi:10.1007/978-1-4471-4399-4.
37. Lozano, R. (Ed.) *Unmanned Aerial Vehicles. Embedded Control*; John Wiley & Sons, Inc.: Hoboken, NJ, USA, 2013, doi:10.1002/9781118599938.
38. Ma, Z.; Hu, T.; Shen, L. Stereo vision guiding for the autonomous landing of fixed-wing UAVs: A saliency-inspired approach. *Int. J. Adv. Robot. Syst.* **2016**, *13*, 43. [CrossRef]
39. Choi, H.; Kim, Y.; Hwang, I. Reactive collision avoidance of unmanned aerial vehicles using a single vision sensor. *J. Guid. Control Dyn.* **2013**, *36*, 1234–1240. [CrossRef]
40. Huh, S.; Shim, D.H. A vision-based automatic landing method for fixed-wing UAVs. *J. Intell. Robot. Syst.* **2010**, *57*, 217–231. [CrossRef]
41. Fan, Y.; Ding, M.; Cao, Y. Vision algorithms for fixed-wing unmanned aerial vehicle landing system. *Sci. China Technol. Sci.* **2017**, *60*, 434–443. [CrossRef]
42. Duan, H.; Li, H.; Luo, Q.; Zhang, C.; Li, C.; Li, P.; Deng, Y. A binocular vision-based UAVs autonomous aerial refueling platform. *Sci. China Inf. Sci.* **2016**, *59*, 053201. [CrossRef]
43. Lyu, Y.; Pan, Q.; Zhao, C.; Zhang, Y.; Hu, J. Feature article: Vision-based UAV collision avoidance with 2D dynamic safety envelope. *IEEE Aerosp. Electron. Syst. Mag.* **2016**, *31*, 16–26. [CrossRef]
44. Fu, Q.; Quan, Q.; Cai, K.Y. Robust pose estimation for multirotor UAVs using off-board monocular vision. *IEEE Trans. Ind. Electron.* **2017**, *64*, 7942–7951. [CrossRef]
45. Le Bras, F.; Hamel, T.; Mahony, R.; Treil, A. Output feedback observation and control for visual servoing of VTOL UAVs. *Int. J. Robust Nonlinear Control* **2011**, *21*, 1008–1030. [CrossRef]
46. Fernández-Caballero, A.; Belmonte, L.M.; Morales, R.; Somolinos, J.A. Generalized Proportional Integral Control for an Unmanned Quadrotor System. *Int. J. Adv. Robot. Syst.* **2015**, *12*, 85. [CrossRef]
47. Belmonte, L.M.; Morales, R.; Fernández-Caballero, A.; Somolinos, J.A. Robust Linear Longitudinal Feedback Control of a Flapping Wing Micro Air Vehicle. In *Artificial Computation in Biology and Medicine*; Ferrández Vicente, J.M., Álvarez-Sánchez, J.R., de la Paz López, F., Toledo-Moreo, F.J., Adeli, H., Eds.; Springer: Cham, Switzerland, 2015; pp. 449–458.
48. Jung, H.K.; Choi, J.S.; Wang, C.; Park, G.J. Analysis and Fabrication of Unconventional Flapping Wing Air Vehicles. *Int. J. Micro Air Veh.* **2015**, *7*, 71–88. [CrossRef]
49. Rongfa, M.N.; Pantuphag, T.; Srigrarom, S. Analysis of Kinematics of Flapping Wing UAV Using OptiTrack Systems. *Aerospace* **2016**, *3*, 23. [CrossRef]
50. Grossman, D. Airships, Dirigibles, Zeppelins & Blimps: What's the Difference? Available online: https://www.airships.net/dirigible/ (accessed on 18 March 2019).
51. Caballero, F.; Merino, L.; Ferruz, J.; Ollero, A. Unmanned aerial vehicle localization based on monocular vision and online mosaicking. *J. Intell. Robot. Syst.* **2009**, *55*, 323–343. [CrossRef]
52. Hygounenc, E.; Jung, I.K.; Souères, P.; Lacroix, S. The Autonomous Blimp Project of LAAS-CNRS: Achievements in Flight Control and Terrain Mapping. *Int. J. Robot. Res.* **2004**, *23*, 473–511. [CrossRef]
53. Rathinam, S.; Kim, Z.W.; Sengupta, R. Vision-based monitoring of locally linear structures using an unmanned aerial vehicle. *J. Infrastruct. Syst.* **2008**, *14*, 52–63.:1(52). [CrossRef]
54. Conte, G.; Doherty, P. Vision-based unmanned aerial vehicle navigation using geo-referenced information. *EURASIP J. Adv. Signal Process.* **2009**, *2009*, 387308. [CrossRef]
55. Holness, A.E.; Bruck, H.A.; Gupta, S.K. Characterizing and modeling the enhancement of lift and payload capacity resulting from thrust augmentation in a propeller-assisted flapping wing air vehicle. *Int. J. Micro Air Veh.* **2018**, 50–60. [CrossRef]
56. Belmonte, L.M.; Castillo, J.C.; Fernández-Caballero, A.; Almansa-Valverde, S.; Morales, R. Flying Depth Camera for Indoor Mapping and Localization. In *Ambient Intelligence—Software and Applications*; Mohamed, A., Novais, P., Pereira, A., Villarrubia, G., Fernández-Caballero, A., Eds.; Springer: Cham, Switzerland, 2015; pp. 243–251.

57. Duan, H.; Zhang, Q. Visual measurement in simulation environment for vision-based UAV autonomous aerial refueling. *IEEE Trans. Instrum. Meas.* **2015**, *64*, 2468–2480. [CrossRef]
58. Lin, S.; Garratt, M.A.; Lambert, A.J. Monocular vision-based real-time target recognition and tracking for autonomously landing an UAV in a cluttered shipboard environment. *Auton. Robot.* **2017**, *41*, 881–901. [CrossRef]
59. Zheng, D.; Wang, H.; Wang, J.; Chen, S.; Chen, W.; Liang, X. Image-based visual servoing of a quadrotor using virtual camera approach. *IEEE/ASME Trans. Mechatron.* **2017**, *22*, 972–982. [CrossRef]
60. Gomez-Balderas, J.E.; Salazar, S.; Guerrero, J.A.; Lozano, R. Vision-based autonomous hovering for a miniature quad-rotor. *Robotica* **2014**, *32*, 43–61. [CrossRef]
61. Altuğ, E.; Ostrowski, J.P.; Taylor, C.J. Control of a quadrotor helicopter using dual camera visual feedback. *Int. J. Robot. Res.* **2005**, *24*, 329–341. [CrossRef]
62. Yu, C.; Cai, J.; Chen, Q. Multi-resolution visual fiducial and assistant navigation system for unmanned aerial vehicle landing. *Aerosp. Sci. Technol.* **2017**, *67*, 249–256. [CrossRef]
63. Li, H.; Duan, H. Verification of monocular and binocular pose estimation algorithms in vision-based UAVs autonomous aerial refueling system. *Sci. China Technol. Sci.* **2016**, *59*, 1730–1738. [CrossRef]
64. Tang, D.; Hu, T.; Shen, L.; Zhang, D.; Kong, W.; Low, K.H. Ground stereo vision-based navigation for autonomous take-off and landing of UAVs: A Chan-Vese model approach. *Int. J. Adv. Robot. Syst.* **2016**, *13*, 67. [CrossRef]
65. Warren, M.; Corke, P.; Upcroft, B. Long-range stereo visual odometry for extended altitude flight of unmanned aerial vehicles. *Int. J. Robot. Res.* **2016**, *35*, 381–403. [CrossRef]
66. Kong, W.; Hu, T.; Zhang, D.; Shen, L.; Zhang, J. Localization framework for real-time UAV autonomous landing: An on-ground deployed visual approach. *Sensors* **2017**, *17*, 1437. [CrossRef]
67. Hein, D.; Kraft, T.; Brauchle, J.; Berger, R. Integrated UAV-Based Real-Time Mapping for Security Applications. *ISPRS Int. J. Geo-Inf.* **2019**, *8*, 219. [CrossRef]
68. Harmat, A.; Trentini, M.; Sharf, I. Multi-camera tracking and mapping for unmanned aerial vehicles in unstructured environments. *J. Intell. Robot. Syst.* **2015**, *78*, 291–317. [CrossRef]
69. García Carrillo, L.R.; Dzul López, A.E.; Lozano, R.; Pégard, C. Combining stereo vision and inertial navigation system for a quad-rotor UAV. *J. Intell. Robot. Syst.* **2012**, *65*, 373–387. [CrossRef]
70. Schauwecker, K.; Zell, A. On-Board Dual-Stereo-Vision for the Navigation of an Autonomous MAV. *J. Intell. Robot. Syst.* **2014**, *74*, 1–16. [CrossRef]
71. Fu, C.; Olivares-Mendez, M.A.; Suarez-Fernandez, R.; Campoy, P. Monocular visual-inertial SLAM-based collision avoidance strategy for fail-safe UAV using fuzzy logic controllers. *J. Intell. Robot. Syst.* **2014**, *73*, 513–533. [CrossRef]
72. Hinas, A.; Roberts, J.; Gonzalez, F. Vision-based target finding and inspection of a ground target using a multirotor UAV system. *Sensors* **2017**, *17*, 2929. [CrossRef] [PubMed]
73. Cesetti, A.; Frontoni, E.; Mancini, A.; Ascani, A.; Zingaretti, P.; Longhi, S. A visual global positioning system for unmanned aerial vehicles used in photogrammetric applications. *J. Intell. Robot. Syst.* **2011**, *61*, 157–168. [CrossRef]
74. García-Pulido, J.; Pajares, G.; Dormido, S.; de la Cruz, J. Recognition of a landing platform for unmanned aerial vehicles by using computer vision-based techniques. *Expert Syst. Appl.* **2017**, *76*, 152–165. [CrossRef]
75. Molloy, T.L.; Ford, J.J.; Mejias, L. Detection of aircraft below the horizon for vision-based detect and avoid in unmanned aircraft systems. *J. Field Robot.* **2017**, *34*, 1378–1391. [CrossRef]
76. Belmonte, L.M.; Morales, R.; Fernández-Caballero, A.; Somolinos, J.A. A Tandem Active Disturbance Rejection Control for a Laboratory Helicopter With Variable-Speed Rotors. *IEEE Trans. Ind. Electron.* **2016**, *63*, 6395–6406. [CrossRef]
77. Belmonte, L.M.; Morales, R.; Fernández-Caballero, A.; Somolinos, J. Robust Decentralized Nonlinear Control for a Twin Rotor MIMO System. *Sensors* **2016**, *16*, 1160. [CrossRef] [PubMed]
78. Belmonte, L.M.; Morales, R.; Fernández-Caballero, A.; Somolinos, J.A. Nonlinear Cascade-Based Control for a Twin Rotor MIMO System. In *Nonlinear Systems—Design, Analysis, Estimation and Control*; InTech: London, UK, 2016. [CrossRef]
79. Siti, I.; Mjahed, M.; Ayad, H.; El Kari, A. New trajectory tracking approach for a quadcopter using genetic algorithm and reference model methods. *Appl. Sci.* **2019**, *9*, 1780. [CrossRef]

80. Amirkhani, A.; Shirzadeh, M.; Papageorgiou, E.I.; Mosavi, M.R. Visual-based quadrotor control by means of fuzzy cognitive maps. *ISA Trans.* **2016**, *60*, 128–142. [CrossRef] [PubMed]
81. Ghommam, J.; Fethalla, N.; Saad, M. Quadrotor circumnavigation of an unknown moving target using camera vision-based measurements. *IET Control Theory Appl.* **2016**, *10*, 1874–1887. [CrossRef]
82. Park, J.; Kim, Y. Landing site searching and selection algorithm development using vision system and its application to quadrotor. *IEEE Trans. Control Syst. Technol.* **2015**, *23*, 488–503. [CrossRef]
83. Andert, F.; Adolf, F.M.; Goormann, L.; Dittrich, J.S. Autonomous vision-based helicopter flights through obstacle gates. *J. Intell. Robot. Syst.* **2010**, *57*, 259–280. [CrossRef]
84. Artieda, J.; Sebastian, J.M.; Campoy, P.; Correa, J.F.; Mondragón, I.F.; Martínez, C.; Olivares, M. Visual 3D SLAM from UAVs. *J. Intell. Robot. Syst.* **2009**, *55*, 299–321. [CrossRef]
85. Benini, A.; Mancini, A.; Longhi, S. An IMU/UWB/vision-based extended Kalman filter for mini-UAV localization in indoor environment using 802.15.4a wireless sensor network. *J. Intell. Robot. Syst.* **2013**, *70*, 461–476. [CrossRef]
86. Caballero, F.; Merino, L.; Ferruz, J.; Ollero, A. Vision-based odometry and SLAM for medium and high altitude flying UAVs. *J. Intell. Robot. Syst.* **2009**, *54*, 137–161. [CrossRef]
87. Campoy, P.; Correa, J.F.; Mondragón, I.; Martínez, C.; Olivares, M.; Mejías, L.; Artieda, J. Computer vision onboard UAVs for civilian tasks. *J. Intell. Robot. Syst.* **2009**, *54*, 105–135. [CrossRef]
88. Ceren, Z.; Altuğ, E. Image based and hybrid visual servo control of an unmanned aerial vehicle. *J. Intell. Robot. Syst.* **2012**, *65*, 325–344. [CrossRef]
89. Cesetti, A.; Frontoni, E.; Mancini, A.; Zingaretti, P.; Longhi, S. A vision-based guidance system for UAV navigation and safe landing using natural landmarks. *J. Intell. Robot. Syst.* **2010**, *57*, 233–257. [CrossRef]
90. Gui, Y.; Guo, P.; Zhang, H.; Lei, Z.; Zhou, X.; Du, J.; Yu, Q. Airborne vision-based navigation method for UAV accuracy landing using infrared lamps. *J. Intell. Robot. Syst.* **2013**, *72*, 197–218. [CrossRef]
91. Magree, D.; Mooney, J.G.; Johnson, E.N. Monocular visual mapping for obstacle avoidance on UAVs. *J. Intell. Robot. Syst.* **2014**, *74*, 17–26. [CrossRef]
92. Martínez, C.; Mondragón, I.F.; Campoy, P.; Sánchez-López, J.L.; Olivares-Méndez, M.A. A hierarchical tracking strategy for vision-based applications on-board UAVs. *J. Intell. Robot. Syst.* **2013**, *72*, 517–539. [CrossRef]
93. Natraj, A.; Ly, D.S.; Eynard, D.; Demonceaux, C.; Vasseur, P. Omnidirectional vision for UAV: Applications to attitude, motion and altitude estimation for day and night conditions. *J. Intell. Robot. Syst.* **2013**, *69*, 459–473. [CrossRef]
94. Ramírez, A.; Espinoza, E.S.; García Carrillo, L.R.; Mondié, S.; García, A.; Lozano, R. Stability analysis of a vision-based UAV controller. *J. Intell. Robot. Syst.* **2014**, *74*, 69–84. [CrossRef]
95. Tarhan, M.; Altuğ, E. EKF based attitude estimation and stabilization of a quadrotor UAV using vanishing points in catadioptric images. *J. Intell. Robot. Syst.* **2011**, *62*, 587–607. [CrossRef]
96. Campa, G.; Napolitano, M.; Fravolini, M. Simulation environment for machine vision based aerial refueling for UAVs. *IEEE Trans. Aerosp. Electron. Syst.* **2009**, *45*, 138–151. [CrossRef]
97. Carrillo, L.R.G.; Dzul, A.; Lozano, R. Hovering quad-rotor control: A comparison of nonlinear controllers using visual feedback. *IEEE Trans. Aerosp. Electron. Syst.* **2012**, *48*, 3159–3170. [CrossRef]
98. Huh, S.; Cho, S.; Jung, Y.; Shim, D.H. Vision-based sense-and-avoid framework for unmanned aerial vehicles. *IEEE Trans. Aerosp. Electron. Syst.* **2015**, *51*, 3427–3439. [CrossRef]
99. Xie, H.; Fink, G.; Lynch, A.F.; Jagersand, M. Adaptive visual servoing of UAVs using a virtual camera. *IEEE Trans. Aerosp. Electron. Syst.* **2016**, *52*, 2529–2538. [CrossRef]
100. Zhang, J.; Liu, W.; Wu, Y. Novel technique for vision-based UAV navigation. *IEEE Trans. Aerosp. Electron. Syst.* **2011**, *47*, 2731–2741. [CrossRef]
101. Zhang, J.; Wu, Y.; Liu, W.; Chen, X. Novel approach to position and orientation estimation in vision-based UAV navigation. *IEEE Trans. Aerosp. Electron. Syst.* **2010**, *46*, 687–700. [CrossRef]
102. Nguyen, P.H.; Kim, K.W.; Lee, Y.W.; Park, K.R. Remote marker-based tracking for UAV landing using visible-light camera sensor. *Sensors* **2017**, *17*, 1987. [CrossRef]
103. Yang, T.; Li, G.; Li, J.; Zhang, Y.; Zhang, X.; Zhang, Z.; Li, Z. A ground-based near infrared camera array system for UAV auto-landing in GPS-denied environment. *Sensors* **2016**, *16*, 1393. [CrossRef]
104. Patruno, C.; Nitti, M.; Stella, E.; D'Orazio, T. Helipad detection for accurate UAV pose estimation by means of a visual sensor. *Int. J. Adv. Robot. Syst.* **2017**, *14*. [CrossRef]

105. Wang, T.; Wang, C.; Liang, J.; Chen, Y.; Zhang, Y. Vision-aided inertial navigation for small unmanned aerial vehicles in GPS-denied environments. *Int. J. Adv. Robot. Syst.* **2013**, *10*, 276. [CrossRef]
106. Yu, Z.; Nonami, K.; Shin, J.; Celestino, D. 3D vision based landing control of a small scale autonomous helicopter. *Int. J. Adv. Robot. Syst.* **2007**, *4*, 7. [CrossRef]
107. Alkowatly, M.T.; Becerra, V.M.; Holderbaum, W. Bioinspired autonomous visual vertical control of a quadrotor unmanned aerial vehicle. *J. Guid. Control Dyn.* **2015**, *38*, 249–262. [CrossRef]
108. Hosen, J.; Helgesen, H.H.; Fusini, L.; Fossen, T.I.; Johansen, T.A. Vision-aided nonlinear observer for fixed-wing unmanned aerial vehicle navigation. *J. Guid. Control Dyn.* **2016**, *39*, 1777–1789. [CrossRef]
109. Lee, D.; Lim, H.; Kim, H.J.; Kim, Y.; Seong, K.J. Adaptive image-based visual servoing for an underactuated quadrotor system. *J. Guid. Control Dyn.* **2012**, *35*, 1335–1353. [CrossRef]
110. Eynard, D.; Vasseur, P.; Demonceaux, C.; Frémont, V. Real time UAV altitude, attitude and motion estimation from hybrid stereovision. *Auton. Robot.* **2012**, *33*, 157–172. [CrossRef]
111. Meier, L.; Tanskanen, P.; Heng, L.; Lee, G.H.; Fraundorfer, F.; Pollefeys, M. PIXHAWK: A micro aerial vehicle design for autonomous flight using onboard computer vision. *Auton. Robot.* **2012**, *33*, 21–39. [CrossRef]
112. Mondragón, I.F.; Olivares-Méndez, M.A.; Campoy, P.; Martínez, C.; Mejias, L. Unmanned aerial vehicles UAVs attitude, height, motion estimation and control using visual systems. *Auton. Robot.* **2010**, *29*, 17–34. [CrossRef]
113. Kim, H.J.; Kim, M.; Lim, H.; Park, C.; Yoon, S.; Lee, D.; Choi, H.; Oh, G.; Park, J.; Kim, Y. Fully autonomous vision-based net-recovery landing system for a fixed-wing UAV. *IEEE/ASME Trans. Mechatron.* **2013**, *18*, 1320–1333. [CrossRef]
114. Xie, H.; Lynch, A.F. Input saturated visual servoing for unmanned aerial vehicles. *IEEE/ASME Trans. Mechatron.* **2017**, *22*, 952–960. [CrossRef]
115. Mejías, L.; Saripalli, S.; Campoy, P.; Sukhatme, G.S. Visual servoing of an autonomous helicopter in urban areas using feature tracking. *J. Field Robot.* **2006**, *23*, 185–199. [CrossRef]
116. Richardson, T.S.; Jones, C.G.; Likhoded, A.; Sparks, E.; Jordan, A.; Cowling, I.; Willcox, S. Automated vision-based recovery of a rotary wing unmanned aerial vehicle onto a moving platform. *J. Field Robot.* **2013**, *30*, 667–684. [CrossRef]
117. Amidi, O.; Kanade, T.; Fujita, K. A visual odometer for autonomous helicopter flight. *Robot. Auton. Syst.* **1999**, *28*, 185–193. [CrossRef]
118. Garcia-Pardo, P.J.; Sukhatme, G.S.; Montgomery, J.F. Towards vision-based safe landing for an autonomous helicopter. *Robot. Auton. Syst.* **2002**, *38*, 19–29. [CrossRef]
119. Kendoul, F.; Fantoni, I.; Nonami, K. Optic flow-based vision system for autonomous 3D localization and control of small aerial vehicles. *Robot. Auton. Syst.* **2009**, *57*, 591–602. [CrossRef]
120. Mondragón, I.F.; Campoy, P.; Martinez, C.; Olivares, M. Omnidirectional vision applied to Unmanned Aerial Vehicles (UAVs) attitude and heading estimation. *Robot. Auton. Syst.* **2010**, *58*, 809–819. [CrossRef]
121. Alizadeh, M.; Mehrandezh, M.; Paranjape, R. Vision-based adaptive prediction, planning, and execution of permissible and smooth trajectories for a 2DOF model helicopter. *Can. Aeronaut. Space J.* **2013**, *59*, 81–92. [CrossRef]
122. Ebrahimi, A.; Janabi-Sharifi, F.; Ghanbari, A. UavisBug: Vision-based 3D motion planning and obstacle avoidance for a mini-UAV in an unknown indoor environment. *Can. Aeronaut. Space J.* **2014**, *60*, 9–21. [CrossRef]
123. Kummer, N.; Beresowskaja, A.; Firouzi, H.; Najjaran, H. Autonomous UAV controlled collision landing via eye-in-hand visual servoing. *Can. Aeronaut. Space J.* **2016**, *61*, 1–22. [CrossRef]
124. Choi, H.; Kim, Y. UAV guidance using a monocular-vision sensor for aerial target tracking. *Control Eng. Pract.* **2014**, *22*, 10–19. [CrossRef]
125. Huh, S.; Shim, D.H. A vision-based landing system for small unmanned aerial vehicles using an airbag. *Control Eng. Pract.* **2010**, *18*, 812–823. [CrossRef]
126. Zhang, X.; Xian, B.; Zhao, B.; Zhang, Y. Autonomous flight control of a nano quadrotor helicopter in a GPS-denied environment using on-board vision. *IEEE Trans. Ind. Electron.* **2015**, *62*, 6392–6403. [CrossRef]
127. Zhao, S.; Hu, Z.; Yin, M.; Ang, K.Z.Y.; Liu, P.; Wang, F.; Dong, X.; Lin, F.; Chen, B.M.; Lee, T.H. A robust real-time vision system for autonomous cargo transfer by an unmanned helicopter. *IEEE Trans. Ind. Electron.* **2015**, *62*, 1210–1219. [CrossRef]

128. Bourquardez, O.; Mahony, R.; Guenard, N.; Chaumette, F.; Hamel, T.; Eck, L. Image-based visual servo control of the translation kinematics of a quadrotor aerial vehicle. *IEEE Trans. Robot.* **2009**, *25*, 743–749. [CrossRef]
129. Guenard, N.; Hamel, T.; Mahony, R. A practical visual servo control for an unmanned aerial vehicle. *IEEE Trans. Robot.* **2008**, *24*, 331–340. [CrossRef]
130. Mebarki, R.; Lippiello, V.; Siciliano, B. Nonlinear visual control of unmanned aerial vehicles in GPS-denied environments. *IEEE Trans. Robot.* **2015**, *31*, 1004–1017. [CrossRef]
131. Aksenov, A.Y.; Kuleshov, S.V.; Zaytseva, A.A. An application of computer vision systems to solve the problem of unmanned aerial vehicle control. *Transp. Telecommun. J.* **2014**, *15*. [CrossRef]
132. Algabri, M.; Mathkour, H.; Mekhtiche, M.A.; Bencherif, M.A.; Alsulaiman, M.; Arafah, M.A.; Ghaleb, H. Wireless vision-based fuzzy controllers for moving object tracking using a quadcopter. *Int. J. Distrib. Sens. Netw.* **2017**, *13*. [CrossRef]
133. Angelopoulou, M.E.; Bouganis, C.S. Vision-based egomotion estimation on FPGA for unmanned aerial vehicle navigation. *IEEE Trans. Circuits Syst. Video Technol.* **2014**, *24*, 1070–1083. [CrossRef]
134. Azinheira, J.R.; Rives, P. Image-based visual servoing for vanishing features and ground lines tracking: Application to a UAV automatic landing. *Int. J. Optomechatron.* **2008**, *2*, 275–295. [CrossRef]
135. Bi, Y.; Duan, H. Implementation of autonomous visual tracking and landing for a low-cost quadrotor. *Opt.-Int. J. Light Electron Opt.* **2013**, *124*, 3296–3300. [CrossRef]
136. Bin, X.; Sen, Y.; Xu, Z. Control of a quadrotor helicopter using the COMPASS (BeiDou) system and on-board vision system. *Opt.-Int. J. Light Electron Opt.* **2016**, *127*, 6829–6838. [CrossRef]
137. Campa, G.; Napolitano, M.R.; Perhinschi, M.; Fravolini, M.L.; Pollini, L.; Mammarella, M. Addressing pose estimation issues for machine vision based UAV autonomous serial refuelling. *Aeronaut. J.* **2007**, *111*, 389–396. [CrossRef]
138. Chen, S.; Duan, H.; Deng, Y.; Li, C. Drogue pose estimation for unmanned aerial vehicle autonomous aerial refueling system based on infrared vision sensor. *Opt. Eng.* **2017**, *56*, 1. [CrossRef]
139. Chen, Y.; Huang, R.; Zhu, Y. A cumulative error suppression method for UAV visual positioning system based on historical visiting information. *Eng. Lett.* **2017**, *25*, 424–430.
140. Chiu, C.C.; Lo, C.T. Vision-only automatic flight control for small UAVs. *IEEE Trans. Veh. Technol.* **2011**, *60*, 2425–2437. [CrossRef]
141. Corke, P. An inertial and visual sensing system for a small autonomous helicopter. *J. Robot. Syst.* **2004**, *21*, 43–51. [CrossRef]
142. de Plinval, H.; Morin, P.; Mouyon, P.; Hamel, T. Visual servoing for underactuated VTOL UAVs: A linear, homography-based framework. *Int. J. Robust Nonlinear Control* **2014**, *24*, 2285–2308. [CrossRef]
143. Eresen, A.; İmamoğlu, N.; Önder Efe, M. Autonomous quadrotor flight with vision-based obstacle avoidance in virtual environment. *Expert Syst. Appl.* **2012**, *39*, 894–905. [CrossRef]
144. Fan, C.; Liu, Y.; Song, B.; Zhou, D. Dynamic visual servoing of a small scale autonomous helicopter in uncalibrated environments. *Sci. China Inf. Sci.* **2011**, *54*, 1855–1867. [CrossRef]
145. Fink, G.; Xie, H.; Lynch, A.F.; Jagersand, M. Dynamic visual servoing for a quadrotor using a virtual camera. *Unmanned Syst.* **2017**, *5*, 1–17. [CrossRef]
146. Fink, G.; Franke, M.; Lynch, A.F.; Röbenack, K.; Godbolt, B. Visual inertial SLAM: Application to unmanned aerial vehicles. *IFAC-PapersOnLine* **2017**, *50*, 1965–1970. [CrossRef]
147. Fravolini, M.L.; Campa, G.; Napolitano, M.R. Evaluation of machine vision algorithms for autonomous aerial refueling for unmanned aerial vehicles. *J. Aerosp. Comput. Inf. Commun.* **2007**, *4*, 968–985. [CrossRef]
148. Ivancsits, C.; Ricky Lee, M. Visual navigation system for small unmanned aerial vehicles. *Sens. Rev.* **2013**, *33*, 267–291. [CrossRef]
149. Jabbari Asl, H.; Yazdani, M.; Yoon, J. Vision-based tracking control of quadrator using velocity of image features. *Int. J. Robot. Autom.* **2016**, *31*. [CrossRef]

150. Jabbari Asl, H.; Yoon, J. Adaptive vision-based control of an unmanned aerial vehicle without linear velocity measurements. *ISA Trans.* **2016**, *65*, 296–306. [CrossRef]
151. Jabbari Asl, H.; Yoon, J. Bounded-input control of the quadrotor unmanned aerial vehicle: A vision-based approach. *Asian J. Control* **2017**, *19*, 840–855. [CrossRef]
152. Jan, I.U.; Khan, M.U.; Iqbal, N. Visual landing of helicopter by divide and conquer rule. *IEICE Electron. Express* **2011**, *8*, 1542–1548. [CrossRef]
153. Jurado, F.; Palacios, G.; Flores, F.; Becerra, H.M. Vision-based trajectory tracking system for an emulated quadrotor UAV. *Asian J. Control* **2014**, *16*, 729–741. [CrossRef]
154. Kemsaram, N.; Thatiparti, V.R.K.; Guntupalli, D.R.; Kuvvarapu, A. Design and development of an on-board autonomous visual tracking system for unmanned aerial vehicles. *Aviation* **2017**, *21*, 83–91. [CrossRef]
155. Kim, Y.; Jung, W.; Bang, H. Visual target tracking and relative navigation for unmanned aerial hehicles in a GPS-denied environment. *Int. J. Aeronaut. Space Sci.* **2014**, *15*, 258–266. [CrossRef]
156. Lee, D.; Kim, Y.; Bang, H. Vision-aided terrain referenced navigation for unmanned aerial vehicles using ground features. *Proc. Inst. Mech. Eng. Part G J. Aerosp. Eng.* **2014**, *228*, 2399–2413. [CrossRef]
157. Lee, D.J.; Kaminer, I.; Dobrokhodov, V.; Jones, K. Autonomous feature following for visual surveillance using a small unmanned aerial vehicle with gimbaled camera system. *Int. J. Control Autom. Syst.* **2010**, *8*, 957–966. [CrossRef]
158. Lee, J.; Lee, K.; Park, S.; Im, S.; Park, J. Obstacle avoidance for small UAVs using monocular vision. *Aircr. Eng. Aerosp. Technol.* **2011**, *83*, 397–406. [CrossRef]
159. Lee, J.O.; Kang, T.; Lee, K.H.; Im, S.K.; Park, J. Vision-based indoor localization for unmanned aerial vehicles. *J. Aerosp. Eng.* **2011**, *24*, 373–377. [CrossRef]
160. Liu, C.; Prior, S.D.; Teacy, W.L.; Warner, M. Computationally efficient visual–inertial sensor fusion for Global Positioning System–denied navigation on a small quadrotor. *Adv. Mech. Eng.* **2016**, *8*. [CrossRef]
161. Mammarella, M.; Campa, G.; Napolitano, M.R.; Fravolini, M.L.; Gu, Y.; Perhinschi, M.G. Machine vision/GPS integration using EKF for the UAV aerial refueling problem. *IEEE Trans. Syst. Man Cybern. Part C Appl. Rev.* **2008**, *38*, 791–801. [CrossRef]
162. Maravall, D.; de Lope, J.; Pablo Fuentes, J. Vision-based anticipatory controller for the autonomous navigation of an UAV using artificial neural networks. *Neurocomputing* **2015**, *151*, 101–107. [CrossRef]
163. Metni, N.; Hamel, T. A UAV for bridge inspection: Visual servoing control law with orientation limits. *Autom. Constr.* **2007**, *17*, 3–10. [CrossRef]
164. Park, J.; Im, S.; Lee, K.H.; Lee, J.O. Vision-based SLAM system for small UAVs in GPS-denied environments. *J. Aerosp. Eng.* **2012**, *25*, 519–529. [CrossRef]
165. Pebrianti, D.; WeiWang.; Iwakura, D.; Song, Y.; Nonami, K. Sliding mode controller for stereo vision based autonomous flight of quad-rotor MAV. *J. Robot. Mechatron.* **2011**, *23*, 137–148. [CrossRef]
166. Rahino Triputra, F.; Riyanto Trilaksono, B.; Adiono, T.; Adhy Sasongko, R. Visual servoing of fixed - wing unmanned aerial vehicle using command filtered backstepping. *Int. J. Electr. Eng. Inform.* **2015**, *7*, 584–604. [CrossRef]
167. Rawashdeh, N.A.; Rawashdeh, O.A.; Sababha, B.H. Vision-based sensing of UAV attitude and altitude from downward in-flight images. *J. Vib. Control* **2017**, *23*, 827–841. [CrossRef]
168. Razinkova, A.; Cho, H.C. Vision-based tracking of a moving ground object by quadcopter UAV using noise filtering. *Int. J. Imaging Robot.* **2016**, *16*, 1–16.
169. Rilanto Trilaksono, B.; Triadhitama, R.; Adiprawita, W.; Wibowo, A.; Sreenatha, A. Hardware-in-the-loop simulation for visual target tracking of octorotor UAV. *Aircr. Eng. Aerosp. Technol.* **2011**, *83*, 407–419. [CrossRef]
170. Saripalli, S.; Montgomery, J.; Sukhatme, G. Visually guided landing of an unmanned aerial vehicle. *IEEE Trans. Robot. Autom.* **2003**, *19*, 371–380. [CrossRef]
171. Silva, C.; Goltz, G.; Shiguemori, E.; Castro, C.D.; Velho, H.D.C.; Braga, A.D. Image matching applied to autonomous navigation of unmanned aerial vehicles. *Int. J. High Perform. Syst. Arch.* **2016**, *6*, 205. [CrossRef]

172. Stefas, N.; Bayram, H.; Isler, V. Vision-based UAV navigation in orchards. *IFAC-PapersOnLine* **2016**, *49*, 10–15. [CrossRef]
173. Tippetts, B.J.; Lee, D.J.; Fowers, S.G.; Archibald, J.K. Real-time vision sensor for an autonomous hovering micro unmanned aerial vehicle. *J. Aerosp. Comput. Inf. Commun.* **2009**, *6*, 570–584. [CrossRef]
174. Vendra, S.; Campa, G.; Napolitano, M.R.; Mammarella, M.; Fravolini, M.L.; Perhinschi, M.G. Addressing corner detection issues for machine vision based UAV aerial refueling. *Mach. Vis. Appl.* **2007**, *18*, 261–273. [CrossRef]
175. Wang, C.L.; Wang, T.M.; Liang, J.H.; Zhang, Y.C.; Zhou, Y. Bearing-only visual SLAM for small unmanned aerial vehicles in GPS-denied environments. *Int. J. Autom. Comput.* **2013**, *10*, 387–396. [CrossRef]
176. Wang, T.; Wang, C.; Liang, J.; Zhang, Y. Rao-Blackwellized visual SLAM for small UAVs with vehicle model partition. *Ind. Robot. Int. J.* **2014**, *41*, 266–274. [CrossRef]
177. Xie, H.; Lynch, A.F. State transformation-based dynamic visual servoing for an unmanned aerial vehicle. *Int. J. Control* **2016**, *89*, 892–908.

[CrossRef]
178. Merriaux, P.; Dupuis, Y.; Boutteau, R.; Vasseur, P.; Savatier, X. A study of VICON system positioning performance. *Sensors* **2017**, *17*, 1591. [CrossRef]

© 2019 by the authors. Licensee MDPI, Basel, Switzerland. This article is an open access article distributed under the terms and conditions of the Creative Commons Attribution (CC BY) license (http://creativecommons.org/licenses/by/4.0/).

2.1.2 Flying Depth Camera for Indoor Mapping and Localization

Publication Data

ABSTRACT:
This paper introduces a flying robot mapping and localization proposal from an onboard depth camera. The miniature flying robot is part of an ongoing project related to ambient assisted living and home health. The flying depth camera is used with a double function; firstly, as a range sensor for mapping from scratch during navigation, and secondly, as a gray-scale camera for localization. The Harris corner detection algorithm is implemented as key point detector for the creation and/or identification of indoor spatial relations. During the localization phase, the spatial relations created from detected corners in the mapping phase are compared to the corners identified in the map. The flying robot position is estimated by matching these spatial relations.

CITATION:
L.M. Belmonte; J.C. Castillo; A. Fernández-Caballero; S. Valverde; R. Morales. "Flying Depth Camera for Indoor Mapping and Localization". *Ambient Intelligence - Software and Applications*. ISAmI 2015. AISC, vol. 376, 243–251. Springer, 2015. ISBN 978-3-319-19694-7. DOI:10.1007/978-3-319-19695-4_25.

Reprinted by permission from Springer Nature: Springer, Ambient Intelligence - Software and Applications. ISAmI 2015. Advances in Intelligent Systems and Computing, by A. Mohamed, P. Novais, A. Pereira, G. Villarrubia González, A. Fernández-Caballero (eds), Copyright 2015.
License Number: 4574840960289. License Date: Apr 23, 2019.

Flying Depth Camera for Indoor Mapping and Localization

Lidia María Belmonte, José Carlos Castillo, Antonio Fernández-Caballero, Sergio Almansa-Valverde and R. Morales

Abstract This paper introduces a flying robot mapping and localization proposal from an onboard depth camera. The miniature flying robot is part of an ongoing project related to ambient assisted living and home health. The flying depth camera is used with a double function; firstly, as a range sensor for mapping from scratch during navigation, and secondly, as a gray-scale camera for localization. The Harris corner detection algorithm is implemented as key point detector for the creation and/or identification of indoor spatial relations. During the localization phase, the spatial relations created from detected corners in the mapping phase are compared to the corners identified in the map. The flying robot position is estimated by matching these spatial relations.

Keywords Ambient assisted living · Miniature flying robot · Flying depth camera · Mapping · Localization

1 Introduction

Autonomous navigation of flying robots in GPS-denied environments such as indoors requires that the flying robot be able to recognize the environment using external sensors [1]. Our research team is engaged in introducing miniature flying robots in ambient assisted living (e.g. [2–4]) and home health [5] applications. Now, dealing with the high amount of obstacles inherent to home facilities is a major challenge for flying vehicles [6]. This why mapping and localization at homes of the flying robot are extremely important challenges.

Mobile robot mapping techniques are usually classified according to the map representation and the underlying estimation technique [7, 8]. One popular map repre-

L.M. Belmonte (✉) · A. Fernández-Caballero · S. Almansa-Valverde · R. Morale
Escuela de Ingenieros Industriales, Universidad de Castilla-La Mancha,
02071 Albacete, Spain

J.C. Castillo
Robotics Lab, Universidad Carlos III de Madrid, 28911 Madrid, Spain

© Springer International Publishing Switzerland 2015

A. Mohamed et al. (eds.), *Ambient Intelligence - Software and Applications*,
Advances in Intelligent Systems and Computing 376,
DOI 10.1007/978-3-319-19695-4_25

sentation is the occupancy grid [9]. Such grid-based approaches are able to represent arbitrary objects [10]. However, such systems rely on predefined feature extractors. In this sense, scan matching approaches demonstrate to produce consistent maps [11]. Now, in mobile robot localization, an appearance-based approach for place recognition involves the matching of scenes based on selected features or landmarks observed within the current local map or sensor view. For each feature a descriptor vector that encodes the local area around that landmark is computed, thus allowing the comparison of features based on appearance. The combination of a location and descriptor vector is denominated a key point [12]. Localization then becomes a matter of identifying places and/or objects by associating key points, or deciding that a place/object was not previously seen.

Key points have been used in vision-based systems which use nearest neighbor voting [13] with SIFT [14] features. Another approach [15] uses a fast-Hessian detector to identify key points in an image and SURF [16]. In a review, detectors and local descriptors of local features for computer vision are described [17]. Another key point detector is the SUSAN corner detector [18] which finds corners based on the fraction of pixels that are similar to the center pixel in a circular region. Also, affine invariant feature extraction for localization in indoor environments, using the Harris corner detector [19] for local point detection, has been proposed [20].

Our proposal deals with specific characteristics of depth cameras [21] to solve the mapping and localization problem. Two constraints have been addressed. First, the generated map increases when new zones are discovered as the environment is unknown. And second, no landmark is introduced to facilitate the localization process since the robot flies in a real environment. Moreover, the looking forward depth camera is firstly used as a range sensor for mapping, and, afterwards as a gray-scale camera for localization. The depth camera, when used as a range sensor, provides a powerful tool for measuring the distance from the detected objects to the flying robot. On the other hand, the depth camera creates an image representing distances which enable extracting trackable features. These points in the space are the basis for the spatial relations used in the localization phase. Finally, the flying robot position is estimated in accordance to the localization information provided through the identified spatial relations. It should be noted that the proposal requires a flight at a constant height.

2 Mapping from Flying Robot

The depth camera is considered a range sensor during the mapping stage due to the simplicity of translating the (x, y) coordinates of each image pixel provided by the camera into map coordinates. The perceived environment is represented in a map containing the probability in each cell of the presence of an element/obstacle.

An occupancy grid model is used to represent the environment. As the size of the environment is unknown a priori, it is not possible to create a fixed-size occupancy grid. This is why, the environment is represented as a collection of modular occu-

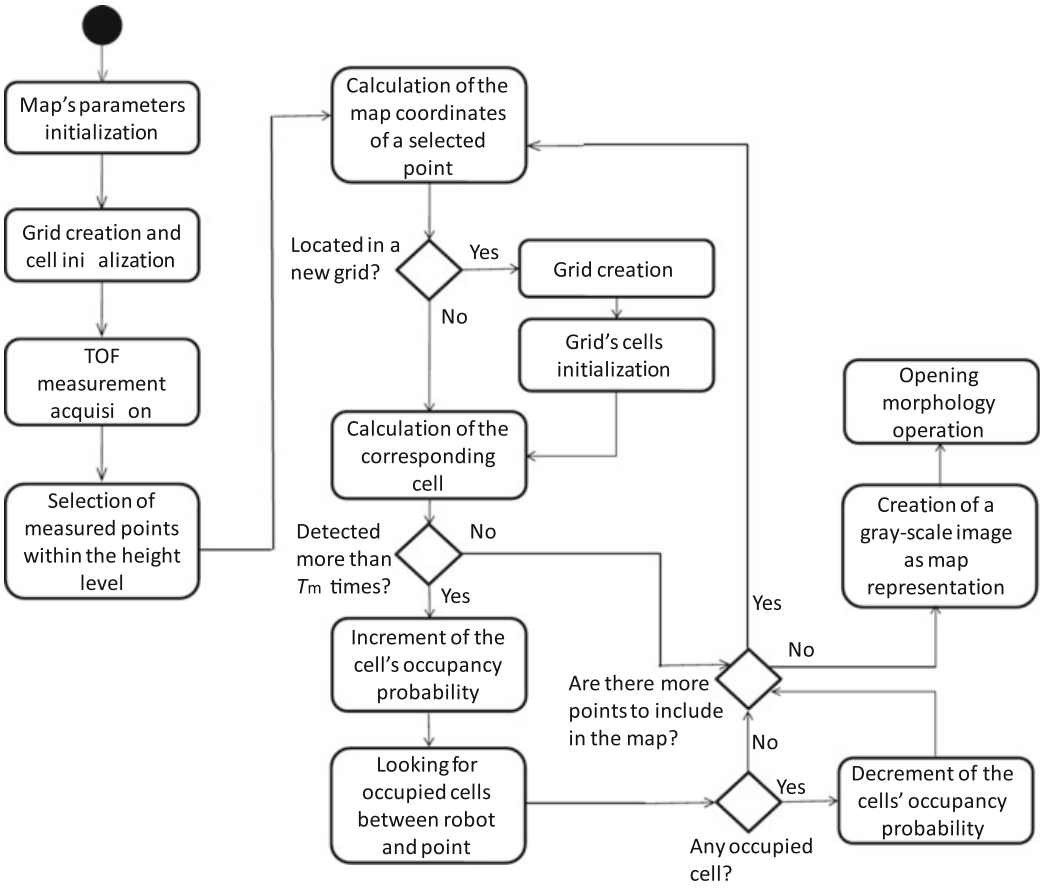

Fig. 1 Flow diagram of the mapping algorithm

pancy grids which are added to the map as far as the robot finds objects outside the existing grids. Therefore, when the robot starts the exploration there exists just one grid, and all necessary grids are added according to the size of the explored environment. Each occupancy grid has the same size and number of cells and is placed in a specific area given by its global coordinates M_x, M_y in the environmental representation. So every point in the environment is located in one and only one grid. For each grid, every cell contains an occupancy value where a value of 0.00 indicates the certainty that the cell is free and a value of 1.00 the certainty that the cell is occupied.

Figure 1 shows a flow diagram of the mapping algorithm. The depth camera provides as output a matrix where each element represents the coordinates (x, y, z) (in meters) of a system. Here the camera is the origin of coordinates, x varies along the horizontal axis, y varies along the vertical axis and z is the distance from the plane defined by the x and y axes. Let us assume that the flying robot position (m_r, x_r, y_r, θ) is known, where m_r is the occupancy grid where the robot is located, x_r and y_r represent the position within that grid, and θ is the robot orientation with respect to the y axis in the grid. On the other hand, the depth camera provides the coordinates of point (x_d, y_d, z_d) as its position relative to the robot's localization. From these two groups of coordinates, it is possible to calculate the position of a point $p(m, x, y, h)$

in the map, being m the occupancy grid where the point is located, x and y represent the position within that grid and h is the height of the point.

In order to visually represent each point detected by the camera some calculations are performed. First, the distance D between the flying robot and the point is calculated as follows:

$$D = \sqrt{x_d^2 + z_d^2} \tag{1}$$

Once the distance is known, the angle α between the robot orientation and the segment given by D is obtained:

$$\sin(\alpha) = \frac{x_d}{D} \rightarrow \alpha = \arcsin(\frac{x_d}{D}) \tag{2}$$

And, finally, through the following equations, the position of the point in the map is also calculated:

$$\begin{aligned} x &= x_r + D\sin(\theta + \alpha) \\ y &= y_r + D\cos(\theta + \alpha) \\ h &= y_d \end{aligned} \tag{3}$$

Next, it is necessary to know whether each new point is located on an existing grid. Otherwise, it is necessary to create a new one. Once the coordinates of every point have been calculated, the new observations must be represented in the grid, updating the occupancy probability of the affected cells. As each cell covers several squared centimeters of the map, it is usual that more than one detected point is located into the same cell for the same observation. Consequently, the occupancy probability of each cell is increased as many times as points are detected to belong to it.

3 Localization from Flying Robot

Only the information provided by the depth camera is used to estimate the flying robot position in the environment. The depth information provided is considered as gray-level values of a traditional image. From these image pixel values, a series of characteristic points (or corners) are extracted to create spatial relations that are placed in the map. When new spatial relations are created from detected corners, they are compared to the previously created ones and identified to calculate their location in the map. Finally the robot position is estimated starting from that information. A flow diagram of the localization algorithm is presented in Fig. 2.

Creating an image representation of the distance measurements enables the use of corner detection algorithm. Concretely, the Harris algorithm has been used for this

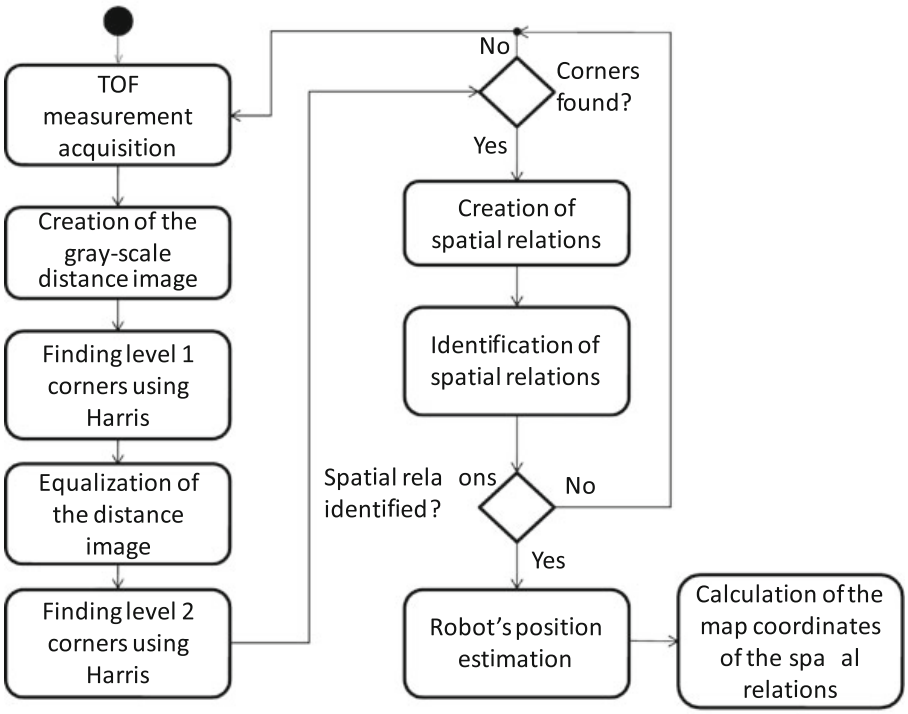

Fig. 2 Flow diagram of the localization algorithm

purpose, mainly because its computational cost is lower than other approaches such as SIFT. Applying Harris algorithm to the distance image results in a list of corners. In our case a hierarchy of two levels of corners is implemented. The first level of corners is composed by those found in the initial distance image, I_d. Usually not many corners are found due to the low contrast of these images, although the gotten corners are quite resistant to noise. Some filters are performed on image I_d to get the second level of corners. A first filter equalizes the image histogram to enhance the contrast. After that, as noise is also enhanced with the equalization, a smoothing Gaussian is applied to the equalized result, obtaining I_f.

Using Harris algorithm on I_f returns more corners than on I_d, but they will be less resistant to noise. Hence, spatial relations based on corners belonging to level 1 are more trusted. So, they have higher priority than those based on corners belonging to level 2. But the last ones are mandatory for a correct localization as level 1 rarely contains enough corners to achieve a good localization.

Once the corners are extracted, spatial relations connecting every pair of points from the same level are established. Some information is associated to these spatial relations in order to define and to identify them. As the map coordinates of the corners are unknown at the beginning, the information associated to spatial relations is independent of the location in the map. The spatial relations information contains the following attributes: priority, according to the level of the corners belonging to the spatial relation, and distance in meters between the two points, N, calculated as follows:

$$N = \sqrt{(x_{d1} - x_{d2})^2 + (y_{d1} - y_{d2})^2 + (z_{d1} - z_{d2})^2} \tag{4}$$

where the first corner has (x_{d1}, y_{d1}, z_{d1}) as camera coordinates, and the second one has coordinates (x_{d2}, y_{d2}, z_{d2}). The third and fourth attributes are the slopes between x and y coordinates and between x and z coordinates of the vector connecting the two corners in the space. The slope between x and y is calculated as follows:

$$S_y = \frac{|x_{d1} - x_{d2}|}{|y_{d1} - y_{d2}|} \tag{5}$$

Figure 3 shows an example of the spatial relations calculated on a depth image taken by the flying robot in our research laboratory.

The next step in the localization algorithm is the identification of new spatial relations to calculate their location in the map (that is, if some points have known positions in the map, new points can also be placed if there are spatial relations between them), to finally estimate the robot position. For this purpose, the attributes of distance and slope are compared to identify the spatial relations. When identifying a spatial relation it is not necessary to find another identical one, but similarity tolerance values τ_{si} and τ_{sl} in the distance between the points and in the slopes, respectively, have been included.

Lastly, the flying robot position can be calculated. Instead of using the coordinates of one point (or corner) like in the mapping algorithm, the coordinates of the two corners that form the spatial relation are used. The system of equations is as follows:

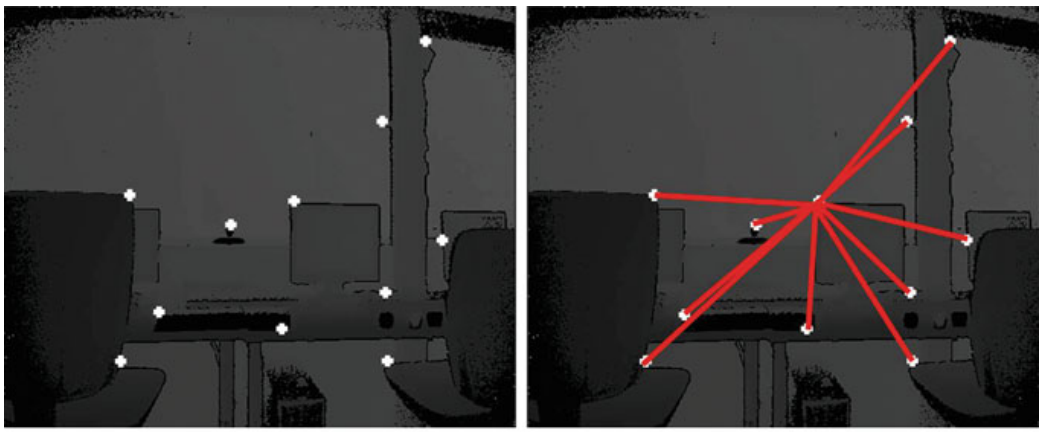

Fig. 3 Example of spatial relations. (a) Depth image with second level corners. (b) Spatial relations corresponding to a random corner

$$
\begin{aligned}
x_r &= x_1 + D_1 \sin(\theta + \pi + \alpha_1) \\
x_r &= x_2 + D_2 \sin(\theta + \pi + \alpha_2) \\
y_r &= y_1 + D_1 \cos(\theta + \pi + \alpha_1) \\
y_r &= y_2 + D_2 \cos(\theta + \pi + \alpha_2)
\end{aligned} \tag{6}
$$

where x_r and y_r are the robot coordinates, θ is the robot orientation, x_1 and y_1 are the coordinates of the first corner, x_2 and y_2 are the coordinates of the second point, D_1 and D_2 are the distances between the robot and each point projected to the floor, and α_1 and α_2 are angles between the flying robot orientation and segments D_1 and D_2, respectively.

From this system of equations, the flying robot orientation is solved as follows:

$$X = x_1 - x_2 \tag{7}$$

$$A = D_1 \cos(\alpha_1) - D_2 \cos(\alpha_2) \tag{8}$$

$$B = D_1 \sin(\alpha_1) - D_2 \sin(\alpha_2) \tag{9}$$

$$\theta = \arccos\left(\frac{-2BX \pm \sqrt{(2BX)^2 - 4(A^2 + B^2)(X^2 - A^2)}}{2(A^2 + B^2)}\right) - \pi \tag{10}$$

After knowing the flying robot orientation, it is possible to calculate the coordinates from the original equation (6).

4 Conclusions

In this paper, the authors have introduced the use of a depth camera for flying robot mapping and localization in home facilities. Firstly, a map building algorithm for flying robots has been introduced. The perceived environment is represented in a map containing in each cell a probability of presence of an object or part of an object. As the size of the environment is unknown a priori, it is not possible to create a fixed-size occupancy grid. The environment is represented as a collection of modular occupancy grids which are added to the map as far as the robot finds objects outside the existing grids.

In our approach the depth camera is exploited as a range sensor for the mapping purpose. Indeed, a depth camera used as a range sensor provides a powerful tool for detecting objects in front of the robot by measuring the distance towards them. Next, for our experiments with localization, the Harris corner detection algorithm is applied. In this case, the depth camera is exploited as a gray-scale camera. The gray-scale image represents distances for the purpose of finding good features to be tracked. These features form the basis of the spatial relations used in the localization

algorithm. The approach to the localization problem is based on the computation of the spatial relations existing among the corners detected. The current spatial relations are matched with the relations gotten during previous navigation.

Acknowledgments This work was partially supported by Spanish Ministerio de Economía y Competitividad / FEDER under TIN2013-47074-C2-1-R grant.

References

1. D. Iwakura, K. Nonami, Indoor localization of flying robot by means of infrared sensors. J. Robot. Mechatron. **25**, 201–210 (2013)
2. A. Fernández-Caballero, J.M. Latorre, J.M. Pastor, A. Fernández-Sotos, Improvement of the elderly quality of life and care through smart emotion regulation, *Ambient Assisted Living and Daily Activities*, pp. 348–355, 2014
3. J.C. Castillo, D. Carneiro, J. Serrano-Cuerda, P. Novais, A. Fernández-Caballero, J. Neves, A multi-modal approach for activity classification and fall detection. Int. J. Syst. Sci. **45**, 810–824 (2014)
4. D. Carneiro, J.C. Castillo, P. Novais, A. Fernández-Caballero, J. Neves, Multimodal behavioral analysis for non-invasive stress detection. Expert Syst. Appl. **39**, 13376–13389 (2012)
5. M. Oliver, F. Montero, A. Fernández-Caballero, P. González, J.P. Molina, RGB-D assistive technologies for acquired brain injury: description and assessment of user experience. Expert Syst. (2014). doi:10.1111/exsy.12096
6. A. Briod, P. Kornatowski, J.-C. Zufferey, D. Floreano, A collision-resilient flying robot. J. Field Robot. **31**, 496–509 (2014)
7. K.M. Wurm, C. Stachniss, G. Grisetti, Bridging the gap between feature- and grid-based SLAM. Robot. Auton. Syst. **58**, 140–148 (2010)
8. J. Martínez-Gómez, A. Fernández-Caballero, I. García-Varea, L. Rodríuez, C. Romero-González, A taxonomy of vision systems for ground mobile robots. Int. J. Adv. Robot. Syst. **11**, 111 (2014)
9. T. Collins, Occupancy grid learning using contextual forward modelling. J. Intell. Robot. Syst. **64**, 505–542 (2011)
10. S. Almansa-Valverde, J.C. Castillo, A. Fernández-Caballero, Mobile robot map building from time-of-flight camera. Expert Syst. Appl. **39**, 8835–8843 (2012)
11. A. Ramisa, A. Goldhoorn, D. Aldavert, R. Toledo, R. Lopez de Mantaras, Combining invariant features and the ALV homing method for autonomous robot navigation based on panoramas. J. Intell. Robot. Syst. **64**, 625–649 (2011)
12. M. Bosse, R. Zlot, Keypoint design and evaluation for place recognition in 2D lidar maps. Robot. Auton. Syst. **57**, 1211–1224 (2009)
13. M. Cummins, P. Newman, FAB-MAP: probabilistic localization and mapping in the space of appearance. Int. J. Robot. Res. **27**, 647–665 (2008)
14. D.G. Lowe, Distinctive image features from scale-invariant keypoints. Int. J. Comput. Vis. **60**, 91–110 (2004)
15. G. Arbeiter, J. Fischer, A. Verl, 3D perception and modeling for manipulation on Care-O-Bot 3, in *2010 IEEE International Conference on Robotics and Automation*, p. 5, 2010
16. H. Bay, A. Ess, T. Tuytelaars, L. Van Gool, SURF: speeded up robust features. Comput. Vis. Image Underst. **110**, 346–359 (2008)
17. J. Li, N.M. Allinson, A comprehensive review of current local features for computer vision. Neurocomputing **71**, 1771–1787 (2008)
18. S. Smith, J. Brady, Susan: a new approach to low-level image-processing. Int. J. Comput. Vis. **23**, 45–78 (1997)

19. C. Harris, M. Stephens, A combined corner and edge detector, in *The Fourth Alvey Vision Conference*, pp. 147–151, 1988
20. J. Lee, H. Ko, Gradient-based local affine invariant feature extraction for mobile robot localization in indoor environments. Pattern Recogn. Lett. **29**, 1934–1940 (2008)
21. A. Fernández-Caballero, M.T. López, S. Saiz-Valverde, Dynamic stereoscopic selective visual attention (DSSVA): integrating motion and shape with depth in video segmentation. Expert Syst. Appl. **34**, 1394–1402 (2008)
22. G. Bennett, Probability inequalities for the sum of independent random variables. J. Am. Stat. Assoc. **57**, 33–45 (1962)

2.2 Simulation of Control Algorithms

One of the main objectives of this thesis is to improve the ability of motion and the stability of UAVs. To achieve this goal, several robust control algorithms have been designed for different models of air vehicles. This section presents the research papers on control schemes which have been validated through simulation tests. Below, the published works are briefly described and presented in different subsections.

The first paper deals with the design of a control scheme for a nonlinear and multivariable quadrotor system model. The quadrotor is a rotatory-wing UAV with four rotors arranged in form of a cross, characterized by its excellent maneuverability, agility, and versatility. For this aircraft model, a generalized proportional integral (GPI) control scheme was designed and its behavior validated by means of numerical simulations in the MATLAB/Simulink® environment. This research was published in the document included in Subsection 2.2.1: "Generalized Proportional Integral Control for an Unmanned Quadrotor System".

The second paper extensively addresses the dynamic modeling and control of a nonlinear, underactuated and multivariable laboratory helicopter denominated Twin Rotor MIMO System (TRMS). This platform, which has been essential in the development of this thesis, is characterized by a high cross-coupling effect that makes it difficult to model and control. Based on the division on mechanical and electrical dynamics, a nonlinear robust control scheme compounded of two nested loops was designed and initially validated by simulation tests. This work was published in the book chapter included in Subsection 2.2.2: "Nonlinear Cascade-Based Control for a Twin Rotor MIMO System".

Lastly, the third paper focuses on a flapping-wing air vehicle. It is a novel type of UAV of very small size that attempts to emulate the flight characteristics of birds and insects. In this case, an observer-based linear output feedback control was designed for trajectory tracking tasks. The controller's development is detailed in the document included in Subsection 2.2.3: "Robust Linear Longitudinal Feedback Control of a Flapping Wing Micro Air Vehicle".

2.2.1 Generalized Proportional Integral Control for an Unmanned Quadrotor System

Publication Data

ABSTRACT:
In this article, a generalized proportional integral (GPI) control approach is presented for regulation and trajectory tracking problems in a nonlinear, multivariable quadrotor system model. In the feedback control law, no asymptotic observers or time discretizations are needed in the feedback loop. The GPI controller guarantees the asymptotically and exponentially stable behaviour of the controlled quadrotor position and orientation, as well as the possibilities of carrying out trajectory tracking tasks. The simulation results presented in the paper show that the proposed method exhibits very good stabilization and tracking performance in the presence of atmospheric disturbances and noise measurements.

CITATION:
A. Fernández-Caballero; L.M. Belmonte; R. Morales; J.A. Somolinos. "Generalized Proportional Integral Control for an Unmanned Quadrotor System". *International Journal of Advanced Robotic Systems*, 12(85), 1–14. InTech, 2015. ISSN 1729-8806. DOI: 10.5772/60833.

© 2015 Author(s). Licensee InTech. This is an open access article distributed under the terms of the Creative Commons Attribution License (http://creativecommons.org/licenses/by/3.0), which permits unrestricted use, distribution, and reproduction in any medium, provided the original work is properly cited.

International Journal of Advanced Robotic Systems

OPEN ACCESS
ARTICLE

Generalized Proportional Integral Control for an Unmanned Quadrotor System

Regular Paper

Antonio Fernández-Caballero[1]*, Lidia María Belmonte[1], Rafael Morales[1] and José Andrés Somolinos[2]

1 Universidad de Castilla-La Mancha, Albacete, Spain
2 Universidad Politécnica de Madrid, Madrid, Spain
*Corresponding author(s) E-mail: Antonio.Fdez@uclm.es

Received 13 January 2015; Accepted 11 May 2015

DOI: 10.5772/60833

© 2015 Author(s). Licensee InTech. This is an open access article distributed under the terms of the Creative Commons Attribution License (http://creativecommons.org/licenses/by/3.0), which permits unrestricted use, distribution, and reproduction in any medium, provided the original work is properly cited.

Abstract

In this article, a generalized proportional integral (GPI) control approach is presented for regulation and trajectory tracking problems in a nonlinear, multivariable quadrotor system model. In the feedback control law, no asymptotic observers or time discretizations are needed in the feedback loop. The GPI controller guarantees the asymptotically and exponentially stable behaviour of the controlled quadrotor position and orientation, as well as the possibilities of carrying out trajectory tracking tasks. The simulation results presented in the paper show that the proposed method exhibits very good stabilization and tracking performance in the presence of atmospheric disturbances and noise measurements.

Keywords Unmanned Aerial Systems, Flatness Approach, Generalized Proportional Integral Control, Tracking Trajectory Planning

1. Introduction

Unmanned aerial vehicles (UAVs) have attracted considerable interest for a wide variety of applications, including meteorological observation, fire monitoring and patrolling, to military purposes such as reconnaissance, monitoring and communication [1]. UAVs can be classified into four main categories based in their aerodynamic configuration [2]: (a) *fixed-wing UAVs*, which require a runway to land and take-off; (b) *rotary-wing UAVs*, which are able to land and take-off vertically and which have high manoeuvrability; (c) *blimp UAVs*, which appear like balloons or airships and which ensure lift by their helium-filled body; and finally (d) *flapping-wing UAVs*, which are inspired by flying insects and which can perform vertical take-off and landing. Nevertheless, rotary-wing platforms have captured a lot of attention in research projects because they present a number of advantages with regard to other UAV platforms. Their high manoeuvrability and ability to vertically take-off and land, as well as the capacity to fly in tough conditions to reach specified areas, make them ideal vehicles for these applications. Among *rotary-wing UAVs*, a new sub-classification can be considered [3]: (a) a *single rotor* is composed by a main rotor on the top and another rotor at the tail to achieve stability (a similar configuration to a helicopter); (b) a *coaxial* presents two propellers mounted in the same shaft rotating in opposite directions; (c) a *quadrotor* consists of four rotors fitted in a cross-like configuration; and (d) a *multi-rotor* consists of six or eight rotors. They are very agile and are able to fly even when a rotor does not work properly (there is redundancy due to the large number of rotors). We should note that, according

to this classification, the quadrotor configuration has been the most widely used.

The quadrotor platform has four powerful rotors, each one of which has independent rotational speed, mounted in a square formation equidistant from the centre. The variation in the speed of the rotors generates the thrust and acceleration in the desired direction. Among the advantages of this platform are low cost, usability and ease of transportation, and it is also able to move at low speeds to ensure good quality images. However, despite the advantages of quadrotors with respect to other UAV platforms, the control of a quadrotor is a challenge due to its high manoeuvrability, its highly coupled multivariable dynamics of a nonlinear nature, and its underactuated condition, taking into account that it has six degrees of freedom (three for position and three for attitude) and only four rotors. For this reason, control techniques for these UAV platforms have witnessed rapidly expanding research to achieve not only autonomous hovering and orientation but also trajectory tracking [4]. Zuo [5] studied the command-filtered backstepping technique in order to stabilize a quadrotor's attitude without calculating analytically the pseudo-control signal derivative, as well as to decrease the dependent degrees of the analytic model. In Bouabdallah *et al.* [6], the application of two different approaches is presented, namely a PID approach assuming a simplified dynamics, and the LQ technique based on a more complete model. La Civita [7] proposed a robust control approach combined with linear rotorcraft models. Madani and Benallegue [8] presented a backstepping control strategy taking into consideration that the quadrotor can be divided into three subsystems: an under-actuated subsystem, a fully-actuated subsystem, and a propeller subsystem. Waslander *et al.* [9] presented two design approaches - integral sliding modes and reinforcement learning - for the altitude control loop. Both techniques resulted in stable controllers with similar response times, showing a significant improvement over linear controllers (which failed to stabilize the system adequately). Formentin and Lovera [10] developed a control law based on the differential flatness property of the position dynamics and the linearization of the system via feedforward and a passivity-based scheme. Furthermore, Gautam and Ha proposed in [11] a self-tuning fuzzy PID controller based on an EKF algorithm for the attitude and position control of a quadrotor. In a recent paper, Chen *et al.* described in [12] a reconfiguration control scheme for a quadrotor helicopter with actuator faults via adaptive control and combined multiple models. Sira-Ramrez studied in [13] an active disturbance rejection control scheme for efficient regulation and trajectory tracking tasks in a nonlinear, multivariable quadrotor system model. Escareño *et al.* [14] developed a nonlinear control strategy based on nested saturations that stabilizes the state of the quadrotor around the origin.

Recently, generalized proportional integral (GPI) controllers have demonstrated good performance in the control of nonlinear systems. GPI control has been found to present a better dynamic response than PID control in terms of the settling time while exhibiting a greater degree of robustness regarding disturbance rejection [15, 16]. GPI control sidesteps the need for traditional asymptotic state observers and directly proceeds to use, in a previously designed state feedback control law, *structural state estimates* in place of the actual state variables. These structural estimates are based on *integral reconstructors* and require only inputs, outputs and iterated integrals of such available signals. The effect of the neglected initial states is suitably compensated by means of a sufficiently large number of additional iterated integral output errors, integral input errors and control actions (see [17] for the relevant theoretical basis and [18]-[20] for the application of these ideas in diverse fields including laboratory experiments).

In this work, we extend the GPI control technique for both stabilization and trajectory tracking tasks of an unmanned quadrotor system. In the control law, neither asymptotic observers nor time discretizations are therefore needed in the feedback loop for the estimation of the states commonly required in traditional state-based feedback controllers for such systems.

The article is structured as follows. Section 2 presents the quadrotor model, and the problem to be solved is formulated. Section 3 establishes the flatness system of the quadrotor model. Next, the GPI controller to be used in the control of the unmanned quadrotor system is derived. In this section, it is proved that the GPI controller produces asymptotically, exponentially convergent tracking-error behaviour in relation to the origin of the coordinates in the error space. Section 4 depicts digital computer simulations showing the performance of the GPI controller and, finally, Section 5 presents the conclusions of the work.

2. Quadrotor Dynamics and Problem Formulation

A quadrotor is an underactuated aircraft with four rotors. The rotors are directed upwards and they are placed in a square formation at an equal distance from the centre of mass of the quadrotor, as shown in Figure 1.

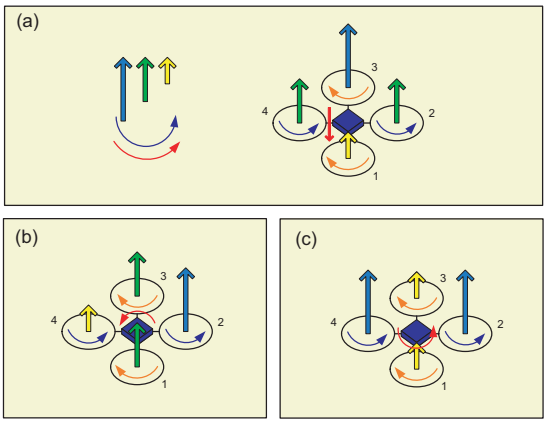

Figure 1. Quadrotor motion principle

In the quadrotor, there are four rotors with fixed angles that are basically the thrust generated by each propeller. The

change of speed in the propellers modifies the lift forces. The pitch movement is obtained by increasing (reducing) the speed of the propeller (1) while reducing (increasing) the speed of the propeller (3). The roll movement is obtained similarly by increasing (reducing) the speed of the propeller (2) while reducing (increasing) the speed of the propeller (4). The yaw movement is achieved by increasing (decreasing) the speed between each pair of propellers.

The dynamic model of the quadrotor can be achieved through the Euler-Lagrange formalism in [22, 23],

$$m\ddot{x} = -uS_\theta \tag{1}$$

$$m\ddot{y} = uC_\theta S_\phi \tag{2}$$

$$m\ddot{z} = uC_\theta C_\phi - mg \tag{3}$$

$$\ddot{\psi} = \tau_\psi \tag{4}$$

$$\ddot{\theta} = \tau_\theta \tag{5}$$

$$\ddot{\phi} = \tau_\phi \tag{6}$$

where $S_\theta \equiv \sin\theta$, $C_\theta \equiv \cos\theta$, $S_\phi \equiv \sin\phi$, $C_\phi \equiv \cos\phi$, m is the mass, g is the gravity acceleration, x and y are coordinates in the horizontal plane, z is the vertical position, the angles ϕ, θ and ψ express the independent orientation angles, u is defined as the total thrust, and τ_ψ, τ_θ and τ_ϕ denote the angular moments (yawing moment, pitching moment and rolling moment, respectively).

Assumption 1: The orientation angles θ and ϕ are upper- and lower-bounded in the intervals $-\frac{\pi}{2} < \phi < \frac{\pi}{2}$ and $-\frac{\pi}{2} < \theta < \frac{\pi}{2}$.

After defining the system dynamics, the problem formulation studied in this work is now stated:

Given a set of smooth reference trajectories (x^*, y^*, z^*, ψ^*), devise a feedback control such that the horizontal coordinates x and y, the vertical position z, and the orientation variable ψ, asymptotically track the given references so that the tracking-error trajectories are ultimately confined to a small neighbourhood of the origin of the tracking-error phase space and the variables θ and ϕ are confined to move in the interval $(-\frac{\pi}{2}, \frac{\pi}{2})$.

3. Control Design

3.1 Flatness of the System

According to the theory of differential flatness [24], a dynamic system, $\dot{\mathbf{x}} = \mathbf{f}(\mathbf{x}, \mathbf{u})$, $\mathbf{y} = \mathbf{h}(\mathbf{x})$, with $\mathbf{x} \in R^n$, $\mathbf{u} \in R^m$ and $\mathbf{y} \in R^p$, is said to be differentially flat if there exist m differentially independent variables, called flat outputs (by differentially independent is meant that they are not related by any differential equation), which are functions of the state vector and, possibly, of a finite number of time derivatives of the state vector (i.e., derivatives of the inputs may be involved in their definition), such that *all* the system variables (states, inputs, outputs, and functions of these variables) can, in turn, be expressed as functions of the flat outputs and of a finite number of their time derivatives. We have the following proposition:

Proposition 1: The quadrotor model given in (1)-(6) is differentially flat, with a flat output vector given by (x, y, z, ψ), i.e., all the system variables in (1)-(6) can be differentially parameterized solely in terms of the flat output vector components x, y, z and ψ, and a finite number of their time derivatives. Their expressions are:

$$u = m\sqrt{\ddot{x}^2 + \ddot{y}^2 + (\ddot{z} + g)^2} \tag{7}$$

$$\phi = \arctan\left(\frac{\ddot{y}}{\ddot{z} + g}\right) \tag{8}$$

$$\theta = -\arctan\left(\frac{\ddot{x}}{\sqrt{\ddot{y}^2 + (\ddot{z} + g)^2}}\right) \tag{9}$$

$$\dot{\phi} = \frac{y^{(3)}(\ddot{z} + g) - \ddot{y}z^{(3)}}{\ddot{y}^2 + (\ddot{z} + g)^2} \tag{10}$$

$$\begin{aligned}\dot{\theta} = &-\frac{1}{\left[\ddot{x}^2 + \ddot{y}^2 + (\ddot{z} + g)^2\right]\sqrt{\ddot{y}^2 + (\ddot{z} + g)^2}} \\ &\times\left[x^{(3)}\left[\ddot{y}^2 + (\ddot{z} + g)^2\right] - \ddot{x}\left[\ddot{y}y^{(3)} + (\ddot{z} + g)z^{(3)}\right]\right]\end{aligned} \tag{11}$$

$$\tau_\psi = \ddot{\psi} \tag{12}$$

$$\begin{aligned}\tau_\phi = &\frac{y^{(4)}(\ddot{z} + g) - \ddot{y}z^{(4)}}{\ddot{y}^2 + (\ddot{z} + g)^2} \\ &-2\frac{\left(y^{(3)}(\ddot{z} + g) - \ddot{y}z^{(3)}\right)\left(\ddot{y}y^{(3)} + (\ddot{z} + g)z^{(3)}\right)}{\left(\ddot{y}^2 + (\ddot{z} + g)^2\right)^2}\end{aligned} \tag{13}$$

$$\begin{aligned}\tau_\theta = &\frac{\Pi\left(\ddot{x}, \ddot{y}, \ddot{z}, x^{(3)}, y^{(3)}, z^{(3)}, x^{(4)}, y^{(4)}, z^{(4)}\right)}{\left[\ddot{x}^2 + \ddot{y}^2 + (\ddot{z} + g)^2\right]\sqrt{\ddot{y}^2 + (\ddot{z} + g)^2}} \\ &+\frac{\left(x^{(3)}\left(\ddot{y}^2 + (\ddot{z} + g)^2\right) - \ddot{x}\left(\ddot{y}y^{(3)} + (\ddot{z} + g)z^{(3)}\right)\right)}{\left(\ddot{x}^2 + \ddot{y}^2 + (\ddot{z} + g)^2\right)^2\left(\ddot{y}^2 + (\ddot{z} + g)^2\right)^{\frac{3}{2}}}\times \\ &\left[2\left(\ddot{x}x^{(3)} + \ddot{y}y^{(3)} + (\ddot{z} + g)z^{(3)}\right)\left(\ddot{y}^2 + (\ddot{z} + g)^2\right)\right. \\ &\left.+\left[\ddot{x}^2 + \ddot{y}^2 + (\ddot{z} + g)^2\right]\cdot\left[\ddot{y}y^{(3)} + (\ddot{z}^2 + g)z^{(3)}\right]\right]\end{aligned} \tag{14}$$

and

$$\Pi\left(\ddot{x},\ddot{y},\ddot{z},x^{(3)},y^{(3)},z^{(3)},x^{(4)},y^{(4)},z^{(4)}\right)=-x^{(4)}\left[\ddot{y}^2+\left(\ddot{z}^2+g\right)\right]$$
$$-x^{(3)}\left[\ddot{y}y^{(3)}+\left(\ddot{z}+g\right)z^{(3)}\right]+\ddot{x}\left[\left(y^{(3)}\right)^2+\ddot{y}y^{(4)}+\left(z^{(3)}\right)^2+\left(\ddot{z}+g\right)z^{(4)}\right] \quad (15)$$

From expressions (7), (13) and (14), it can be seen that the relationship between the control input vector, $(u,\tau_\phi,\tau_\theta,\tau_\psi)$, and the flat output's highest derivatives, is not invertible. This reveals an obstacle in the input vector to achieve static feedback linearization, and points to the need for a second-order dynamic extension of the control input u in order to exactly linearize the system (see [25] for details on the use of dynamic feedback). This yields:

$$\ddot{u}=m\frac{\left(x^{(3)}\right)^2+\ddot{x}x^{(4)}+\left(y^{(3)}\right)^2+\ddot{y}y^{(4)}+\left(z^{(3)}\right)^2\left(\ddot{z}+g\right)z^{(4)}}{\sqrt{\ddot{x}^2+\ddot{y}^2+\left(\ddot{z}+g\right)^2}}$$
$$-m\frac{\left(\ddot{x}x^{(3)}+\ddot{y}y^{(3)}+\left(\ddot{z}+g\right)z^{(3)}\right)^2}{\left(\ddot{x}^2+\ddot{y}^2+\left(\ddot{z}+g\right)^2\right)^{\frac{3}{2}}} \quad (16)$$

Proof: By squaring expressions (1), (2) and (3), adding the resulting terms and rearranging, it follows that

$$u=m\sqrt{\ddot{x}^2+\ddot{y}^2+\left(\ddot{z}+g\right)^2} \quad (17)$$

Now, from expressions (2) and (3), it is obtained that

$$\left.\begin{aligned}m\ddot{y}&=uC_\theta S_\phi\\ m(\ddot{z}+g)&=uC_\theta C_\phi\end{aligned}\right\}\Rightarrow\phi=\arctan\left(\frac{\ddot{y}}{\ddot{z}+g}\right) \quad (18)$$

and

$$S_\phi=\frac{\ddot{y}}{\sqrt{\ddot{y}^2+(\ddot{z}+g)^2}};\quad C_\phi=\frac{\ddot{z}+g}{\sqrt{\ddot{y}^2+(\ddot{z}+g)^2}} \quad (19)$$

Then, by squaring solely expressions (2) and (3), adding the resulting terms and rearranging, yields the following result

$$uC_\phi=m\sqrt{\ddot{y}^2+(\ddot{z}+g)^2} \quad (20)$$

Operating with expressions (1) and (19), we readily obtain

$$\theta=-\arctan\left(\frac{\ddot{x}}{\sqrt{\ddot{y}^2+\left(\ddot{z}+g\right)^2}}\right) \quad (21)$$

and

$$S_\theta=-\frac{\ddot{x}}{\sqrt{\ddot{x}^2+\ddot{y}^2+(\ddot{z}+g)^2}};\quad C_\theta=\frac{\sqrt{\ddot{y}^2+(\ddot{z}+g)^2}}{\sqrt{\ddot{x}^2+\ddot{y}^2+(\ddot{z}+g)^2}} \quad (22)$$

Now, if the ψ angle is differentiated twice we arrive at

$$\tau_\psi=\ddot{\psi} \quad (23)$$

On the other hand, if the expressions (1), (2) and (3) are differentiated with regard to the time and the terms are rearranged,

$$mx^{(3)}=-\dot{u}S_\theta-uC_\theta\dot{\theta} \quad (24)$$

$$my^{(3)}=\dot{u}C_\theta S_\phi-uS_\theta S_\phi\dot{\theta}+uC_\theta C_\phi\dot{\phi} \quad (25)$$

$$mz^{(3)}=\dot{u}C_\theta C_\phi-uS_\theta C_\phi\dot{\theta}-uC_\theta S_\phi\dot{\phi} \quad (26)$$

and, expressed in matrix notation,

$$\begin{bmatrix}x^{(3)}\\ y^{(3)}\\ z^{(3)}\end{bmatrix}=\underbrace{\frac{1}{m}\begin{bmatrix}-S_\theta & -uC_\theta & 0\\ C_\theta S_\phi & -uS_\theta S_\phi & uC_\theta C_\phi\\ C_\theta C_\phi & -uS_\theta C_\phi & -uC_\theta S_\phi\end{bmatrix}}_{\mathbf{N}^{-1}(u,\theta,\phi)}\begin{bmatrix}\dot{u}\\ \dot{\theta}\\ \dot{\phi}\end{bmatrix} \quad (27)$$

or

$$\begin{bmatrix}\dot{u}\\ \dot{\theta}\\ \dot{\phi}\end{bmatrix}=\underbrace{m\begin{bmatrix}-S_\theta & C_\theta S_\phi & C_\theta C_\phi\\ -\frac{C_\theta}{u} & -\frac{S_\theta S_\phi}{u} & -\frac{S_\theta C_\phi}{u}\\ 0 & \frac{C_\phi}{uC_\theta} & -\frac{S_\phi}{uC_\theta}\end{bmatrix}}_{\mathbf{N}(u,\theta,\phi)}\begin{bmatrix}x^{(3)}\\ y^{(3)}\\ z^{(3)}\end{bmatrix} \quad (28)$$

If the expression (26) is differentiated now with regard to the time, and the terms are rearranged taking into consideration that $\tau_\theta=\ddot{\theta}$ and $\tau_\phi=\ddot{\phi}$, we obtain the following:

$$mx^{(4)}=-\ddot{u}S_\theta-2\dot{u}\dot{\theta}C_\theta+u\dot{\theta}^2S_\theta-u\ddot{\theta}C_\theta \quad (29)$$

$$my^{(4)}=\ddot{u}C_\theta S_\phi-2\dot{u}\dot{\theta}S_\theta S_\phi+2\dot{u}\dot{\phi}C_\theta C_\phi-2u\dot{\theta}\dot{\phi}S_\theta C_\phi$$
$$-u\dot{\theta}^2C_\theta S_\phi-u\dot{\phi}^2C_\theta S_\phi-u\ddot{\theta}S_\theta S_\phi+u\ddot{\phi}C_\theta C_\phi \quad (30)$$

$$mz^{(4)}=\ddot{u}C_\theta C_\phi-2\dot{u}\dot{\theta}S_\theta C_\phi-2\dot{u}\dot{\phi}C_\theta S_\phi+2u\dot{\theta}\dot{\phi}S_\theta S_\phi$$
$$-u\dot{\theta}^2C_\theta C_\phi-u\dot{\phi}^2C_\theta C_\phi-u\ddot{\theta}S_\theta C_\phi-u\ddot{\phi}C_\theta S_\phi \quad (31)$$

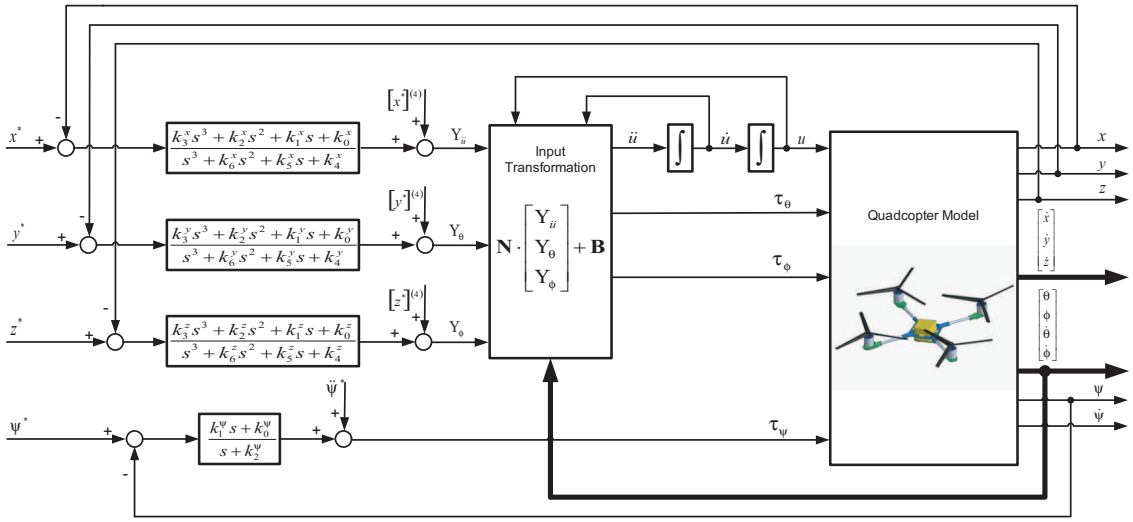

Figure 2. GPI control scheme

and, expressed in matrix notation,

$$\begin{bmatrix} x^{(4)} \\ y^{(4)} \\ z^{(4)} \end{bmatrix} = \mathbf{N}^{-1}(u,\theta,\phi)\begin{bmatrix} \ddot{u} \\ \tau_\theta \\ \tau_\phi \end{bmatrix} + \underbrace{\frac{1}{m}\begin{bmatrix} -2\dot{u}\dot{\theta}C_\theta + u\dot{\theta}^2 S_\theta \\ -2\dot{u}\dot{\theta}S_\theta S_\phi + 2\dot{u}\dot{\phi}C_\theta C_\phi - 2u\dot{\theta}\dot{\phi}S_\theta C_\phi - uC_\theta S_\phi\left(\dot{\theta}^2+\dot{\phi}^2\right) \\ -2\dot{u}\dot{\theta}S_\theta C_\phi - 2\dot{u}\dot{\phi}C_\theta S_\phi + 2u\dot{\theta}\dot{\phi}S_\theta S_\phi - uC_\theta C_\phi\left(\dot{\theta}^2+\dot{\phi}^2\right) \end{bmatrix}}_{\mathbf{T}(u,\phi,\theta,\dot{u},\dot{\phi},\dot{\theta})} \tag{32}$$

or

$$\begin{bmatrix} \ddot{u} \\ \tau_\theta \\ \tau_\phi \end{bmatrix} = \mathbf{N}(u,\theta,\phi)\begin{bmatrix} x^{(4)} \\ y^{(4)} \\ z^{(4)} \end{bmatrix} + \underbrace{\begin{bmatrix} u\left(\dot{\theta}^2+\dot{\phi}^2 C_\theta^2\right) \\ -\dfrac{2\dot{u}\dot{\theta}}{u} - \dot{\phi}^2 S_\theta C_\theta \\ -\dfrac{2\dot{u}\dot{\phi}}{u} + 2\dot{\theta}\dot{\phi}\dfrac{S_\theta}{C_\theta} \end{bmatrix}}_{\mathbf{B}(u,\phi,\theta,\dot{u},\dot{\phi},\dot{\theta})} \tag{33}$$

Finally, the proof is completed after substituting (16), (18), (21) and (27) in (32). □

3.2 GPI Controller Design

As was described in Section 1, GPI control consists of the defective integral reconstruction of the state which, *a priori*, neglects the effects of unknown initial conditions and the effect of possible classical perturbation inputs (constant and low-order time polynomial errors, such as ramps and parabolic signals). They are based on the central observation that the states of observable linear systems may be integrally parameterized in terms of inputs and outputs alone (i.e., linear combinations of inputs, outputs and of a finite number of iterated integrals of signals). The errors of integral reconstruction are to be compensated, later, by a suitable linear controller containing a sufficient number of iterated integrals of the tracking error or else of the input error [21]. The control scheme proposed for the control of the quadrotor model is illustrated in Figure 2.

From the developments obtained in the previous section, the following input-to-highest-derivative of the flat outputs' relations is achieved:

$$\begin{bmatrix} \ddot{u} \\ \tau_\theta \\ \tau_\phi \end{bmatrix} = \mathbf{N}\cdot\begin{bmatrix} x^{(4)} \\ y^{(4)} \\ z^{(4)} \end{bmatrix} + \mathbf{B} \qquad \tau_\psi = \ddot{\psi} \tag{34}$$

Now, if we define the virtual input vector,

$$\begin{bmatrix} \Upsilon_{\ddot{u}} \\ \Upsilon_\theta \\ \Upsilon_\phi \end{bmatrix} = \mathbf{N}^{-1}\cdot\left(\begin{bmatrix} \ddot{u} \\ \tau_\theta \\ \tau_\phi \end{bmatrix} - \mathbf{B}\right) \tag{35}$$

and this input transformation is applied to the dynamical system (33), the whole dynamics model is now expressed as

$$x^{(4)} = \Upsilon_{\ddot{u}} \tag{36}$$

$$y^{(4)} = \Upsilon_\theta \tag{37}$$

$$z^{(4)} = \Upsilon_\phi \tag{38}$$

$$\ddot{\psi} = \tau_\psi \tag{39}$$

The GPI-based flat output feedback controller is synthesized as follows: Expression (35) is a fourth-order system in which is regulated the x -position of the quadrotor model towards a given smooth reference trajectory, $x^*(t)$, with $\ddot{u}$ acting as an auxiliary control input. Clearly, if there exists an auxiliary open-loop control input $\ddot{u}^*(t)$ that ideally achieves the tracking of $x^*(t)$ for suitable initial conditions, it thus satisfies the fourth-order dynamics

$$\left[x^*\right]^{(4)} = \Upsilon_{\ddot{u}}^* \tag{40}$$

Subtracting (39) from (35) yields the following:

$$e_x^{(4)} = e_{\Upsilon_{\ddot{u}}} \tag{41}$$

where $e_x = x - x^*(t)$ and $e_{\ddot{u}} = \ddot{u} - \ddot{u}^*(t)$. If we assume that we are able to measure the variables $e_x^{(3)}$, $\ddot{e}_x$ and $\dot{e}_x$, the following control law could be proposed:

$$e_{\Upsilon_{\ddot{u}}} = -k_6^x e_x^{(3)} - k_5^x \ddot{e}_x - k_4^x \dot{e}_x - k_3^x e_x \tag{42}$$

In such a case, the closed-loop tracking error for the x - position variable evolves, and is governed by

$$e_x^{(4)} + k_6^x e_x^{(3)} + k_5^x \ddot{e}_x + k_4^x \dot{e}_x + k_3^x e_x = 0 \tag{43}$$

The design parameters $\{k_6^x, k_5^x, k_4^x, k_3^x\}$ are then chosen so as to render the closed-loop characteristic polynomial into a Hurwitz polynomial with desirable roots. The signals $e_x^{(3)}$, $\ddot{e}_x$ and $\dot{e}_x$ have to be either measured or else estimated by means of an observer. In practice, the estimation requires the use of online calculations based on high-frequency samples of the variable's trajectory $e_x(t)$. Using integral reconstructors based on the integration of the system dynamics, such estimations - or time discretizations - are unnecessary. We resort to the following integral reconstructors for such signals,

$$\hat{e}_x^{(3)} = \int_0^t e_{\Upsilon_{\ddot{u}}}(\tau)d\tau \tag{44}$$

$$\ddot{\hat{e}}_x = \int_0^t \int_0^\tau e_{\Upsilon_{\ddot{u}}}(\lambda)d\lambda d\tau \tag{45}$$

$$\hat{\dot{e}}_x = \int_0^t \int_0^\tau \int_0^\lambda e_{\Upsilon_{\ddot{u}}}(\sigma)d\sigma d\lambda d\tau \tag{46}$$

The relation between the structural estimates and the real values of the states of the system are given by

$$e_x^{(3)} = \hat{e}_x^{(3)} + e_x^{(3)}(0) \tag{47}$$

$$\ddot{e}_x = \ddot{\hat{e}}_x + e_x^{(3)}(0)t + \ddot{e}_x(0) \tag{48}$$

$$\dot{e}_x = \hat{\dot{e}}_x + e_x^{(3)}(0)\frac{t^2}{2} + \ddot{e}_x(0)t + \dot{e}_x(0) \tag{49}$$

where $e_x^{(3)}(0)$, $\ddot{e}_x(0)$ and $\dot{e}_x(0)$ are the unknown initial conditions of the states of the system. It is observed in (46)-(48) that the difference between the structural estimates and the real values exhibits a combination of parabolic error, ramp error and offset error due to the constant initial conditions. This immediately prompts us to consider the possibility of using a modified feedback controller including an integral error term, a double integral error term and a triple integral error term, to reject the possible effects of the possibly non-zero initial conditions $e_x^{(3)}(0)$, $\ddot{e}_x(0)$ and $\dot{e}_x(0)$. We thus proceed to propose the following controller:

$$\begin{aligned} e_{\Upsilon_{\ddot{u}}} &= -k_6^x \hat{e}_x^{(3)} - k_5^x \ddot{\hat{e}}_x - k_4^x \hat{\dot{e}}_x - k_3^x e_x - k_2^x \int_0^t e_x(\tau)d\tau \\ &-k_1^x \int_0^t \int_0^\tau e_x(\lambda)d\lambda d\tau - k_0^x \int_0^t \int_0^\tau \int_0^\lambda e_x(\sigma)d\sigma d\lambda d\tau \end{aligned} \tag{50}$$

Substituting (43)-(45) in (49), and after some rearrangements, we achieve

$$\begin{aligned} e_{\Upsilon_{\ddot{u}}} &= -k_6^x \int_0^t e_{\Upsilon_{\ddot{u}}}(\tau)d\tau - k_5^x \int_0^t \int_0^\tau e_{\Upsilon_{\ddot{u}}}(\lambda)d\lambda d\tau \\ &-k_4^x \int_0^t \int_0^\tau \int_0^\lambda e_{\Upsilon_{\ddot{u}}}(\sigma)d\sigma d\lambda d\tau - k_3^x e_x - k_2^x \int_0^t e_x(\tau)d\tau \\ &-k_1^x \int_0^t \int_0^\tau e_x(\lambda)d\lambda d\tau - k_0^x \int_0^t \int_0^\tau \int_0^\lambda e_x(\sigma)d\sigma d\lambda d\tau \end{aligned} \tag{51}$$

After using Laplace's transform in (50), we obtain the final form for the auxiliary control input variable $e_{\ddot{u}}$,

$$e_{\Upsilon_{\ddot{u}}}(s) = -\frac{k_3^x s^3 + k_2^x s^2 + k_1^x s + k_0^x}{s^3 + k_6^x s^2 + k_5^x s + k_4^x} \; e_x(s) \tag{52}$$

On the other hand, the use of (46)-(48) on the modified controller expression (49) results from the substitution of expression (40) and differentiating on three occasions in the following seventh-order linear tracking-error dynamics:

$$e_x^{(7)} + k_6^x e_x^{(6)} + k_5^x e_x^{(5)} + k_4^x e_x^{(4)} + k_3^x e_x^{(3)} + k_2^x \ddot{e}_x + k_1^x \dot{e}_x + k_0^x e_x = 0 \tag{53}$$

The design coefficients $\{k_6^x, k_5^x, \ldots, k_1^x, k_0^x\}$ are chosen so as to render the closed-loop characteristic polynomial

$$s^7 + k_6^x s^6 + k_5^x s^5 + k_4^x s^4 + k_3^x s^3 + k_2^x s^2 + k_1^x s + k_0^x = 0 \tag{54}$$

into a Hurwitz polynomial with desirable roots. Therefore, the specification of the set of design coefficients

$\{k_6^x, k_5^x, \ldots, k_1^x, k_0^x\}$ is chosen so as to locate the desired closed-loop poles in the left half of the complex plane. The control parameters were selected so as to achieve the following desired closed-loop characteristic polynomial,

$$p_x^{des}(s) = \left(s^2 + 2\zeta_x \omega_{nx} s + \omega_{nx}^2\right)^3 \left(s + p_x\right) \tag{55}$$

where ζ_x, ω_{nx} and p_x are positive quantities. Therefore, the design coefficients $\{k_6^x, k_5^x, \ldots, k_1^x, k_0^x\}$ are given by:

$$\begin{aligned}
k_6^x &= 6\zeta_x \omega_{nx} + p_x \\
k_5^x &= 12\zeta_x^2 \omega_{nx}^2 + 3\omega_{nx}^2 + 6\zeta_x \omega_{nx} p_x \\
k_4^x &= 12\zeta_x \omega_{nx}^3 + 8\zeta_x^3 \omega_{nx}^3 + 12\zeta_x^2 \omega_{nx}^2 p_x + 3\omega_{nx}^2 p_x \\
k_3^x &= 12\zeta_x^2 \omega_{nx}^2 + 2\omega_{nx}^4 + 12\zeta_x \omega_{nx}^3 p_x + 8\zeta_x^3 \omega_{nx}^3 p_x \\
k_2^x &= 6\zeta_x \omega_{nx}^5 + 12\zeta_x^2 \omega_{nx}^2 p_x + 2\omega_{nx}^4 p_x \\
k_1^x &= \omega_{nx}^6 + 6\zeta_x \omega_{nx}^5 p_x \\
k_0^x &= \omega_{nx}^6 p_x
\end{aligned} \tag{56}$$

With a view to avoiding repetition, similar control laws are developed for the position variables y and z (given in expressions (36) and (37)). Substituting the pair $\langle x, \ddot{u} \rangle$ by $\langle y, \theta \rangle$ and $\langle z, \phi \rangle$, respectively, the following feedback control laws are obtained for the variables y and z :

$$e_{\Upsilon_\theta}(s) = -\frac{k_3^y s^3 + k_2^y s^2 + k_1^y s + k_0^y}{s^3 + k_6^y s^2 + k_5^y s + k_4^y} \; e_y(s) \tag{57}$$

$$e_{\Upsilon_\phi}(s) = -\frac{k_3^z s^3 + k_2^z s^2 + k_1^z s + k_0^z}{s^3 + k_6^z s^2 + k_5^z s + k_4^z} \; e_z(s) \tag{58}$$

On the other hand, the dynamics given in (38) comprise a second-order system in order to control the orientation angle ψ of the quadrotor towards a given smooth reference trajectory, $\psi^*(t)$, with τ_ψ acting as the control input. In this case, the open-loop control input $\tau_\psi^*(t)$ that ideally achieves the tracking of $\psi^*(t)$ for suitable initial conditions satisfies the following second-order dynamics:

$$\ddot{\psi}^* = \tau_\psi^* \tag{59}$$

Subtracting (58) from (38) yields

$$\ddot{e}_\psi = e_{\tau_\psi} \tag{60}$$

where $e_\psi = \psi - \psi^*(t)$ and $e_{\tau_\psi} = \tau_\psi - \tau_\psi^*(t)$. A PD feedback controller, specifying the input tracking error, is given by

$$e_{\tau_\psi} = -k_2^\psi \dot{e}_\psi - k_1^\psi e_\psi \tag{61}$$

This yields, evidently, a differential equation for the output tracking error, e_ψ, given by

$$\ddot{e}_\psi + k_2^\psi \dot{e}_\psi + k_1^\psi e_\psi = 0 \tag{62}$$

The characteristic polynomial, associated with this equation is

$$s^2 + k_2^\psi s + k_1^\psi = 0 \tag{63}$$

Thus, the design problem reduces to an appropriate choice of the feedback controller gain so as to make the above polynomial like Hurwitz's. However, the tracking controller (60) requires knowledge of the signal $\dot{e}_\psi$. We resort to an integral reconstructor for such a signal, aware of the fact that such a reconstructor differs from the actual signal by an unknown constant quantity fixed by the unchangeable initial condition. We proceed by integrating (38) once and, later on, by disregarding the constant error due to the tracking-error velocity's initial condition $\dot{e}_\psi(0)$. The estimated error velocity $\hat{\dot{e}}_\psi$ can be computed in the following form:

$$\hat{\dot{e}}_\psi = \dot{e}_\psi - \dot{e}_\psi(0) = \int_0^t e_{\tau_\psi}(\tau) d\tau \tag{64}$$

When the reconstructor is used in the derivative part of the PD controller, the constant error is suitably compensated by the addition of an integral error term to reject the effect of the unknown constant initial conditions $\dot{e}_\psi(0)$. We thus proceed to propose the following controller:

$$e_{\tau_\psi} = -k_2^\psi \hat{\dot{e}}_\psi - k_1^\psi e_\psi - k_0^\psi \int_0^t e_\psi(\tau) d\tau \tag{65}$$

Substituting (63) in (64), and after some rearrangement, we achieve

$$e_{\tau_\psi} = -k_2^\psi \int_0^t e_{\tau_\psi}(\tau) d\tau - k_1^\psi e_\psi - k_0^\psi \int_0^t e_\psi(\tau) d\tau \tag{66}$$

Following a similar procedure to that used for the variables x, y and z, and using Laplace's transform, the following result is yielded for the control input variable e_{τ_ψ} :

$$e_{\tau_\psi}(s) = -\frac{k_1^\psi s + k_0^\psi}{s + k_2^x} \; e_\psi(s) \tag{67}$$

Now, using (63) in the modified controller (64) results upon substitution of (59), and differentiating once with regard to time for the following third-order linear tracking-error dynamics,

$$e_{\psi}^{(3)} + k_2^{\psi}\ddot{e}_{\psi} + k_1^{\psi}\dot{e}_{\psi} + k_0^{\psi}e_{\psi} = 0 \tag{68}$$

the characteristic polynomial, associated with the previous equation, is easily shown to be

$$s^3 + k_2^{\psi}s^2 + k_1^{\psi}s + k_0^{\psi} = 0 \tag{69}$$

where the set of design coefficients $\{k_2^{\psi}, k_1^{\psi}, k_0^{\psi}\}$ are chosen so as to make the above polynomial like Hurwitz's with desirable roots. In order to specify the parameters $\{k_2^{\psi}, k_1^{\psi}, k_0^{\psi}\}$, we can choose to locate the desired closed-loop poles in the left half of the complex plane. In particular, they were selected so as to achieve the following desired closed-loop characteristic polynomial,

$$p_{\psi}^{des}(s) = \left(s^2 + 2\zeta_{\psi}\omega_{n\psi}s + \omega_{n\psi}^2\right)\left(s + p_{\psi}\right) \tag{70}$$

where ζ_{ψ}, $\omega_{n\psi}$ and p_{ψ} are positive quantities. Identifying each term of the expression (68) with those of (69), we obtain directly the value of the set of coefficients $\{k_2^{\psi}, k_1^{\psi}, k_0^{\psi}\}$, which are given by

$$k_2^{\psi} = 2\zeta_{\psi}\omega_{n\psi} + p_{\psi} \tag{71}$$

$$k_1^{\psi} = 2\zeta_{\psi}\omega_{n\psi}p_{\psi} + \omega_{n\psi}^2 \tag{72}$$

$$k_0^{\psi} = \omega_{n\psi}^2 p_{\psi} \tag{73}$$

Next, using (34), the following result is obtained:

$$\begin{bmatrix} \ddot{u} \\ \tau_{\theta} \\ \tau_{\phi} \end{bmatrix} = \mathbf{N} \cdot \begin{bmatrix} \Upsilon_{u} \\ \Upsilon_{\theta} \\ \Upsilon_{\phi} \end{bmatrix} + \mathbf{B} \tag{74}$$

Finally, the section is concluded by stating the following proposition, as proved in the above developments:

Proposition 2: Given a set of smooth reference trajectories (x^*, y^*, z^*, ψ^*), for the horizontal coordinates x and y, the vertical position z and the orientation variable ψ in the quadrotor dynamics, defined by expressions (1)-(6), then the feedback controller defined by expressions (51), (56), (57), (66) and (71) produces the closed-loop behaviour of the tracking errors, $e_x = x - x^*(t)$, $e_y = y - y^*(t)$, $e_z = z - z^*(t)$ and $e_{\psi} = \psi - \psi^*(t)$, which is locally governed by the linear dynamics

$$\begin{aligned} e_i^{(7)} + k_6^i e_i^{(6)} + k_5^i e_i^{(5)} + k_4^i e_i^{(4)} + k_3^i e_i^{(3)} + k_2^i \ddot{e}_i + k_1^i \dot{e}_i + k_0^i e_i = 0 \\ e_{\psi}^{(3)} + k_2^{\psi}\ddot{e}_{\psi} + k_1^{\psi}\dot{e}_{\psi} + k_0^{\psi}e_{\psi} = 0 \end{aligned} \tag{75}$$

where the sub-index $i = x, y, z$, the design coefficients of which can be chosen according to expressions (55) and (70) so as to render the origin of the tracking-error space into an exponential asymptotically equilibrium point.

4. Numerical Simulations

Numerical simulations were carried out in order to verify the efficiency of the proposed approach in terms of the quick convergence of the tracking errors to a small neighbourhood of zero, smooth transient responses and low control effort. In the simulations, in order to evaluate the performance of the proposed controller, it is desirable to track the following sinusoidal trajectories for the variables x and y (defined as $x^*(t)$ and $y^*(t)$ respectively),

$$x^*(t) = R\left(\sin at + \sin bt\right) \tag{76}$$

$$y^*(t) = R\left(\cos at - \cos bt\right) \tag{77}$$

whereby $R = 4[m]$, $a = 0.0625[rad/s]$ and $b = 0.1875[rad/s]$. The trajectory defined for the flat output z, defined as $z^*(t)$, is a smooth trajectory defined during a finite interval of the form $[t_i, t_f]$, from an initial value $z^*(t_i) = \bar{z}_i$, to a final desired value $z^*(t_f) = \bar{z}_f$. We set, for instance,

$$z^*(t) = \bar{z}_i + \left(\bar{z}_f - \bar{z}_i\right)\varphi(t, t_f, t_i) \tag{78}$$

with $\bar{z}_i = 0[m]$ and $\bar{z}_f = 5[m]$, $t_i = 0[s]$, and where $t_f = 25[s]$ and $\varphi(t, t_f, t_i)$ are defined as a Bezier polynomial smoothly interpolating between 0 and 1 in the time interval $[t_i, t_f]$. We choose a 16th-order Bezier polynomial:

$$\varphi(t, t_i, t_f) = \begin{cases} 0 \text{ for } t < t_i \\ \left[\frac{t - t_i}{t_f - t_i}\right]^8 \left[r_1 - r_2\left(\frac{t - t_i}{t_f - t_i}\right) + r_3\left(\frac{t - t_i}{t_f - t_i}\right)^2 - \ldots + r_9\left(\frac{t - t_i}{t_f - t_i}\right)^8\right] \\ \text{for } t_i \le t \le t_f \\ 1 \text{ for } t > t_f \end{cases} \tag{79}$$

where the coefficients $r_1, \ldots, r_9$ were obtained with polynomial interpolation satisfying the following restrictions:

$$
\begin{aligned}
&z_i = z(t_i); \quad z_f = z(t_f) \\
&\dot{z}(t_i) = \ddot{z}(t_i) = z^{(3)}(t_i) = \ldots = z^{(7)}(t_i) = 0 \\
&\dot{z}(t_f) = \ddot{z}(t_f) = z^{(3)}(t_f) = \ldots = z^{(7)}(t_f) = 0
\end{aligned} \tag{80}
$$

We find that:

$$
\begin{aligned}
&r_1 = 12870 \quad r_2 = 91520 \quad r_3 = 288288 \\
&r_4 = 524160 \quad r_5 = 600600 \quad r_6 = 443520 \\
&r_7 = 205920 \quad r_8 = 54912 \quad r_9 = 6435
\end{aligned} \tag{81}
$$

Finally, the trajectory for the flat output variable ψ, defined as ψ^*, is designed as a linear evolution as

$$
\psi^* = \frac{\pi}{2} + ct \tag{82}
$$

with $c = 0.8[rad/s]$.

On the other hand, the sets of coefficients of the GPI controller $\{k_6^x, k_5^x, k_4^x, \ldots, k_0^x\}$, $\{k_6^y, k_5^y, k_4^y, \ldots, k_0^y\}$, $\{k_6^z, k_5^z, k_4^z, \ldots, k_0^z\}$ and $\{k_2^\psi, k_1^\psi, k_0^\psi\}$ were designed with the help of the following dominating Hurwitz characteristic polynomials $(s^2 + 2\zeta_x\omega_{nx}s + \omega_{nx}^2)^3(s + p_x)$, $(s^2 + 2\zeta_y\omega_{ny}s + \omega_{ny}^2)^3(s + p_y)$, $(s^2 + 2\zeta_z\omega_{nz}s + \omega_{nz}^2)^3(s + p_z)$ and $(s^2 + 2\zeta_\psi\omega_{n\psi}s + \omega_{n\psi}^2)(s + p_\psi)$ with $\zeta_x = 1$, $\omega_{nx} = 2$, $p_x = 2$, $\zeta_y = 1$, $\omega_{ny} = 2$, $p_y = 2$, $\zeta_z = 1$, $\omega_{nz} = 2$, $p_z = 2$, $\zeta_\psi = 1$, $\omega_{n\psi} = 1$ and $p_\psi = 1$. The time-sampling used in the simulations is set as $1 \cdot 10^{-3}[s]$.

Two sets of simulations were developed to establish a comparison between the GPI control presented in this paper and a classical PID control. The comparison is carried out on the basis of the following aspects: (1) the stabilization process and trajectory tracking; (2) performance when the signals are noisy; and (3) responses to environmental uncertainties, such as gusty winds. These simulations will be described in detail in what follows.

4.1 Simulation under Ideal Conditions

In this computer simulation, the quadrotor has to track the trajectory defined by expressions (73), (75) and (78) under ideal conditions, which implies that the measured signals are not corrupted by noise and that there are no environmental uncertainties.

The time evolution of the closed-loop centre of mass position-variables using the GPI and the PID control is illustrated in Figure 3, and the controlled evolution of the centre of mass of the quadrotor in 3D is depicted in Figure 4. As can be observed, the tracking of the variables x, y and z of the prescribed trajectory illustrates that the GPI control drives the system towards perfect tracking of the prescribed trajectories, showing an important improvement with respect to the PID control. This fact is demonstrated in full in the tracking trajectory of the quadrotor in 3D. Additionally, the tracking for the ψ variable presents better behaviour using the GPI controller, as is observed in Figure 5. Furthermore, in Figure 5 is shown the evolution of all the closed-loop attitude variables of the quadrotor using the GPI and PID controllers. Finally, the evolution of the control input variables is displayed in Figure 6, using the GPI and the PID control, illustrating the efforts made by the feedback controllers in guiding the errors of the states towards a fairly small neighbourhood close to zero.

4.2 Robustness with Respect to Noisy Signals and Environmental Perturbations

In this computer simulation, the measured controlled variables $\tilde{x}$, $\tilde{y}$, $\tilde{z}$ and $\tilde{\psi}$ are affected by an additive, zero mean, high-frequency noise $\mu_n(t)$, for $n = x, y, z, \psi$, such that,

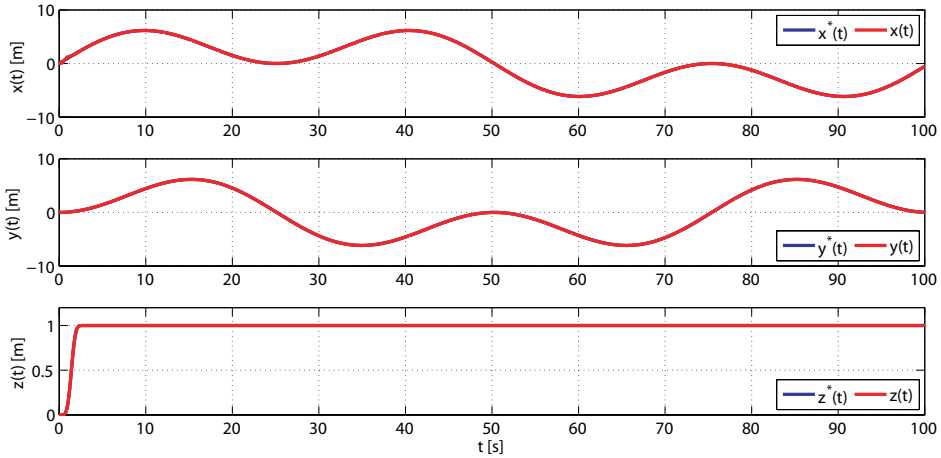

Figure 3. Position variables and reference variables of the centre of mass of the quadrotor

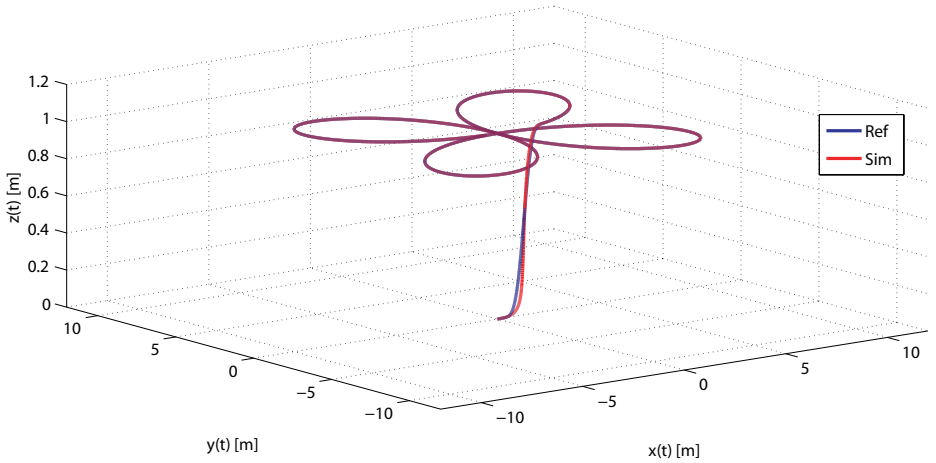

Figure 4. 3D centre of mass quadrotor trajectory

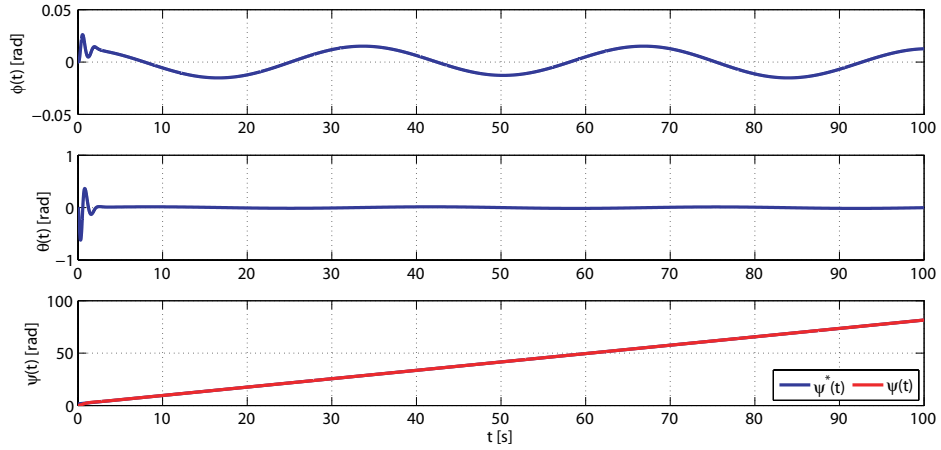

Figure 5. Attitude variables of the quadrotor

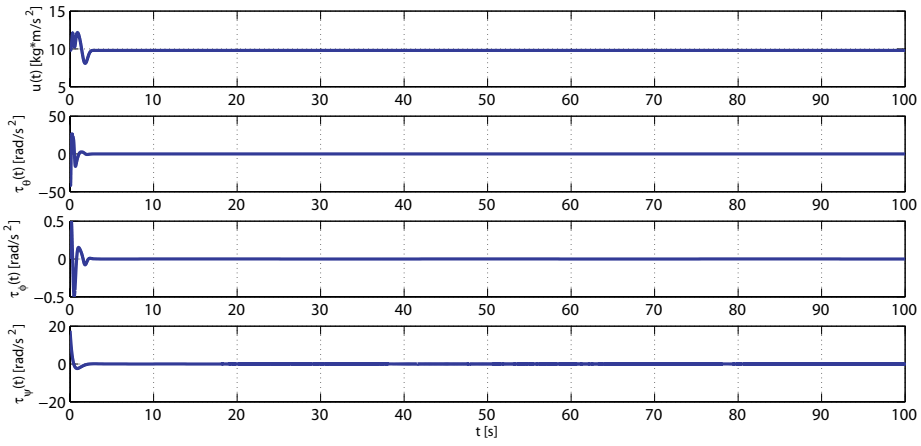

Figure 6. Applied control inputs

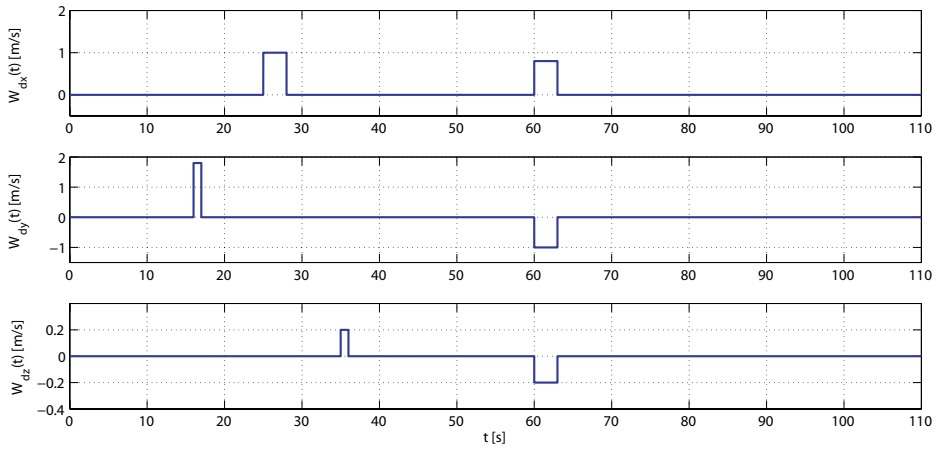

Figure 7. Atmospheric disturbances used in the simulations

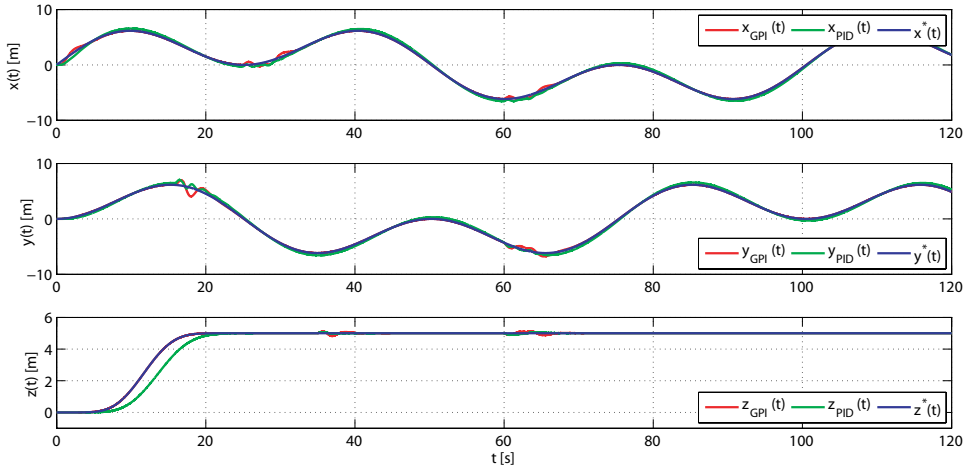

Figure 8. Position variables and reference variables of the centre of mass of the quadrotor under noisy measurements and with gusts of wind

$$\tilde{x}(t) = x(t) + \mu_x(t) \tag{83}$$

$$\tilde{y}(t) = y(t) + \mu_y(t) \tag{84}$$

$$\tilde{z}(t) = z(t) + \mu_z(t) \tag{85}$$

$$\tilde{\psi}(t) = \psi(t) + \mu_\psi(t) \tag{86}$$

where the selected standard deviations $\mu_n(t)$, for $n = x, y, z$, were set to be $3.17 \cdot 10^{-4}$, and the standard deviation for $\mu_\psi(t)$ was set to be $3.17 \cdot 10^{-4}$. Additionally, we introduced in the simulation the atmospheric disturbances (gusty wind) shown in Figure 7 and defined as in [26]. Figure 8 depicts the controlled evolution of the position variables of the centre of mass of the quadrotor under noisy measurements and atmospheric disturbances, and Figure 9 displays the evolution of the centre of mass of the quadrotor in 3D under these new conditions. Similarly as with the previous simulations, the performance of the quadrotor using the GPI control is improved significantly in comparison to that obtained with the PID control. It is observed that, when the atmospheric disturbances affect the quadrotor, the GPI controller corrects these undesirable effects and again drives the tracking error trajectories to a small neighbourhood on the origin of the tracking-error phase space. In Figure 10 is presented the evolution of all the closed-loop attitude variables of the quadrotor using the GPI and PID controllers as well as the tracking for the variable ψ, showing again improved behaviour with respect to the PID controller. Finally, in Figure 11 is displayed the evolution of the control inputs using the GPI and the PID controllers. In this figure the high robustness of the GPI control is

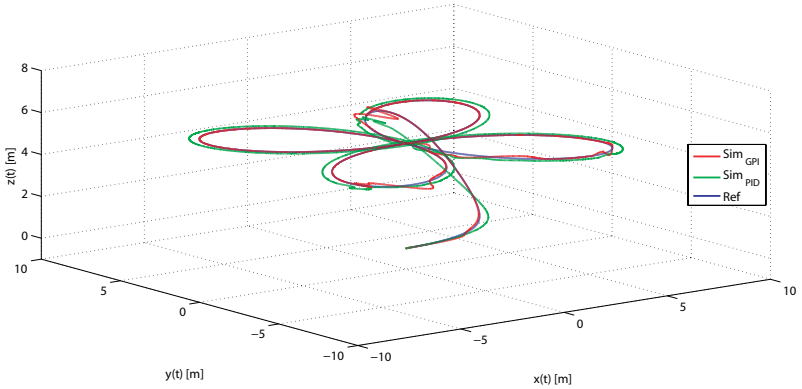

Figure 9. 3D centre of mass quadrotor trajectory under noisy measurements and with gusts of wind

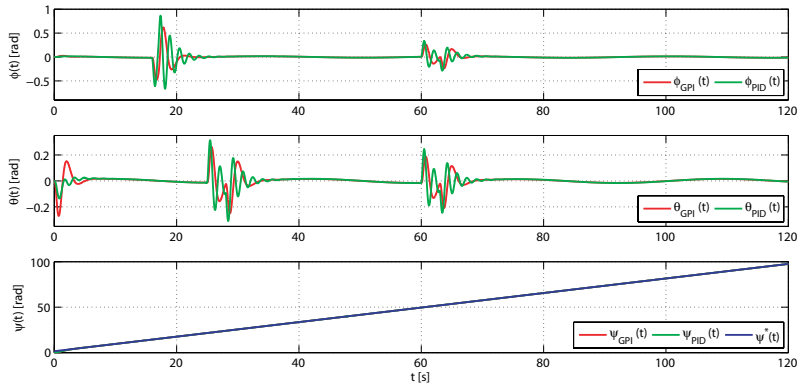

Figure 10. Attitude variables of the quadrotor under noisy measurements and with gusts of wind

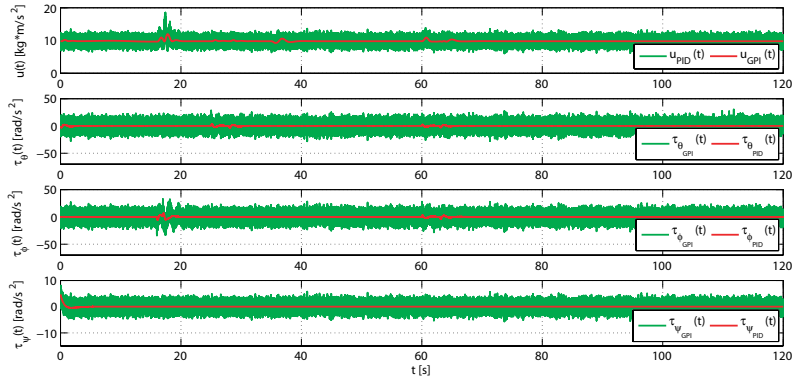

Figure 11. Applied control inputs under noisy measurements and with gusts of wind

demonstrated in comparison with the PID control when the measured controlled signals are affected by noise.

5. Conclusions

In this paper, the theoretical applicability of the GPI controller technique for regulation and trajectory tracking problems in a quadrotor has been investigated. The proposed scheme renders state observers and time discretizations completely unnecessary. GPI control sidesteps the need for traditional asymptotic state observers and proceeds directly to use structural state estimates in place of the actual state variables. The effect of such structural estimates in the controller are neglected in the feedback

control law by means of suitable integral output tracking-error feedback control actions. Numerical simulations were provided to demonstrate the effectiveness of the proposed approach in comparison with the classical PID control in the following terms: (a) stabilization and trajectory tracking tasks; (b) performance when the measured signals are corrupted by noise; and (c) dynamic response when atmospheric disturbances, such as gusty wind, affect the quadrotor. The results show that the behaviour of the proposed approach improves the behaviour of the system in all aspects in comparison to the PID controller. Future work will be devoted to verifying the effectiveness of the proposed control algorithm through use in experiments with a real platform. This will be the topic of future publications.

6. Acknowledgements

This work is partially supported by the Spanish Ministerio de Economía y Competitividad / FEDER under TIN2013-47074-C2-1-R grant.

7. References

[1] Nonami A, Kendoul F, Suzuki S, Wang W, Makazawa D. Autonomous Flying Robots - Unmanned Aerial Vehicles and Micro Aerial Vehicles. New York: Springer; 2010. DOI: 10.1007/978-4-431-53856-1

[2] Garca Carrillo LR, Dzul AE, Lozano R, C.égard. Quad Rotorcrarft Control - Vision-based Hovering and Navigation. New York: Springer; 2013. DOI: 10.1007/978-1-4471-4399-4

[3] Eisenbeiss H. UAV Photogrammetry [thesis]. Zürich: Institut für Geodäsie und Photogrammetrie Eidgeössische Technische Hochschule Zürich; 2009

[4] Castillo Garca P, Lozano R, Dzul AE. Modelling and Control of Mini-flying Machines. New York: Springer; 2013. DOI: 10.1007/1-84628-179-2

[5] Zuo Z. Trajectory tracking control design with command-filtered compensation of a quadrotor. IET Control Theory Applications. 2010;4:2343-2355. DOI: 10.1049/iet-cta.2009.0336

[6] Bouabdallah S, Noth A, Siegwart R. PID vs LQ control techniques applied to an indoor micro quadrotor. In: Proceedings of the 2004 IEEE/RSJ International Conference on Intelligent Robots and Systems vol. 3: 28 September - 2 October 2004; Sendai. New York: IEEE; 2004. p. 2451-2456

[7] La Civita M. Integrated Modeling and Robust Control for Full-envelope Flight of Robotic Helicopters [thesis]. Pittsburgh: Carnegie Mellon University; 2003

[8] Madani T, Benallegue A. Backstepping control for a quadrotor helicopter. In: Proceedings of the 2006 IEEE/RSJ International Conference on Intelligent Robots and Systems: 9-15 October 2006; Beijing. New York: IEEE; 2006. p. 3255-3260

[9] Waslander SL, Hoffmann GM, Jang JS. Multi-agent quadrotor testbed control design: integral sliding mode vs. reinforcement learning. In: Proceedings of the 2005 IEEE/RSJ International Conference on Intelligent Robots and Systems: 2-6 August 2005; Edmonton. New York: IEEE; 2005. p. 3712-3717

[10] Formentin S, Lovera M. Flatness-based control of a quadrotor helicopter via feedforward linearization In: Proccedings of the 50th IEEE Conference on Decision and Control and European Control Conference: 12-15 December 2011; Orlando. New York: IEEE; 2011. p. 6171-6176

[11] Gautam D, Ha C. Control of a quadrotor using a smart self-tuning fuzzy PID controller. International Journal of Advanced Robotic Systems. 2013;10:380. DOI: 10.5772/56911

[12] Chen F, Wu Q, Tao G, Jiang B. A reconfiguration control scheme for a quadrotor helicopter via combined multiple models. International Journal of Advanced Robotic Systems. 2014;11:122. DOI: 10.5772/58833

[13] Sira-Ramrez H. On the linear control of the quadrotor system. In: Proceedings of the 2011 American Control Conference: 29 June - 1 July 2011; San Francisco. New York: IEEE; 2011. p. 3178-3183

[14] Escareño J, Salazar-Cruz C, Lozano R. Embedded control of a four-rotor UAV. In: Proceedings of the 2006 American Control Conference: 14-16 June 2006; Minneapolis. New York: IEEE; 2006. p 3936-3941

[15] Zurita-Bustamante EW, Linares-Flores J, Guzmán-Ramrez E, Sira-Ramrez H. A comparison between the GPI and PID controllers for the stabilization of a DC-DC "buck" converter. IEEE Transactions on Industrial Electronics. 2011;58:5251-5262. DOI: 10.1109/TIE.2011.2123857

[16] Morales R, Feliu V, Jaramillo V. Position control of very lightweight single-link flexible arms with large payload variations by using disturbance observers. Robotics and Autonomous Systems. 2012;60:532-547. DOI: 10.1016/j.robot.2011.11.016

[17] Fliess M, Marquez R, Delaleau E, Sira-Ramrez H. Correcteurs proportionnels-intégraux génralisés. ESAIM: Control, Optimisation and Calculus of Variations. 2002;7:23-41. DOI: 10.1051/cocv:200202

[18] Sira-Ramrez H. On the generalized PI sliding mode control of DC-to-DC power converters: a tutorial. International Journal of Control. 2003;76:1018-1033. DOI: 10.1080/0020717031000099047

[19] Morales R, Feliu V, Sira-Ramrez H. Nonlinear control for magnetic levitation systems based on fast online algebraic identification of the input gain.

IEEE Transactions on Control Systems Technology, 2011;19:757-771. DOI: 10.1109/TCST.2010.2057511

[20] Morales R, Sira-Ramrez H, Feliu V. Adaptive control based on fast online algebraic identification and GPI control for magnetic levitation systems with time-varying input gain. International Journal of Control. 2014;87:1604-1621. DOI: 10.1080/00207179.2014.880129

[21] Morales R, Sira-Ramrez H. Trajectory tracking for the magnetic ball levitation system via exact feedforward linearization and GPI control. International Journal of Control. 2010;83:1155-1166. DOI: 10.1080/00207171003642196

[22] Castillo P, Dzul A, Lozano R. Real-time stabilization and tracking of a four rotor mini rotorcraft. IEEE Transactions on Control Systems Technology. 2004;12:510-516. DOI: 10.1109/TCST.2004.825052

[23] Lozano R. Unmanned Aerial Vehicles - Embedded Control. Chichester: Wiley; 2010. DOI: 10.1002/9781118599938

[24] Sira-Ramrez H, Agrawal S. Differentially Flat Systems. New York: CRC Press; 2004. ISBN: 9780824754709

[25] Fliess M, Lévine J, Rouchon P. Flatness and defects of nonlinear systems: introductory theory and examples. International Journal of Control. 1995;61:1327-1361. DOI: 10.1080/00207179508921959

[26] Sarwar SS, Rehman S. Supervising control for unmanned aerial vehicles. Mathematical Problems in Engineering. 2013;2013:564803. DOI: 10.1155/2013/564803

2.2.2 Nonlinear Cascade-Based Control for a Twin Rotor MIMO System

Publication Data

ABSTRACT:
This research is focused on the development of a nonlinear cascade-based control algorithm for a laboratory helicopter-denominated Twin Rotor MIMO System (TRMS). The TRMS is an underactuated nonlinear multivariable system, characterised by a coupling effect between the dynamics of the propellers and the body structure, which is caused by the action-reaction principle originated in the acceleration and deceleration of the propeller groups. Firstly, this work introduces an extensive description of the platform's dynamics, which was carried out by splitting the system into its electrical and mechanical parts. Secondly, we present a design of a nonlinear cascade-based control algorithm that locally guarantees an asymptotically and exponentially stable behaviour of the controlled generalised coordinates of the TRMS. Lastly, a demonstration of the effectiveness of the proposed approach is provided by means of numerical simulations performed under the MATLAB®/Simulink® environment.

CITATION:
L.M. Belmonte; R. Morales; A. Fernández-Caballero; J.A. Somolinos. "Nonlinear Cascade-Based Control for a Twin Rotor MIMO System". *Nonlinear Systems - Design, Analysis, Estimation and Control*, 265–292. InTech, 2016. ISBN 978-953-51-2714-7. DOI: 10.5772/64875.

© 2016 The Author(s). Licensee InTech. This chapter is distributed under the terms of the Creative Commons Attribution License (http://creativecommons.org/licenses/by/3.0), which permits unrestricted use, distribution, and reproduction in any medium, provided the original work is properly cited.

Chapter 11

Nonlinear Cascade-Based Control for a Twin Rotor MIMO System

Lidia María Belmonte, Rafael Morales,
Antonio Fernández-Caballero and
José Andrés Somolinos

Additional information is available at the end of the chapter

http://dx.doi.org/10.5772/64875

Abstract

This research is focused on the development of a nonlinear cascade-based control algorithm for a laboratory helicopter-denominated Twin Rotor MIMO System (TRMS). The TRMS is an underactuated nonlinear multivariable system, characterised by a coupling effect between the dynamics of the propellers and the body structure, which is caused by the action-reaction principle originated in the acceleration and deceleration of the propeller groups. Firstly, this work introduces an extensive description of the platform's dynamics, which was carried out by splitting the system into its electrical and mechanical parts. Secondly, we present a design of a nonlinear cascade-based control algorithm that locally guarantees an asymptotically and exponentially stable behaviour of the controlled generalised coordinates of the TRMS. Lastly, a demonstration of the effectiveness of the proposed approach is provided by means of numerical simulations performed under the MATLAB®/Simulink® environment.

Keywords: nonlinear control, timescale modelling, twin rotor, MIMO systems, laboratory platform

1. Introduction

Currently, there are many possible uses for unmanned aerial vehicles (UAVs), such as inspection operation, battle field operation, forest fire detection, meteorological observation, or search and rescue operation, among others. All these applications require achieving precise control systems. This has motivated an increased interest in the last years from researchers in

INTECH
open science | open minds

© 2016 The Author(s). Licensee InTech. This chapter is distributed under the terms of the Creative Commons Attribution License (http://creativecommons.org/licenses/by/3.0), which permits unrestricted use, distribution, and reproduction in any medium, provided the original work is properly cited. (cc) BY

developing effective control algorithms for UAVs [1–4]. In many cases, the development of new control strategies requires the use of software and platforms which are able to simulate the operation of the UAVs in order to perform experimental tests for evaluating the different designs. The use of this kind of tools increases the productivity and reduces the development time. For this purpose, different laboratory test rigs have been specifically designed for teaching and research in flight dynamics and control. One such platform is the laboratory helicopter used in this research, namely the Twin Rotor MIMO System (TRMS) [5]. The TRMS is a nonlinear, multivariable and underactuated system, characterised by a coupling effect between the dynamics of the propellers and the body structure, which is caused by the action-reaction principle originated in acceleration and deceleration of the motor-propeller groups. All these features make the control of the TRMS to be perceived as a challenging engineering problem (note that the TRMS, and other laboratory platforms with similar dynamics are more difficult to control than a real helicopter platform [6]). The achievement of an accurate system dynamics model is a challenging problem, whilst, at the same time, an important issue is to develop accurate and efficient control systems.

The development of the dynamic model for the TRMS has been studied by an important number of researches. Ahmad et al. presented mathematical models for the dynamic characterisation of the TRMS, using a black box system identification technique [7] and radial basis function (RBF) networks [8]. Shaheed modelled the dynamics of the TRMS by means of a nonlinear autoregressive process through external input (NARX) approach with a feed-forward neural work and a resilient propagation (RPROP) algorithm [9]. Rahideh and Shaheed have also contributed to the study of the TRMS dynamics by using both Newton- and Lagrange-based methods [10], and two models based on neural networks using Levenberg-Marquardt (LM) and gradient descent (GD) algorithms [11]. Toha and Tokhi presented an adaptive neuro-fuzzy inference system (ANFIS) network design, which was deployed and used for the TRMS modelling [12]. Finally, Tastemirov et al. developed a complete dynamic TRMS model using the Euler-Lagrange method [13].

On the other hand, the design of the control system for the TRMS has been widely discussed through several investigations. Ahmad et al. developed the dynamic model and implemented a feed-forward/open-loop control [14] and a linear quadratic Gaussian control [15]. López-Martínez et al. studied the design of a longitudinal controller based on Lyapunov functions [16], and the application of a nonlinear L_2 controller [17]. Rahideh et al. presented an experimental implementation of an adaptive dynamic nonlinear model inversion control law using artificial neural networks [18]. Other interesting works are those of Tao et al. who designed a parallel distributed fuzzy linear quadratic regulator (LQR) controller [19]. Studies of Reynoso-Meza et al. developed a holistic multi-objective optimisation design technique for controller tuning [20], or the use of a particle swarm optimisation (PSO) algorithm for the proportional-integral-derivative (PID) controller optimisation developed by Coelho et al. [21].

The aim of the present research is to develop a nonlinear cascade-based control algorithm in order to locally guarantee an asymptotically and exponentially stable behaviour of the controlled generalised coordinates of the TRMS. Additionally, the effectiveness of the proposed

Nonlinear Cascade-Based Control for a Twin Rotor MIMO System 267
http://dx.doi.org/10.5772/64875

nonlinear feedback controller in terms of stabilisation and position tracking performance is demonstrated by means of numerical simulations. Finally, the paper is organised as follows.

Section 2 introduces a description of the TRMS platform by illustrating the details of the dynamics model obtained into two phases: electrical and mechanical parts. Section 3 describes the nonlinear cascade-based controller scheme proposed. The results of the numerical simulations performed under the MATLAB®/Simulink® environment are depicted in Section 4, and, finally, Section 5 is devoted to the conclusions of the work.

2. System description

The TRMS (see **Figure 1**) is a laboratory helicopter platform manufactured by *Feedback Instruments Ltd*©. The TRMS is composed of two propellers that are perpendicular to each other and placed in the extreme of a beam that can rotate freely in both vertical and horizontal planes. Each propeller is driven by a DC motor, thus forming the main and tail rotor of the platform. A main feature of the TRMS is that its movement, unlike a real helicopter, is not achieved by varying the angle of attack of the blades. In this case, the movement of the platform is gotten by means of the variation in the angular velocity of each propeller, which is caused by the change in the control input voltage of each motor.

Figure 1. Twin rotor MIMO system.

This constructive simplification in the TRMS model substantially complicates the dynamics of the system, because a coupling effect between rotors dynamics and the body of the model appears. This effect is caused by the action-reaction principle originated in acceleration and deceleration of the motor-propeller groups.

In addition, the TRMS is an underactuated system. This implies that the number of variables that act as control inputs (voltages applied to the main and the tail rotor; u_m and u_t respectively) is lower than the number of degrees of freedom (DoF) of the system. The DoF are: the pitch (ψ) and the yaw (ϕ) angles, both measured by digital encoders, as well as the angular velocities of the rotors (ω_m for the main rotor and $\omega_t$for the tail), both measured by DC tachometers. Finally, we have to remark that the laboratory platform is locked mechanically, so it cannot move more than ± 2.82 rad in the horizontal plane from -1.05 to $+1.22$ rad in the vertical plane [22]. In other words, $-2.82 \text{ rad} \leq \phi \leq +2.82 \text{ rad}$ and $-1.05 \text{ rad} \leq \psi \leq +1.22 \text{ rad}$.

2.1. Dynamic model of the TRMS

The development of an efficient control algorithm requires a model that represents the dynamic behaviour of the platform under study as accurately as possible. In the particular case of the Twin Rotor MIMO System, the modelling has been addressed from several approaches [7–13]. However, not all of them provide a model that represents the entire complex dynamic behaviour of this experimental platform. For instance, models based on identification techniques have difficulties in representing the effects of coupling, which are characteristic in this platform [7], and neuronal networks and learning algorithms allow obtaining accurate models, but limited to a range of input values and frequencies [11]. Based on previous works developed for the dynamic model of this platform [13, 22–24], a detailed dynamic model of the TRMS has been developed by dividing the whole dynamics of the system in their electrical and mechanical parts. This approach allows not only to adequately capture the complex dynamics behaviour of the TRMS but also the development of novel control algorithms based on nested feedback loops that offer a higher performance than classical control schemes. Moreover, the use of the Euler-Lagrange method in the modelling of the mechanical structure of the TRMS allows a higher adjustment with the real control laboratory platform in comparison with other analytical methods based on the Newtonian approach [25]. The dynamic modelling has been developed in two stages and validated by our research group by means of experimental identification trials. It is presented in the following subsections. The first subsection illustrates the dynamic model of the electrical part, and the second depicts the dynamic model of the mechanical part of the system.

2.1.1. Dynamics of the electrical part

The electrical part of the system is formed by the interface circuit and the DC motors of the main and tail rotors. The interface circuit is the internal electrical circuit that adapts the input control voltages, applied in MATLAB®/Simulink® (u_m for the main rotor and u_t for the tail rotor), to the actual voltage value of the DC motors (v_m for the main rotor and v_t for the tail

Nonlinear Cascade-Based Control for a Twin Rotor MIMO System 269
http://dx.doi.org/10.5772/64875

rotor). This interface can be modelled as a linear relationship [13], obtaining the following result:

$$v_m = k_{u_m} u_m \tag{1}$$

$$v_t = k_{u_t} u_t \tag{2}$$

where k_{u_m} and k_{u_t} denote the constant gains for the main and tail rotors, respectively. With regard to the DC motors, there are two identical permanent magnet motors, one in each rotor of the TRMS, with the only difference of the mechanical loads (the propellers). Bearing in mind that the dynamics of the motor´s current can be neglected [13], the DC motor dynamics for the main rotor and the tail rotor are the following ones:

$$v_m = R_m i_m + k_{v_m} \omega_m \tag{3}$$

$$v_t = R_t i_t + k_{v_t} \omega_t \tag{4}$$

where i_m and i_t are the motor currents (the subscripts m and t mean "main" and "tail"), R_m and R_t represent the motor resistances, and $k_{v_m} \omega_m$ and $k_{v_t} \omega_t$ denote the electromotive forces of each motor (ω_m and ω_t represent the angular velocities of the each motor). On the other hand, the electromechanical balance of the torques acting on each motor is expressed as:

$$I_{m_1} \dot{\omega}_m = k_{t_m} i_m - f_{v_m} \omega_m - C_{Q_m} \omega_m |\omega_m| \tag{5}$$

$$I_{t_1} \dot{\omega}_t = k_{t_t} i_t - f_{v_t} \omega_t - C_{Q_t} \omega_t |\omega_t| \tag{6}$$

being I_{m_1} and I_{t_1} are the moment of the inertia rotors, $k_{t_m} i_m$ and $k_{t_t} i_t$ denote the electromechanical torques generated by the DC motors, $f_{v_m} \omega_m$ and $f_{v_t} \omega_t$ are the friction torques and $C_{Q_m} \omega_m |\omega_m|$ and $C_{Q_t} \omega_t |\omega_t|$ illustrate the aerodynamic torques.

After substituting the expression for the current intensity of the respective motors [obtained from Eqs. (3) and (4)] and the linear relationships for the interface circuit Eqs. (1) and (2), in

Eqs. (5) and (6), and after operating and rearranging terms, the following two equations are yielded for the main and tail rotors of the TRMS:

$$I_{m_1}\dot{\omega}_m = \frac{k_{t_m}}{R_m}k_{u_m}u_m - \left(\frac{k_{t_m}k_{v_m}}{R_m} + f_{v_m}\right)\omega_m - C_{Q_m}\omega_m|\omega_m| \tag{7}$$

$$I_{t_1}\dot{\omega}_t = \frac{k_{t_t}}{R_t}k_{u_t}u_t - \left(\frac{k_{t_t}k_{v_t}}{R_t} + f_{v_t}\right)\omega_t - C_{Q_t}\omega_t|\omega_t| \tag{8}$$

The dynamics of the electrical part of the TRMS is now expressed in a matrix form, using the following compact notation:

$$\dot{\boldsymbol{\omega}}(t) = \boldsymbol{N}\boldsymbol{u}(t) + \boldsymbol{\Gamma}(\boldsymbol{\omega}(t)) \tag{9}$$

where $\boldsymbol{\omega}(t) = \left[\omega_m, \omega_t\right]^T$ and $\boldsymbol{u}(t) = \left[u_m, u_t\right]^T$ represent the vector of angular velocities and the input control voltages, respectively, and, $\boldsymbol{N}$= $diag(n_m, \quad n_t)$ and $\boldsymbol{\Gamma}(\boldsymbol{\omega}(t)) = \left[\Gamma_m, \Gamma_t\right]^T$ are defined by:

$$\boldsymbol{N} = \begin{bmatrix} n_m & 0 \\ 0 & n_t \end{bmatrix} = \begin{bmatrix} \dfrac{k_{t_m}k_{u_m}}{I_{m_1}R_m} & 0 \\ 0 & \dfrac{k_{t_t}k_{u_t}}{I_{t_1}R_t} \end{bmatrix} \tag{10}$$

$$\boldsymbol{\Gamma}(\boldsymbol{\omega}(t)) = \begin{bmatrix} \Gamma_m \\ \Gamma_t \end{bmatrix} = \begin{bmatrix} -\left(\dfrac{k_{t_m}k_{v_m}}{R_m} + f_{v_m}\right)\dfrac{\omega_m}{I_{m_1}} - \dfrac{C_{Q_m}}{I_{m_1}}\omega_m|\omega_m| \\ -\left(\dfrac{k_{t_t}k_{v_t}}{R_t} + f_{v_t}\right)\dfrac{\omega_t}{I_{t_1}} - \dfrac{C_{Q_t}}{I_{t_1}}\omega_t|\omega_t| \end{bmatrix} \tag{11}$$

Finally, in order to complete the dynamic model of the electrical part of the TRMS, **Tables 1** and **2** show the parameters used in the model, indicating the description of the parameters, their values and their corresponding units. These values, which are based on the data presented in [13], have been experimentally tuned and validated in the dynamics identification tests that we have performed during our research.

Nonlinear Cascade-Based Control for a Twin Rotor MIMO System 271
http://dx.doi.org/10.5772/64875

Symbol	Parameter	Value	Units
k_{v_m}	Motor velocity constant	0.0202	$\mathrm{V\ rad^{-1}\ s}$
R_m	Motor armature resistance	8	Ω
L_m	Motor armature inductance	0.86×10^{-3}	H
k_{t_m}	Electromagnetic constant torque motor	0.0202	$\mathrm{N\ m\ \ A^{-1}}$
k_{u_m}	Coefficient linear relationship interface circuit	8.5	–
$C_{Q_m}^{+}$	Load factor ($\omega_m \geq 0$)	2.695×10^{-7}	$\mathrm{N\ m\ s^2\ rad^{-2}}$
$C_{Q_m}^{-}$	Load factor ($\omega_m < 0$)	2.46×10^{-7}	$\mathrm{N\ m\ s^2\ rad^{-2}}$
f_{v_m}	Viscous friction coefficient	3.89×10^{-6}	$\mathrm{N\ m\ rad^{-1}\ s}$
I_{m_1}	Moment of inertia about the axis of rotation	1.05×10^{-4}	$\mathrm{kg\ m^2}$

Table 1. Parameters of the main rotor.

Symbol	Parameter	Value	Units
k_{v_t}	Motor velocity constant	0.0202	$\mathrm{V\ rad^{-1}\ s}$
R_t	Motor armature resistance	8	Ω
L_t	Motor armature inductance	0.86×10^{-3}	H
k_{t_t}	Electromagnetic constant torque motor	0.0202	$\mathrm{N\ m\ A^{-1}}$
k_{u_t}	Coefficient linear relationship interface circuit	6.5	–
C_{Q_t}	Load factor	1.164×10^{-8}	$\mathrm{N\ m\ s^2\ rad^{-2}}$
f_{v_t}	Viscous friction coefficient	1.715×10^{-6}	$\mathrm{N\ m\ rad^{-1}\ s}$
I_{t_1}	Moment of inertia about the axis of rotation	2.1×10^{-5}	$\mathrm{kg\ m^2}$

Table 2. Parameters of the tail rotor.

2.1.2. Dynamics of the mechanical part

In the development of the dynamic model of the mechanical part, we consider the mechanics of the TRMS as an assembly of the following three components explained next. The first component is formed by the two rotors, their shields and the free-free beam that links together both rotors. The second component consists in the counterbalance and counterweight beam,

and finally, the third component is the pivoted beam. **Figure 2** helps to clarify the different components considered in the dynamics of the mechanical part of the system. From the previous division, and bearing in mind the notation used in **Figures 3** and **4**, the development of the dynamic model is achieved by means of the application of the Euler-Lagrange formulation. It can be summarised in the following steps:

1. Resolution of the forward kinematics of the three subsystems.
2. Evaluation of the kinetic energy.
3. Evaluation of the potential energy.
4. Obtaining the equations of motion.

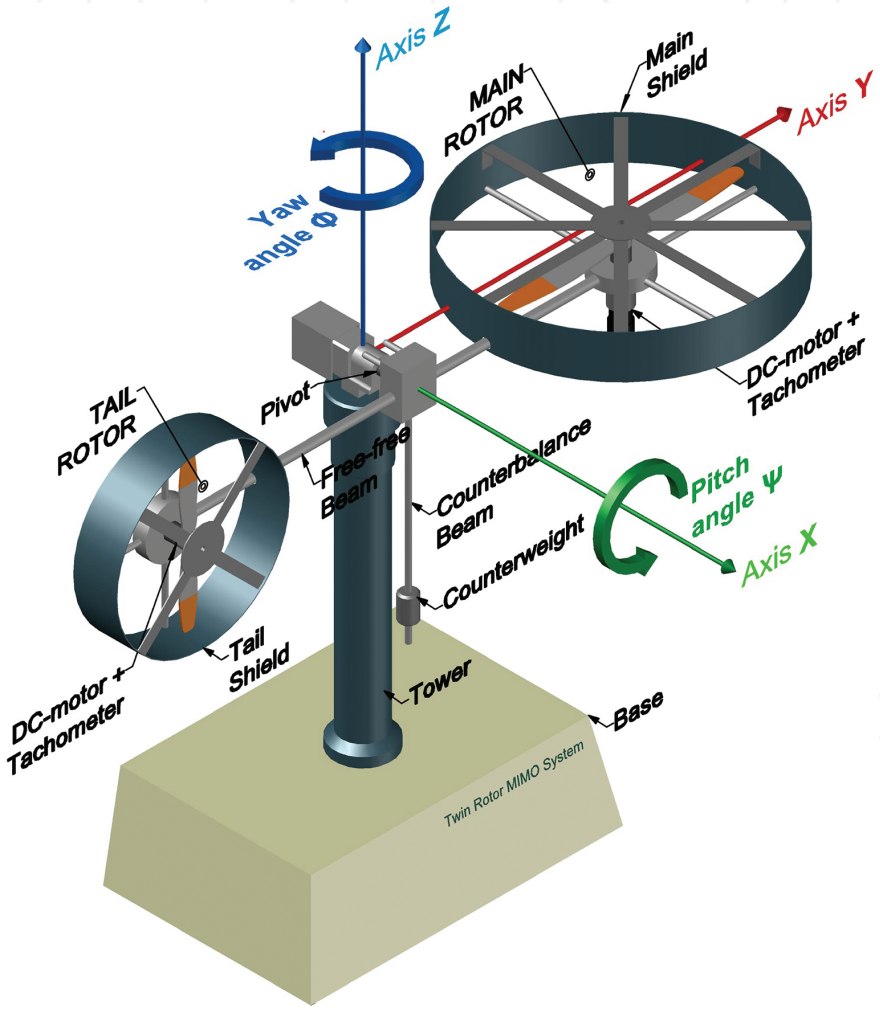

Figure 2. Twin rotor MIMO system (TRMS) prototype platform.

Nonlinear Cascade-Based Control for a Twin Rotor MIMO System 273
http://dx.doi.org/10.5772/64875

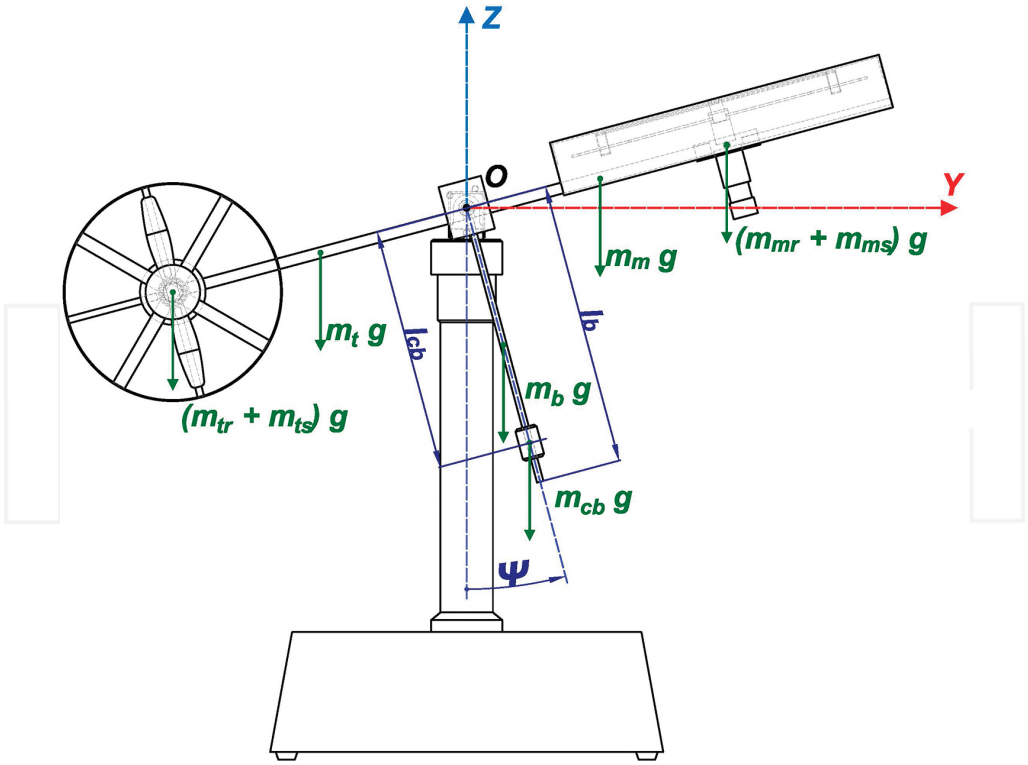

Figure 3. View of the TRMS on a vertical plane.

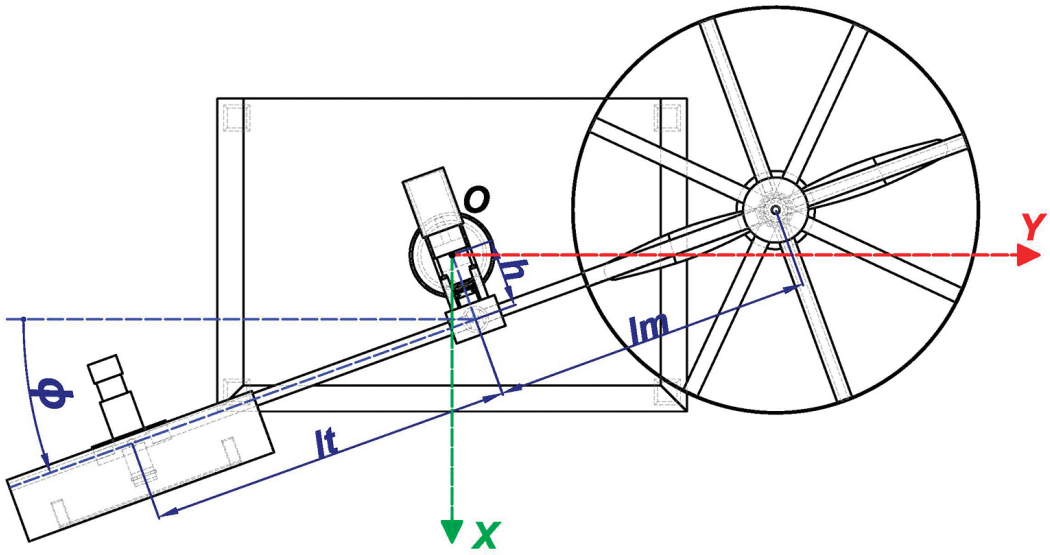

Figure 4. View of the TRMS on a horizontal plane.

2.1.2.1. Resolution of the forward kinematics of the system

The problem of direct kinematics of the TRMS consists in determining the spatial position of the three subsystems considered, according to the reference system located in the upper part of the platform (see **Figures 3** and **4**). Using the Denavit-Hartenberg method, we can express the position of a point on each subsystem (P_1, P_2, P_3) parameterised by R_1, R_2, R_3, which represents the distances between the considerate points and the reference system associated to each subsystem. The results of these positions are expressed in the following three equations (where: $S_\psi \equiv \sin\Psi$, $C_\psi \equiv \cos\Psi$, $S_\phi \equiv \sin\phi$ and $C_\phi \equiv \cos\phi$):

$$\boldsymbol{P}_1 = \begin{bmatrix} P_{1_x} & P_{1_y} & P_{1_z} \end{bmatrix}^T = \begin{bmatrix} -R_1 S_\phi C_\psi + hC_\phi & R_1 C_\phi C_\psi + hS_\phi & R_1 S_\psi \end{bmatrix}^T \tag{12}$$

$$\boldsymbol{P}_2 = \begin{bmatrix} P_{2_x} & P_{2_y} & P_{2_z} \end{bmatrix}^T = \begin{bmatrix} -R_2 S_\phi S_\psi + hC_\phi & R_2 C_\phi S_\psi + hS_\phi & -R_2 C_\psi \end{bmatrix}^T \tag{13}$$

$$\boldsymbol{P}_3 = \begin{bmatrix} P_{3_x} & P_{3_y} & P_{3_z} \end{bmatrix}^T = \begin{bmatrix} R_3 C_\phi & R_3 S_\phi & 0 \end{bmatrix}^T \tag{14}$$

2.1.2.2. Evaluation of the kinetic energy

In order to carry out the evaluation of the total kinetic energy of the TRMS, it is necessary to calculate the kinetic energy corresponding to each of the three subsystems previously defined. Starting with the first subsystem, its kinetic energy, T_1, yields:

$$T_1 = \frac{1}{2}\int |v_1|^2 \, dm(R_1) = \frac{1}{2} J_1 \left(C_\psi{}^2 \dot{\phi}^2 + \dot{\psi}^2 \right) + \frac{1}{2} h^2 m_{T_1} \dot{\phi}^2 - h S_\psi l_{T_1} m_{T_1} \dot{\phi}\dot{\psi} \tag{15}$$

$$|v_1|^2 = \left(R_1{}^2 C_\psi{}^2 + h^2 \right) \dot{\phi}^2 + R_1{}^2 \dot{\psi}^2 - 2 R_1 h S_\psi \dot{\phi}\dot{\psi} \tag{16}$$

where ψ and ϕ represent the yaw and the pitch angle, respectively, and m_{T_1}, l_{T_1}, and J_1 are obtained from the following expressions:

$$\int dm(R_1) = m_{\mathrm{m}} + m_{\mathrm{mr}} + m_{\mathrm{ms}} + m_{\mathrm{t}} + m_{\mathrm{tr}} + m_{\mathrm{ts}} = m_{T_1} \tag{17}$$

$$l_{T_1} = \frac{\int R_1 dm(R_1)}{\int dm(R_1)} = \frac{\left(\frac{m_{\mathrm{t}}}{2} + m_{\mathrm{tr}} + m_{\mathrm{ts}} \right) l_t - \left(\frac{m_{\mathrm{m}}}{2} + m_{\mathrm{mr}} + m_{\mathrm{ms}} \right) l_m}{m_{T_1}} \tag{18}$$

$$J_1 = \left(\frac{1}{3} m_{\mathrm{t}} + m_{\mathrm{tr}} + m_{\mathrm{ts}} \right) l_t{}^2 + \left(\frac{1}{3} m_{\mathrm{m}} + m_{\mathrm{mr}} + m_{\mathrm{ms}} \right) l_m{}^2 + m_{\mathrm{ts}} r_{\mathrm{ts}}{}^2 + \frac{1}{2} m_{\mathrm{ms}} r_{\mathrm{ms}}{}^2 \tag{19}$$

Nonlinear Cascade-Based Control for a Twin Rotor MIMO System 275
http://dx.doi.org/10.5772/64875

On the other hand, the kinetic energy for the second subsystem, T_2, results in:

$$T_2 = \frac{1}{2}\int |v_2|^2 \, dm(R_2) = \frac{1}{2} J_2 \left({S_\psi}^2 \dot{\phi}^2 + \dot{\psi}^2 \right) + \frac{1}{2} h^2 m_{T_2} \dot{\phi}^2 + h C_\psi l_{T_2} m_{T_2} \dot{\phi}\dot{\psi} \tag{20}$$

$$|v_2|^2 = \left({R_2}^2 {S_\psi}^2 + h^2 \right) \dot{\phi}^2 + {R_2}^2 \dot{\psi}^2 + 2 R_2 h C_\psi \dot{\phi}\dot{\psi} \tag{21}$$

in which the terms m_{T_2}, l_{T_2} and J_2 are the following:

$$\int dm(R_2) = m_{\mathrm{b}} + m_{\mathrm{cb}} = m_{T_2} \tag{22}$$

$$l_{T_2} = \frac{\int R_2 dm(R_2)}{\int dm(R_2)} = \frac{m_{\mathrm{b}} \frac{l_b}{2} + m_{\mathrm{cb}} l_{mcb}}{m_{T_2}} \tag{23}$$

$$J_2 = \frac{1}{3} m_{\mathrm{b}} {l_b}^2 + m_{\mathrm{cb}} {l_{cb}}^2 \tag{24}$$

On the other hand, the kinetic energy for the third subsystem, T_3, gives the following result:

$$T_3 = \frac{1}{2}\int |v_3|^2 \, dm(R_3) = \frac{1}{2} J_3 \dot{\phi}^2 \tag{25}$$

$$|v_3|^2 = {R_3}^2 \dot{\phi}^2 \tag{26}$$

being $J_3 = \frac{1}{3} m_h {l_h}^2$.

Finally, the total kinetic energy of the TRMS, T, is obtained as the sum of the kinetic energy of each subsystem (Eqs. (15), (20) and (25)). One obtains the following result:

$$\begin{aligned} T = T_1 + T_2 + T_3 = {} & \frac{1}{2}\left(J_1 {C_\psi}^2 + J_2 {S_\psi}^2 + J_3 + h^2 \left(m_{T_1} + m_{T_2} \right) \right) \dot{\phi}^2 \\ & + \frac{1}{2}\left(J_1 + J_2 \right) \dot{\psi}^2 + h\left(l_{T_2} m_{T_2} C_\psi - l_{T_1} m_{T_1} S_\psi \right) \dot{\phi}\dot{\psi} \end{aligned} \tag{27}$$

2.1.2.3. Evaluation of the potential energy

Following a similar procedure to the one used in the computation of the kinetic energy, the total potential energy of the TRMS, V, consists of the sum of the potential energy of each of the three subsystems, the free-free beam (including rotors and shields), the counterbalance beam and the pivoted beam. The following result is obtained:

$$V = V_1 + V_2 + V_3 = g\left(S_\psi l_{T_1} m_{T_1} - C_\psi l_{T_2} m_{T_2}\right) \tag{28}$$

where:

$$V_1 = g\int r_{z_1}(R_1)\,dm(R_1) = g\int P_{1_z}\,dm(R_1) = gS_\psi l_{T_1} m_{T_1} \tag{29}$$

$$V_2 = g\int r_{z_2}(R_2)\,dm(R_2) = g\int P_{2_z}\,dm(R_2) = -gC_\psi l_{T_2} m_{T_2} \tag{30}$$

$$V_3 = g\int r_{z_3}(R_3)\,dm(R_3) = g\int P_{3_z}\,dm(R_3) = 0 \tag{31}$$

2.1.2.4. Equations of motion of the TRMS

The last step in the mechanical dynamic model of the TRMS is obtaining the equations of motion of the system. The first step is the computation of the Lagrangian of the system, defined as the difference between the total kinetic energy, defined in Eq. (27), and the total potential energy, defined in Eq. (28), yielding the following:

$$\begin{aligned} L = T - V = {} & \frac{1}{2}\left(J_1 {C_\psi}^2 + J_2 {S_\psi}^2 + J_3 + h^2\left(m_{T_1} + m_{T_2}\right)\right)\dot{\phi}^2 \\ & + \frac{1}{2}\left(J_1 + J_2\right)\dot{\psi}^2 + h\left(l_{T_2} m_{T_2} C_\psi - l_{T_1} m_{T_1} S_\psi\right)\dot{\phi}\dot{\psi} - g\left(S_\psi l_{T_1} m_{T_1} - C_\psi l_{T_2} m_{T_2}\right) \end{aligned} \tag{32}$$

Once the Lagrangian function has been obtained, the equations of motion of the TRMS can be derived using Lagrange's formulation:

$$\frac{d}{dt}\left(\frac{\partial L}{\partial \dot{\psi}}\right) - \frac{\partial L}{\partial \psi} = \sum M_{iv} \tag{33}$$

Nonlinear Cascade-Based Control for a Twin Rotor MIMO System 277
http://dx.doi.org/10.5772/64875

$$\frac{d}{dt}\left(\frac{\partial L}{\partial \dot{\phi}}\right)-\frac{\partial L}{\partial \phi}=\sum M_{ih} \tag{34}$$

where $\sum \boldsymbol{M_{iv}}$ and $\sum \boldsymbol{M_{ih}}$ represent the sum of the torques of the external forces along the vertical and horizontal axes, respectively. The following expressions illustrate several partial results necessary to achieve the equations of motion represented by Eqs. (33) and (34):

$$\frac{\partial L}{\partial \dot{\psi}}=\left(J_1+J_2\right)\dot{\psi}+h\left(l_{T_2}m_{T_2}C_{\psi}-l_{T_1}m_{T_1}S_{\psi}\right)\dot{\phi} \tag{35}$$

$$\frac{\partial L}{\partial \psi}=\left(\left(J_2-J_1\right)C_{\psi}S_{\psi}\right)\dot{\phi}^2-h\left(l_{T_1}m_{T_1}C_{\psi}+l_{T_2}m_{T_2}S_{\psi}\right)\dot{\phi}\dot{\psi}-g\left(l_{T_1}m_{T_1}C_{\psi}+l_{T_2}m_{T_2}S_{\psi}\right) \tag{36}$$

$$\frac{\partial L}{\partial \dot{\phi}}=\left(J_1{C_{\psi}}^2+J_2{S_{\psi}}^2+J_3+h^2\left(m_{T_1}+m_{T_2}\right)\right)\dot{\phi}+h\left(l_{T_2}m_{T_2}C_{\psi}-l_{T_1}m_{T_1}S_{\psi}\right)\dot{\psi} \tag{37}$$

$$\frac{\partial L}{\partial \phi}=0 \tag{38}$$

$$\frac{d}{dt}\left(\frac{\partial L}{\partial \dot{\psi}}\right)=h\left(l_{T_2}m_{T_2}C_{\psi}-l_{T_1}m_{T_1}S_{\psi}\right)\ddot{\phi}+\left(J_1+J_2\right)\ddot{\psi}-h\left(l_{T_1}m_{T_1}C_{\psi}+l_{T_2}m_{T_2}S_{\psi}\right)\dot{\phi}\dot{\psi} \tag{39}$$

$$\begin{aligned}\frac{d}{dt}\left(\frac{\partial L}{\partial \dot{\phi}}\right)=&\left(J_1{C_{\psi}}^2+J_2{S_{\psi}}^2+J_3+h^2\left(m_{T_1}+m_{T_2}\right)\right)\ddot{\phi}-h\left(l_{T_1}m_{T_1}S_{\psi}-l_{T_2}m_{T_2}C_{\psi}\right)\ddot{\psi}\\&-h\left(l_{T_1}m_{T_1}C_{\psi}+l_{T_2}m_{T_2}S_{\psi}\right)\dot{\psi}^2+2\left(\left(J_2-J_1\right)C_{\psi}S_{\psi}\right)\dot{\phi}\dot{\psi}\end{aligned} \tag{40}$$

The sum of the external torques in the vertical axis is shown next:

$$\begin{aligned}&\sum M_{iv}=M_{T_m}-M_{R_t}-M_{F_{\psi}}+M_{I_t}\\&\sum M_{iv}=C_{T_m}\omega_m\left|\omega_m\right|l_m-C_{R_t}\omega_t\left|\omega_t\right|-\left(f_{v_{\psi}}\dot{\psi}+f_{c_{\psi}}sgn\left(\dot{\psi}\right)\right)+k_t\dot{\omega}_t\end{aligned} \tag{41}$$

where $M_{T_m}=C_{T_m}\omega_m\left|\omega_m\right|l_m$ expresses the aerodynamic thrust torque caused by the rotation of the main propeller, $M_{R_t}=C_{R_t}\omega_t\left|\omega_t\right|$ denotes the load torque created by air resistance in the tail rotor, $M_{F_{\psi}}=\left(f_{v_{\psi}}\dot{\psi}+f_{c_{\psi}}sgn\left(\dot{\psi}\right)\right)$ represents the load torque as a result of the friction (including the viscous effects and the Coulomb friction), and $M_{I_t}=k_t\dot{\omega}_t$ represents the inertial counter torque that is caused by the reaction produced by a change in the rotational speed of the tail rotor.

On the other hand, the sum of the external torques in the horizontal axis is as follows:

$$\begin{aligned}\sum M_{ih} &= M_{T_t} - M_{R_m} - M_{F_\phi} - M_c + M_{I_m} \\ \sum M_{ih} &= C_{T_T}\omega_t|\omega_t|l_t C_\psi - C_{R_m}\omega_m|\omega_m|C_\psi \\ &\quad -\left(f_{v_\phi}\dot{\phi} + f_{c_\phi} sgn\left(\dot{\phi}\right)\right) - C_c\left(\phi - \phi_0\right) + k_m\dot{\omega}_m C_\psi\end{aligned} \tag{42}$$

where $M_{T_t} = C_{T_T}\omega_t|\omega_t|l_t C_\psi$ expresses the aerodynamic thrust torque of the tail propeller, $M_{R_m} = C_{R_m}\omega_m|\omega_m|C_\psi$ represents the load torque created by air resistance in the main rotor, $M_{F_\phi} = (f_{v_\phi}\dot{\phi} + f_{c_\phi} sgn(\dot{\phi}))$ denotes the load torque as a result of the friction (including the viscous effects and the Coulomb friction), $M_c = C_c(\phi - \phi_0)$ is the magnitude of torque exerted by the cable (it has a certain stiffness that allows to model it as a spring)), and finally $M_{I_m} = k_m\dot{\omega}_m C_\psi$ represents the inertial counter torque that is caused by the reaction produced by a change in the rotational speed of the main rotor.

Upon merging Eq. (33) to Eq. (42), and after performing some rearrangements, one obtains the following result for the equations of motion:

$$\begin{aligned}&\left(J_1 + J_2\right)\ddot{\psi} + h\left(l_{T_2} m_{T_2} C_\psi - l_{T_1} m_{T_1} S_\psi\right)\ddot{\phi} + \left(\frac{\left(J_1 - J_2\right)}{2} S_{2\psi}\right)\dot{\phi}^2 + g\left(l_{T_1} m_{T_1} C_\psi + l_{T_2} m_{T_2} S_\psi\right) \\ &= C_{T_m}\omega_m|\omega_m|l_m - C_{R_t}\omega_t|\omega_t| - \left(f_{v_\psi}\dot{\psi} + f_{c_\psi} sgn\left(\dot{\psi}\right)\right) + k_t\dot{\omega}_t\end{aligned} \tag{43}$$

$$\begin{aligned}&h\left(l_{T_2} m_{T_2} C_\psi - l_{T_1} m_{T_1} S_\psi\right)\ddot{\psi} + \left(J_1 {C_\psi}^2 + J_2 {S_\psi}^2 + J_3 + h^2\left(m_{T_1} + m_{T_2}\right)\right)\ddot{\phi} - \\ &h\left(l_{T_1} m_{T_1} C_\psi + l_{T_2} m_{T_2} S_\psi\right)\dot{\psi}^2 + \left(\left(J_2 - J_1\right) S_{2\psi}\right)\dot{\phi}\dot{\psi} \\ &= C_{T_T}\omega_t|\omega_t|l_t C_\psi - C_{R_m}\omega_m|\omega_m|C_\psi - \left(f_{v_\phi}\dot{\phi} + f_{c_\phi} sgn\left(\dot{\phi}\right)\right) - C_c\left(\phi - \phi_0\right) + k_m\dot{\omega}_m C_\psi\end{aligned} \tag{44}$$

If we use matrix notation, the dynamic model of the mechanical part of the TRMS can be expressed in a compact form:

$$\boldsymbol{M}\left(\boldsymbol{q}(t)\right)\ddot{\boldsymbol{q}}(t) + \boldsymbol{C}\left(\boldsymbol{q}(t), \dot{\boldsymbol{q}}(t)\right)\dot{\boldsymbol{q}}(t) + \boldsymbol{\eta}(\boldsymbol{q}(t), \dot{\boldsymbol{q}}(t), \dot{\boldsymbol{\omega}}(t)) = \boldsymbol{E}\left(\boldsymbol{q}(t)\right)\boldsymbol{\Omega}(t) \tag{45}$$

in which $\boldsymbol{q}(t) = [\psi(t), \ \ \phi(t)]^T$ is the vector of generalised coordinates of the TRMS, $\boldsymbol{\omega}(t) = \left[\omega_m(t), \ \ \omega_t(t)\right]^T$ is the angular velocity vector, and the matrices $\boldsymbol{M}(\boldsymbol{q}(t))$, $\boldsymbol{C}(\boldsymbol{q}(t), \dot{\boldsymbol{q}}(t))$, $\boldsymbol{E}(\boldsymbol{q}(t))$, and the vectors $\boldsymbol{\Omega}(t)$ and $\boldsymbol{\eta}(\boldsymbol{q}(t), \dot{\boldsymbol{q}}(t), \dot{\boldsymbol{\omega}}(t))$ are given by:

Nonlinear Cascade-Based Control for a Twin Rotor MIMO System 279
http://dx.doi.org/10.5772/64875

$$\boldsymbol{M}\left(\boldsymbol{q}(t)\right)=\begin{bmatrix} J_1+J_2 & h\left(l_{T_2}m_{T_2}C_\psi - l_{T_1}m_{T_1}S_\psi\right) \\ h\left(l_{T_2}m_{T_2}C_\psi - l_{T_1}m_{T_1}S_\psi\right) & J_1{C_\psi}^2+J_2{S_\psi}^2+J_3+h^2\left(m_{T_1}+m_{T_2}\right) \end{bmatrix} \tag{46}$$

$$\boldsymbol{C}\left(\boldsymbol{q}(t),\dot{\boldsymbol{q}}(t)\right)=\begin{bmatrix} 0 & \frac{1}{2}\left(J_1-J_2\right)S_{2\psi}\dot{\phi} \\ -h\left(l_{T_1}m_{T_1}C_\psi + l_{T_2}m_{T_2}S_\psi\right)\dot{\psi} & \left(J_2-J_1\right)S_{2\psi}\dot{\psi} \end{bmatrix} \tag{47}$$

$$\boldsymbol{E}\left(\boldsymbol{q}(t)\right)=\begin{bmatrix} C_{T_m}l_m & -C_{R_t} \\ -C_{R_m}C_\psi & C_{T_T}l_tC_\psi \end{bmatrix} \tag{48}$$

$$\boldsymbol{\Omega}(t)=\begin{bmatrix} \omega_m|\omega_m| \\ \omega_t|\omega_t| \end{bmatrix} \tag{49}$$

$$\boldsymbol{\eta}\left(\boldsymbol{q}(t),\dot{\boldsymbol{q}}(t),\dot{\boldsymbol{\omega}}(t)\right)=\boldsymbol{G}\left(\boldsymbol{q}(t)\right)+\boldsymbol{F}\left(\dot{\boldsymbol{q}}(t)\right)+\boldsymbol{T}\left(\boldsymbol{q}(t),\dot{\boldsymbol{\omega}}(t)\right) \tag{50}$$

$$\boldsymbol{G}\left(\boldsymbol{q}(t)\right)=\begin{bmatrix} g\left(l_{T_1}m_{T_1}C_\psi + l_{T_2}m_{T_2}S_\psi\right) \\ 0 \end{bmatrix} \tag{51}$$

$$\boldsymbol{F}\left(\dot{\boldsymbol{q}}(t)\right)=\boldsymbol{F}_v\dot{\boldsymbol{q}}(t)+\boldsymbol{F}_c\left(\dot{\boldsymbol{q}}(t)\right)=\begin{bmatrix} f_{v_\psi} & 0 \\ 0 & f_{v_\phi} \end{bmatrix}\dot{\boldsymbol{q}}(t)+\begin{bmatrix} f_{c_\psi}sgn\left(\dot{\psi}\right) \\ f_{c_\phi}sgn\left(\dot{\phi}\right) \end{bmatrix}=\begin{bmatrix} f_{v_\psi}\dot{\psi}+f_{c_\psi}sgn\left(\dot{\psi}\right) \\ f_{v_\phi}\dot{\phi}+f_{c_\phi}sgn\left(\dot{\phi}\right) \end{bmatrix} \tag{52}$$

$$\begin{aligned} \boldsymbol{T}\left(\boldsymbol{q}(t),\dot{\boldsymbol{\omega}}(t)\right) &= \boldsymbol{M}_{\boldsymbol{c}}\left(\boldsymbol{q}(t)\right)-\boldsymbol{M}_{\boldsymbol{g}}\left(\boldsymbol{q}(t)\right)\dot{\boldsymbol{\omega}}(t)=\begin{bmatrix} 0 \\ C_c(\phi-\phi_0) \end{bmatrix}-\begin{bmatrix} 0 & k_t \\ k_mC_\psi & 0 \end{bmatrix}\dot{\boldsymbol{\omega}}(t) \\ &= \begin{bmatrix} -k_t\dot{\omega}_t \\ C_c(\phi-\phi_0)-k_m\dot{\omega}_mC_\psi \end{bmatrix} \end{aligned} \tag{53}$$

Finally, after substituting Eqs. (51)–(53) into Eq. (50), the following yields:

$$\boldsymbol{\eta}\left(\boldsymbol{q}(t),\dot{\boldsymbol{q}}(t),\dot{\boldsymbol{\omega}}(t)\right)=\begin{bmatrix} g\left(l_{T_1}m_{T_1}C_\psi + l_{T_2}m_{T_2}S_\psi\right)+f_{v_\psi}\dot{\psi}+f_{c_\psi}sgn\left(\dot{\psi}\right)-k_t\dot{\omega}_t \\ f_{v_\phi}\dot{\phi}+f_{c_\phi}sgn\left(\dot{\phi}\right)+C_c\left(\phi-\phi_0\right)-k_m\dot{\omega}_mC_\psi \end{bmatrix} \tag{54}$$

Symbol	Parameter	Value	Units
l_{t}	Length of the tail part of the free-free beam	0.282	m
l_{m}	Length of the main part of the free-free beam	0.246	m
l_{b}	Length of the counterbalance beam	0.290	m
l_{cb}	Distance between the counterweight and the join	0.276	m
r_{ms}	Radius of the main shield	0.155	m
r_{ts}	Radius of the tail shield	0.1	m
h	Length of the pivoted beam	0.06	m
m_{tr}	Mass of the tail DC motor and tail rotor	0.221	kg
m_{mr}	Mass of the main DC motor and main rotor	0.236	kg
m_{cb}	Mass of the counterweight	0.068	kg
m_{t}	Mass of the tail part of the free-free beam	0.015	kg
m_{m}	Mass of the main part of the free-free beam	0.014	kg
m_{b}	Mass of the counterbalance beam	0.022	kg
m_{ts}	Mass of the tail shield	0.119	kg
m_{ms}	Mass of the main shield	0.219	kg
m_{h}	Mass of pivoted beam	0.01	kg

Table 3. Mechanical parameters.

Symbol	Parameter	Value	Units
$C_{T_m}^{+}$	Thrust torque coefficient of the main rotor ($\omega_m \geq 0$)	1.53×10^{-5}	$\mathrm{N\,s^2\,rad^{-2}}$
$C_{T_m}^{-}$	Thrust torque coefficient of the main rotor ($\omega_m < 0$)	8.8×10^{-6}	$\mathrm{N\,s^2\,rad^{-2}}$
C_{R_t}	Load torque coefficient of the tail rotor	9.7×10^{-8}	$\mathrm{N\,m\,s^2\,rad^{-2}}$
f_{v_ψ}	Viscous friction coefficient	0.0024	$\mathrm{N\,m\,s\,rad^{-1}}$
f_{c_ψ}	Coulomb friction coefficient	5.69×10^{-4}	N m
k_{t}	Coefficient of the inertial counter torque created by the change in ω_t	2.6×10^{-5}	$\mathrm{N\,m\,s^2\,rad^{-1}}$

Table 4. Parameters of the pitch movement.

Nonlinear Cascade-Based Control for a Twin Rotor MIMO System 281
http://dx.doi.org/10.5772/64875

Symbol	Parameter	Value	Units
$C_{T_t}^{+}$	Thrust torque coefficient of the tail rotor ($\omega_t \geq 0$)	3.25×10^{-6}	N s^2 rad^{-1}
$C_{T_t}^{-}$	Thrust torque coefficient of the tail rotor ($\omega_t < 0$)	1.72×10^{-6}	N s^2 rad^{-2}
$C_{R_m}^{+}$	Load torque coefficient of the main rotor ($\omega_m \geq 0$)	4.9×10^{-7}	N m s^2 rad^{-2}
$C_{R_m}^{-}$	Load torque coefficient of the main rotor ($\omega_m < 0$)	4.1×10^{-7}	N m s^2 rad^{-2}
f_{v_ϕ}	Viscous friction coefficient	0.03	N m s rad^{-1}
f_{c_ϕ}	Coulomb friction coefficient	3×10^{-4}	N m
C_c	Coefficient of the elastic force torque created by the cable	0.016	N m rad^{-1}
ϕ_0	Constant for the calculation of the torque of the cable	0	rad
k_m	Coefficient of the inertial counter torque created by the change in ω_m	2×10^{-4}	N m s^2 rad^{-1}

Table 5. Parameters of the yaw movement.

Finally, in order to complete the dynamic modelling for the mechanical part of the TRMS, **Tables 3–5** show in detail the parameters used in the model. For each parameter, its description, its value and the corresponding units is included. The initial approximation of these values was based in the developments described in [13]. Additionally, some values of the parameters have been tuned by carrying out several identification trials.

3. Design of the control system

In this section, the proposed nonlinear control for the TRMS platform is described. The proposed control is based on the division between the electrical and mechanical dynamics of the system and uses a cascade-type nonlinear control algorithm. **Figure 5** displays the proposed control scheme. As it can be observed, the proposed design is composed of two independent stages (or control loops) that are utilised to achieve stabilisation and precise trajectory tracking tasks for the controlled position of the generalised system coordinates. It should be noted that the proposed solution has been designed to overcome one of the limitations of the TRMS, which is the fact of being an underactuated system. As result of this fact, it only has two control actions (the input voltages of the main and tail rotors) to control the four degrees of freedom of the system (the pitch and yaw angles, and the angular velocities of the propellers). In this way, in order to meet this objective, once the dynamics of the TRMS have been decoupled, a nonlinear multivariable inner loop is closed to control the vector of the

angular velocities, and then, a nonlinear multivariable outer loop is closed to control the vector of the generalised coordinates of the system. This solution, based on a control scheme with two nested loops, allows a simplification in the design procedure as a result of its division into two simpler processes. Moreover, the scheme can be implemented more easily and safely than the standard controllers.

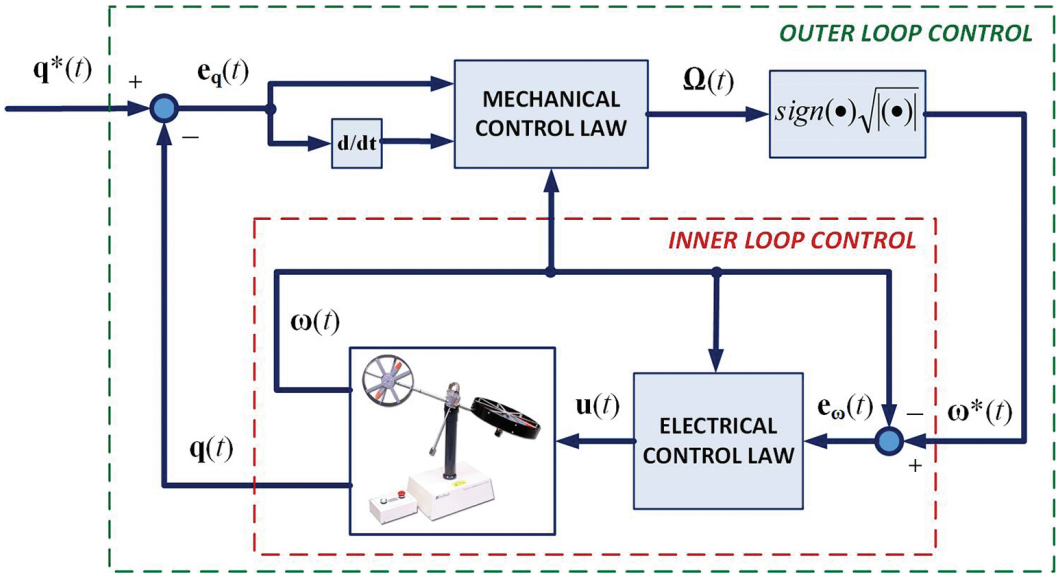

Figure 5. Nonlinear control scheme for the TRMS.

In the following subsections we describe the specifications and objectives of each control loop, defined as the inner loop or electrical controller and the outer loop or mechanical controller.

3.1. Inner loop control

The objective of the inner loop control is to determine the input voltages of the main and tail rotors (simulated in the MATLAB®/Simulink® environment), $\boldsymbol{u}(t) = \left[u_m, u_t\right]^T$, in order to eliminate the difference between the vector of reference angular velocities, $\boldsymbol{\omega}^*(t) = \left[\omega_m^*, \omega_t^*\right]^T$, calculated in the outer loop stage (as will be described in the next subsection), and the current vector of angular velocities of the propellers of the TRMS, $\boldsymbol{\omega}(t) = \left[\omega_m, \omega_t\right]^T$.

The magnitude of the input control voltage vector, $\boldsymbol{u}(t)$, necessary to achieve an asymptotically stable convergent behaviour of the tracking error trajectories, is calculated as the following nonlinear control law:

$$\boldsymbol{u}(t) = \boldsymbol{N}^{-1}\left[\boldsymbol{\gamma}_e(t) - \boldsymbol{\Gamma}(\boldsymbol{\omega}(t))\right] \tag{55}$$

Nonlinear Cascade-Based Control for a Twin Rotor MIMO System 283
http://dx.doi.org/10.5772/64875

where $\boldsymbol{N}$ and $\boldsymbol{\Gamma}(\boldsymbol{\omega}(t))$ where defined in Eqs. (10) and (11), respectively, and $\boldsymbol{\gamma_e}(t) = \left[\gamma_m, \gamma_t\right]^T$ represents a vector of auxiliary control inputs, given by the following expression:

$$\boldsymbol{\gamma}_e(t) = -\boldsymbol{K}_P^e \boldsymbol{e}_{\boldsymbol{\omega}}(t) = -\boldsymbol{K}_P^e[\boldsymbol{\omega}(t) - \boldsymbol{\omega}^*(t)] \tag{56}$$

where $\boldsymbol{K_P^e} \in \mathbb{R}^{2\times 2}$ is a constant diagonal positive definite matrix that represents the design elements of a vector-valued classical proportional controller and $\boldsymbol{e}_{\boldsymbol{\omega}}(t) = \boldsymbol{\omega}(t) - \boldsymbol{\omega}^*(t)$ is the angular velocity error vector, which satisfies the following predominantly linear dynamic:

$$\dot{\boldsymbol{\omega}}(t) + \boldsymbol{K}_P^e \boldsymbol{e}_{\boldsymbol{\omega}}(t) = \boldsymbol{0} \tag{57}$$

Finally, the coefficients of the matrix $\boldsymbol{K}_P^e$ are chosen so as to render the closed-loop characteristic polynomial vectors into a Hurwitz polynomial vector with desirable roots.

3.2. Outer loop control

The aim of the outer loop control (mechanical controller) is to determine the required values for the angular velocities of the two rotors, $\boldsymbol{\omega}^*(t) = \left[\omega_m^*, \omega_t^*\right]^T$, which will be the reference inputs of the electrical loop (described in the above subsection), in order to eliminate the difference between the generalised coordinates of the TRMS, $\boldsymbol{q}(t) = [\psi, \phi]^T$, and the reference trajectories for the generalised coordinates of the TRMS $\boldsymbol{q}^*(t) = [\psi^*, \phi^*]^T$.

As a previous step for determining the mechanical control law, a simplification in the dynamic mechanical modelling of the TRMS has been considered. If we assume that the movement of the platform is sufficiently smooth, the terms of the inertial counter torques, which are caused by the reaction produced by the changes in the rotational speed of each rotor, $M_{I_t} = k_t \dot{\omega}_t$ and $M_{I_m} = k_m \dot{\omega}_m C_\psi$ included in Eqs. (53) and (54), can be considered negligible in comparison with the other terms. In this way, the dynamic equation of the mechanical part of the TRMS can be rewritten as:

$$\boldsymbol{M}\left(\boldsymbol{q}(t)\right)\ddot{\boldsymbol{q}}(t) + \boldsymbol{D}\left(\boldsymbol{q}(t), \dot{\boldsymbol{q}}(t)\right) = \boldsymbol{E}\left(\boldsymbol{q}(t)\right)\boldsymbol{\Omega}(t) \tag{58}$$

where the matrices $\boldsymbol{M}(\boldsymbol{q}(t))$, $\boldsymbol{E}(\boldsymbol{q}(t))$, and $\boldsymbol{\Omega}(t)$ were defined in the previous section and the new matrix $\boldsymbol{D}(\boldsymbol{q}(t), \dot{\boldsymbol{q}}(t)) = \left[D_\psi, D_\phi\right]^T$ is given by:

$$D_\psi = \frac{1}{2}\left(J_1 - J_2\right) S_{2\psi} \dot{\phi}^2 + g\left(l_{T_1} m_{T_1} C_\psi + l_{T_2} m_{T_2} S_\psi\right) + \left(f_{v_\psi}\dot{\psi} + f_{c_\psi} sgn\left(\dot{\psi}\right)\right) \tag{59}$$

$$D_\phi = -h\left(l_{T_1} m_{T_1} C_\psi + l_{T_2} m_{T_2} S_\psi\right)\dot{\psi}^2 + \left(\left(J_2 - J_1\right) S_{2\psi}\right)\dot{\phi}\dot{\psi} + \left(f_{v_\phi}\dot{\phi} + f_{c_\phi} sgn\left(\dot{\phi}\right)\right) + C_c\left(\phi - \phi_0\right) \tag{60}$$

The following nonlinear feedback control input vector, $\boldsymbol{\Omega}(t)$, is synthesised as a multivariable proportional-derivative (PD) controller with a cancellation term:

$$\boldsymbol{\Omega}(t) = \boldsymbol{E}^{-1}\left(\boldsymbol{q}(t)\right)\left[\boldsymbol{M}\left(\boldsymbol{q}(t)\right)\boldsymbol{\gamma}_{\boldsymbol{m}}(t) + \boldsymbol{D}\left(\boldsymbol{q}(t), \dot{\boldsymbol{q}}(t)\right)\right] \tag{61}$$

where $\boldsymbol{\gamma}_m(t) = \left[\gamma_\psi, \gamma_\phi\right]^T$ is given by the following expression:

$$\boldsymbol{\gamma}_{\boldsymbol{m}}(t) = \ddot{\boldsymbol{q}}(t) = \ddot{\boldsymbol{q}}^*(t) - \boldsymbol{K}_{\boldsymbol{D}}^{\boldsymbol{m}}\left(\dot{\boldsymbol{q}}(t) - \dot{\boldsymbol{q}}^*(t)\right) - \boldsymbol{K}_{\boldsymbol{P}}^{\boldsymbol{m}}\left(\boldsymbol{q}(t) - \boldsymbol{q}^*(t)\right) \tag{62}$$

in which $\boldsymbol{K}_{\boldsymbol{D}}^{\boldsymbol{m}}$ and $\boldsymbol{K}_{\boldsymbol{P}}^{\boldsymbol{m}} \in \mathbb{R}^{2\times 2}$ are the diagonal positive definite matrices that represent the design elements of a vector-valued classical PD controller. Thereby, for the mechanical part, the closed loop tracking error vector, $\boldsymbol{e}_{\boldsymbol{q}}(t) = \boldsymbol{q}(t) - \boldsymbol{q}^*(t)$, evolves governed by:

$$\ddot{\boldsymbol{e}}_{\boldsymbol{q}}(t) + \boldsymbol{K}_{\boldsymbol{D}}^{\boldsymbol{m}}\dot{\boldsymbol{e}}_{\boldsymbol{q}}(t) + \boldsymbol{K}_{\boldsymbol{P}}^{\boldsymbol{m}}\boldsymbol{e}_{\boldsymbol{q}}(t) = 0 \tag{63}$$

The controller design matrices $\boldsymbol{K}_{\boldsymbol{D}}^{\boldsymbol{m}}$ and $\boldsymbol{K}_{\boldsymbol{P}}^{\boldsymbol{m}}$ have been selected based in the philosophy used for the electrical controller. They must be selected to render closed-loop characteristic polynomial vectors into a Hurwitz polynomial vector with desirable roots. Finally, the necessary angular velocity vector values, $\boldsymbol{\omega}^*(t) = \left[\omega_m^*, \omega_t^*\right]^T$, are obtained from the input control vector, $\boldsymbol{\Omega}(t) = \left[\omega_m\left|\omega_m\right| \;\; \omega_t\left|\omega_t\right|\right]^T$, by performing the following operation:

$$\boldsymbol{\omega}^*\left(t\right) = \begin{bmatrix} \omega_m^* \\ \omega_t^* \end{bmatrix} = \begin{bmatrix} sgn\left(\omega_m\left|\omega_m\right|\right)\cdot\sqrt{\left|\omega_m\left|\omega_m\right|\right|} \\ sgn\left(\omega_t\left|\omega_t\right|\right)\cdot\sqrt{\left|\omega_t\left|\omega_t\right|\right|} \end{bmatrix} \tag{64}$$

4. Results

This section describes the numerical simulations carried out in the MATLAB®/Simulink® environment for the sake of verifying the efficiency of the proposed control approach in terms of quick convergence of the tracking errors to a small neighbourhood of zero, smooth transient

Nonlinear Cascade-Based Control for a Twin Rotor MIMO System 285
http://dx.doi.org/10.5772/64875

responses and low control effort. In the simulations, the desired reference trajectory for the pitch (ψ) and the yaw (ϕ) angles have been defined by the next expression:

$$\boldsymbol{q}^{*}(t)=\begin{bmatrix}\psi^{*}\\ \phi^{*}\end{bmatrix}=\begin{bmatrix}A_{0_\psi}+A_{1_\psi}\left(2\sin\left(\omega_{1_\psi}t\right)+\sin\left(\omega_{2_\psi}t\right)\right)\\ A_{1_\phi}\sin\left(\omega_{1_\phi}t\right)+A_{2_\phi}\left(\sin\left(\omega_{2_\phi}t\right)+\sin\left(\omega_{3_\phi}t\right)\right)\end{bmatrix} \tag{65}$$

where $\boldsymbol{q}^{*}(t)=[\psi^{*}(t),\phi^{*}(t)]^{T}$ is the reference trajectory vector of the generalised coordinates, and the values of the constants used in the above expressions are given by:

$$A_{0_\psi}=0.4\text{ rad};\quad A_{1_\psi}=0.1\text{ rad};\quad A_{1_\phi}=0.8\text{ rad};\quad A_{2_\phi}=0.3\text{ rad}; \tag{66}$$

$$\omega_{1_\psi}=0.0785\text{ rad/s};\quad \omega_{2_\psi}=0.0157\text{ rad/s}; \tag{67}$$

$$\omega_{1_\phi}=0.157\text{ rad/s};\quad \omega_{2_\phi}=0.0785\text{ rad/s};\quad \omega_{3_\phi}=0.0157\text{ rad/s}; \tag{68}$$

On the other hand, the values used in the simulation of the dynamic model of the TRMS, electrical parameters (main and tail rotors), mechanical parameters and dimensional parameters of the platform are detailed in **Tables 1–5**. The initial position of the TRMS has been defined as $\boldsymbol{q}_0(t)=\left[\psi_0,\phi_0\right]^{T}=[0,0]^{T}$ rad, representing a different value of the initial position than the reference trajectory vector. This choice of the starting position has been made to demonstrate the exponential convergence of the desired trajectories. With regard to the controller design parameters, it must be remarked that they have been selected to make the dynamics of the inner loop much faster than the outer loop dynamics, all this in order to ensure the functioning of the cascade controller [26]. The resulting values are as follows:

$$\boldsymbol{K}_{\boldsymbol{P}}^{\boldsymbol{e}}=diag(10.5,6.2); \tag{69}$$

$$\boldsymbol{K}_{\boldsymbol{D}}^{\boldsymbol{m}}=diag\left(8.20,3.85\right);\quad \boldsymbol{K}_{\boldsymbol{P}}^{\boldsymbol{m}}=diag(13.20,2.205); \tag{70}$$

Figures 6 and **7** show the performance of the proposed control scheme. **Figure 6** illustrates a comparative between the desired trajectory, $\boldsymbol{q}^{*}(t)=[\psi^{*}(t),\phi^{*}(t)]^{T}$, and the real trajectory of the TRMS, $\boldsymbol{q}(t)=[\psi(t),\phi(t)]^{T}$. The difference between these trajectories, or, in other words, the error vector of generalised coordinates, $\boldsymbol{e}_{\boldsymbol{q}}(t)=\boldsymbol{q}(t)-\boldsymbol{q}^{*}(t)=[\psi(t)-\psi^{*}(t),\phi(t)-\phi^{*}(t)]^{T}$, is represented in **Figure 7**. The exponential convergence of the desired trajectories is observed,

with the error bounded to a small neighbourhood to zero, and the robustness against large initial errors.

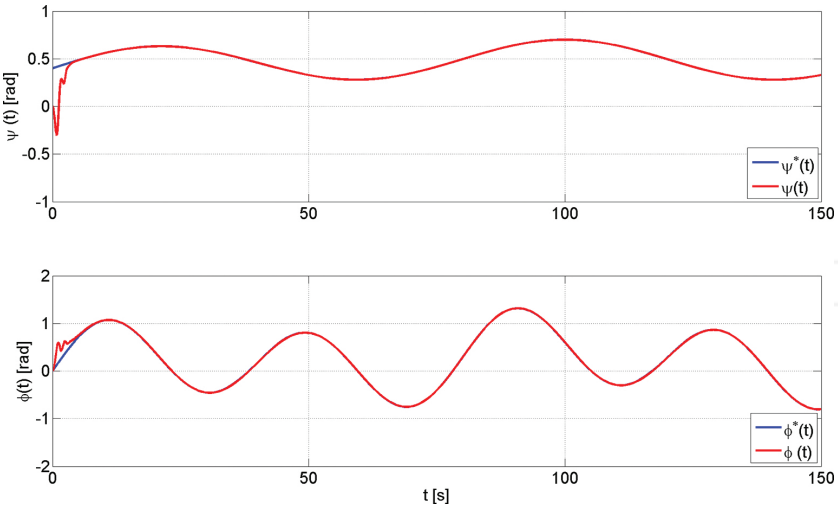

Figure 6. Real and desired evolution of the vector of generalised coordinates of the TRMS, $\boldsymbol{q}(t) = [\psi(t), \phi(t)]^T$.

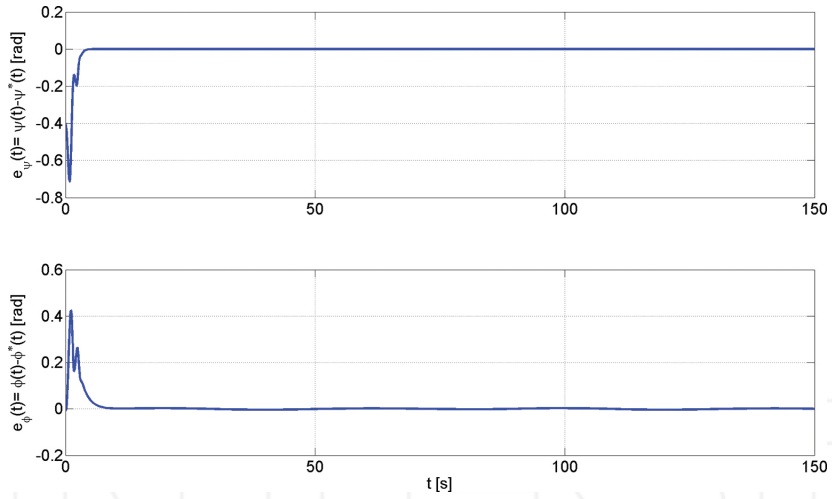

Figure 7. Evolution of the error vector of the generalised coordinates of the TRMS, $\boldsymbol{e_q}(t) = \boldsymbol{q}(t) - \boldsymbol{q}^*(t) = [\psi(t) - \psi^*(t), \phi(t) - \phi^*(t)]^T$.

Another graph that shows the excellent performance of the outer control loop is shown in **Figure 8**, where the auxiliary control input vector of the mechanical proportional-derivative (PD) controller (Eq. (62)) can be observed. This figure shows the quick convergence of the auxiliary control inputs of the mechanical controller to a small value of the origin in the

Nonlinear Cascade-Based Control for a Twin Rotor MIMO System 287
http://dx.doi.org/10.5772/64875

reference trajectory tracking vector error phase space, $\boldsymbol{e_q}(t)$, in a globally asymptotic exponential dominated manner.

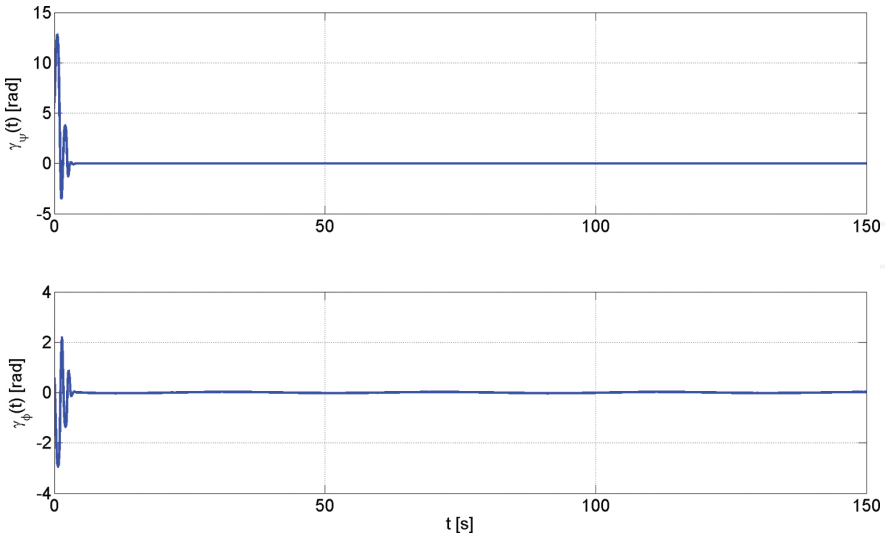

Figure 8. Evolution of the auxiliary control input vector of the mechanical multivariable PD controller, $\boldsymbol{\gamma}_m(t) = \left[\gamma_\psi(t), \gamma_\phi(t)\right]^T$.

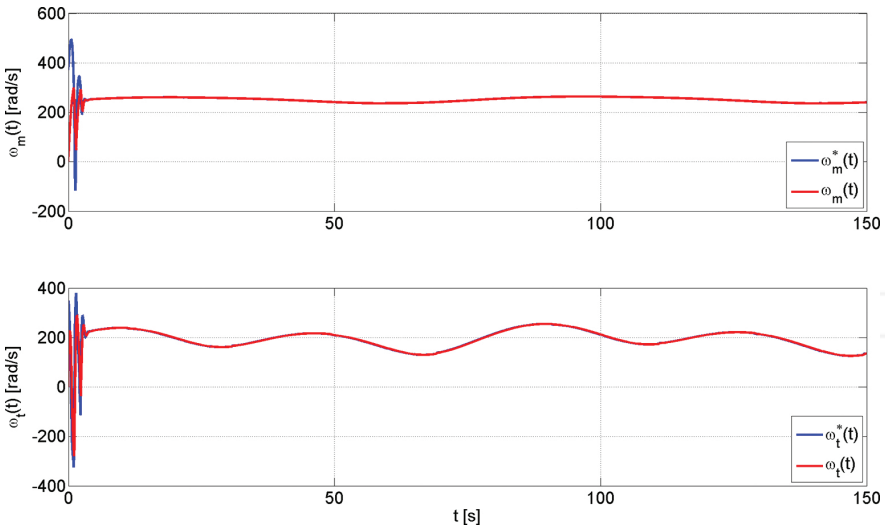

Figure 9. Real and desired evolution trajectories of the angular velocity vector, $\boldsymbol{\omega}^*(t) = \left[\omega_m^*(t),\ \omega_t^*(t)\right]^T$ and $\boldsymbol{\omega}(t) = \left[\omega_m(t),\ \omega_t(t)\right]^T$.

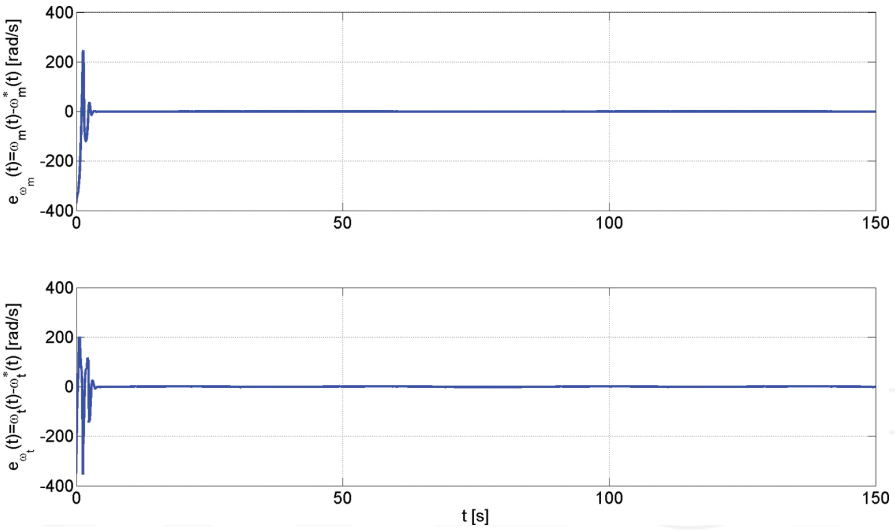

Figure 10. Evolution of the angular velocity error vector, $e_{\omega}(t) = \omega(t) - \omega^*(t) = [\omega_m(t) - \omega_m^*(t), \omega_t(t) - \omega_t^*(t)]\,T$.

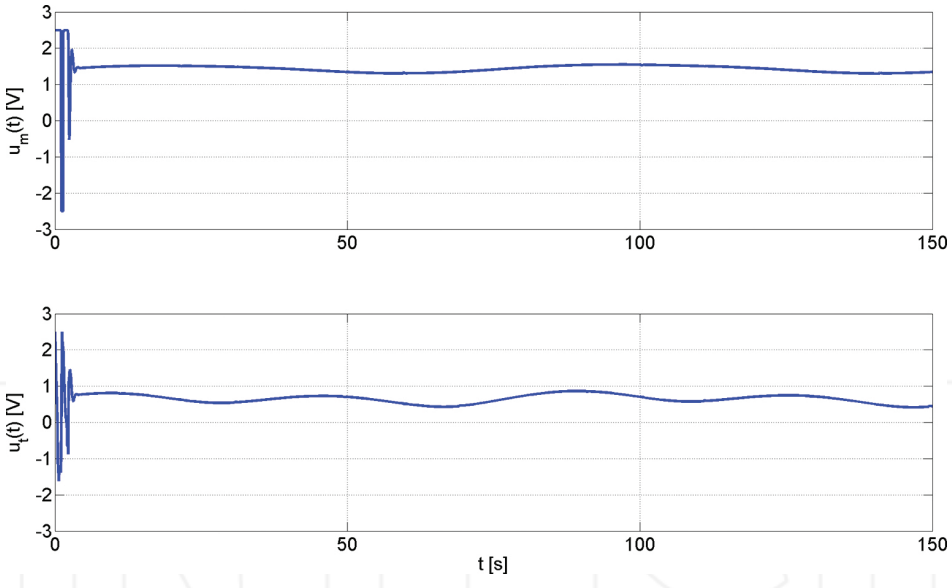

Figure 11. Evolution of the input voltage vector of the TRMS, $\boldsymbol{u}(t) = \left[u_m(t),\ u_t(t)\right]^T$.

On the other hand, the efficiency of the inner loop control (electrical controller) is depicted in **Figure 9**, including a comparative between the reference angular velocity vector, $\boldsymbol{\omega}^*(t) = \left[\omega_m^*(t), \omega_t^*(t)\right]^T$, obtained from the output of the outer loop, and the real magnitudes

http://dx.doi.org/10.5772/64875

of angular velocity vector, $\boldsymbol{\omega}(t) = \left[\omega_m(t), \omega_t(t)\right]^T$. The evolution of the angular velocity error vector, $\boldsymbol{e}_{\boldsymbol{\omega}}(t) = \boldsymbol{\omega}(t) - \boldsymbol{\omega}^*(t) = \left[\omega_m(t) - \omega_m^*(t), \omega_t(t) - \omega_t^*(t)\right]^T$, is also shown in **Figure 10**.

To conclude this section, the input voltages in the MATLAB®/Simulink® environment, $\boldsymbol{u}(t) = \left[u_m(t), u_t(t)\right]^T$, for the main and tail rotors, are represented in **Figure 11**. From these graphs, it can be observed that the proposed control scheme has been realised to avoid saturations on these voltages, which in the simulation MATLAB®/Simulink® environment have been set to ± 2.5 V (similarly to the real prototype platform).

5. Conclusions

In this research, a novel nonlinear cascade-based control has been developed for the TRMS platform. The performance of the controller shows very satisfactory results in terms of convergence of the tracking errors for the generalised coordinates of the TRMS to a small neighbourhood to zero, smooth transient responses, low control efforts and robustness against large initial errors and parametric uncertainties in the model. The proposed control is an important base for the subsequent design of novel robust control algorithms in UAV platforms, which interest is notably increasing in recent years thanks to their multiple possibilities and applications. This will be the topic of our future research.

Acknowledgements

This work has been partially supported by Spanish Ministerio de Economía y Competitividad/FEDER under TEC2016-80986-R, DPI2016-80894-R, TIN2013-47074-C2-1-R and DPI2014-53499-R grants. Lidia M. Belmonte holds an FPU Scholarship (FPU014/05283) from the Spanish Government.

Author details

Lidia María Belmonte[1], Rafael Morales[1*], Antonio Fernández-Caballero[1] and José Andrés Somolinos[2]

*Address all correspondence to: Rafael.Morales@uclm.es

1 University of Castilla-La Mancha, School of Industrial Engineering, Albacete, Spain

2 Polytechnic University of Madrid, School of Naval Engineering, Madrid, Spain

References

[1] Castillo P., Lozano R., Dzul A.E. Modelling and control of mini-flying machines. London: Springer; 2005. doi:10.1007/1-84628-179-2

[2] Raffo G.V., Ortega M.G., Rubio F.R. An integral predictive/nonlinear H_∞ control structure for a quadrotor helicopter. Automatica. 2010; 46(1):29–39. doi:10.1016/j.automatica.2009.10.018

[3] Cai G., Chen B.M., Dong X., Lee T.H. Design and implementation of a robust and nonlinear flight control system for an unmanned helicopter. Mechatronics. 2011; 21(5): 803–820. doi:10.1016/j.mechatronics.2011.02.002

[4] Fernández-Caballero A., Belmonte L.M., Morales R., Somolinos J.A. Generalized proportional integral control for an unmanned quadrotor system. International Journal of Advanced Robotic Systems. 2015; 12(85): 1–14. doi:10.5772/60833

[5] Feedback Co. Twin rotor MIMO system 33-220 user manual. 1998

[6] Mullhaupt P., Srinivasan B., Lévine J., Bonvin D. A toy more difficult to control than the real thing. In: Proceedings of the European Control Conference (ECC'97). Brussels, July 1997

[7] Ahmad S.M., Chipperfield A.J., Tokhi M.O. Parametric modelling and dynamic characterization of a two-degree-of-freedom twin-rotor multi-input multi-output system. Proceedings of the Institution of Mechanical Engineers Part G, Journal of Aerospace Engineering. 2001; 215(2):63–78. doi:10.1243/0954410011531772

[8] Ahmad S.M., Shaheed M.H., Chipperfield A.J., Tokhi M.O. Non-linear modelling of a one-degree-of-freedom twin-rotor multi-input multi-output system using radial basis function networks. Proceedings of the Institution of Mechanical Engineers Part G, Journal of Aerospace Engineering. 2002; 216(4):197–208.doi: 10.1243/09544100260369731

[9] Shaheed M.H. Feedforward neural network based non-linear dynamic modelling of a TRMS using RPROP algorithm. Aircraft Engineering and Aerospace Technology: An International Journal. 2005; 77(1):13–22. doi:10.1108/00022660510576000

[10] Rahideh A., Shaheed M.H. Mathematical dynamic modelling of a twin-rotor multiple input-multiple output system. Proceedings of the Institution of Mechanical Engineers Part I, Journal of Systems and Control Engineering. 2007; 221(1): 89–101. doi: 10.1243/09596518JSCE292

[11] Rahideh A., Shaheed M.H., Huijberts H.J.C Dynamic modelling of a TRMS using analytical and empirical approaches. Control Engineering Practice. 2008; 16(3): 241–259. doi:10.1016/j.conengprac.2007.04.008

[12] Toha S.F., Tokhi M.O. ANFIS modelling of a twin rotor system using particle swarm optimisation and RLS. In: Cybernetic Intelligent Systems (CIS), 2010 IEEE 9th International Conference on; 1–2 Sept. 2010. IEEE. doi:10.1109/UKRICIS.2010.5898130

[13] Tastemirov A., Lecchini-Visintini A., Morales R.M. Complete dynamic model of a twin rotor MIMO System (TRMS) with experimental validation. In: 39th European Rotorcraft Forum 2013 (ERF 2013); 3–6 Sept. 2013. Moscow, Russia. ISBN: 978-1-5108-1007-5

[14] Ahmad S.M., Chipperfield A.J., Tokhi M.O. Dynamic modelling and open-loop control of a twin rotor multi-input multi-output system. Proceedings of the Institution of Mechanical Engineers Part I, Journal of Systems and Control Engineering. 2002; 216(6): 477–496. doi:10.1177/095965180221600604

[15] Ahmad S.M., Chipperfield A.J., Tokhi M.O. Dynamic modelling and linear quadratic Gaussian control of a twin-rotor multi-input multi-output system. Proceedings of the Institution of Mechanical Engineers Part I, Journal of Systems and Control Engineering. 2003; 217(3):203–227. doi:10.1177/095965180321700304

[16] López-Martínez M., Rubio F.R. Longitudinal control for a laboratory helicopter via constructive approximate backstepping. IFAC Proceedings Volumes. 2005; 38(1):289–294. doi:10.3182/20050703-6-CZ-1902.00448

[17] López-Martínez M., Ortega M.G., Vivas C., Rubio F.R. Nonlinear L_2 control of a laboratory helicopter with variable speed rotors. Automatica. 2007; 43(4): 655–661. doi: 10.1016/j.automatica.2006.10.013

[18] Rahideh A., Bajodah A.H., Shaheed M.H. Real time adaptive nonlinear model inversion control of a twin rotor MIMO system using neural networks. Engineering Applications of Artificial Intelligence. 2012; 25(6):1289–1297. doi:10.1016/j.engappai.2011.12.006

[19] Tao C.W., Taur J.S., Chen Y.C. Design of a parallel distributed fuzzy LQR controller for the twin rotor multi-input multi-output system. Fuzzy Sets and Systems. 2010; 161(15): 2081–2103. doi:10.1016/j.fss.2009.12.007

[20] Reynoso-Meza, G., Garcia-Nieto S., Sanchis J., Blasco, F.X. Controller tuning by means of multi-objective optimization algorithms: a global tuning framework. IEEE Transactions on Control Systems Technology. 2013; 21(2): 445–458. doi:10.1109/TCST.2012.2185698

[21] Coelho J., Matos R., Lebres C., Santos V., Fonseca N.M., Solteiro E.J., Tenreiro J.A. Application of fractional algorithms in the control of a twin rotor multiple input-multiple output system. In: 6th European Nonlinear Dynamics Conference (ENOC 2008). June 30–July 4, 2008. Saint Petersburg, Russia

[22] Christensen R., Fogh N., Hansen R.H., Jensen M.S., Larse S., Paramanathan A. Modelling and control of a twin-rotor MIMO system. Technical report, Aalborg University, Denmark; 2006

[23] Ekbote A.K., Srinivasan N.S., Mahindrakar A.D. Terminal sliding mode control of a twin rotor multiple-input multiple-output system. IFAC Proceedings Volumes. 2011; 44(1):10952–10957. doi:10.3182/20110828-6-IT-1002.00645

[24] Rotondo D., Nejjari F., Puig V. Quasi-LPV modeling, identification and control of a twin rotor MIMO system. Control Engineering Practice. 2013; 21(6): 829–846. doi:10.1016/j.conengprac.2013.02.004

[25] Feedback Co. Twin Rotor MIMO system. Advanced Teaching Manual 1. Manual: 33-007-4M5 Ed01. 1998

[26] Son Y.I., Kim I.H., Choi D.S., Shim D. Robust cascade control of electric motor drives using dual reduced-order PI observer. IEEE Transactions on Industrial Electronics. 2015; 62(6): 3672–3682. doi:10.1109/TIE.2014.2374571

INTECH

2.2.3 Robust Linear Longitudinal Feedback Control of a Flapping Wing Micro Air Vehicle

Publication Data

ABSTRACT:
This paper falls under the idea of introducing biomimetic miniature air vehicles in ambient assisted living and home health applications. The concepts of active disturbance rejection control and flatness based control are used in this paper for the trajectory tracking tasks in the flapping-wing miniature air vehicle (FWMAV) time-averaged model. The generalized proportional integral (GPI) observers are used to obtain accurate estimations of the flat output associated phase variables and of the time-varying disturbance signals. This information is used in the proposed feedback controller in (a) approximate, yet close, cancelations, as lumped unstructured time-varying terms, of the influence of the highly coupled nonlinearities and (b) the devising of proper linear output feedback control laws based on the approximate estimates of the string of phase variables associated with the flat outputs simultaneously provided by the disturbance observers. Numerical simulations are provided to illustrate the effectiveness of the proposed approach.

CITATION:
L.M. Belmonte; R. Morales; A. Fernández-Caballero; J.A. Somolinos. "Robust Linear Longitudinal Feedback Control of a Flapping Wing Micro Air Vehicle". *Artificial Computation in Biology and Medicine*. IWINAC 2015, LNCS, vol. 9107, 449–458. Springer, 2015. ISBN 978-3-319-18914-7. DOI:10.1007/978-3-319-18914-7_47.

Reprinted by permission from Springer Nature: Springer, Artificial Computation in Biology and Medicine. IWINAC 2015. Lecture Notes in Computer Science, by J. Ferrández Vicente, J. Álvarez-Sánchez, F. de la Paz López, F. Toledo-Moreo, H. Adeli (eds), Copyright 2015.
License Number: 4574850412156. License Date: Apr 23, 2019.

Robust Linear Longitudinal Feedback Control of a Flapping Wing Micro Air Vehicle

Lidia María Belmonte[1], R. Morales[1], Antonio Fernández-Caballero[1(✉)], and José A. Somolinos[2]

[1] Escuela de Ingenieros Industriales, Universidad de Castilla-La Mancha, 02071-Albacete, Spain
antonio.fdez@uclm.es

[2] Escuela Técnica Superior de Ingenieros Navales, Universidad Politécnica de Madrid, 28040-Madrid, Spain

Abstract. This paper falls under the idea of introducing biomimetic miniature air vehicles in ambient assisted living and home health applications. The concepts of active disturbance rejection control and flatness based control are used in this paper for the trajectory tracking tasks in the flapping-wing miniature air vehicle (FWMAV) time-averaged model. The generalized proportional integral (GPI) observers are used to obtain accurate estimations of the flat output associated phase variables and of the time-varying disturbance signals. This information is used in the proposed feedback controller in (a) approximate, yet close, cancelations, as lumped unstructured time-varying terms, of the influence of the highly coupled nonlinearities and (b) the devising of proper linear output feedback control laws based on the approximate estimates of the string of phase variables associated with the flat outputs simultaneously provided by the disturbance observers. Numerical simulations are provided to illustrate the effectiveness of the proposed approach.

1 Introduction

The creation of flapping wing micro air vehicles (FWMAV) is a challenging problem. The potential benefits for insect-like flapping wing micro air vehicles are numerous [1]. The hovering ability of insects, coupled with the ability for a quick transition to forward flight, provide an ideal indoor/outdoor reconnaissance platform for search and rescue, reconnaissance and surveillance and ambient assisted living and home health, among others [2]-[8]. Indeed, this paper falls within a project called "Improvement of the Elderly Quality of Life and Care through Smart Emotion Regulation". The long-term objective of the project is to find solutions for improving the quality of life and care of ageing adults at home by using emotion detection and regulation techniques. We believe that miniature air vehicles at home settings are capable of including some sensors that capture the mood of the ageing adults.

Different control methods have been found in the literature. Deng *et al.* developed in [9] a nominal state-space linear time-invariant model in hover through

© Springer International Publishing Switzerland 2015
J.M. Ferrández Vicente et al. (Eds.): IWINAC 2015, Part I, LNCS 9107, pp. 449–458, 2015.
DOI: 10.1007/978-3-319-18914-7_47

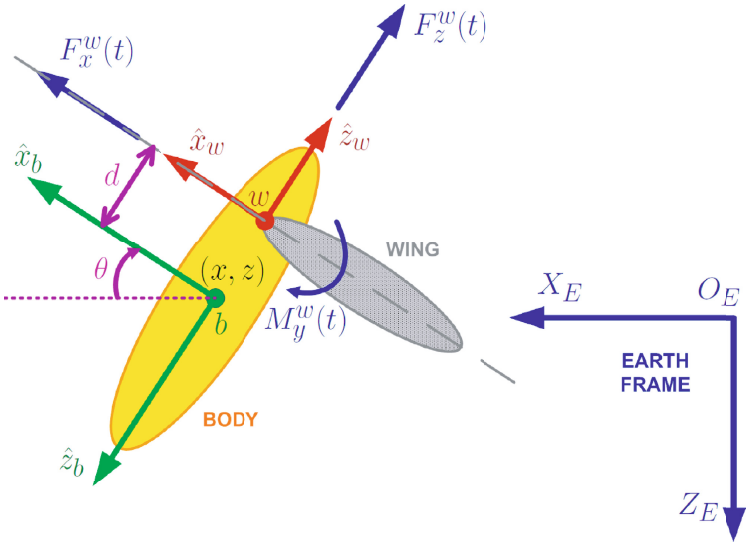

Fig. 1. Coordinate systems and longitudinal motion of FWMAV with respect to the earth frame

linear estimation. Also, a LQG controller was designed and compared with a PD controller. A state feedback attitude controller control scheme using the sensor output as feedback was designed by Schenato *et al.* [10]. Campolo *et al.* realized in [11] a geometric approach to robust attitude estimation, derived from multiple and possibly redundant bio-inspired navigation sensors, for attitude stabilization of a micromechanical flying insect.

The use of time-averaging theory has been used within the control of FWMAV because it helps to simplify the complex aerodynamics associated to the flapping wings [12]-[13] because the aerodynamic forces and torques, generated by the wings, affect the behavior of the FWMAV only by their mean values since the dynamics of the body are much slower than the flapping wings ones. Deng *et al.* provided a methodology to approximate the time-varying body dynamics caused by the aerodynamic forces with time-invariant dynamics using averaging theory and a biomimetic parametrization of wing trajectories [14]. Also, a Linear Quadratic Gaussian (LQG) controller was designed which does not require the knowledge of an accurate model for the insect morphological parameters, such as moment of inertia and mechanical part's sizes, nor an accurate model of the aerodynamics. Rifaï *et al.* developed in [15] a bounded state feedback control of the forces and torques and takes into account the saturation of the actuators driving the flapping wings and Khan *et al.* realized in [16] a differential flatness based non-linear controller based on the time-averaging theory for the control of the longitudinal dynamics of FWMAV.

Taking into consideration the highly nonlinear nature of the FWMAV, active disturbance rejection control (ADRC) appears as an excellent methodology for the control of uncertain linear and nonlinear systems (see the work of Han [17] for the initial theoretical aspects of this new area of research). The objective of ADRC stems in the accurate estimation of the unknown part of the controlled system dy-

namics and proceed to cancel its effects in the feedback control law. Gao and its coworkers have proposed new advances in controllers, including practical applications, in a similar manner to that of Han [18], [19].On the other hand, Sira-Ramírez and its coworkers have contribute to the area emphasizing the use of *generalized proportional integral (GPI) observers* [20]-[22].

In this line of action, in this article, we propose a robust observer-based linear output feedback control scheme for the trajectory tracking tasks in the flapping-wing miniature air vehicle time-averaged model. The linear observer-based controller design approach rests on using highly simplified models of the inputs differential parameterizations, provided by the flatness property. Within the simplification task proposed, only the order of integration of the subsystems and the control inputs, along with their associated matrix gains, are retained in full detail. All the additive nonlinearities, including their state couplings and complexities, are regarded as, unstructured, time-varying signals that need to be online estimated, and canceled, at the controller specification within an Active Disturbance Rejection Control Scheme. After input gain matrix cancelation, the resulting system consists of pure integration (linear) perturbed systems with time-varying additive disturbances. A set of linear extended observers, here denominated as *GPI observers*, are capable of accurate on-line estimations of: (1) the output related phase variables; (2) the, state dependent, additive perturbation input signal itself; and (3) the estimation of a certain number of the perturbation input time derivatives. This last feature facilitates the task of perturbation input prediction as GPI observers are the most naturally applicable to the control of perturbed differentially flat nonlinear systems [23]-[25].

The remainder of the article is structured as follows: Section 2 presents the flapping-wing miniature air vehicle time-averaged model and its flatness property. Additionally, this section proposes a simplified model of the system and formulates the problem to be solved. Section 3 describes the active disturbance rejection controller design and the results are applied for the stabilization and trajectory tracking problem of the time-averaged model for the flapping-wing miniature air vehicle. Section 4 presents the obtained simulation results and, finally, Section 5 is devoted for the conclusions of this study and future works.

2 Problem Formulation and Its Flatness Property

2.1 System Dynamics

Consider the following time-averaged model for the flapping-wing miniature air vehicle (FWMAV) based on Newtonian approach derived in [16]:

$$\dot{x} = v_x C_\theta + v_z S_\theta \tag{1}$$

$$\dot{z} = -v_x S_\theta + v_z C_\theta \tag{2}$$

$$\dot{\theta} = \omega \tag{3}$$

$$\dot{v}_x = -g S_\theta - \omega v_z + F_x \tag{4}$$

$$\dot{v}_z = -g C_\theta + \omega v_x - F_z \tag{5}$$

$$\dot{\omega} = -\frac{F_x}{E} \tag{6}$$

where $S_\theta = \sin\theta, C_\theta = \cos\theta$, g is the gravity acceleration, (x, z) are the coordinates of the center of mass in the earth frame, θ represents the pitch angle, (v_x, v_z) express the velocity of the body of the FWMAV in the body frame and ω is the angular velocity of the body and (F_x, F_z) represent the aerodynamic forces. The constant $E = \frac{I_b}{md}$, being I_b the moment of inertia of the body about the y axis of the body frame, m is the mass and d denotes the distance from the axis of oscillation to the center of mass of the body. Fig. 1 shows the coordinate systems and longitudinal motion of the FWMAV with regard to the earth frame.

2.2 Flatness of the System

According to the theory of differential flatness [21], a dynamic system, $\dot{\mathbf{x}} = \mathbf{f}(\mathbf{x}, \mathbf{u})$, with $\mathbf{x} \in \mathbb{R}^n$ and $\mathbf{u} \in \mathbb{R}^m$, is said to be differentially flat if there exist, m, differentially independent variables called *flat outputs* (differentially independent meaning that they are not related by differential equations), which are functions of the state vector and, possibly, of a finite number of time derivatives of the state vector (i.e., derivatives of the inputs may be involved in their definition), such that *all* system variables (states, inputs, outputs, and functions of these variables) can, in turn, be expressed as functions of the flat outputs and of a finite number of their time derivatives. This parameterization establishes a one-to-one mapping from the states and the inputs to the flat outputs.

The proposed system is differentially flat with flat outputs given by the coordinates of the *Huygens center of oscillation* [22] given by:

$$F = x + ES_\theta, \quad L = z + EC_\theta \tag{7}$$

Proposition 1. *The flapping-wing miniature air vehicle given in (1)-(6) is differentially flat, with flat outputs given by F and L, i.e., all system variables in (1)-(6) can be differentially parameterized solely in terms of F, L, and a finite number of their time derivatives.*

Proof. If the equations given in (7) are differentiated with regard to time, we obtain the first and second derivatives of the flat outputs:

$$\dot{F} = \dot{x} + E\omega C_\theta = v_x C_\theta + v_z S_\theta + E\omega C_\theta \tag{8}$$

$$\dot{L} = \dot{z} - E\omega S_\theta = -v_x S_\theta + v_z C_\theta - E\omega S_\theta \tag{9}$$

$$\ddot{F} = \xi S_\theta \tag{10}$$

$$\ddot{L} = g + \xi C_\theta \tag{11}$$

where $\xi = -\left(F_z - E\omega^2\right)$ is defined as a new virtual input vector. Upon operating with (10) and (11) we achieve:

$$\xi = \sqrt{\ddot{F}^2 + \left(\ddot{L} - g\right)^2}; \quad \theta = \arctan\left(\frac{\ddot{F}}{\ddot{L} - g}\right) \tag{12}$$

$$S_\theta = \frac{\ddot{F}}{\sqrt{\ddot{F}^2 + \left(\ddot{L} - g\right)^2}}; \quad C_\theta = \frac{\ddot{L} - g}{\sqrt{\ddot{F}^2 + \left(\ddot{L} - g\right)^2}} \tag{13}$$

If the expressions (10) and (11) are differentiated with regard to time, it is obtained

$$F^{(3)} = \dot{\xi}S_\theta + \xi\omega C_\theta; \quad L^{(3)} = \dot{\xi}C_\theta - \xi\omega S_\theta \tag{14}$$

Rearranging terms in (14) yields

$$\dot{\xi} = \frac{\ddot{F}F^{(3)} + \left(\ddot{L} - g\right)L^{(3)}}{\sqrt{\ddot{F}^2 + \left(\ddot{L} - g\right)^2}}; \quad \omega = \dot{\theta} = \frac{F^{(3)}\left(\ddot{L} - g\right) - L^{(3)}\ddot{F}}{\ddot{F}^2 + \left(\ddot{L} - g\right)^2} \tag{15}$$

Now, operating with (4) and (5) one obtains

$$v_x = \dot{x}C_\theta - \dot{z}S_\theta = \dot{F}C_\theta - \dot{L}S_\theta - E\omega \tag{16}$$

$$v_z = \dot{x}S_\theta + \dot{z}C_\theta = \dot{F}S_\theta + \dot{L}C_\theta \tag{17}$$

Combining (16) and (17) with (13) and (15), we conclude that v_x and v_z are also functions of $(\dot{F}, \dot{L}, \ddot{F}, \ddot{L}, F^{(3)}, L^{(3)})$. On the other hand, differentiating expressions (14) with regard to time and rearranging terms

$$F^{(4)} = S_\theta\ddot{\xi} - \frac{\xi C_\theta}{E}F_x - \omega^2\xi S_\theta + 2\dot{\xi}\omega C_\theta \tag{18}$$

$$L^{(4)} = C_\theta\ddot{\xi} + \frac{\xi S_\theta}{E}F_x - \omega^2\xi C_\theta - 2\dot{\xi}\omega S_\theta \tag{19}$$

Similarly, upon operating with (18), it is achieved

$$\ddot{\xi} = S_\theta F^{(4)} + C_\theta L^{(4)} + \omega^2\xi \tag{20}$$

$$F_x = \frac{-EC_\theta}{\xi}F^{(4)} + \frac{ES_\theta}{\xi}L^{(4)} + 2\frac{E\omega\dot{\xi}}{\xi} \tag{21}$$

Finally, substituting (12), (13) and (15) into (20) shows that all the system variables can be expressed as a function of (F, L) and their derivatives, proving that the flat output vector composed by (F, L) constitute a flat output vector for system (1)-(6).

2.3 Simplified Model and Problem Formulation

On the basis of (20), we adopt the following simplified perturbed model for the underlying FWMAV (18):

$$\begin{bmatrix} F^{(4)} \\ L^{(4)} \end{bmatrix} = \underbrace{\begin{bmatrix} S_\theta & -\frac{\xi C_\theta}{E} \\ C_\theta & \frac{\xi S_\theta}{E} \end{bmatrix}}_{\mathcal{N}(\theta,\xi)} \begin{bmatrix} \ddot{\xi} \\ F_x \end{bmatrix} + \underbrace{\begin{bmatrix} \varphi_F \\ \varphi_L \end{bmatrix}}_{\boldsymbol{\varphi}(t)} \tag{22}$$

where $\boldsymbol{\varphi}(t) = [\varphi_F, \varphi_L]^T$ involves state dependent expressions, the possibly unmodeled dynamics and external unknown disturbances affecting the system. We lump

all these uncertain terms into an unknown but uniformly absolutely bounded disturbance input that needs to be on-line estimated by means of an observer and, subsequently, canceled from the simplified system dynamics via feedback in order to regulate the flat output vector, $[F, L]^T$, towards the desired reference trajectories $[F^*, L^*]^T$. Finally,the formulation of the problem is stated as follows: *Given a desired flat output vector of reference trajectories* $[F^*, L^*]^T$*, devise a linear multi-input output feedback controller for system (22) such that the flat output vector* $[F, L]^T$ *is forced to track the given reference flat output vector* $[F^*, L^*]^T$*. This objective must be achieved even in the presence of unknown disturbances and coupling nonlinearities, represented by* $[\varphi_F, \varphi_L]^T$.

3 GPI Observer-Based Active Disturbance Rejection Controller

A GPI observer including a reasonable, self-updating, time-polynomial model is considered for each unknown component disturbance input vector $\boldsymbol{\varphi}(t)$. For this internal model, we use for each component of $\boldsymbol{\varphi}(t)$ an unspecified element of a fifth order family of time-polynomials, denoted by $\boldsymbol{\varphi}_1^{(6)}(t) = [\varphi_{1F}^{(6)}, \varphi_{1L}^{(6)}]^T = \mathbf{0}$. The GPI observer based flat output feedback controller is devised as follows:

$$\begin{bmatrix} \dot{\xi} \\ F_x \end{bmatrix} = \underbrace{\begin{bmatrix} S_{\hat{\theta}_s} & C_{\hat{\theta}_s} \\ -\frac{EC_{\hat{\theta}_s}}{\hat{x}i_s} & \frac{ES_{\hat{\theta}_s}}{\hat{x}i_s} \end{bmatrix}}_{\mathcal{N}^{-1}(\theta,\xi)} \begin{bmatrix} \nu_F \\ \nu_L \end{bmatrix} \tag{23}$$

with

$$\begin{aligned} \nu_F &= -\hat{\varphi}_{1Fs} + [F^*(t)]^{(4)} - \sum_{i=0}^{3} k_i^F \left(\hat{F}_s^{(i)} - [F^*]^{(i)} \right) \\ \nu_L &= -\hat{\varphi}_{1Ls} + [L^*(t)]^{(4)} - \sum_{i=0}^{3} k_i^L \left(\hat{L}_s^{(i)} - [L^*]^{(i)} \right) \end{aligned} \tag{24}$$

where the quantities with subindex s are smoothing observer variables which are carried out by means of the following *clutching function*, avoiding possible large peaks in their high gain induced responses:

$$s_f(t) = \begin{cases} 1 \text{ for } t > \varepsilon \\ \sin^8\left(\frac{\pi t}{2\varepsilon}\right) \text{ for } t \leq \varepsilon \end{cases} \tag{25}$$

with $\epsilon = 2\,[s]$. The design coefficients k_i^F and k_i^L, $i = 0, 1, 2, 3$, are chosen so that the dominant characteristic polynomials are 4th-degree Hurwitz polynomials, i.e.,

$$\begin{aligned} p_F(s) &= s^4 + k_3^F s^3 + k_2^F s^2 + k_1^F s + k_0^F \in \text{Hurwitz}_4(s) \\ p_L(s) &= s^4 + k_3^L s^3 + k_2^L s^2 + k_1^L s + k_0^L \in \text{Hurwitz}_4(s) \end{aligned} \tag{26}$$

render an asymptotically, exponentially convergence of the flat output error vector, $[e_F, e_L]^T = [F - F^*, L - L^*]^T$, towards a small vicinity of the origin of the

tracking error phase space. Furthermore, the variables $\hat{F}^{(j)} = F_j$ and $\hat{L}^{(j)} = L_j$, $j = 0, 1, \ldots, 3$ are generated by:

$$\begin{aligned}
\dot{F}_0 &= F_1 + \lambda_8^F (F - F_0) \\
\dot{F}_1 &= F_2 + \lambda_7^F (F - F_0) \\
\dot{F}_2 &= F_3 + \lambda_6^F (F - F_0) \\
\dot{F}_3 &= S_\theta \ddot{\xi} - \frac{\xi C_\theta}{E} F_x + \varphi_{1F} + \lambda_5^F (F - F_0) \\
\dot{\varphi}_{1F} &= \varphi_{2F} + \lambda_4^F (F - F_0) \\
\dot{\varphi}_{2F} &= \varphi_{3F} + \lambda_3^F (F - F_0) \\
\dot{\varphi}_{3F} &= \varphi_{4F} + \lambda_2^F (F - F_0) \\
\dot{\varphi}_{4F} &= \varphi_{5F} + \lambda_1^F (F - F_0) \\
\dot{\varphi}_{5F} &= \lambda_0^F (F - F_0)
\end{aligned} \tag{27}$$

$$\begin{aligned}
\dot{L}_0 &= L_1 + \lambda_8^L (L - L_0) \\
\dot{L}_1 &= L_2 + \lambda_7^L (L - L_0) \\
\dot{L}_2 &= L_3 + \lambda_6^L (L - L_0) \\
\dot{L}_3 &= C_\theta \ddot{\xi} + \frac{\xi S_\theta}{E} F_x + \varphi_{1L} + \lambda_5^L (L - L_0) \\
\dot{\varphi}_{1L} &= \varphi_{2L} + \lambda_4^L (L - L_0) \\
\dot{\varphi}_{2L} &= \varphi_{3L} + \lambda_3^L (L - L_0) \\
\dot{\varphi}_{3L} &= \varphi_{4L} + \lambda_2^L (L - L_0) \\
\dot{\varphi}_{4L} &= \varphi_{5L} + \lambda_1^L (L - L_0) \\
\dot{\varphi}_{5L} &= \lambda_0^L (L - L_0)
\end{aligned} \tag{28}$$

where the design coefficients λ_i^F and λ_i^L, $i = 0, 1, \ldots, 8$, are chosen so that the reconstruction error dynamics dominant characteristic polynomials are 9th-degree Hurwitz polynomials, i.e.,

$$\begin{aligned}
p_{Fo}(s) &= s^9 + \lambda_8^F s^8 + \lambda_7^F s^7 + \ldots + \lambda_1^F s + \lambda_0^F \in \text{Hurwitz}_9(s) \\
p_{Lo}(s) &= s^9 + \lambda_8^L s^8 + \lambda_7^L s^7 + \ldots + \lambda_1^L s + \lambda_0^L \in \text{Hurwitz}_9(s)
\end{aligned} \tag{29}$$

and their roots are located sufficiently far from the imaginary axis, in the left half of the complex plane, then the trajectories of the flat output estimation error vector, $[\tilde{e}_F, \tilde{e}_L]^T = [F - F_0, L - L_0]^T$, and of its time derivatives, will converge to a small neighborhood of the origin of the phase space of the observer estimation error. The further away the roots are located in the left half of the complex plane, the smaller the radius of the disk representing the neighborhood around the origin of the estimation error phase space will be.

4 Numerical Simulations

Numerical simulations were carried out in order to verify the efficiency of the proposed approach in terms of quick convergence of the tracking errors to a small neighborhood of zero and smooth transient responses. The system parameters are: $m = 2.5 \cdot 10^{-3}\,[kg]$ and $I_b = 8.125 \cdot 10^{-7}\,[kg\,m^2]$.The flat output vector $[F, L]^T$ has been designed to track the following reference trajectories:

$$F^* = R \sin(At) + E \sin(\alpha(t)) \tag{30}$$

$$L^* = R\,[\cos(At) - 1] - z_0 + E \cos(\alpha(t)) \tag{31}$$

where $R = 7\,[m]$, $z_0 = 0.5\,[m]$, $A = 2\pi/30\,[rad/s]$ and $\alpha(t) = B_1 \sin(B_2 t)$ being $B_1 = \pi/180\,[rad]$ and $B_2 = 2\pi/30\,[rad/s]$.

The time sampling used in all the simulations is $T = 0.001\,[s]$. The observer gains, $\{\lambda_8^F, \ldots, \lambda_0^F\}$ and $\{\lambda_8^L, \ldots, \lambda_0^L\}$ were selected by identifying, term by term, the coefficients of the polynomials given in expression (29) with those of a desired Hurwitz polynomial given by $p_{obs}(s) = \left(s^2 + 2\zeta_o\omega_{no}s + \omega_{no}^2\right)^4 \cdot (s + p_o)$, with $\omega_{no} = 15, \zeta_o = 1.5$ and $p_o = 15$. On the other hand, the controller gains, $\{k_3^F, \ldots, k_0^F\}$ and $\{k_3^L, \ldots, k_0^L\}$, governing the dominant dynamics, were set by identifying, term by term, the coefficients of the polynomials given in expression (26) with the Hurwitz polynomial $p_{cont}(s) = \left(s^2 + 2\zeta_c\omega_{nc}s + \omega_{nc}^2\right)^2$, with $\omega_{nc} = 2, \zeta_c = 1$. Fig. 4a and Fig. 4b illustrate the path tracking and the closed loop trajectories for the coordinates of the center of mass (x, z) in the earth frame showing that the system follows the desired trajectory in an accurate manner. On the other hand, Fig. 4c

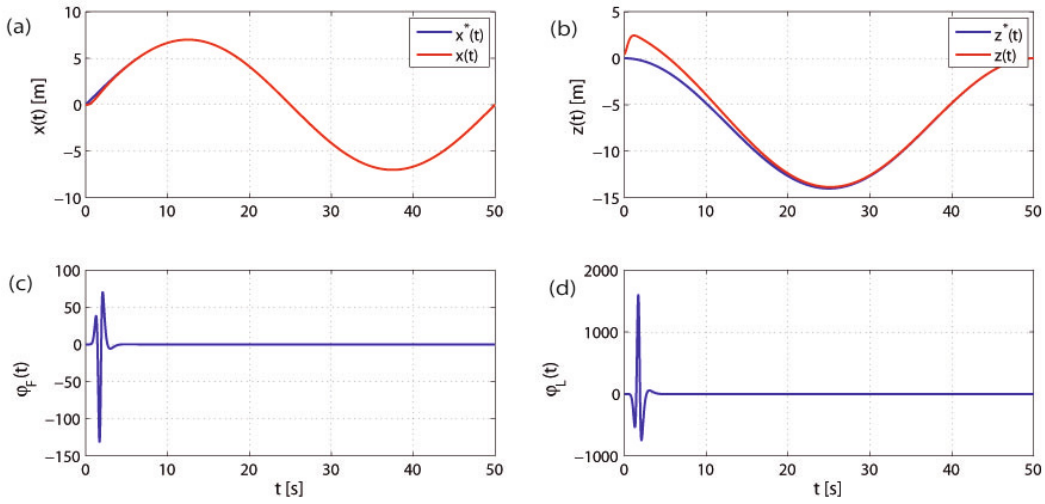

Fig. 2. Evolution of: (a) Coordinate x of the center of mass in the earth frame; (b) Coordinate z of the center of mass in the earth frame; (c) State-dependent estimated disturbance φ_F and; (d) State-dependent estimated disturbance φ_L

and Fig. 4d depict the evolution of the GPI observer state dependent disturbance estimation.

5 Conclusions and Future Work

This paper is related to the introduction of biomimetic miniature air vehicles in ambient assisted living and home health applications. Indeed, the proposal described falls within the complete project "Improvement of the Elderly Quality of Life and Care through Smart Emotion Regulation". The long-term objective of the project is to find solutions for improving the quality of life and care of the elderly who can or wants to continue living at home by using emotion detection and regulation techniques. We believe that miniature air vehicles at home settings can carry some fundamental sensors to capture the mood of the ageing adult.

In this way, this particular work has explored, within the context of the trajectory tracking problem, the use of approximate, yet accurate, total active disturbance rejection schemes, based on linear GPI observers, for the flapping-wing miniature air vehicle time-averaged model. Numerical simulations were provided where the efficiency of the proposed control method is assessed. Finally, in future work, we try to extend this control scheme to the full 6 DOF flight dynamics.

Acknowledgments. This work was partially supported by Spanish Ministerio de Economía y Competitividad / FEDER under TIN2013-47074-C2-1-R grant.

References

1. Ellington, C.P.: The novel aerodynamics of insect flight: Applications to microair vehicles. The Journal of Experimental Biology 202, 3439–3448 (1999)
2. de Clerq, K.M.E., de Kat, R., Remes, B., van Oudheusden, B.W., Bijl, H.: Aerodynamic experiments on delfly ii: unsteady lift enhancement. In: Proceedings of the 2009 European Micro-air Vehicle Conference and Competition 2009, pp. 255–262 (2009)
3. Conn, A., Burgess, S., Hyde, R., Ling, C.S.: From natural flyers to the mechanical realization of a flapping wing micro air vehicle. In: Proceedings of the 2006 IEEE International Conference on Robotics and Biomimetics, pp. 439–444 (2006)
4. Fenelon, M.A.A.: Biomimetic flapping wing aerial vehicle. In: Proceedings of the 2008 IEEE International Conference on Robotics and Biomimetics, pp. 1053–1058 (2009)
5. Fernández-Caballero, A., Latorre, J.M., Pastor, J.M., Fernández-Sotos, A.: Improvement of the elderly quality of life and care through smart emotion regulation. In: Pecchia, L., Chen, L.L., Nugent, C., Bravo, J. (eds.) IWAAL 2014. LNCS, vol. 8868, pp. 348–355. Springer, Heidelberg (2014)
6. Castillo, J.C., Carneiro, D., Serrano-Cuerda, J., Novais, P., Fernández-Caballero, A., Neves, J.: A multi-modal approach for activity classification and fall detection. International Journal of Systems Science 45, 810–824 (2014)
7. Carneiro, D., Castillo, J.C., Novais, P., Fernández-Caballero, A., Neves, J.: Multimodal behavioral analysis for non-invasive stress detection. Expert Systems with Applications 39, 13376–13389 (2012)

8. Oliver, M., Montero, F., Fernández-Caballero, A., González, P., Molina, J.P.: RGB-D assistive technologies for acquired brain injury: description and assessment of user experience. Expert Systems (2014), doi:10.1111/exsy.12096
9. Deng, X., Schenato, L., Sastry, S.: Model identification and attitude control scheme for a micromechanical flying insect. In: International Conference on Control, Automation, Robotic and Vision, pp. 1007–1012 (2002)
10. Schenato, L., Wu, W.-C., Sastry, S.: Attitude control for a micromechanical flying insect via sensor output feedback. IEEE Transaction on Robotics and Automation 20, 93–106 (2004)
11. Campolo, D., Barbera, G., Schenato, L., Pi, L., Deng, X., Guglielmelli, E.: Attitude stabilization of a biologically inspired robotic housefly via dynamic multimodal attitude estimation. Advanced Robotics 23, 955–977 (2009)
12. Guckenheimer, J., Holmes, P.: Nonlinear Oscillations, Dynamical Systems, and Bifurcations of Vector Fields. Springer (1990)
13. Sanders, J.A., Verhulst, F.: Averaging Methods in Non-Linear Dynamical Systems. Springer (1985)
14. Deng, X., Schenato, L., Wu, W.-C., Sastry, S.: Flapping flight for biomimetic robotic insects: part II–flight control design. IEEE Transactions on Robotics 22, 789–803 (2006)
15. Rifaï, H., Marchand, N., Poulin-Vittrant, G.: Bounded control of an underactuated biomimetic aerial vehicle–Validation with robustness tests. Robotics and Autonomous Systems 60, 1165–1178 (2012)
16. Khan, Z.A., Agrawal, S.K.: Control of longitudinal flight dynamics of a flapping-wing micro air vehicle using time-averaged model and differential flatness based controller. In: Proceedings of the 2007 American Control Conference, pp. 5284–5289 (2007)
17. Han, J.: From PID to active disturbance rejection control. IEEE Transactions on Industrial Electronics 56, 900–906 (2009)
18. Radke, A., Gao, Z.: A survey of state and disturbance observers for practicioners. In: Proceedings of the 2006 American Control Conference, pp. 5183–5188 (2006)
19. Qing, Z., Gao, Z.: On practical applications of active disturbance rejection control. In: Proceedings of the 29th Chinese Control Conference, pp. 6095–6100 (2010)
20. Luviano-Juárez, A., Cortés-Romero, J., Sira-Ramírez, H.: Synchronization of chaotic oscillators by means of generalized proportional integral observers. International Journal of Bifurcation and Chaos 20, 1509–1517 (2010)
21. Fliess, M., Lévine, J., Martin, P., Rouchon, P.: Flatness and defect of nonlinear systems: Introductory theory and examples. International Journal of Control 61, 1327–1361 (1995)
22. Sira-Ramírez, H., Agrawal, S.: Differentially Flat Systems. Marcel Dekkert Inc. (2004)
23. Sira-Ramírez, H., Núñez, C., Visairo, N.: Robust sigma-delta generalized proportional integral observer based on a 'buck' converter with uncertain loads. International Journal of Control 83, 1631–1640 (2009)
24. Morales, R., Sira-Ramírez, H., Somolinos, J.A.: Robust control of underactuated wheeled mobile manupulators using GPI disturbance observers. Multibody Systems Dynamics 32, 511–533 (2014)
25. Morales, R., Sira-Ramírez, H., Somolinos, J.A.: Linear active disturbance rejection control of the hovercraft vessel model. Ocean Engineering 96, 100–108 (2015)

2.3 Experimentation of Control Algorithms

In order to complete the study on control algorithms for UAVs, a series of laboratory experiments were performed. In this stage, the Twin Rotor MIMO System, introduced in the previous section, was the platform selected to implement and test robust control schemes. This section presents the two publications that summarize the work carried out in this regard.

Firstly, the development of a two-stage active disturbance rejection control (ADRC) is detailed in the publication included in Subsection 2.3.1: "A Tandem Active Disturbance Rejection Control for a Laboratory Helicopter With Variable Speed Rotors". This paper demonstrates the excellent performance of the application of ADRC based on GPI observers in the design of decentralized strategies in hierarchical systems such as the TRMS platform.

Secondly, the document described in Subsection 2.3.2: "Robust Decentralized Nonlinear Control for a Twin Rotor MIMO System" presents a two-stage nonlinear, multivariable and robust control scheme for the TRMS. This paper extends our previous work [2] and provides experimental trials and a complete comparison with two more classical control schemes. The results highlight the excellent performance of the cascade-based controller in terms of stability and trajectory tracking.

2.3.1 A Tandem Active Disturbance Rejection Control for a Laboratory Helicopter With Variable Speed Rotors

Publication Data

ABSTRACT:
This paper introduces a laboratory helicopter with a variable-speed rotor system based on decentralized active disturbance rejection control. The new control scheme is composed of two independent stages that are utilized to achieve the precise trajectory tracking of the generalized coordinates of the system. A simplified model is proposed at each stage, which highly simplifies the controller design task. High-gain generalized proportional integral observers are considered in order to locally estimate all the disturbances affecting each subsystem online. These estimated disturbances are used in the control law of each stage to eliminate the effects of these disturbances on the system performance. Some of the advantages of the proposed control are: 1) it only requires the knowledge of the input gain to the subsystems (minimum information required from the dynamical models to control them); 2) the robust controller design procedure is simplified; 3) easier and safer implementation with regard to standard controllers; and 4) high robustness to large initial errors, unmodeled unmatched perturbations, noisy measurements, and parametric uncertainties in the model. The effectiveness of the proposed approach has been verified with real experiments conducted on a laboratory platform.

CITATION:
L.M. Belmonte; R. Morales; A. Fernández-Caballero; J.A. Somolinos. "A Tandem Active Disturbance Rejection Control for a Laboratory Helicopter with Variable Speed Rotors". *IEEE Transactions on Industrial Electronics*, 63(10), 6395–6406. IEEE, 2016. ISSN 0278-0046. DOI:10.1109/TIE.2016.2587238.

© 2016 IEEE. Reprinted, with permission, from L.M. Belmonte, R. Morales, A. Fernández-Caballero, J.A. Somolinos, A Tandem Active Disturbance Rejection Control for a Laboratory Helicopter with Variable Speed Rotors, IEEE Transactions on Industrial Electronics, 2016.

IEEE TRANSACTIONS ON INDUSTRIAL ELECTRONICS, VOL. 63, NO. 10, OCTOBER 2016 6395

A Tandem Active Disturbance Rejection Control for a Laboratory Helicopter With Variable-Speed Rotors

Lidia M. Belmonte, Rafael Morales, Antonio Fernández-Caballero, and José A. Somolinos

***Abstract*—This paper introduces a laboratory helicopter with a variable-speed rotor system based on decentralized active disturbance rejection control. The new control scheme is composed of two independent stages that are utilized to achieve the precise trajectory tracking of the generalized coordinates of the system. A simplified model is proposed at each stage, which highly simplifies the controller design task. High-gain generalized proportional integral observers are considered in order to locally estimate all the disturbances affecting each subsystem online. These estimated disturbances are used in the control law of each stage to eliminate the effects of these disturbances on the system performance. Some of the advantages of the proposed control are: 1) it only requires the knowledge of the input gain to the subsystems (minimum information required from the dynamical models to control them); 2) the robust controller design procedure is simplified; 3) easier and safer implementation with regard to standard controllers; and 4) high robustness to large initial errors, unmodeled unmatched perturbations, noisy measurements, and parametric uncertainties in the model. The effectiveness of the proposed approach has been verified with real experiments conducted on a laboratory platform.**

***Index Terms*—Disturbance estimation rejection, generalized proportional integral (GPI) control, observer design.**

I. Introduction

RESEARCH interest in the design of controllers for unmanned aerial vehicles has received a great deal of attention from a considerable number of researchers [1], [2]. There is also a growing interest in the use of laboratory platforms to simulate complex aircraft manoeuvres [3]. This interest stems from the fact that, in certain aspects, these laboratory platforms have a behavior that resembles that of a real helicopter, which is characterized by the fact that it has high nonlinearity and high coupled dynamics. Various models and control methods have been proposed in the literature concerning this sort of laboratory platforms: In [4], Kumar-Pandey and Laxmi proposed numerical results for the control of a *Twin Rotor MIMO System* (TRMS) using a PID controller and an optimal state feedback controller based on the LQR technique. In [5], Rahideh *et al.* developed the dynamic modeling of a TRMS using both analytical- and empirical-based methods. In [6], Mullhaupt *et al.* provided a detailed model of a helicopter-like setup (called *Toycopter*) and developed a nonlinear controller that used flat approximation based on physical insight and numerical and experimental results were also provided.

Taking into consideration the highly nonlinear coupled nature of the system and the difficulty involved in adequately modeling all the terms of which its dynamics is composed, *active disturbance rejection control* (ADRC) would appear to be an excellent methodology for the control of this sort of uncertain nonlinear system [7]. The objective of ADRC stems in the accurate estimation of the unknown part of the controlled system dynamics and the subsequent canceling of its effects in the feedback control law. Gao *et al.* have proposed new advances in these controllers, including practical applications [8]. On the other hand, Sira-Ramírez *et al.* have contributed to the area by emphasizing the use of *generalized proportional integral (GPI) observers* [9]. GPI observers provide an efficient disturbance estimation of the effects of all uncertain state-dependent nonlinearities (endogenous) and exogenous perturbation inputs (defined as a pure time-varying function without any particular structure) with the additional advantage of its simple and easy implementation and that it is based on a linear configuration. The results reported for other applications [10]–[12] encourage the use of GPI control schemes as an alternative to other control methods. However, the application of GPI observers to systems that naturally have a tandem or cascade connection has still not been exploited adequately [13]. In this paper, we demonstrate the excellent performance of the application of ADRC based on GPI observers in the design of decentralized strategies in tandem systems. In particular, we propose a linearizing global approach for the robust output feedback controller design for output trajectory tracking tasks on the perturbed tandem systems of which the TRMS system is composed. The key idea is that each individual feedback scheme is based on the use of a classical feedback controller and a suitably extended high-gain linear observer; thus, aiding the feedback controller in two important tasks: 1) the accurate estimation of the input–output system model nonlinearities, and

Manuscript received October 10, 2015; revised March 9, 2016 and May 2, 2016; accepted May 16, 2016. Date of publication July 7, 2016; date of current version September 9, 2016. This work was supported in part by the Spanish Ministerio de Economía y Competitividad/FEDER under Grant TEC2016-80986-R, Grant TIN2013-47074-C2-1R, and Grant DPI2014-53499R, and in part by the FPU Scholarship FPU014/05283 from the Spanish Government. *(Corresponding author: Rafael Morales.)*

L. M. Belmonte, R. Morales, and A. Fernández-Caballero are with the Escuela de Ingenieros Industriales de Albacete, Universidad de Castilla-La Mancha, 02071 Albacete, Spain (e-mail: LidiaMaria.Belmonte@uclm.es; Rafael.Morales@uclm.es; Antonio.Fdez@uclm.es).

J. A. Somolinos is with the Escuela Ténica Superior de Ingenieros Navales, Universidad Politécnica de Madrid, 28040 Madrid, Spain (e-mail: joseandres.somolinos@upm.es).

Color versions of one or more of the figures in this paper are available online at http://ieeexplore.ieee.org.

Digital Object Identifier 10.1109/TIE.2016.2587238

0278-0046 © 2016 IEEE. Personal use is permitted, but republication/redistribution requires IEEE permission.
See http://www.ieee.org/publications_standards/publications/rights/index.html for more information.

6396 IEEE TRANSACTIONS ON INDUSTRIAL ELECTRONICS, VOL. 63, NO. 10, OCTOBER 2016

TABLE I
PARAMETERS OF THE TRMS

Symbol	Parameter	Value	Units
	Parameters of the Main Rotor		
k_{vm}	Motor velocity constant	0.0202	V rad^{-1} s
R_m	Motor armature resistance	8	Ω
L_m	Motor armature inductance	0.86×10^{-3}	H
k_{tm}	Electromagnetic constant torque motor	0.0202	N m A^{-1}
k_{um}	Coefficient linear relationship interface circuit	8.5	–
C^{+}_{Qm}	Load factor ($\omega_m \geq 0$)	2.695×10^{-7}	N m s^2 rad^{-2}
C^{-}_{Qm}	Load factor ($\omega_m < 0$)	2.46×10^{-7}	N m s^2 rad^{-2}
f_{vm}	Viscous friction coefficient	3.89×10^{-6}	N m rad^{-1} s
I_{m1}	Moment of inertia about the axis of rotation	1.05×10^{-4}	kg $\cdot$ m^2
	Parameters of the Tail Rotor		
k_{vt}	Motor velocity constant	0.0202	V rad^{-1} s
R_t	Motor armature resistance	8	Ω
L_t	Motor armature inductance	0.86×10^{-3}	H
k_{tt}	Electromagnetic constant torque motor	0.0202	N m A^{-1}
k_{ut}	Coefficient linear relationship interface circuit	6.5	–
C_{Qt}	Load factor	1.164×10^{-8}	N m s^2 rad^{-2}
f_{vt}	Viscous friction coefficient	1.715×10^{-6}	N m rad^{-1} s
I_{t1}	Moment of inertia about the axis of rotation	2.1×10^{-5}	kg $\cdot$ m^2
	Mechanical Parameters		
l_t	Length of the tail part of the free-free beam	0.282	m
l_m	Length of the main part of the free-free beam	0.246	m
l_b	Length of the counterbalance beam	0.290	m
l_{cb}	Distance between the counterweight and the join	0.276	m
r_{ms}	Radius of the main shield	0.155	m
r_{ts}	Radius of the tail shield	0.1	m
h	Length of the pivoted beam	0.06	m
m_{tr}	Mass of the tail dc motor and tail rotor	0.221	kg
m_{mr}	Mass of the main DC motor and main rotor	0.236	kg
m_{cb}	Mass of the counterweight	0.068	kg
m_t	Mass of the tail part of the free-free beam	0.015	kg
m_m	Mass of the main part of the free-free beam	0.014	kg
m_b	Mass of the counterbalance beam	0.022	kg
m_{ts}	Mass of the tail shield	0.119	kg
m_{ms}	Mass of the main shield	0.219	kg
m_h	Mass of the pivoted beam	0.01	kg
	PARAMETERS OF THE PITCH MOVEMENT		
C^{+}_{Tm}	Thrust torque coefficient of the main rotor ($\omega_m \geq 0$)	1.53×10^{-5}	N s^2 rad^{-2}
C^{-}_{Tm}	Thrust torque coefficient of the main rotor ($\omega_m < 0$)	8.8×10^{-6}	N s^2 rad^{-2}
C_{Rt}	Load torque coefficient of the tail rotor	9.7×10^{-8}	N m s^2 rad^{-2}
$f_{v\psi}$	Viscous friction coefficient	0.0024	N m s rad^{-1}
$f_{c\psi}$	Coulomb friction coefficient	5.69×10^{-4}	N m
k_t	Coefficient of the inertial counter torque created by the change in ω_t	2.6×10^{-5}	N m s^2 rad^{-2}
	PARAMETERS OF THE YAW MOVEMENT		
C^{+}_{Tt}	Thrust torque coefficient of the tail rotor ($\omega_t \geq 0$)	3.25×10^{-6}	N s^2 rad^{-2}
C^{-}_{Tt}	Thrust torque coefficient of the tail rotor ($\omega_t < 0$)	1.72×10^{-6}	N s^2 rad^{-2}
C^{+}_{Rm}	Load torque coefficient of the main rotor ($\omega_m \geq 0$)	4.9×10^{-7}	N m s^2 rad^{-2}
C^{-}_{Rm}	Load torque coefficient of the main rotor ($\omega_m < 0$)	4.1×10^{-7}	N m s^2 rad^{-2}
$f_{v\phi}$	Viscous friction coefficient	0.03	N m s rad^{-1}
$f_{c\phi}$	Coulomb friction coefficient	3×10^{-4}	N m
c_c	Coefficient of the elastic force torque created by the cable	0.016	N m rad^{-1}
ϕ_0	Constant for the calculation of the torque of the cable	0	rad
k_m	Coefficient of the inertial counter torque created by the change in ω_m	2×10^{-4}	N m s^2 rad^{-2}

2) the accurate estimation of the unmeasured phase variables associated with each of the linearizing output variables. These two key pieces of information are used in the proposed feedback controller to: 1) cancel the influence of the nonlinearities as a lumped unstructured time-varying term, and 2) design an output feedback control law based on the approximate estimates of the output associated phase variables.

Finally, the remainder of this paper is organized as follows. Section II presents a detailed description of the TRMS. A reduced model for each subsystem is explained in Section III. Section IV illustrates some of the background results obtained for the ADRC method based on GPI observers for the robust decentralized control of interconnected nonlinear systems. Section V establishes the tandem GPI observer-based controller

with a disturbance estimation-rejection methodology used to achieve both the stabilization and trajectory tracking tasks for the TRMS. Section VI illustrates experimental results obtained with the proposed control algorithm and compared with other control algorithms. Finally, Section VII is devoted to our conclusion and suggestions for further work.

II. System Description

The TRMS platform is a laboratory helicopter that is characterized by its multivariable, underactuated, nonlinear, strongly coupled, and nonminimum phase behavior [14]. It is composed of a beam that is pivoted on its base and which can rotate freely in the horizontal and vertical planes. There are two propellers at each end of the beam which are perpendicular to each other and are driven by two dc motors. The main rotor produces a lifting force that allows the beam to rise vertically, causing a rotation around the pitch axis. Furthermore, the tail rotor causes the beam to turn (left or right) around the yaw axis. The system is additionally equipped with a pendulum counterweight which hangs from the beam and is in charge of balancing the angular momentum when in steady state or with load. In order to obtain the dynamic model of the whole system, as in [5], the design has been divided into the following two stages: First, the electrical part of the platform is modeled, including the interface circuit, the dc motors and the propulsive forces produced by these motors. Second, a Lagrangian-based model is employed for the remaining mechanical structure. This is dealt with in the following sections.

A. Dynamics of the Electrical Part

The main and tail rotors (hereafter denominated as m and t, respectively) are assumed to be identical with different mechanical loads. The mathematical expressions governing the main and tail rotors are presented below

$$\dot{\boldsymbol{\omega}}(t) = \mathbf{N}\mathbf{u}(t) + \boldsymbol{\Gamma}(\boldsymbol{\omega}(t)) \tag{1}$$

where it has been assumed that the dynamics of the current of the motors is negligible. The system constant parameters are illustrated in Table I, $\boldsymbol{\omega}(t) = [\omega_m(t), \omega_t(t)]^T$ represents the angular velocity of the propellers, $\mathbf{N} = \text{diag}(n_m, n_t)$ is a diagonal positive definite matrix in which $n_m = \frac{k_{t_m} k_{u_m}}{I_{m_1} R_m}$ and $n_t = \frac{k_{t_t} k_{u_t}}{I_{t_1} R_t}$, $\mathbf{u}(t) = [u_m(t), u_t(t)]^T$ expresses the magnitude input voltages of the main and tail rotors in the MATLAB/Simulink environment, and $\boldsymbol{\Gamma}(\boldsymbol{\omega}(t)) = [\Gamma_m(t), \Gamma_t(t)]^T$ is given by

$$\Gamma_m(t) = -\left(\frac{k_{t_m} k_{v_m}}{R_m} + f_{v_m}\right)\frac{\omega_m}{I_{m_1}} - \frac{C_{Q_m}}{I_{m_1}}\omega_m|\omega_m|$$

$$\Gamma_t(t) = -\left(\frac{k_{t_t} k_{v_t}}{R_t} + f_{v_t}\right)\frac{\omega_t}{I_{t_1}} - \frac{C_{Q_t}}{I_{t_1}}\omega_t|\omega_t|.$$

B. Dynamics of the Mechanical Part

If the developments reported in [5] are used as a basis, the dynamics of the TRMS can be derived using Lagrange's

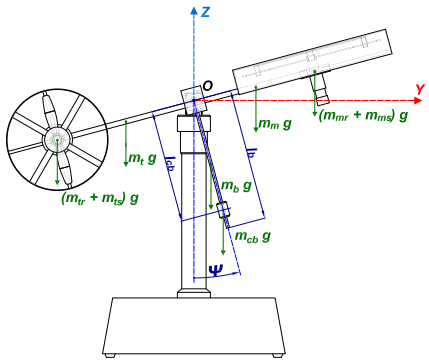

Fig. 1. View of the TRMS on a vertical plane.

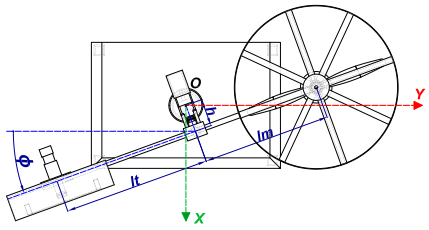

Fig. 2. View of the TRMS on a horizontal plane.

formulation (see also Figs. 1 and 2)

$$\underbrace{\begin{bmatrix} m_{11} & m_{12} \\ m_{21} & m_{22} \end{bmatrix}}_{\mathbf{M}(\mathbf{q}(t))} \underbrace{\begin{bmatrix} \ddot{\psi} \\ \ddot{\phi} \end{bmatrix}}_{\ddot{\mathbf{q}}(t)} = \underbrace{\begin{bmatrix} e_{11} & e_{12} \\ e_{21} & e_{22} \end{bmatrix}}_{\mathbf{E}(\mathbf{q}(t))} \underbrace{\begin{bmatrix} \omega_m\,|\omega_m| \\ \omega_t\,|\omega_t| \end{bmatrix}}_{\boldsymbol{\Omega}(t)} + \underbrace{\begin{bmatrix} \Upsilon_\psi \\ \Upsilon_\phi \end{bmatrix}}_{\boldsymbol{\Upsilon}(t)} \tag{2}$$

where $\mathbf{q}(t) = [\psi(t), \phi(t)]^T$ denotes the vector of generalized coordinates, $\mathbf{E}(\mathbf{q}(t)) \cdot \boldsymbol{\Omega}(t)$ represents the vector of aerodynamical thrust torques acting along the ψ and ϕ angles, respectively, and the aerodynamical cross-couplings effects generated by the propellers and $\boldsymbol{\Upsilon}(t)$ defines a vector which includes the Coriolis and centripetal forces, the gravitational forces, the electromechanical forces generated by the propellers, the viscous forces that model the dissipative effects that are present in the system and the elastic force created by the cable. The values of expression (2) are the following (where $S_\psi \equiv \sin\psi$, $C_\psi \equiv \cos\psi$, $S_\phi \equiv \sin\phi$ and $C_\phi \equiv \cos\phi$):

$$\begin{aligned}\Upsilon_\psi &= -\frac{1}{2}(J_1 - J_2)\,S_{2\psi}\dot{\phi}^2 - g\,(l_{T_1} m_{T_1} C_\psi + l_{T_2} m_{T_2} S_\psi) \\ &\quad - \left(f_{v\psi}\dot{\psi} + f_{c\psi}\,\text{sgn}\left(\dot{\psi}\right)\right) + k_t\dot{\omega}_t \\ \Upsilon_\phi &= h\,(l_{T_1} m_{T_1} C_\psi + l_{T_2} m_{T_2} S_\psi)\,\dot{\psi}^2 - ((J_2 - J_1)\,S_{2\psi})\,\dot{\phi}\dot{\psi} \\ &\quad - \left(f_{v\phi}\dot{\phi} + f_{c\phi}\,\text{sgn}\left(\dot{\phi}\right)\right) - C_c\,(\phi - \phi_0) + k_m\,\dot{\omega}_m\,C_\psi\end{aligned}$$

$$\begin{aligned}m_{11} &= J_1 + J_2; \quad m_{12} = m_{21} \\ &= h\,(l_{T_2} m_{T_2} C_\psi - l_{T_1} m_{T_1} S_\psi) \\ m_{22} &= J_1 C_\psi^2 + J_2 S_\psi^2 + J_3 + h^2\,(m_{T_1} + m_{T_2})\end{aligned}$$

$$e_{11} = C_{T_m} l_m; \quad e_{12} = -C_{R_t}$$
$$e_{21} = -C_{R_m} C_\psi; \quad e_{22} = C_{T_t} l_t C_\psi$$

$$J_1 = m_{\rm ts} r_{\rm ts}^2 + \frac{1}{2} m_{\rm ms} r_{\rm ms}^2 + \left(\frac{1}{3} m_t + m_{\rm tr} + m_{\rm ts}\right) l_t^2 + \left(\frac{1}{3} m_m + m_{\rm mr} + m_{\rm ms}\right) l_m^2$$
$$m_{T_1} = m_m + m_{\rm mr} + m_{\rm ms} + m_t + m_{\rm tr} + m_{\rm ts}$$
$$l_{T_1} = \frac{\left(\frac{m_t}{2} + m_{\rm tr} + m_{\rm ts}\right) l_t - \left(\frac{m_m}{2} + m_{\rm mr} + m_{\rm ms}\right) l_m}{m_{T_1}}$$
$$J_2 = \frac{1}{3} m_b l_b^2 + m_{\rm cb} l_{\rm cb}^2; \quad m_{T_2} = m_b + m_{\rm cb}$$
$$l_{T_2} = \frac{m_b \frac{l_b}{2} + m_{\rm cb} l_{\rm cb}}{m_{T_2}}; \quad J_3 = \frac{1}{3} m_h l_h^2.$$

III. Simplified System

The dynamics of the TRMS platform given by expressions (1) and (2) may be significantly reduced to the following perturbed, nonphenomenological, simplified models.

A. Simplified Model of the Electrical Part

Starting from expression (1), it is assumed that the matrix $\mathbf{N}$ is known while it is assumed that the vector $\mathbf{\Gamma}(\boldsymbol{\omega}(t))$ is not readily available for imprecise knowledge of some of the parameters involved. Let us suppose that we wish to track a given angular velocity reference trajectory vector of the propellers, $\boldsymbol{\omega}^*(t) = [\omega_m^*(t), \omega_t^*(t)]^T$. The nominal system, computed on the basis of the desired angular velocity trajectory vector is therefore merely a copy of the original system represented by expression (1)

$$\dot{\boldsymbol{\omega}}^*(t) = \mathbf{N}\mathbf{u}^*(t) + \mathbf{\Gamma}(\boldsymbol{\omega}^*(t)) \tag{3}$$

where the term $\mathbf{\Gamma}(\boldsymbol{\omega}^*(t))$ is also unknown in the electrical nominal system model. In this case, the nominal control voltage input vector $\mathbf{u}^*(t)$ that gives the desired angular velocity reference trajectory vector $\boldsymbol{\omega}^*(t)$ cannot be known, *a priori* with precision. The subtraction of expressions (1) and (3) yields the following expression for the simplified open-loop tracking angular velocity error dynamics $\mathbf{e}_{\boldsymbol{\omega}}(t) = \boldsymbol{\omega}(t) - \boldsymbol{\omega}^*(t) = [\omega_m(t) - \omega_m^*(t), \omega_t(t) - \omega_t^*(t)]^T$:

$$\dot{\mathbf{e}}_{\boldsymbol{\omega}}(t) = \mathbf{N}\mathbf{u}(t) + \mathbf{z}_1^{\rm e}(t) \tag{4}$$

where the vector $\mathbf{z}_1^{\rm e}(t) = \mathbf{\Gamma}(\boldsymbol{\omega}(t)) - \mathbf{\Gamma}(\boldsymbol{\omega}^*(t)) - \mathbf{N}\mathbf{u}^*(t) = [\delta_m(t), \delta_t(t)]^T$ involves all external disturbances and the effect of the nonlinearities that affect the electrical subsystem behavior, which is here regarded as *an unknown but uniformly absolutely bounded disturbance input vector*[1] that needs to be estimated online by means of an observer and subsequently canceled from the simplified system dynamics via feedback in order to regulate the angular velocity of the propellers $\boldsymbol{\omega}(t) = [\omega_m(t), \omega_t(t)]^T$ toward the desired velocities $\boldsymbol{\omega}^*(t) = [\omega_m^*(t), \omega_t^*(t)]^T$.

B. Simplified Model of the Mechanical Part

Upon operating with (2), and assuming possible modeling errors in the matrix $\mathbf{E}(\mathbf{q}(t))$, we obtain the following simplified model for the mechanical part:

$$\ddot{\mathbf{q}}(t) = \mathbf{D_0}(\mathbf{q}(t))\mathbf{\Omega}(t) + \mathbf{z}_1^{\rm m}(t) \tag{5}$$

where $\mathbf{D_0}(\mathbf{q}(t)) = \mathbf{M}^{-1}(\mathbf{q}(t))\mathbf{E_0}(\mathbf{q}(t))$ is constituted by the nominal values, and the vector $\mathbf{z}_1^{\rm m}(t) = [\delta_\psi(t), \delta_\phi(t)]^T = \mathbf{M}^{-1}(\mathbf{q}(t))[(\mathbf{E}(\mathbf{q}(t)) - \mathbf{E_0}(\mathbf{q}(t)))\mathbf{\Omega}(t) + \mathbf{\Upsilon}(t)]$ represents all external disturbances and the effect of the nonlinearities, including the control input through the unknown input gain deviation $\mathbf{M}^{-1}(\mathbf{q}(t))[\mathbf{E}(\mathbf{q}(t)) - \mathbf{E_0}(\mathbf{q}(t))]$, that affect the mechanical subsystem behavior, which is here again regarded as an *unknown but uniformly absolutely bounded disturbance input vector*[1] that needs to be estimated online by means of an observer and subsequently canceled from the simplified system dynamics via feedback in order to regulate the vector of generalized coordinates $\mathbf{q}(t) = [\psi(t), \phi(t)]^T$ toward the desired reference trajectory vector of generalized coordinates $\mathbf{q}^*(t) = [\psi^*(t), \phi^*(t)]^T$.

IV. Background Results

In this section, we provide the interested reader with the rigorous mathematical developments on which the ADRC based on GPI observers for interconnected systems technique [13] is based.

A. Description of the Interconnected Network of Systems

Let us consider a set of N interconnected nonlinear systems $\sum_i$, $i = 1, 2, \ldots, N$, each of which has a measured output scalar function, $y_i \in \mathbb{R}$, $i = 1, 2, \ldots, N$, fulfilling the following expression:

$$\sum_i : y_i^{(n_i)} = \Psi(t, y_i) u_i + z_{i,1}(t, \underline{\mathbf{y}}_1, \underline{\mathbf{y}}_2, \ldots, \underline{\mathbf{y}}_i, \ldots, \underline{\mathbf{y}}_N, u_1, \ldots, u_{i-1}, u_{i+1}, \ldots, u_N) \tag{6}$$

where y_i denotes the output measured from subsystem i, $\underline{\mathbf{y}}_k \in \mathbb{R}^{n_k}$ expresses the n_k-dimensional vector of phase variables associated with the output y_k under the sole responsibility of the kth agent $\left(\underline{\mathbf{y}}_k = (y_k, \dot{y}_k, \ldots, y_k^{(n_k-1)})\right)$, u_j expresses the scalar control input of the jth agent to its own system and, finally, the vector $\mathbf{y} = (y_1, y_2, \ldots, y_N)$ represents a N-dimensional vector. The following assumptions are taken into consideration.

1) A smooth $\mathbf{C}^\infty$ reference trajectory y_i^*, $i = 1, 2, \ldots, N$, is provided for each subsystem represented in (6). It is additionally assumed that the agents do not cooperate.
2) The control input gain $\Psi(t, y_i)$ is accurately known by agent i.

[1] This assumption cannot be verified *a priori* when $\mathbf{z}_1^{\rm e}(t)$ and $\mathbf{z}_1^{\rm m}(t)$ are completely unknown. However, those cases in which the nonlinearity is unknown except for some of their parameters, as is the case of the TRMS, its validity can be assessed.

3) All the exogenous disturbances that affect the i-subsystem dynamics are lumped in the function $z_{i,1}(\cdot)$, along with the network interaction and endogenous nonlinearities that affect subsystem i. For positive integers, m_i, $i = 1, 2, \ldots, N$, the nonlinear time function $z_{i,1}(\cdot)$, which affects the i-subsystem, is completely unknown by the agent i except for the fact that it is uniformly absolutely bounded and a finite number of its time derivatives $z_{i,1}^{(j)}(\cdot)$, for $j = 1, 2, \ldots, m_i$, are also uniformly absolutely bounded, i.e., $z_{1,1}^{(m_1)}(\cdot), z_{1,2}^{(m_2)}(\cdot), \ldots, z_{1,N}^{(m_N)}(\cdot)$ are $\mathcal{L}_\infty$ scalar functions.[2] If this condition is not satisfied almost everywhere for any finite integer m_i, then the solutions of $y_i(t)$ in (6) do not exist at all for any finite output $u_i(t)$ (proofs of this result may be found in [15]).

B. Problem Formulation

Given a desired $\mathbf{C}^\infty$ output reference trajectory composed of the N-dimensional time vector[3]

$$\mathbf{y}^*(t) = (y_1^*(t), y_2^*(t), \ldots, y_N^*(t)) \tag{7}$$

devise for each subsystem given in (6) a smooth output feedback controller, $u_i(t, y_i, y_i^*(t), \dot{y}_i^*(t), \ldots, [y_i^*(t)]^{(n_i)}) = u_i(t, y_i, \underline{\mathbf{y}}_i^*(t))$, which tracks the desired trajectory vector $\mathbf{y}^*(t)$. The output feedback control law for the ith subsystem should be composed by using only the local information seconded to subsystem (6), i.e., on the basis of $(y_i, y_i^*, \Psi_i(t, y_i))$.

C. ADRC-Based GPI Observer Approach for Interconnected Network of Systems

The ADRC approach proposes that each agent i with regard to the nonlinear complex interaction term

$$z_{i,1}(t, \underline{\mathbf{y}}_1, \underline{\mathbf{y}}_2, \ldots, \underline{\mathbf{y}}_i, \ldots, \underline{\mathbf{y}}_N, u_1, \ldots, u_{i-1}, u_{i+1}, \ldots, u_N), \quad \text{for } i = 1, \ldots, N \tag{8}$$

as a time-varying function of unknown structure except for the fact that it is uniformly absolutely bounded and a finite number of its time derivatives $z_{i,1}^{(j)}(t)$, $j = 1, 2, \ldots, m_i$ are also absolutely bounded, implying that

$$\sup_t |z_{i,1}^{(j)}(t)| \leq K_{i,j}, \text{ for } j = 1, 2, \ldots, m_i \text{ and } i = 1, 2, \ldots, N \tag{9}$$

which additively perturbs its subsystem behavior. The set of integers m_i for $i = 1, \ldots, N$ are selected to be a low integer (typically, $m_i = 2, 3, 4$ for $i = 1, \ldots, N$). The ith agent online asymptotically estimates this complex interaction term with the help of a linear observer subject to a nonlinear input injection by means of the known subsystem control input gain $\Psi(t, y_i)$.

[2]This assumption cannot be verified *a priori* when $z_{i,1}(\cdot)$, $i = 1, 2, \ldots, N$ are completely unknown. However, those cases in which the nonlinearity is unknown except for some of their parameters, as is the case of the TRMS, its validity can be assessed.

[3]Knowledge of the output reference trajectory, $y_i^*(t)$, $i = 1, \ldots, N$, is assumed to imply knowledge of the analytic expression of such a time function. The calculation of their derivatives: $[y_i^*(t)]^{(j)}$, $i = 1, \ldots, N$, for any finite order j is therefore trivial. $\underline{\mathbf{y}}_i^*(t)$ is used to express the vector $\underline{\mathbf{y}}_i^*(t) = (y_i^*(t), \dot{y}_i^*(t), \ldots, [y_i^*(t)]^{(n_i)})$ of dimension $n_i + 1$.

The linear observer design strategy consists of estimating the perturbation input $z_{i,1}(\cdot)$ of the i-subsystem using an instantaneous internal time polynomial model, realized in the form of a chain of integrators of length $p_i - 1$ at the observer stage for a fixed, sufficiently large integer p_i. When forcing the dominantly linear perturbed output estimation error dynamics of the i-subsystem to exhibit an asymptotically convergent behavior, the internal model for the interaction term $z_{i,1}(\cdot)$ is automatically and continuously self-updated. As a consequence of this, we may safely assume that the term $z_{i,1}(\cdot)$ and a finite number of its time derivatives $z_{i,1}^{(j)}(\cdot)$ for $j = 1, 2, \ldots, p_i$ are uniformly absolutely bounded for a sufficiently large p_i. The ith subsystem decentralized output feedback controller is therefore given by the following GPI observer-based feedback linearizing controller ($i = 1, 2, \ldots, N$)

$$\begin{aligned}
\dot{\hat{y}}_{i,0} &= \hat{y}_{i,1} + \lambda_{i,n_i+p_i-1}(y_i - \hat{y}_{i,0}) \\
\dot{\hat{y}}_{i,k-1} &= \hat{y}_{i,k} + \lambda_{i,n_i+p_i-k}(y_i - \hat{y}_{i,0}), \quad k = 2, \ldots, n_i - 1 \\
\dot{\hat{y}}_{i,n_i-1} &= \Psi(t, y_i)u_i + \hat{z}_{i,1} + \lambda_{i,p_i}(y_i - \hat{y}_{i,0}) \\
\dot{\hat{z}}_{i,j} &= \hat{z}_{i,j+1} + \lambda_{i,p_i-1}(y_i - \hat{y}_{i,0}), \quad j = 1, \ldots, p_i - 1 \\
\dot{\hat{z}}_{i,p_i} &= \lambda_{i,0}(y_i - \hat{y}_{i,0}) \\
u_i &= \frac{1}{\Psi(t, y_i)} \left[-\hat{z}_{i,1} + [y_i^*(t)]^{(n_i)} \right. \\
&\qquad \left. - \sum_{m=0}^{n_i-1} \kappa_{i,m} \left(\hat{y}_{i,m} - [y_i^*(t)]^{(m)} \right) \right]
\end{aligned} \tag{10}$$

where the redundant estimate $\hat{y}_{i,0}$ of the ith subsystem output should be replaced with the measured output y_i. The controller gain parameters of the i-subsystem, $\{\kappa_{i,0}, \kappa_{i,1}, \ldots, \kappa_{i,n_i-1}\}$, are designed in such a way that the roots of the dominant characteristic polynomial in the complex variable s, $p_{c_d}^i(s)$, are Hurwitz

$$p_{c_d}^i(s) = s^{n_i} + \kappa_{i,n_i-1}s^{n_i-1} + \cdots + \kappa_{i,1}s + \kappa_{i,0}. \tag{11}$$

Furthermore, the observer gain parameters of the i-subsystem, $\{\lambda_{i,0}, \lambda_{i,1}, \ldots, \lambda_{i,n_i+p_i-1}\}$, were similarly chosen so as to obtain the following desired closed-loop Hurwitz characteristic polynomial $p_{\text{obs}_d}^i(s)$ in the complex variable s

$$p_{\text{obs}_d}^i(s) = s^{n_i+p_i} + \lambda_{i,n_i+p_i-1}s^{n_i+p_i-1} + \cdots + \lambda_{i,1}s + \lambda_{i,0}. \tag{12}$$

Upon defining the output local estimation error for the i-subsystem as $\tilde{e}_i(t) = \tilde{e}_{i,0}(t) = y_i(t) - \hat{y}_{i,0}(t)$ and the local closed-loop output tracking error as $e_i(t) = y_i(t) - y_i^*(t)$, the following perturbed scalar high-order differential equations are satisfied:

$$\tilde{e}_i^{(n_i+p_i)} + \sum_{j=0}^{n_i+p_i-1} \lambda_{i,j}\tilde{e}_i^{(j)} = z_{i,1}^{(p_i)}(\cdot) \tag{13}$$

$$e_i^{(n_i)} + \sum_{j=0}^{n_i-1} \kappa_{i,j}e_i^{(j)} = [z_{i,1}(\cdot) - \hat{z}_{i,1}] + \sum_{j=0}^{n_i-1} \kappa_{i,j}\tilde{e}_i^{(j)}. \tag{14}$$

Remark 1: It is easy to see from (6), (13), and (14) that if the output local estimation error $\tilde{e}_i(t) = \tilde{e}_{i,0}(t)$ is identically zero, then, $\tilde{e}_{i,1}(t) = \tilde{e}_{i,2}(t) = \cdots = \tilde{e}_{i,n_i-1}(t) = 0$ and $\hat{z}_{i,1} = z_{i,1}(\cdot)$. This implies that $\hat{z}_{i,1}$ would be an *exact* local estimate of the nonlinear interaction term: $z_{i,1}(\cdot)$. This is an ideal situation which will be utilized in this study of the stability of the closed-loop system [given by expressions (13) and (14)] by using singular perturbation analysis [16]. Without loss of generality, we may assume that the local GPI observer gains $\lambda_{i,j}$ are designed in such a way that the injected local estimation error dynamics is reducible to normal form, written as a linear differential operator

$$\left(\frac{d}{dt} + \frac{\lambda_i}{\varepsilon_i}\right)^{n_i+p_i} \tilde{e}_i = z_{i,1}^{(p_i)}$$
$$(t, \underline{\mathbf{y}}_1, \underline{\mathbf{y}}_2, \ldots, \underline{\mathbf{y}}_i, \ldots, \underline{\mathbf{y}}_N, u_1, \ldots, u_{i-1}, u_{i+1}, \ldots, u_N) \quad (15)$$

where ε_i, λ_i, are strictly positive real parameters (with, say, $\lambda_i > 1$). If we multiply both sides in the previous expression by $\varepsilon^{n_i+p_i}$ the following equivalent system is attained:

$$\left(\varepsilon_i \frac{d}{dt} + \lambda_i\right)^{n_i+p_i} \tilde{e}_i = \varepsilon^{n_i+p_i} z_{i,1}^{(p_i)}(\cdot). \quad (16)$$

According to [17], the reduced order system is achieved by selecting the value $\varepsilon_i = 0$ in (16) yielding that the only trivial equilibrium of the singularity local perturbed observer dynamics is obtained in $\tilde{e}_{i_f} = 0$. Taking into consideration *Remark 1*, $\hat{z}_{i,1} = z_{i,1}(\cdot)$ and $\tilde{e}_{i_f,0}(t) = \tilde{e}_{i_f,1}(t) = \tilde{e}_{i_f,2}(t) = \cdots = \tilde{e}_{i_f,n_i-1}(t) = 0$, the reduced order system for the local tracking error dynamics is the following:

$$\bar{e}_i^{(n_i)} + \sum_{j=0}^{n_i-1} \kappa_{i,j} \bar{e}_i^{(j)} = 0 \quad (17)$$

and using the fact that the controller gain parameters of the i-subsystem, $\{\kappa_{i,0}, \kappa_{i,1}, \ldots, \kappa_{i,n_i-1}\}$, were designed to be Hurwitz, the reduced order system for the local tracking error dynamics (17) has an asymptotically exponentially stable equilibrium point to the origin of the local trajectory tracking phase space: $(\bar{e}_i, \dot{\bar{e}}_i, \ldots, \bar{e}_i^{(i)})$. Furthermore, the boundary layer system in the stretched time scale, $\tau = t/\varepsilon_i$, satisfies the asymptotically stable linear homogeneous differential equation

$$\left(\frac{d}{d\tau} + \lambda_i\right)^{n_i+p_i} \tilde{e}_{\text{is}} = 0 \quad (18)$$

where $\tilde{e}_{\text{is}}$ represents the *slow* component of the local estimation error dynamics. The equilibrium $\tilde{e}_{\text{is}} = 0$ is asymptotically stable independently of the initial condition given by $e_i(0)$ and, given any initial condition, $\tilde{e}_{\text{is}}(0)$, for the boundary system (18) is, trivially, in its domain of attraction. The value of λ_i in (18) is strictly negative and it is designed to be smaller than a finite fixed negative real number $-c_i$ by setting $\lambda_i > c_i$.

From the previous analysis, all the hypothesis of Tikhonov's theorem [16] are satisfied. Therefore, for a sufficiently small ε_i, the local GPI observer error $\tilde{e}_i$ and its time derivatives uniformly ultimately evolve, in a stable fashion, inside an arbitrarily small neighborhood of the origin of the local GPI error phase space

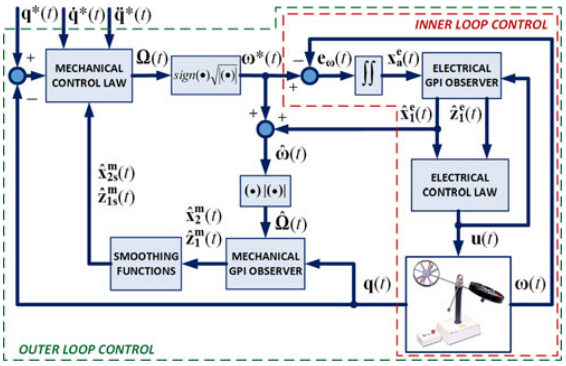

Fig. 3. Tandem robust ADRC scheme.

$(\tilde{e}_i, \dot{\tilde{e}}_i, \ldots, \tilde{e}_i^{(n_i+p_i-1)})$ determined by ε_i. An estimate of the radius of such a uniformly bounding open neighborhood for $\tilde{e}_i$ is obtained from the steady state of (16) by selecting $\frac{d}{dt} = 0$. This estimate is simply given by $\left(\frac{\varepsilon_i}{\lambda_i}\right)^{n_i+p_i} K_{i,m_i}$, where K_{i,m_i} is the uniform absolute upper bound hypothesized in $z_{i,1}^{(m_i)}(\cdot)$. Under these circumstances, the difference $z_{i,1}(\cdot) - \hat{z}_i$ is also arbitrarily small and the right-hand side of the tracking error dynamics is, at most, of the order ε_i.

The fundamental result of ADRC based on GPI observers, as adapted to the decentralized output tracking control problems, is the following:

Proposition 1: The local estimation error phase variables given by $(\tilde{e}_i, \ldots, \tilde{e}_i^{(n_i)})$ asymptotically uniformly, ultimately, converge toward a small vicinity of the origin of the ith subsystem output phase space for sufficiently large Hurwitz gains $\lambda_{i,j}$. Additionally, from the GPI observer defined in expression (10), and bearing in mind the uniform absolute boundedness of $z_{i,1}^{(m_i)}(\cdot)$, the quantities $\hat{z}_{i,1}(t)$, $i = 1, \ldots, N$, respectively, estimate the time evolution of $z_{i,1}(\cdot)$, $i = 1, \ldots, N$ in an arbitrary close manner. The local perturbed closed-loop tracking error phase variables: $(e_i, \ldots, e^{(n_i-1)})$, for moderately large Hurwitz gains $\kappa_{i,j}$, therefore, asymptotically uniformly, ultimately, converge toward a small vicinity of the origin of their phase space. Such a vicinity can be made as small as desired by properly choosing the gains $\kappa_{i,j}$'s. Proofs of this result may be found in [18] and [19] for nonlinear monovariable systems and in [20] and [21] for the multivariable case. The result remains valid for the decentralized case at hand.

V. Tandem GPI Observer-Based Controller With Disturbance Estimation Rejection

The general control scheme proposed in this paper is shown in Fig. 3. In this control scheme, a robust ADRC based on GPI observers (denoted as the *inner loop control*) is first closed in order to control the vector of the angular velocities of the propellers, and another robust ADRC based on GPI observers (denoted as the *outer loop*) is then closed in order to control the vector of the generalized coordinates of the TRMS platform. If the dynamics of the *inner loop* is made much faster than the dynamics

of the mechanical part (5), the procedure used to design the whole control system can be separated into two independent design processes [22]: The design of the *inner loop* controller and the design of the *outer loop* controller. In the scheme shown in Fig. 3, the *outer loop* controller generates an auxiliary command reference vector $\boldsymbol{\omega}^*(t) = [\omega_m^*(t), \omega_t^*(t)]^T$ for the velocities of the propellers on the basis of the tracking objective for the vector of generalized coordinates: $\mathbf{q}(t) = [\psi(t), \phi(t)]^T$. The inner loop controller takes the command vector signal generated by the outer loop $\boldsymbol{\omega}^*(t)$ as its reference for the *inner loop* propeller velocity control system. The different parts of the proposed control scheme are explained as follows.

A. Inner Loop Controller

The objective of the *inner loop controller* is to specify the magnitude input voltages of the main and tail rotors in the MATLAB/Simulink environment, $\mathbf{u}(t) = [u_m(t), u_t(t)]^T$, in terms of the subsystem output vector, $\boldsymbol{\omega}(t) = [\omega_m(t), \omega_t(t)]^T$, while taking the designed auxiliary control input vector, $\boldsymbol{\omega}^*(t) = [\omega_m^*(t), \omega_t^*(t)]^T$, as a reference trajectory vector for the internal variable $\boldsymbol{\omega}(t)$. If we consider the simplified dynamical model for the electrical part given by (4), the electrical control law to be designed will be robust with regard to the unknown disturbance vector $\mathbf{z}_1^{\mathrm{e}}(t) = [\delta_m(t), \delta_t(t)]^T$. It is necessary to estimate, even if in an approximately as desired fashion, the unknown uniformly absolutely bounded time varying electrical disturbance vector $\mathbf{z}_1^{\mathrm{e}}(t) = [\delta_m(t), \delta_t(t)]^T$ and, then, to include a cancelation term of these disturbance effects in the design of the control input vector provided by the electrical control law, $\mathbf{u}(t) = [u_m(t), u_t(t)]^T$ and, then, asymptotically impose a linear stable closed-loop dynamics by appropriately feeding back the measured angular velocity vector of the propellers $\boldsymbol{\omega}(t) = [\omega_m(t), \omega_t(t)]^T$. A high-gain GPI observer is considered, including a reasonable self-updating instantaneous time-polynomial model for each unknown component, state dependent, disturbance input vector $\mathbf{z}_1^{\mathrm{e}}(t)$. In this case, by trial and error and engineering judgment based on the value of the estimation error vector dynamics $\tilde{\mathbf{e}}_{\mathrm{a}}(t) = \mathbf{x}_{\mathrm{a}}^{\mathrm{e}}(t) - \hat{\mathbf{x}}_{\mathrm{a}}^{\mathrm{e}}(t)$ defined below, we have used a second-degree family of time polynomials, denoted as $\hat{\mathbf{z}}_1^{\mathrm{e}}(t) = [\hat{\delta}_m(t), \hat{\delta}_t(t)]^T$, to define each component of the internal model. The expression $\ddot{\mathbf{z}}_1^{\mathrm{e}}(t) = \mathbf{0}$ represents the internal model of the disturbance input for the observer proposed for the electrical part of the TRMS. Moreover, in the design of this controller, the measurements of the angular velocities of the propellers of the TRMS (obtained with two dc tachometers) are affected by significant sensor noises, i.e., the output of this subsystem can now be defined as $\boldsymbol{\varpi}(t) = \boldsymbol{\omega}(t) + \mathbf{d}(t)$, where $\mathbf{d}(t) \in \mathbb{R}^{2\times 1}$ is the measurement vector noise that corrupts the output vector signal $\boldsymbol{\omega}(t)$. In these cases, the performance of the GPI observer would not be satisfactory since it would affect the observer convergence. In order to deal with these noisy measurements and, bearing in mind that signal integration can annihilate random noisy effects, the structure of the GPI observer is augmented with the following two fictitious state vector variables in order to improve the measurement noise rejection characteristics (with a respective increment in the settling time) [23]

$$\mathbf{x}_0^{\mathrm{e}}(t) = \int_0^t (\boldsymbol{\varpi}(\tau) - \boldsymbol{\omega}^*(\tau))\, d\tau = \int_0^t (\mathbf{e}_{\boldsymbol{\omega}}(\tau) + \mathbf{d}(\tau))\, d\tau$$
$$\mathbf{x}_{\mathrm{a}}^{\mathrm{e}}(t) = \int_0^t \mathbf{x}_0^{\mathrm{e}}(\tau) d\tau = \int_0^t \int_0^\sigma (\mathbf{e}_{\boldsymbol{\omega}}(\sigma) + \mathbf{d}(\sigma))\, d\sigma d\tau \quad (19)$$

where $\mathbf{e}_{\boldsymbol{\omega}}(t) = \boldsymbol{\omega}(t) - \boldsymbol{\omega}^*(t)$ denotes the angular velocity error vector. The augmented GPI observer for the estimation of the angular velocity error vector $\hat{\mathbf{e}}_{\boldsymbol{\omega}}(t)$ and the electrical disturbance input vector $\hat{\mathbf{z}}_1^{\mathrm{e}}(t)$ can therefore now be described as:

$$\begin{aligned}
\dot{\hat{\mathbf{x}}}_{\mathrm{a}}^{\mathrm{e}}(t) &= \hat{\mathbf{x}}_0^{\mathrm{e}}(t) + \boldsymbol{\lambda}_4^{\mathrm{e}} (\mathbf{x}_{\mathrm{a}}^{\mathrm{e}}(t) - \hat{\mathbf{x}}_{\mathrm{a}}^{\mathrm{e}}(t)) \\
\dot{\hat{\mathbf{x}}}_0^{\mathrm{e}}(t) &= \hat{\mathbf{x}}_1^{\mathrm{e}}(t) + \boldsymbol{\lambda}_3^{\mathrm{e}} (\mathbf{x}_{\mathrm{a}}^{\mathrm{e}}(t) - \hat{\mathbf{x}}_{\mathrm{a}}^{\mathrm{e}}(t)) \\
\dot{\hat{\mathbf{x}}}_1^{\mathrm{e}}(t) &= \mathbf{N}\mathbf{u}(t) + \hat{\mathbf{z}}_1^{\mathrm{e}}(t) + \boldsymbol{\lambda}_2^{\mathrm{e}} (\mathbf{x}_{\mathrm{a}}^{\mathrm{e}}(t) - \hat{\mathbf{x}}_{\mathrm{a}}^{\mathrm{e}}(t)) \\
\dot{\hat{\mathbf{z}}}_1^{\mathrm{e}}(t) &= \hat{\mathbf{z}}_2^{\mathrm{e}}(t) + \boldsymbol{\lambda}_1^{\mathrm{e}} (\mathbf{x}_{\mathrm{a}}^{\mathrm{e}}(t) - \hat{\mathbf{x}}_{\mathrm{a}}^{\mathrm{e}}(t)) \\
\dot{\hat{\mathbf{z}}}_2^{\mathrm{e}}(t) &= \boldsymbol{\lambda}_0^{\mathrm{e}} (\mathbf{x}_{\mathrm{a}}^{\mathrm{e}}(t) - \hat{\mathbf{x}}_{\mathrm{a}}^{\mathrm{e}}(t))
\end{aligned} \quad (20)$$

where $\mathbf{x}_1^{\mathrm{e}}(t) = \mathbf{e}_{\boldsymbol{\omega}}(t)$ and $\hat{\mathbf{x}}_1^{\mathrm{e}}(t) = \hat{\mathbf{e}}_{\boldsymbol{\omega}}(t)$ have been set. The observer design parameters $\{\boldsymbol{\lambda}_0^{\mathrm{e}}, \ldots, \boldsymbol{\lambda}_4^{\mathrm{e}}\} \in \mathbb{R}^{2\times 2}$ are diagonal positive definite matrices. Using (4) and (20), the estimation error vector dynamics, $\tilde{\mathbf{e}}_{\mathrm{a}}(t) = \mathbf{x}_{\mathrm{a}}^{\mathrm{e}}(t) - \hat{\mathbf{x}}_{\mathrm{a}}^{\mathrm{e}}(t)$, evolves according to the following linear perturbed dynamics:

$$\begin{aligned}
&\tilde{\mathbf{e}}_{\mathrm{a}}^{(5)}(t) + \boldsymbol{\lambda}_4^{\mathrm{e}} \tilde{\mathbf{e}}_{\mathrm{a}}^{(4)}(t) + \boldsymbol{\lambda}_3^{\mathrm{e}} \tilde{\mathbf{e}}_{\mathrm{a}}^{(3)}(t) + \boldsymbol{\lambda}_2^{\mathrm{e}} \ddot{\tilde{\mathbf{e}}}_{\mathrm{a}}(t) \\
&\qquad + \boldsymbol{\lambda}_1^{\mathrm{e}} \dot{\tilde{\mathbf{e}}}_{\mathrm{a}}(t) + \boldsymbol{\lambda}_0^{\mathrm{e}} \tilde{\mathbf{e}}_{\mathrm{a}}(t) = \ddot{\mathbf{z}}_1^{\mathrm{e}}(t) + \mathbf{d}^{(3)}(t).
\end{aligned} \quad (21)$$

Taking into consideration that the term $\ddot{\mathbf{z}}_1^{\mathrm{e}}(t) + \mathbf{d}^{(3)}(t)$ is by assumption a uniformly absolutely bounded time varying function, and if the selection of the constant observer gain matrices $\{\boldsymbol{\lambda}_0^{\mathrm{e}}, \ldots, \boldsymbol{\lambda}_4^{\mathrm{e}}\}$ are designed in such a way that the dominant characteristic 2×2 complex valued diagonal matrix

$$\mathbf{p}_{\mathbf{obs}}^{\mathrm{e}}(s) = \mathbf{I}^{2\times 2} s^5 + \boldsymbol{\lambda}_4^{\mathrm{e}} s^4 + \boldsymbol{\lambda}_3^{\mathrm{e}} s^3 + \boldsymbol{\lambda}_2^{\mathrm{e}} s^2 + \boldsymbol{\lambda}_1^{\mathrm{e}} s + \boldsymbol{\lambda}_0^{\mathrm{e}} \quad (22)$$

is composed of fifth-degree Hurwitz polynomials whose roots are located sufficiently far into the left half on the complex plane, then the trajectories of the estimation error vector, $\tilde{\mathbf{e}}_{\mathrm{a}}(t)$, and their corresponding time derivatives converge to a small vicinity around the origin of the phase space of the observer estimation error vector. The constant gain matrices of the electrical GPI observer $\{\boldsymbol{\lambda}_0^{\mathrm{e}}, \ldots, \boldsymbol{\lambda}_4^{\mathrm{e}}\}$ were designed in order to locate the desired closed-loop poles at a common root of the real line, given by $\mathbf{I}^{2\times 2} s = -\mathbf{p}_{\mathrm{o}}^{\mathrm{e}}$, where $\mathbf{p}_{\mathrm{o}}^{\mathrm{e}}$ is a diagonal matrix whose terms are clearly strictly positive. We use the following 2×2 complex valued diagonal matrix:

$$\mathbf{p}_{\mathbf{obs_d}}^{\mathrm{e}}(s) = \left(\mathbf{I}^{2\times 2} s + \mathbf{p}_{\mathrm{o}}^{\mathrm{e}}\right)^5 \quad (23)$$

where the matrix $\mathbf{p}_{\mathrm{o}}^{\mathrm{e}}$ represents the desired location of the poles. Upon identifying each term of the expression (22) with those in expression (23), we directly obtain the values of the set of gain matrices $\boldsymbol{\lambda}_0^{\mathrm{e}}, \ldots, \boldsymbol{\lambda}_4^{\mathrm{e}}$. Note that the proposed solution for the electrical GPI observer partially decouples the noise dynamics from the observer gain matrices (the proof is shown in [23]), thus improving the electrical GPI observer convergence without changing its gain matrices (with the exception of the two extra gain matrices of the extended state observer that needs to be

tuned). The feedback control input, $\mathbf{u}(t) = [u_m(t), u_t(t)]^T$, for the simplified electrical dynamics of the TRMS (1) is synthesized as a classical proportional controller with a cancelation term

$$\mathbf{u}(t) = \mathbf{N}^{-1}\left[-\mathbf{K}_{\mathbf{P}}^{\mathbf{e}}\,\hat{\mathbf{e}}_{\boldsymbol{\omega}}(t) - \hat{\mathbf{z}}_{\mathbf{1}}^{\mathbf{e}}(t)\right] \tag{24}$$

where $\mathbf{K}_{\mathbf{P}}^{\mathbf{e}} \in \mathbb{R}^{2\times 2}$ is a constant diagonal positive definite matrix that represents the design elements of a vector-valued classical proportional controller, $\hat{\mathbf{z}}_{\mathbf{1}}^{\mathbf{e}}(t) = [\hat{\delta}_m(t), \hat{\delta}_t(t)]^T$ denotes the estimate of the electrical disturbance input vector $\mathbf{z}_{\mathbf{1}}^{\mathbf{e}}(t)$, and $\hat{\mathbf{e}}_{\boldsymbol{\omega}}(t) = \hat{\mathbf{x}}_{\mathbf{1}}^{\mathbf{e}}(t)$ represents an estimation of the tracking angular velocity vector of the propellers of the TRMS $\mathbf{e}_{\boldsymbol{\omega}}(t) = \boldsymbol{\omega}(t) - \boldsymbol{\omega}^*(t)$. The controller design matrix $\mathbf{K}_{\mathbf{P}}^{\mathbf{e}}$ is designed so as to render the following 2×2 complex valued diagonal matrix $\mathbf{p}_{\mathbf{c}}^{\mathbf{e}}(s)$ defined as

$$\mathbf{p}_{\mathbf{c}}^{\mathbf{e}}(s) = \mathbf{I}^{2\times 2}s + \mathbf{K}_{\mathbf{P}}^{\mathbf{e}} \tag{25}$$

as first-degree Hurwitz polynomials, with desirable root locations. The constant controller gain matrix $\mathbf{K}_{\mathbf{P}}^{\mathbf{e}}$ of the closed-loop characteristic polynomial was determined by means of a term-by-term comparison with the following desired Hurwitz 2×2 diagonal matrix:

$$\mathbf{p}_{\mathbf{c_d}}^{\mathbf{e}}(s) = \mathbf{I}^{2\times 2}s + \mathbf{p}_{\mathbf{c}}^{\mathbf{e}} \tag{26}$$

where $\mathbf{p}_{\mathbf{c}}^{\mathbf{e}} \in \mathbb{R}^{2\times 2}$ is a diagonal positive definite matrix representing the desired position of the poles in closed loop. The closed-loop tracking error dynamics illustrated in expression (25) is less severely affected by the uncertainties than the observer estimation error dynamics given in expression (22). This results in smaller magnitudes of the feedback gains $\mathbf{K}_{\mathbf{P}}^{\mathbf{e}}$ than those used for the design of the GPI observers in the electrical part. The closed-loop tracking error vector, $\mathbf{e}_{\boldsymbol{\omega}}(t) = \boldsymbol{\omega}(t) - \boldsymbol{\omega}^*(t)$, for the electrical part is obtained after substituting expression (24) in the simplified model (4), thus achieving

$$\dot{\mathbf{e}}_{\boldsymbol{\omega}}(t) + \mathbf{K}_{\mathbf{P}}^{\mathbf{e}}\,\mathbf{e}_{\boldsymbol{\omega}} = \mathbf{z}_{\mathbf{1}}^{\mathbf{e}}(t) - \hat{\mathbf{z}}_{\mathbf{1}}^{\mathbf{e}}(t) + \boldsymbol{\chi}^{\mathbf{e}}(t) \tag{27}$$

where $\boldsymbol{\chi}^{\mathbf{e}}(t) = \mathbf{K}_{\mathbf{P}}^{\mathbf{e}}\,(\mathbf{e}_{\boldsymbol{\omega}} - \hat{\mathbf{e}}_{\boldsymbol{\omega}})$ represents a vector depending on the error of the estimation of the propeller angular velocity vector which, thanks to the performance of the electrical GPI observer, asymptotically exponentially converges toward a small neighborhood of the null tracking error space.

B. Outer Loop Controller

The fundamental idea involved in regulating the mechanical part of the TRMS is to use the reduced model (5). To implement this, we primarily estimate, even if in an approximately as desired manner, the unknown mechanical disturbance vector $\mathbf{z}_{\mathbf{1}}^{\mathbf{m}}(t) = [\delta_\psi(t), \delta_\phi(t)]^T$, and then include a cancelation term of these disturbance effects in the design of the auxiliary control input vector provided by the mechanical control law $\boldsymbol{\omega}^*(t) = [\omega_m^*(t), \omega_t^*(t)]^T$. We next asymptotically impose a stable closed-loop dynamics by appropriately feeding back the estimated time derivatives of the measured generalized coordinates vector $\mathbf{q}(t) = [\psi(t), \phi(t)]^T$. A high-gain GPI observer is considered, including a reasonable self-updating instantaneous time-polynomial model for each unknown component, state dependent, disturbance input vector $\mathbf{z}_{\mathbf{1}}^{\mathbf{m}}(t)$. In our case, we used a second-degree family of time polynomials, denoted as $\hat{\mathbf{z}}_{\mathbf{1}}^{\mathbf{m}}(t) = [\hat{\delta}_\psi(t), \hat{\delta}_\phi(t)]^T$, to define each component of the internal model. The expression $\ddot{\mathbf{z}}_{\mathbf{1}}^{\mathbf{m}}(t) = \mathbf{0}$, therefore, expresses the internal model of the disturbance input for the observer proposed for the mechanical part of the TRMS. The auxiliar feedback control input, $\boldsymbol{\Omega}(t) = [\Omega_m(t), \Omega_t(t)]^T$, for the simplified mechanical dynamics of the TRMS (5) is synthesized as a classical proportional derivative (PD) controller with a cancelation term

$$\boldsymbol{\Omega}(t) = \mathbf{D}_{\mathbf{0}}^{-1}(\mathbf{q}(t))\left[\boldsymbol{\nu}_{\mathbf{m}}(t) - \hat{\mathbf{z}}_{\mathbf{1s}}^{\mathbf{m}}(t)\right] \tag{28}$$

in which

$$\begin{aligned}\boldsymbol{\nu}_{\mathbf{m}}(t) = \ddot{\mathbf{q}}(t) = \ddot{\mathbf{q}}^*(t) - \mathbf{K}_{\mathbf{D}}^{\mathbf{m}}\left(\dot{\hat{\mathbf{q}}}_{\mathbf{s}}(t) - \dot{\mathbf{q}}^*(t)\right)\\ -\mathbf{K}_{\mathbf{P}}^{\mathbf{m}}\left(\mathbf{q}(t) - \mathbf{q}^*(t)\right)\end{aligned} \tag{29}$$

where $\mathbf{K}_{\mathbf{D}}^{\mathbf{m}}$ and $\mathbf{K}_{\mathbf{P}}^{\mathbf{m}} \in \mathbb{R}^{2\times 2}$ are the diagonal positive definite matrix that represents the design elements of a vector-valued classical PD controller, $\hat{\mathbf{z}}_{\mathbf{1s}}^{\mathbf{m}}(t) = [\hat{\delta}_{\psi_s}(t), \hat{\delta}_{\phi_s}(t)]^T$ denotes the smoothed estimate of the mechanical disturbance input vector $\mathbf{z}_{\mathbf{1}}^{\mathbf{m}}(t)$, and $\hat{\dot{\mathbf{q}}}_{\mathbf{s}}(t)$ represents an smoothed estimation of the generalized joint velocity vector $\dot{\mathbf{q}}(t) = [\dot{\psi}(t), \dot{\phi}(t)]^T$. These smoothings, which are geared toward eliminating possibly large peaks characteristic in high-gain observers, may be achieved by using the following (nonunique) time function which smoothly increases from 0 to 1 (denoted as a *clutching function*), during a small time interval $[0, \alpha]$

$$s_f(t) = \begin{cases} \sin^\rho\left(\frac{\pi t}{2\alpha}\right), & \text{for } 0 \le t \le \alpha \\ 1, & \text{for } t > \alpha \end{cases} \tag{30}$$

where ρ is a suitably large positive even integer. The smoothing of the observer variables is therefore achieved as $F_s(t) = F(t)s_f(t)$. Furthermore, the set of GPI observers for the estimation of the generalized joint velocity vector $\hat{\dot{\mathbf{q}}}(t)$ and the mechanical disturbance input vector $\hat{\mathbf{z}}_{\mathbf{1}}^{\mathbf{m}}(t)$ are given by

$$\begin{aligned}\dot{\hat{\mathbf{x}}}_{\mathbf{1}}^{\mathbf{m}}(t) &= \hat{\mathbf{x}}_{\mathbf{2}}^{\mathbf{m}}(t) + \boldsymbol{\lambda}_{\mathbf{3}}^{\mathbf{m}}\left(\mathbf{x}_{\mathbf{1}}^{\mathbf{m}}(t) - \hat{\mathbf{x}}_{\mathbf{1}}^{\mathbf{m}}(t)\right)\\ \dot{\hat{\mathbf{x}}}_{\mathbf{2}}^{\mathbf{m}}(t) &= \mathbf{D_0}(\mathbf{q}(t))\hat{\boldsymbol{\Omega}}(t) + \hat{\mathbf{z}}_{\mathbf{1}}^{\mathbf{m}}(t) + \boldsymbol{\lambda}_{\mathbf{2}}^{\mathbf{m}}\left(\mathbf{x}_{\mathbf{1}}^{\mathbf{m}}(t) - \hat{\mathbf{x}}_{\mathbf{1}}^{\mathbf{m}}(t)\right)\\ \dot{\hat{\mathbf{z}}}_{\mathbf{1}}^{\mathbf{m}}(t) &= \hat{\mathbf{z}}_{\mathbf{2}}^{\mathbf{m}}(t) + \boldsymbol{\lambda}_{\mathbf{1}}^{\mathbf{m}}\left(\mathbf{x}_{\mathbf{1}}^{\mathbf{m}}(t) - \hat{\mathbf{x}}_{\mathbf{1}}^{\mathbf{m}}(t)\right)\\ \dot{\hat{\mathbf{z}}}_{\mathbf{2}}^{\mathbf{m}}(t) &= \boldsymbol{\lambda}_{\mathbf{0}}^{\mathbf{m}}\left(\mathbf{x}_{\mathbf{1}}^{\mathbf{m}}(t) - \hat{\mathbf{x}}_{\mathbf{1}}^{\mathbf{m}}(t)\right)\end{aligned} \tag{31}$$

in which $\mathbf{x}_{\mathbf{1}}^{\mathbf{m}}(t) = \mathbf{q}(t)$, $\hat{\mathbf{x}}_{\mathbf{1}}^{\mathbf{m}}(t) = \hat{\mathbf{q}}(t)$, $\hat{\mathbf{x}}_{\mathbf{2}}^{\mathbf{m}}(t) = \hat{\dot{\mathbf{q}}}(t)$, $\hat{\boldsymbol{\omega}}(t) = \hat{\mathbf{x}}_{\mathbf{1}}^{\mathbf{e}}(t) + \boldsymbol{\omega}^*(t) = \hat{\mathbf{e}}_{\boldsymbol{\omega}}(t) + \boldsymbol{\omega}^*(t)$, and $\hat{\boldsymbol{\Omega}}(t) = [\hat{\Omega}_m(t), \hat{\Omega}_t(t)]^T = [\hat{\omega}_m|\hat{\omega}_m|, \hat{\omega}_t|\hat{\omega}_t|]^T$ have been set. The observer design parameters $\{\boldsymbol{\lambda}_{\mathbf{0}}^{\mathbf{m}}, \ldots, \boldsymbol{\lambda}_{\mathbf{3}}^{\mathbf{m}}\} \in \mathbb{R}^{2\times 2}$ are diagonal positive definite matrices. The estimation error vector dynamics, $\tilde{\mathbf{e}}_{\mathbf{q}}(t) = \mathbf{x}_{\mathbf{1}}^{\mathbf{m}}(t) - \hat{\mathbf{x}}_{\mathbf{1}}^{\mathbf{m}}(t)$, evolves with the linear perturbed dynamics

$$\begin{aligned}\tilde{\mathbf{e}}_{\mathbf{q}}^{(4)}(t) + \boldsymbol{\lambda}_{\mathbf{3}}^{\mathbf{m}}\tilde{\mathbf{e}}_{\mathbf{q}}^{(3)}(t) + \boldsymbol{\lambda}_{\mathbf{2}}^{\mathbf{m}}\ddot{\tilde{\mathbf{e}}}_{\mathbf{q}}(t) + \boldsymbol{\lambda}_{\mathbf{1}}^{\mathbf{m}}\dot{\tilde{\mathbf{e}}}_{\mathbf{q}}(t) + \boldsymbol{\lambda}_{\mathbf{0}}^{\mathbf{m}}\tilde{\mathbf{e}}_{\mathbf{q}}(t)\\ = \ddot{\mathbf{z}}_{\mathbf{1}}^{\mathbf{m}}(t) + \boldsymbol{\eta}^{\mathbf{m}}(t)\end{aligned} \tag{32}$$

where $\boldsymbol{\eta}^{\mathbf{m}}(t) = \frac{d^2}{dt^2}\left[\mathbf{D_0}(\mathbf{q}(t))\left(\boldsymbol{\Omega}(t) - \hat{\boldsymbol{\Omega}}(t)\right)\right]$. Bearing in mind that the vector $\mathbf{z}_{\mathbf{1}}^{\mathbf{m}}(t)$ is by assumption a uniformly

absolutely bounded time varying function, thanks to the fast performance of the electrical GPI observer $\left(\boldsymbol{\Omega}(t) \approx \hat{\boldsymbol{\Omega}}(t)\right)$, then in order to achieve the convergence of the estimation error dynamics to a small vicinity around the origin of the estimation error phase space, the constant observer gain matrices $\{\boldsymbol{\lambda}_{\mathbf{0}}^{\mathbf{m}}, \ldots, \boldsymbol{\lambda}_{\mathbf{3}}^{\mathbf{m}}\}$ are chosen in such a manner that all the nonzero components of the 2×2 complex valued diagonal matrix, $\mathbf{p}_{\mathbf{obs}}^{\mathbf{m}}(s)$, defined as

$$\mathbf{p}_{\mathbf{obs}}^{\mathbf{m}}(s) = \mathbf{I}^{2\times 2} s^4 + \boldsymbol{\lambda}_{\mathbf{3}}^{\mathbf{m}} s^3 + \boldsymbol{\lambda}_{\mathbf{2}}^{\mathbf{m}} s^2 + \boldsymbol{\lambda}_{\mathbf{1}}^{\mathbf{m}} s + \boldsymbol{\lambda}_{\mathbf{0}}^{\mathbf{m}} \tag{33}$$

are all fourth-degree Hurwitz polynomials whose roots are located sufficiently far into the left half on the complex plane. Since the order of the high-gain observer for the estimation error dynamics (33) is an even number, the constant observer gain matrices $\{\boldsymbol{\lambda}_{\mathbf{0}}^{\mathbf{m}}, \ldots, \boldsymbol{\lambda}_{\mathbf{3}}^{\mathbf{m}}\}$ were chosen so as to obtain the following desired closed-loop characteristic 2×2 complex valued diagonal matrix

$$\mathbf{p}_{\mathbf{obs_d}}^{\mathbf{m}}(s) = \left(\mathbf{I}^{2\times 2} s^2 + 2\boldsymbol{\zeta}_{\mathbf{o}}^{\mathbf{m}} \boldsymbol{\omega}_{\mathbf{o}}^{\mathbf{m}} s + (\boldsymbol{\omega}_{\mathbf{o}}^{\mathbf{m}})^2\right)^2 \tag{34}$$

where $\boldsymbol{\zeta}_{\mathbf{o}}^{\mathbf{m}}$ and $\boldsymbol{\omega}_{\mathbf{o}}^{\mathbf{m}} \in \mathbb{R}^{2\times 2}$ are diagonal positive definite matrices representing the damping and natural frequencies, respectively. The values of the constant observer gain matrices $\{\boldsymbol{\lambda}_{\mathbf{0}}^{\mathbf{m}}, \ldots, \boldsymbol{\lambda}_{\mathbf{3}}^{\mathbf{m}}\}$ are directly obtained by identifying each term of the expression (33) with those of (34). The trajectories of the estimation error vector $\tilde{\mathbf{e}}_{\mathbf{q}}(t)$ and of their time derivatives, therefore, converge to a small neighborhood of the origin of the phase space of the observer estimation error vector. The further away the roots are located in the left half of the complex plane, the smaller the radius of the disk representing the neighborhood around the origin of the estimation error phase space will be. The closed-loop tracking error vector, $\mathbf{e}_{\mathbf{q}}(t) = \mathbf{q}(t) - \mathbf{q}^*(t)$, for the mechanical part is obtained after substituting expression (28) in the simplified model (5), yielding the following expression:

$$\ddot{\mathbf{e}}_{\mathbf{q}}(t) + \mathbf{K}_{\mathbf{D}}^{\mathbf{m}} \dot{\mathbf{e}}_{\mathbf{q}}(t) + \mathbf{K}_{\mathbf{P}}^{\mathbf{m}} \mathbf{e}_{\mathbf{q}}(t) = \mathbf{z}_{\mathbf{1}}^{\mathbf{m}}(t) - \hat{\mathbf{z}}_{\mathbf{1s}}^{\mathbf{m}}(t) + \boldsymbol{\chi}^{\mathbf{m}}(t) \tag{35}$$

where $\boldsymbol{\chi}^{\mathbf{m}}(t) = \mathbf{K}_{\mathbf{D}}^{\mathbf{m}} \left(\dot{\mathbf{q}}(t) - \dot{\hat{\mathbf{q}}}_{\mathbf{s}}(t)\right)$ represents a vector depending on the error of the estimation of the generalized joint velocity vector which, thanks to the performance of the high-gain GPI observer designed for the mechanical part of the TRMS, asymptotically exponentially converges toward a small neighborhood of the null tracking error space. The controller design matrices $\mathbf{K}_{\mathbf{D}}^{\mathbf{m}}$ and $\mathbf{K}_{\mathbf{P}}^{\mathbf{m}}$ are selected in accordance with the same high-gain philosophy used for the observer design coefficients. They must be selected so as to render the following 2×2 complex valued diagonal matrix, $\mathbf{p}_{\mathbf{c}}^{\mathbf{m}}(s)$, defined as

$$\mathbf{p}_{\mathbf{c}}^{\mathbf{m}}(s) = \mathbf{I}^{2\times 2} s^2 + \mathbf{K}_{\mathbf{D}}^{\mathbf{m}} s + \mathbf{K}_{\mathbf{P}}^{\mathbf{m}} \tag{36}$$

as second-degree Hurwitz polynomials with desirable root locations. The constant controller gains $\mathbf{K}_{\mathbf{D}}^{\mathbf{m}}$ and $\mathbf{K}_{\mathbf{P}}^{\mathbf{m}}$ of the closed-loop characteristic polynomial were determined by using a term-by-term comparison with the following desired Hurwitz 2×2 complex valued diagonal matrix:

$$\mathbf{p}_{\mathbf{c_d}}^{\mathbf{m}}(s) = \mathbf{I}^{2\times 2} s^2 + 2\boldsymbol{\zeta}_{\mathbf{c}}^{\mathbf{m}} \boldsymbol{\omega}_{\mathbf{c}}^{\mathbf{m}} s + (\boldsymbol{\omega}_{\mathbf{c}}^{\mathbf{m}})^2 \tag{37}$$

where $\boldsymbol{\zeta}_{\mathbf{c}}^{\mathbf{m}}$ and $\boldsymbol{\omega}_{\mathbf{c}}^{\mathbf{m}} \in \mathbb{R}^{2\times 2}$ are diagonal positive definite matrices representing the damping and natural frequencies, respectively. Note that the closed-loop tracking error dynamics illustrated in expression (35) is less severely affected by the uncertainties than the observer estimation error dynamics given in expression (33). This results in smaller magnitudes of the feedback gains $\mathbf{K}_{\mathbf{D}}^{\mathbf{m}}$ and $\mathbf{K}_{\mathbf{P}}^{\mathbf{m}}$ than those used for the design of the GPI observers [20]. Furthermore, the generated vector signal $\boldsymbol{\Omega}(t) = [\Omega_m(t), \Omega_t(t)]^T = [\omega_m|\omega_m|(t), \omega_t|\omega_t|(t)]^T$, which is defined as the auxiliary control input vector, regulates the vector of generalized coordinates $\mathbf{q}(t) = [\psi(t), \phi(t)]^T$ to the desired reference trajectory vector of generalized coordinates $\mathbf{q}^*(t) = [\psi^*(t), \phi^*(t)]^T$. Moreover, the signal $\boldsymbol{\Omega}(t)$ should be viewed as a reference signal for the *inner design stage*, denoted as $\boldsymbol{\omega}^*(t) = [\omega_m^*(t), \omega_t^*(t)]^T$, after carrying out the following manipulation:

$$\boldsymbol{\omega}^*(t) = \begin{bmatrix} \omega_m^*(t) \\ \omega_t^*(t) \end{bmatrix} = \begin{bmatrix} \text{sign}\left(\Omega_m(t)\right) \cdot \sqrt{|\Omega_m(t)|} \\ \text{sign}\left(\Omega_t(t)\right) \cdot \sqrt{|\Omega_t(t)|} \end{bmatrix}. \tag{38}$$

Finally, note that, in the proposed tandem ADRC scheme, the design values of the diagonal matrix $\mathbf{p}_{\mathbf{c}}^{\mathbf{e}}$ in the inner loop controller are chosen to be much larger than the design values of the diagonal matrix $\boldsymbol{\omega}_{\mathbf{c}}^{\mathbf{m}}$ in the outer loop controller, so that $\boldsymbol{\omega}(t) \approx \boldsymbol{\omega}^*(t)$ in view of the variations of $\mathbf{q}^*(t)$ and $\mathbf{q}(t)$ (or similarly that the inner loop scheme behaves approximately as $\mathbf{I}^{2\times 2}$ when $s = j\omega$ in the frequency range $\mathbf{0} \leq \mathbf{I}^{2\times 2}\omega \leq \mathbf{p}_{\mathbf{c}}^{\mathbf{e}}$)[24]. It is also necessary to note that the generalized coordinates vector, $\mathbf{q}(t) = [\psi(t), \phi(t)]^T$, is measured by employing digital encoders with a nonsignificant measurement noise, thus making the search for solutions to attenuate the measurement noise unnecessary.

VI. Experimental Results

In this section, we carry out an experimental implementation to assess the performance of the proposed tandem ADRC based on GPI observers scheme on the TRMS. In the trials, it is desirable to track the following desired reference trajectory vector of generalized coordinates $\mathbf{q}^*(t) = [\psi^*(t), \phi^*(t)]^T$:

$$\begin{bmatrix} \psi^*(t) \\ \phi^*(t) \end{bmatrix} = \begin{bmatrix} A_{0\psi} + A_{1\psi}(2\sin(\omega_{1\psi}t) + \sin(\omega_{2\psi}t)) \\ A_{0\phi} + A_{1\phi}\sin(\omega_{1\phi}t) + A_{2\phi}(\sin(\omega_{2\phi}t) + \sin(\omega_{3\phi}t)) \end{bmatrix}$$

whereby $A_{0\psi} = 0.48$ rad, $A_{1\psi} = 0.1$ rad, $\omega_{1\psi} = 0.0785$ rad/s, $\omega_{2\psi} = 0.0157$ rad/s, $A_{0\phi} = -0.2$ rad, $A_{1\phi} = -0.64$ rad, $A_{2\phi} = -0.3$ rad, $\omega_{1\phi} = 0.1885$ rad/s, $\omega_{2\phi} = 0.1178$ rad/s, and $\omega_{3\phi} = 0.0236$ rad/s. The values of the physical parameters of the TRMS are depicted in Table I but we have to remark that due to the difficulty involved in adequately modeling all the dynamics terms, the discrepancies in the model due to modeling errors is around 5%. Furthermore, in order to demonstrate the exponential convergence of the desired trajectories, the initial values for the generalized coordinates of the TRMS, $\mathbf{q_0}(t) = [\psi_0, \phi_0]^T = [0, 0]^T$ rad, were selected with different values to the initial values used for the desired reference trajectory vector $\mathbf{q}^*(t)$. Moreover, the proposed ADRC scheme

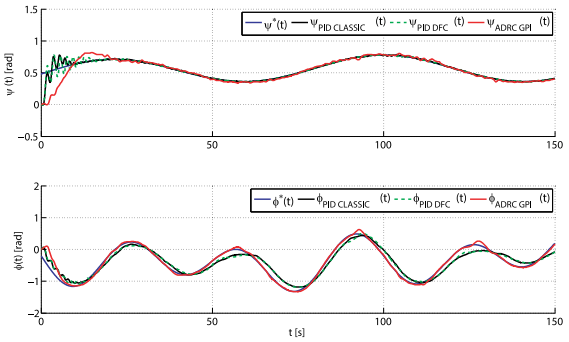

Fig. 4. Real and desired evolution trajectories of the vector of generalized coordinates of the TRMS, $\mathbf{q}(t) = [\psi(t), \phi(t)]^T$.

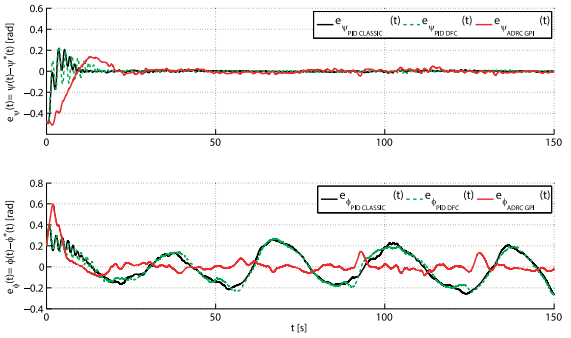

Fig. 5. Evolution of the error vector of generalized coordinates of the TRMS, $\mathbf{e_q}(\mathbf{t}) = \mathbf{q}(t) - \mathbf{q}^*(t) = [\psi(t) - \psi^*(t), \phi(t) - \phi^*(t)]^T$.

has been designed to be as fast as possible, but care must be taken owing to possible saturations of the input voltages of the motors in the MATLAB/Simulink environment, which occur at ± 2.5 V. All gain vectors were tuned according to the procedure explained in Section V by using the pairs of (22) and (23), (25) and (26), (33), and (34), and (36) and (37), by considering pure real roots and taking into consideration the performance of the tracking errors $\mathbf{e_\omega}(t)$ and $\mathbf{e_q}(\mathbf{t})$. For the *outer loop controller*, the values of the matrices of the desired Hurwitz polynomial vector for the feedback controller are $\boldsymbol{\zeta}_\mathbf{c}^\mathbf{m} = \text{diag}(1.25, 1.25)$ and $\boldsymbol{\omega}_\mathbf{c}^\mathbf{m} = \text{diag}(1, 1)$ while the values of the matrices of the desired Hurwitz polynomial vector for the GPI observer are $\boldsymbol{\zeta}_\mathbf{o}^\mathbf{m} = \text{diag}(1, 1)$ and $\boldsymbol{\omega}_\mathbf{o}^\mathbf{m} = \text{diag}(2.5, 2.5)$. The design parameters of the clutching functions were set to be $\rho = 8$ and $\alpha = 2\ s$. Furthermore, for the *inner loop controller*, the values of the desired Hurwitz 2×2 complex diagonal matrix for the feedback controller are $\mathbf{p}_\mathbf{c}^\mathbf{e} = \text{diag}(3, 4)$ while the values of the desired Hurwitz 2×2 complex diagonal matrix for the GPI observer are $\mathbf{p}_\mathbf{o}^\mathbf{e} = \text{diag}(15, 20)$. Three sets of experiments were developed using the real TRMS platform in order to establish a comparison between the robust tandem ADRC control presented in this paper, a standard PID control [25] (denoted in the graphs as *PID CLASSIC*) and a PID control with derivative filter coefficient [26] (denoted in the graphs as *PID DFC*). The comparison is carried out on the basis of the following aspects:

1) robustness with regard to large initial errors;
2) quick convergence of the tracking errors to a small neighborhood of zero;
3) smooth transient responses;
3) low control effort;
4) endogenous and exogenous disturbances;
5) robustness when dealing with noisy measurements.

The quality of the trajectory tracking performance of the vector of generalized coordinates of the TRMS, $\mathbf{q}(t) = [\psi(t), \phi(t)]^T$, with the three control algorithms is depicted in Fig. 4. Although the robustness with respect to large initial errors and the convergence to the tracking errors to a small neighborhood of zero are obtained with the three control algorithms, one observes that the proposed robust ADRC control scheme presents the smoothest transient response. Fig. 5 shows the closed-loop tracking error vector, $\mathbf{e_q}(\mathbf{t}) = \mathbf{q}(t) - \mathbf{q}^*(t) = [\psi(t) - \psi^*(t), \phi(t) - \phi^*(t)]^T$. In this graph, it can be observed that the smallest tracking error vector $\mathbf{e_q}(\mathbf{t})$ is obtained with the proposed control algorithm, remaining bounded within a vicinity of radius $[0.03,\ 0.15]^T$ rad, while a value of $[0.02,\ 0.26]^T$ rad for the standard PID control and a value of $[0.02,\ 0.28]^T$ rad for the PID with derivative filter coefficient are achieved, which indicates that in spite of the unmatched nature of the mechanical perturbation vector, $\mathbf{z}_\mathbf{1}^\mathbf{m}(t) = [\delta_\psi(t), \delta_\phi(t)]^T$, the proposed tandem ADRC scheme efficiently corrects the undesirable effects of this perturbation vector. Fig. 6 illustrates the mechanical disturbance estimations $\hat{\mathbf{z}}_\mathbf{1}^\mathbf{m}(t) = [\hat{\delta}_\psi(t), \hat{\delta}_\phi(t)]^T$, associated with the outer control loop for the proposed robust ADRC scheme. The evolution of the angular velocity vectors is shown in Fig. 7. The figure illustrates that a good stabilization and an accurate tracking trajectory velocity vector were achieved with all three control algorithms. However, observes that the system response using the proposed algorithm exhibits the best transient response, the smaller dynamic behavior of the system in the presence of noisy signals and the lowest angular velocity error vector $\mathbf{e_\omega}(t) = \boldsymbol{\omega}(t) - \boldsymbol{\omega}^*(t) = [\omega_m - \omega_m^*, \omega_t - \omega_t^*]^T$ as illustrated in Fig. 8. Note that the angular velocity error vector $\mathbf{e_\omega}(t)$ remains bounded within a vicinity of radius $[8.5, 65]^T$ rad/s for the proposed algorithm. Values of $[28, 270]^T$ rad/s and $[32, 255]^T$ rad/s are achieved for the standard PID control and the PID with derivative

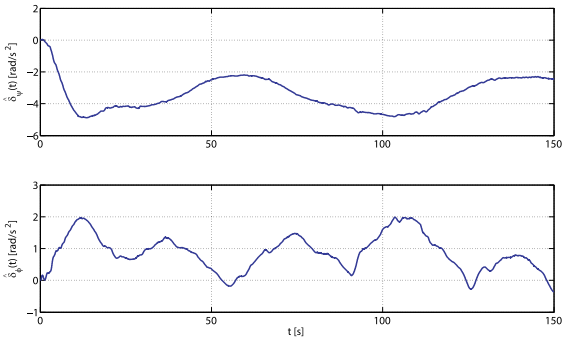

Fig. 6. Estimation of the mechanical disturbance vector $\hat{\mathbf{z}}_\mathbf{1}^\mathbf{m}(t) = [\hat{\delta}_\psi(t), \hat{\delta}_{\phi(t)}(t)]^T$.

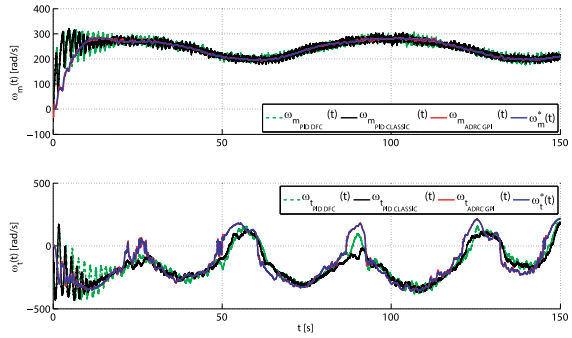

Fig. 7. Real and desired evolution trajectories of the angular velocity vector, $\boldsymbol{\omega}^*(t) = [\omega_m^*(t), \omega_t^*(t)]^T$ and $\boldsymbol{\omega}(t) = [\omega_m(t), \omega_t(t)]^T$.

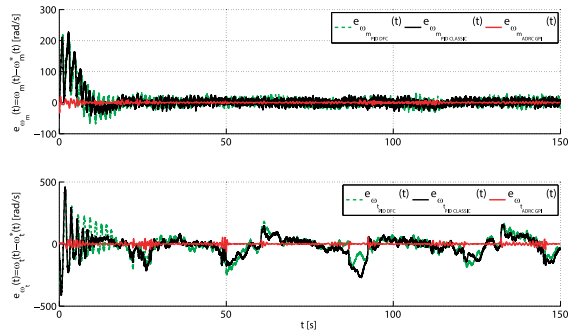

Fig. 8. Evolution of the angular velocity error vector, $\mathbf{e}_{\boldsymbol{\omega}}(t) = \boldsymbol{\omega}(t) - \boldsymbol{\omega}^*(t) = [\omega_m(t) - \omega_m^*(t), \omega_t(t) - \omega_t^*(t)]^T$.

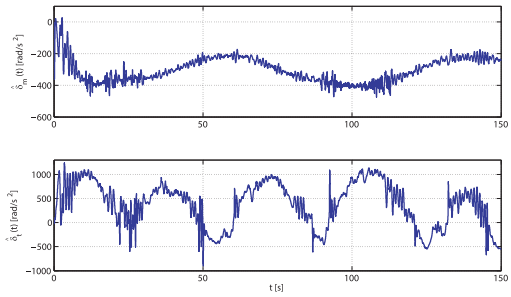

Fig. 9. Estimation of the electrical disturbance vector $\hat{\mathbf{z}}_{\mathbf{1}}^{\mathbf{e}}(t) = [\hat{\delta}_m(t), \hat{\delta}_t(t)]^T$.

filter coefficient, respectively, indicating that in spite of the undesirable effects of the noisy measurements obtained from the dc tachometers and the unmatched nature of the electrical perturbation vector, $\mathbf{z}_{\mathbf{1}}^{\mathbf{e}}(t) = [\delta_m(t), \delta_t(t)]^T$, the proposed tandem ADRC scheme efficiently corrects these undesirable effects. Fig. 9 shows the electrical disturbance estimations $\hat{\mathbf{z}}_{\mathbf{1}}^{\mathbf{e}}(t) = [\hat{\delta}_m(t), \hat{\delta}_t(t)]^T$, associated with the inner control loop in the proposed controller, and Fig. 10 illustrates the evolution of the input voltage vector, $\mathbf{u}(t) = [u_m(t), u_t(t)]^T$, in the MATLAB/Simulink environment for the three control algorithms. From the results obtained, it will be observed that the new control algorithm proposed in this paper provides the smallest control input effort. Also, note that the electrical disturbance

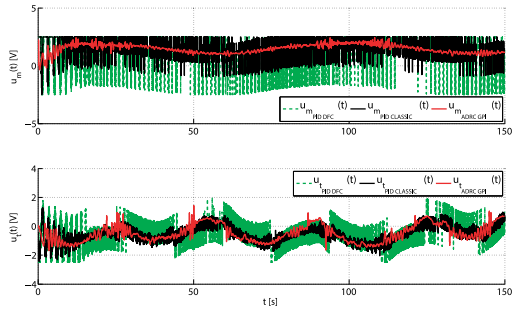

Fig. 10. Evolution of the input voltage vector, $\mathbf{u}(t) = [u_m(t), u_t(t)]^T$, in the MATLAB/Simulink environment.

estimation vector $\hat{\mathbf{z}}_{\mathbf{1}}^{\mathbf{e}}(t)$ depicted in Fig. 9 determines the shape of the control voltage vector for the robust ADRC controller $\mathbf{u}(t)$ produced (shown in Fig. 10) which tends to cancel out the effects of the additive disturbance input vector $\mathbf{z}_{\mathbf{1}}^{\mathbf{e}}(t)$. In conclusion, after comparing the experimental results obtained for the three different control laws, the new proposed control algorithm enhances the behavior of the system in the following aspects:

1) improvement to the transient response;
2) better stabilization process and small trajectory tracking errors;
3) higher robustness with regard to noisy disturbance signals;
4) better response to modeling errors and environment uncertainties;
5) smaller steady-state errors;
6) less control effort.

VII. Conclusion and Future Work

In this paper, we have described the design of an observer-based robust linear output feedback controller for the TRMS. The approach has been treated as a decentralized control of cascade nonlinear systems and we have proposed a tandem ADRC based on GPI observers as a solution. The main advantage of the proposed approach is that the controller of each subsystem of which the tandem is composed requires a minimum cooperation between the inputs in charge of controlling each subsystem. In particular, the information available for each controller is limited to the knowledge of its subsystem order, the local control input gain function, the local output and the centrally prescribed individual output reference trajectory signal. The controllers have been designed using a set of linear pure integrator systems. The controller integration systems are influenced by additive absolutely bounded, yet observable, perturbation input signals, and all the unknown state-dependent nonlinearities, externally unmodeled inputs and the interacting dynamics of the plant have been lumped together as a disturbance to be estimated and canceled. The convincing experimental results validate the effectiveness of the tandem ADRC based on GPI observers, demonstrating that it successfully deals with large initial errors, unmodeled unmatched perturbations, noisy measurements, and parametric uncertainties in the model. Finally, future work will be devoted to verify the effectiveness of the proposed ADRC control algorithm in other cascade nonlinear systems.

REFERENCES

[1] P. Castillo, A. Dzul, and R. Lozano, "Real-time stabilization and tracking of a four-rotor mini rotorcraft," *IEEE Trans. Control Syst. Technol.*, vol. 12, no. 4, pp. 510–516, Jul. 2004.

[2] A. Fernández-Caballero, L. M. Belmonte, R. Morales, and J. A. Somolinos, "Generalized proportional integral control for an unmanned quadrotor system," *Int. J. Adv. Robot. Syst.*, vol. 12, no. 85, Jul. 2015.

[3] J.-H. Yang and W.-C. Hsu, "Adaptive backstepping control for electrically driven unmanned helicopter," *Control Eng. Practice*, vol. 17, no. 8, pp. 903–913, Aug. 2009.

[4] S. Pandey and V. Laxmi, "Optimal control of twin rotor MIMO system using LQR technique," *Smart Innovation, Syst. Technol.*, vol. 31, pp. 11–21, 2015.

[5] A. Rahideh, M. Shaheed, and H. Huijberts, "Dynamic modelling of a TRMS using analytical and empirical approaches," *Control Eng. Practice*, vol. 16, no. 3, pp. 241–259, Mar. 2008.

[6] P. Mullhaupt, B. Srinivasan, J. Levine, and D. Bonvin, "Control of the toycopter using a flat approximation," *IEEE Trans. Control Syst. Technol.*, vol. 16, no. 5, pp. 882–896, Sep. 2008.

[7] J. Han, "From PID to active disturbance rejection control," *IEEE Trans. Ind. Electron.*, vol. 56, no. 3, pp. 900–906, Mar. 2009.

[8] A. Radke and Z. Gao, "A survey of state and disturbance observers for practitioners," presented at the American Control Conf., Minneapolis, MN, USA, Jun. 2006.

[9] A. Luviano-Juárez, J. Cortés-Romero, and H. Sira-Ramírez, "Synchronization of chaotic oscillators by means of generalized proportional integral observers," *Int. J. Bifurcation Chaos*, vol. 20, no. 5, pp. 1509–1517, May. 2010.

[10] R. Morales, H. Sira-Ramírez, and J. A. Somolinos, "Robust control of underactuated wheeled mobile manipulators using GPI disturbance observers," *Multibody Syst. Dyn.*, vol. 32, no. 4, pp. 511–533, Oct. 2014.

[11] J. Chocoteco, R. Morales, V. Feliu, and H. Sira-Ramírez, "Robust output feedback control for the trajectory tracking of robotic wheelchairs," *Robotica*, vol. 33, no. 1, pp. 41–59, Jan. 2015.

[12] R. Morales, H. Sira-Ramírez, and J. A. Somolinos, "Linear active disturbance rejection control of the hovercraft vessel model," *Ocean Eng.*, vol. 96, pp. 100–108, Mar. 2015.

[13] H. Sira-Ramírez, Z. Gao, and E. Canuto, "An active disturbance rejection control approach for decentralized tracking in interconnected systems," in *Proc. Eur. Control Conf.*, Jun. 2014, pp. 588–593.

[14] *Twin Rotor MIMO System, 33-220 User Manual*, Feedback Intruments Ltd., Crowborough, U.K., 1998.

[15] Y. Gliklikh, "Necessary and sufficient conditions for global-in-time existence of solutions of ordinary, stochastic, and parabolic differential equations," *Abstract Appl. Anal.*, vol. 2006, pp. 1–17, 2006.

[16] P. Kokotovic and H. K. Khalil, *Singular Perturbation Methods in Control: Analysis and Design.* Philadelphia, PA, USA: SIAM, 1999, vol. 25.

[17] H. K. Khalil, *Nonlinear Systems.* 2nd ed., Englewood Cliffs, NJ, USA: Prentice-Hall, 1996.

[18] W. Zhou, S. Shao, and Z. Gao, "A stability study of the active disturbance rejection control problem by a singular perturbation approach," *Appl. Math. Sci.*, vol. 3, no. 10, pp. 491–508, 2009.

[19] J. Lee, R. Mukherjee, and H. K. Khalil, "Application of dynamic inversion with extended high-gain observers to inverted pendulum on a cart," in *Proc. Amer. Control Conf.*, Jun. 2013, pp. 4234–4238.

[20] B.-Z. Guo and Z.-L. Zhao, "On convergence of the nonlinear active disturbance rejection control for MIMO systems," *SIAM J. Control Optim.*, vol. 51, no. 2, pp. 1727–1757, 2013.

[21] H. Sira-Ramírez, F. González-Montañez, J. A. Cortés-Romero, and A. Luviano-Juárez, "A robust linear field-oriented voltage control for the induction motor: Experimental results," *IEEE Trans. Ind. Electron.*, vol. 60, no. 8, pp. 3025–3033, Aug. 2013.

[22] R. Morales, V. Feliu, and V. Jaramillo, "Position control of very lightweight single-link flexible arms with large payload variations by using disturbance observers," *Robot. Auton. Syst.*, vol. 60, no. 4, pp. 532–547, Apr. 2012.

[23] D. L. Martinez-Vazquez, A. Rodriguez-Angeles, and H. Sira-Ramirez, "Robust GPI observer under noisy measurements," in *Proc. 6th Int. Conf. Elect. Eng. Comput. Sci. Autom. Control*, Jan. 2009, pp. 1–5.

[24] Y. I. Son, I. H. Kim, D. S. Choi, and H. Shim, "Robust cascade control of electric motor drives using dual reduced-order PI observer," *IEEE Trans. Ind. Electron.*, vol. 62, no. 6, pp. 3672–3682, Jun. 2015.

[25] *Twin Rotor MIMO System. Control Experiments, Manual 33-949S*, 1st ed., Feedback Intruments Ltd., Crowborough, U.K., 2008.

[26] S. K. Pandey and V. Laxmi, "Control of twin rotor MIMO system using PID controller with derivative filter coefficient," in *Proc. IEEE Students' Conf. Electr., Electron. Comput. Sci.*, Mar. 2014, pp. 1–6.

Lidia M. Belmonte received the B.Sc. degree in industrial engineering (Hons.) from the University of Castilla-La Mancha, Albacete, Spain, in 2008, and the M.Sc. degree in industrial engineering from the Universidad Nacional de Educación a Distancia, Madrid, Spain, in 2013. She is currently working toward the Ph.D. degree with an FPU grant in the School of Industrial Engineering, University of Castilla-La Mancha.

Her research interests include the modeling and control of unmanned aerial vehicles.

Rafael Morales received the M.Sc. and Ph.D. degrees in industrial engineering from the University of Castilla-La Mancha, Albacete, Spain, in 2002 and 2006, respectively.

He is a full-time Lecturer in the School of Industrial Engineering, University of Castilla-La Mancha. From 2007 to 2008, he was a Visiting Researcher with the Robotics Institute, Carnegie Mellon University, Pittsburgh, PA, USA. His research interests include the design, development, and control of industrial robots, assistance robots, and unmanned aerial vehicles. He is the author or coauthor of more than 80 papers published in refereed professional journals and international conference proceedings.

Dr. Morales is a Member of the Editorial Board of the *International Journal of Advanced Robotics Systems* and *Mathematical Problems in Engineering*. He received the Industrial Robot Highly Commended Award in 2007 and the Highly Commended Paper at the Literati Network Awards for Excellence 2008 from the *Industrial Robot Journal*.

Antonio Fernández-Caballero received the M.Sc. degree from the Universidad Politécnica de Madrid, Madrid, Spain, in 1993, and the Ph.D. degree from the Department of Artificial Intelligence, Universidad Nacional de Educación a Distancia, Madrid, Spain, in 2001, both in computer science.

He is a Full Professor in the Department of Computer Science, Universidad de Castilla-La Mancha, Albacete, Spain. He is the Head of the Natural and Artificial Interaction Systems Research Group, which is part of LoUISE, Albacete Research Institute of Informatics, Albacete, Spain. His research interests include image processing, cognitive vision, mobile robotics, affective computing, and intelligent agents. He has authored more than 300 peer-reviewed papers.

Prof. Fernández-Caballero is an Associate Editor of *Pattern Recognition Letters*, the Topic Editor-in-Chief of Vision Systems of the International Journal of Advanced Robotic Systems, and the Specialty Chief Editor of Vision Systems Theory, Tools and Applications of Frontiers in Robotics and AI, among other editorship tasks.

José A. Somolinos received the M.Sc. (Hons.) and Ph.D. (Premio Extraordinario) degrees in industrial engineering from the Universidad Nacional de Educación a Distancia, Madrid, Spain, in 1995 and 1999, respectively.

From 1995 to 2006, he was with the Department of Electrical Engineering, Universidad de Castilla-La Mancha, where he became an Associate Professor in 2002. From 2006 to 2008, he was a Visiting Professor with the Control and Automation Department, Universidad Carlos III. He is currently a Member of the Department of Oceanic Systems, Universidad Politécnica de Madrid, Madrid, Spain. He is the author or coauthor of more than 80 papers published in refereed professional journals and international conference proceedings. His research interests include the modeling and control of robotic systems, instrumentation, and industrial electronics.

2.3.2 Robust Decentralized Nonlinear Control for a Twin Rotor MIMO System

Publication Data

ABSTRACT:
This article presents the design of a novel decentralized nonlinear multivariate control scheme for an underactuated, nonlinear and multivariate laboratory helicopter denominated the twin rotor MIMO system (TRMS). The TRMS is characterized by a coupling effect between rotor dynamics and the body of the model, which is due to the action-reaction principle originated in the acceleration and deceleration of the motor-propeller groups. The proposed controller is composed of two nested loops that are utilized to achieve stabilization and precise trajectory tracking tasks for the controlled position of the generalized coordinates of the TRMS. The nonlinear internal loop is used to control the electrical dynamics of the platform, and the nonlinear external loop allows the platform to be perfectly stabilized and positioned in space. Finally, we illustrate the theoretical control developments with a set of experiments in order to verify the effectiveness of the proposed nonlinear decentralized feedback controller, in which a comparative study with other controllers is performed, illustrating the excellent performance of the proposed robust decentralized control scheme in both stabilization and trajectory tracking tasks.

CITATION:
L.M. Belmonte; R. Morales; A. Fernández-Caballero; J.A. Somolinos. "Robust Decentralized Nonlinear Control for a Twin Rotor MIMO System". *Sensors*, 16(8), article 1160. MDPI, 2016. ISSN 1424-8220. DOI:10.3390/s16081160.

© 2016 by the authors; licensee MDPI, Basel, Switzerland. This article is an open access article distributed under the terms and conditions of the Creative Commons Attribution (CC-BY) license (http://creativecommons.org/licenses/by/4.0/).

sensors

MDPI

Article

Robust Decentralized Nonlinear Control for a Twin Rotor MIMO System

Lidia María Belmonte [1], Rafael Morales [1,*], Antonio Fernández-Caballero [1] and José Andrés Somolinos [2]

[1] Escuela de Ingenieros Industriales de Albacete, Universidad de Castilla-La Mancha, 02071 Albacete, Spain; LidiaMaria.Belmonte@uclm.es (L.M.B.); Antonio.Fdez@uclm.es (A.F.-C.)

[2] Escuela Técnica Superior de Ingenieros Navales, Universidad Politécnica de Madrid, 28040 Madrid, Spain; joseandres.somolinos@upm.es

* Correspondence: Rafael.Morales@uclm.es; Tel.: +34-967-599-200 (ext. 2542); Fax: +34-967-599-224

Academic Editor: Gonzalo Pajares Martinsanz
Received: 10 June 2016; Accepted: 19 July 2016; Published: 27 July 2016

Abstract: This article presents the design of a novel decentralized nonlinear multivariate control scheme for an underactuated, nonlinear and multivariate laboratory helicopter denominated the twin rotor MIMO system (TRMS). The TRMS is characterized by a coupling effect between rotor dynamics and the body of the model, which is due to the action-reaction principle originated in the acceleration and deceleration of the motor-propeller groups. The proposed controller is composed of two nested loops that are utilized to achieve stabilization and precise trajectory tracking tasks for the controlled position of the generalized coordinates of the TRMS. The nonlinear internal loop is used to control the electrical dynamics of the platform, and the nonlinear external loop allows the platform to be perfectly stabilized and positioned in space. Finally, we illustrate the theoretical control developments with a set of experiments in order to verify the effectiveness of the proposed nonlinear decentralized feedback controller, in which a comparative study with other controllers is performed, illustrating the excellent performance of the proposed robust decentralized control scheme in both stabilization and trajectory tracking tasks.

Keywords: decentralized control; nonlinear control; time-scale model; Euler–Lagrange model; TRMS

1. Introduction

In the last few years, there has been an increased interest from researchers in developing control algorithms for unmanned aerial vehicles (UAVs) [1–6], due to the multiple applications and uses of this type of vehicle. This has motivated the use of new laboratory platforms capable of simulating the operation of the UAVs. This way, it is possible to perform experimental tests for evaluating the different designs developed. We can highlight the three-DOF hover system [7], the three-DOF helicopter system [8] and the twin rotor MIMO system (TRMS) [9], which is the platform used in this research.

The TRMS is a nonlinear and multivariate laboratory helicopter specifically designed to test and evaluate control algorithms by means of the MATLAB/Simulink® software environment. The dynamic behavior of the system is similar to a real helicopter, but with some differences due to the construction of the model that greatly hinder the modeling and design of control algorithms for this platform. As can be seen in Figure 1, the TRMS is formed by a base attached to a tower, at which end is a two-dimensional pivot that allows the mobile structure to rotate freely. The mobile part is composed of two metal beams: the horizontal beam in which ends the main and tail rotors with the corresponding propellers are positioned in perpendicular planes and the counterbalance beam affixed to the horizontal beam at the pivot to move the equilibrium point of the system.

Sensors **2016**, *16*, 1160

Figure 1. Twin rotor MIMO system (TRMS).

The electrical part of the TRMS is mainly composed of two DC motors that drive the propellers of both rotors and the interface circuit, an internal electrical circuit that adapts the input control voltages, applied in MATLAB/Simulink®, to the actual voltage value applied to each DC motor. Thus, a change in the control voltages produces a variation in the supply voltages of the motors, which results in a variation of the rotational speed of each propeller, measured by a tachometer. This way, a change in propulsive forces finally results in the movement of the platform. The movement, in the vertical and horizontal planes, is measured by two encoders that determine the pitch and yaw angles, respectively.

The movement of the TRMS presents not only a high cross-coupling between the two rotors as in a real helicopter, but also a coupling effect between rotor dynamics and the body of the model. This is due to the action-reaction principle originated in the acceleration and deceleration of the motor-propeller groups. Therefore, the control system of the TRMS generates a significant difference with regard to a real helicopter by varying the voltages applied to the rotors, which greatly complicates the system dynamics. On the other hand, the TRMS is also an underactuated system as a result of fewer control actions, which are the voltages applied to the respective rotors, compared to the four degrees of freedom of the system, which are: the pitch and yaw angles and the angular velocities of the propellers. Moreover, there are many physical parameters that cannot be measured exactly, and some of the parameters supplied by the manufacturer are changed by time, such as the friction coefficients. All of this makes the modeling and control of the system a difficult task to achieve.

There are many research works that have addressed this challenging experimental platform. In fact, the dynamic modeling of the TRMS has been studied from different approaches. Rahideh et al. define the dynamic model of the TRMS using Newtonian and Lagrangian methods and also by means of two models based on neuronal networks using Levenberg–Marquardt (LM) and gradient descent (GD) algorithms [10]. Toha et al. develop a parametric model for the TRMS based on dynamic spread factor particle swarm optimization [11]. A linear parameter varying (LPV) method of identification, by taking a local approach, is considered in order to derive an LPV model for TRMS by means of interpolation and approximation in the work of Tanaka et al. [12]. The Euler–Lagrange method is employed in the research of Tastermirov [13] to obtain a complete dynamic model of the TRMS, which is tuned and validated experimentally. More recently, a model based on first-principle modeling and later improved by gray box modeling, has been presented in [14]. The design of control algorithms for the TRMS platform has been also investigated via several approaches and control methods. Among the different contributions in this area, we can cite the following works. Juang and colleagues present a comparative study [15], by means of numerical simulations, between classical control schemes, based on the Ziegler–Nichols proportional-integral-derivative (PID) rule, the gain margin and phase margin rule, the pole placement method and novel controllers based on fuzzy logic and genetic algorithms. In the research of Wen et al. [16], the dynamic model for the TMRS is decoupled into two single

input single output (SISO) systems in order to apply a PID-based robust deadbeat control scheme for each of them, thus achieving the control of the platform. The design and experimental validation of a multi-step Newton-type model predictive control (MPC) to control the TRMS is presented in [17] where a nonlinear dynamic model of the platform is also developed. An adaptive fuzzy controller to stabilize the TRMS in a desired position or to track a specified trajectory is discussed in [18]. The work of Pandey et al. [19] in which two conventional PID controllers, improved by the use of derivative filter coefficients, are employed to the control of the pitch and yaw angles, the work of Belmonte et al. based on active disturbance rejection control (ADRC) [20] and the research of Alagoz et al. [21] about a reference model-based optimization approach for the online auto-tuning of PIDs using the stochastic multi-parameters divergence optimization (SMDO) method are other interesting investigations that are focused in the design of control schemes for the TRMS.

In the particular case of this research, we present the design of a novel decentralized nonlinear controller for the TRMS, composed of two control loops in a cascade scheme. The development of the proposed control scheme has been separated into two independent stages: the design of the inner loop or electrical controller, which is used to control the angular velocity of each propeller, and the design of the outer loop or mechanical controller, which is employed to determine the necessary velocities to control the space position of the TRMS. The effectiveness of the proposed scheme is validated by means of the experiments performed in the laboratory platform in which the proposed nonlinear controller shows an excellent performance for both stabilization and tracking tasks.

The rest of the article is organized as follows: Section 2 introduces the dynamic model of the TRMS, showing the modeling of the electrical part formed by the interface circuit and the DC motors, and the modeling of the mechanical part composed by the equations of motion of the system. Next, the design of the proposed decentralized control scheme is detailed in Section 3. The experiments carried out in order to verify the efficiency of the proposed control algorithm are presented in Section 4, where we detail the experimental setup and the obtained results, which include a comparative study with other classical controllers. Finally, some conclusions are provided in Section 5.

2. Dynamic Model

This section describes the dynamic modeling of the TRMS, and according to [10], it has been divided into the following two stages. In the first place, the electrical part of the platform is modeled, including the interface circuit, the DC motors and the propulsive forces produced by these motors. Then, a Lagrangian-based model is employed for the remaining mechanical structure. Next, each part of the dynamic model is dealt with in the next subsections.

2.1. Dynamics of the Electrical Part

The main and tail rotors (denominated as m and t, respectively) are assumed to be identical with different mechanical loads. The mathematical expressions governing the main and tail rotors are the following:

- Main rotor:

$$L_m \frac{di_m}{dt} = v_m - k_{v_m}\omega_m - R_m i_m \quad (1)$$

$$I_{m_1}\dot{\omega}_m = k_{t_m} i_m - f_{v_m}\omega_m - C_{Q_m}\omega_m|\omega_m| \quad (2)$$

- Tail rotor:

$$L_t \frac{di_t}{dt} = v_t - k_{v_t}\omega_t - R_t i_t \quad (3)$$

$$I_{t_1}\dot{\omega}_t = k_{t_t} i_t - f_{v_t}\omega_t - C_{Q_t}\omega_t|\omega_t| \quad (4)$$

where i_m and i_t are the main and tail motor currents, respectively, L_m and L_t represent the motor inductances, R_m and R_t denote the motor resistances, k_{v_m} and k_{v_t} express the motor back electromotive force (EMF) constants, ω_m and ω_t are the angular velocities of the propellers and v_m and v_t represent the input voltage of the DC motors. I_{m_1} and I_{t_1} define the moment of inertia of the rotors; the terms $k_{t_m} i_m$ and $k_{t_t} i_t$ express the main and tail electromechanical torques generated by the DC motors; $C_{Q_m}\omega_m|\omega_m|$ and $C_{Q_t}\omega_t|\omega_t|$ illustrate the aerodynamic torques; and $f_{v_m}\omega_m$ and $f_{v_t}\omega_t$ denote the friction torques. Following a similar argument as [13], the dynamics of the current of the motors defined in Expressions (1) and (3) is ignored due to the higher value of the DC motor mechanical time constants against the electrical ones. In fact, the DC motor mechanical constants (c_{m_m} and c_{m_t}) are in the order of 10^3-times higher than the DC motor electrical constants (c_{e_m} and c_{e_t}), as you may observe in Table 1, which shows the parameters of both rotors. Thereby, for the DC motor circuits, the following algebraic equations are obtained:

$$v_m - k_{v_m}\omega_m - R_m i_m = 0 \tag{5}$$

$$v_t - k_{v_t}\omega_t - R_t i_t = 0 \tag{6}$$

Table 1. Dynamic model of the TRMS: electrical parameters.

Symbol	Parameter	Value	Units
	Parameters of the Main Rotor		
k_{v_m}	Motor velocity constant	0.0202	$V \cdot rad^{-1} \cdot s$
R_m	Motor armature resistance	8	Ω
L_m	Motor armature inductance	0.86×10^{-3}	H
k_{t_m}	Electromagnetic constant torque motor	0.0202	$N \cdot m \cdot A^{-1}$
k_{u_m}	Coefficient linear relationship interface circuit	8.5	–
$C^{+}_{Q_m}$	Load factor ($\omega_m \geq 0$)	2.695×10^{-7}	$N \cdot m \cdot s^2 \cdot rad^{-2}$
$C^{-}_{Q_m}$	Load factor ($\omega_m < 0$)	2.46×10^{-7}	$N \cdot m \cdot s^2 \cdot rad^{-2}$
f_{v_m}	Viscous friction coefficient	3.89×10^{-6}	$N \cdot m \cdot rad^{-1} \cdot s$
I_{m1}	Moment of inertia about the axis of rotation	1.05×10^{-4}	$kg \cdot m^2$
c_{e_m}	Electrical time constant (L_m / R_m)	1.075×10^{-4}	s
c_{m_m}	Mechanical time constant ($I_{m1} R_m / k_{t_m} k_{v_m}$)	2.058	s
	Parameters of the Tail Rotor		
k_{v_t}	Motor velocity constant	0.0202	$V \cdot rad^{-1}\, s$
R_t	Motor armature resistance	8	Ω
L_t	Motor armature inductance	0.86×10^{-3}	H
k_{t_t}	Electromagnetic constant torque motor	0.0202	$N \cdot m \cdot A^{-1}$
k_{u_t}	Coefficient linear relationship interface circuit	6.5	–
C_{Q_t}	Load factor	1.164×10^{-8}	$N \cdot m \cdot s^2 \cdot rad^{-2}$
f_{v_t}	Viscous friction coefficient	1.715×10^{-6}	$N \cdot m \cdot rad^{-1} \cdot s$
I_{t1}	Moment of inertia about the axis of rotation	2.1×10^{-5}	$kg \cdot m^2$
c_{e_t}	Electrical time constant (L_t / R_t)	1.075×10^{-4}	s
c_{m_t}	Mechanical time constant ($I_{t1} R_t / k_{t_t} k_{v_t}$)	0.4117	s

It should be noted that the magnitude input voltages of the main and tail rotors in the MATLAB/Simulink® environment, defined as u_m and u_t, respectively, and the motor terminal voltages, defined as v_m and v_t, respectively, are nonlinear (the signals pass through a circuit interface), as was demonstrated in [10]. In our developments, it is assumed that the relationship between the control signals and the motor voltages is linear and that the differences will be canceled at the

controller stage. Therefore, the relationships between the control signals and the MATLAB/Simulink® environment are the following:

$$v_m = k_{u_m} u_m \quad (7)$$

$$v_t = k_{u_t} u_t \quad (8)$$

in which k_{u_m} and k_{u_t} are defined as constant gains. Upon operating with Equations (1)–(8) and rearranging terms, the following two equations are yielded for the main and rail rotors of the TRMS:

$$\dot{\omega}_m = \frac{k_{t_m} k_{u_m}}{I_{m_1} R_m} u_m - \left(\frac{k_{t_m} k_{v_m}}{R_m} + f_{v_m} \right) \frac{\omega_m}{I_{m_1}} - \frac{C_{Q_m}}{I_{m_1}} \omega_m |\omega_m| \quad (9)$$

$$\dot{\omega}_t = \frac{k_{t_t} k_{u_t}}{I_{t_1} R_t} u_t - \left(\frac{k_{t_t} k_{v_t}}{R_t} + f_{v_t} \right) \frac{\omega_t}{I_{t_1}} - \frac{C_{Q_t}}{I_{t_1}} \omega_t |\omega_t| \quad (10)$$

in which the value and units of each parameter of the main and tail rotors are detailed in Table 1. Finally, if we use matrix notation, the dynamic model of the electrical part of the TRMS can be expressed by means of the following expression:

$$\dot{\boldsymbol{\omega}}(t) = \mathbf{N}\mathbf{u}(t) + \boldsymbol{\Gamma}(\boldsymbol{\omega}(t)) \quad (11)$$

where $\boldsymbol{\omega}(t) = [\omega_m(t), \omega_t(t)]^T$ is the angular velocity vector, $\mathbf{u}(t) = [u_m(t), u_t(t)]^T$ is the input control voltage vector and, finally, the diagonal positive matrix $\mathbf{N} = diag(n_m, n_t)$ and the vector $\boldsymbol{\Gamma}(\boldsymbol{\omega}(t)) = [\Gamma_m(t), \Gamma_t(t)]^T$ are given by:

$$\mathbf{N} = \begin{bmatrix} n_m & 0 \\ 0 & n_t \end{bmatrix} = \begin{bmatrix} \frac{k_{t_m} k_{u_m}}{I_{m_1} R_m} & 0 \\ 0 & \frac{k_{t_t} k_{u_t}}{I_{t_1} R_t} \end{bmatrix} \quad (12)$$

$$\boldsymbol{\Gamma}(\boldsymbol{\omega}(t)) = \begin{bmatrix} \Gamma_m(t) \\ \Gamma_t(t) \end{bmatrix} = \begin{bmatrix} -\left(\frac{k_{t_m} k_{v_m}}{R_m} + f_{v_m} \right) \frac{\omega_m}{I_{m_1}} - \frac{C_{Q_m}}{I_{m_1}} \omega_m |\omega_m| \\ -\left(\frac{k_{t_t} k_{v_t}}{R_t} + f_{v_t} \right) \frac{\omega_t}{I_{t_1}} - \frac{C_{Q_t}}{I_{t_1}} \omega_t |\omega_t| \end{bmatrix} \quad (13)$$

2.2. Dynamics of the Mechanical Part

If the developments reported in [10] are used as a basis, the dynamics of the TRMS can be derived using Lagrange's formulation:

$$\frac{d}{dt} \left(\frac{\partial L}{\partial \dot{\mathbf{q}}} \right) - \frac{\partial L}{\partial \mathbf{q}} = \mathbf{Q} \quad (14)$$

where $L = K - V$ is the Lagrangian function, K and V are the kinetic and potential energies of the TRMS, $\mathbf{q}(t) = [\psi(t), \phi(t)]^T$ is a vector of generalized coordinates and $\mathbf{Q}(t) = [Q_\psi(t), Q_\phi(t)]^T$ denotes the vector of generalized forces in the TRMS. All of the necessary terms of (14) are obtained in the following subsections.

2.2.1. Evaluation of the Kinetic Energy

In order to calculate the energy of the TRMS, we consider the platform as divided into the following three subsystems: (1) the subsystem composed of the free-free beam (tail and main beam), tail rotor, main rotor, tail shield and main shield; (2) the counterbalance beam with the counterweight; and (3) the pivoted beam (see Figures 2–4). The positions of the subsystems can be expressed as the position of a point for each one, P_1, P_2, P_3, parametrized by the distance between it and the point

where the subsystem can rotate, as can be observed in the following expressions (where $S_\psi \equiv \sin\psi$, $C_\psi \equiv \cos\psi$, $S_\phi \equiv \sin\phi$ and $C_\phi \equiv \cos\phi$):

$$\mathbf{P_1}(R_1) = \begin{bmatrix} P_{1_x} & P_{1_y} & P_{1_z} \end{bmatrix}^T = \begin{bmatrix} -R_1 S_\phi C_\psi + hC_\phi & R_1 C_\phi C_\psi + hS_\phi & R_1 S_\psi \end{bmatrix}^T \quad (15)$$

$$\mathbf{P_2}(R_2) = \begin{bmatrix} P_{2_x} & P_{2_y} & P_{2_z} \end{bmatrix}^T = \begin{bmatrix} -R_2 S_\phi S_\psi + hC_\phi & R_2 C_\phi S_\psi + hS_\phi & -R_2 C_\psi \end{bmatrix}^T \quad (16)$$

$$\mathbf{P_3}(R_3) = \begin{bmatrix} P_{3_x} & P_{3_y} & P_{3_z} \end{bmatrix}^T = \begin{bmatrix} R_3 C_\phi & R_3 S_\phi & 0 \end{bmatrix}^T \quad (17)$$

where R_1 and R_2 are the distances from point O_1 to P_1 and P_2, respectively, and R_3 is the distance from P_3 to the center of the reference system, that is the point O.

In this way, the total amount of kinetic energy consists of the sum of the following three terms:

$$K = \sum_{i=1}^{3} K_i = \frac{1}{2} \sum_{i=1}^{3} \int \mathbf{v}_i^2(R_i) dm(R_i) \quad (18)$$

where K_i denotes the kinetic energy of each subsystem and $\mathbf{v}_i(R_i)$ is the velocity of each subsystem parameterized by R_i, which represents the distances R_1, R_2 and R_3 that have been defined above. The calculations of these energies are the following:

$$K_1 = \frac{1}{2} J_1 \left(C_\psi^2 \dot{\phi}^2 + \dot{\psi}^2 \right) + \frac{1}{2} h^2 m_{T_1} \dot{\phi}^2 - h S_\psi l_{T_1} m_{T_1} \dot{\phi}\dot{\psi} \quad (19)$$

$$K_2 = \frac{1}{2} J_2 \left(S_\psi^2 \dot{\phi}^2 + \dot{\psi}^2 \right) + \frac{1}{2} h^2 m_{T_2} \dot{\phi}^2 + h C_\psi l_{T_2} m_{T_2} \dot{\phi}\dot{\psi} \quad (20)$$

$$K_3 = \frac{1}{2} J_3 \dot{\phi}^2 \quad (21)$$

where:

$$\begin{aligned}
J_1 &= m_{ts} r_{ts}^2 + \frac{1}{2} m_{ms} r_{ms}^2 + \left(\frac{1}{3} m_t + m_{tr} + m_{ts} \right) l_t^2 + \left(\frac{1}{3} m_m + m_{mr} + m_{ms} \right) l_m^2 \\
m_{T_1} &= m_m + m_{mr} + m_{ms} + m_t + m_{tr} + m_{ts} \\
l_{T_1} &= \frac{\left(\frac{m_t}{2} + m_{tr} + m_{ts} \right) l_t - \left(\frac{m_m}{2} + m_{mr} + m_{ms} \right) l_m}{m_{T_1}} \\
J_2 &= \frac{1}{3} m_b l_b^2 + m_{cb} l_{cb}^2 \\
m_{T_2} &= m_b + m_{cb} \\
l_{T_2} &= \frac{m_b \frac{l_b}{2} + m_{cb} l_{cb}}{m_{T_2}} \\
J_3 &= \frac{1}{3} m_h l_h^2
\end{aligned}$$

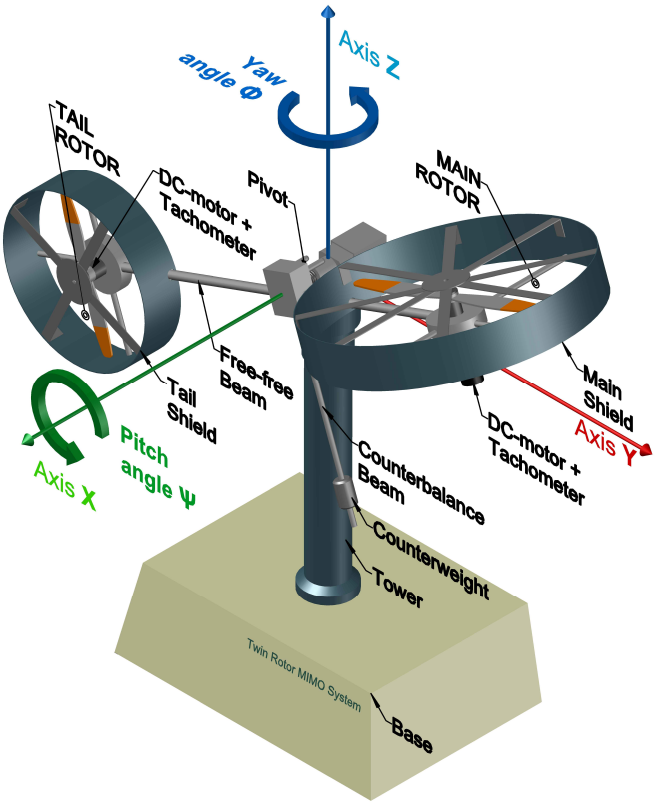

Figure 2. Twin rotor MIMO system (TRMS) prototype platform.

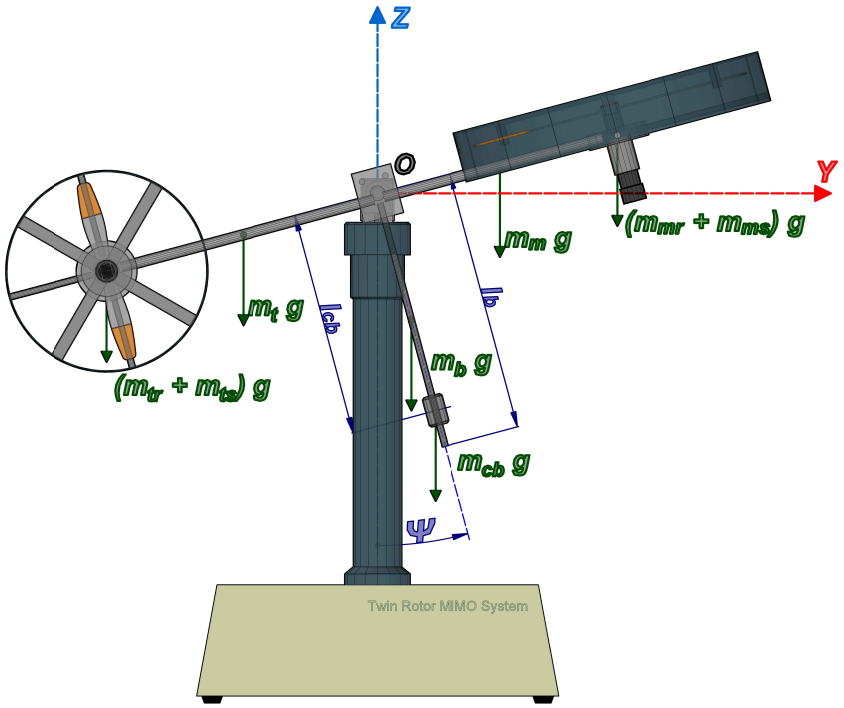

Figure 3. View of the TRMS on the vertical plane.

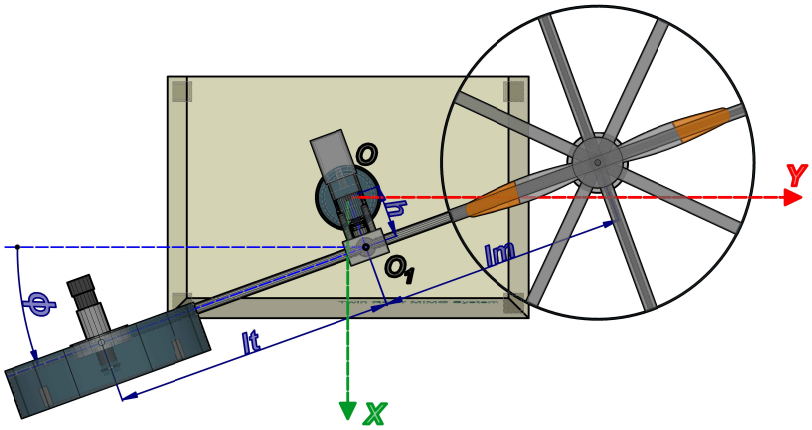

Figure 4. View of the TRMS on the horizontal plane.

2.2.2. Evaluation of the Potential Energy

The total potential energy consists of the sum of the following three terms:

$$V = \sum_{i=1}^{3} V_i = g \sum_{i=1}^{3} \int r_{zi}(R_i) dm(R_i) \tag{22}$$

where g denotes the gravity constant, V_i represents the potential energy of each one of the three subsystems in which we have divided the platform and $r_{zi}(R_i)$ is the coordinate on the z-axis of the position of each subsystem (P_{i_z}). The calculation of these energies is as follows:

$$V_1 = g S_\psi l_{T_1} m_{T_1} \tag{23}$$

$$V_2 = -g C_\psi l_{T_2} m_{T_2} \tag{24}$$

$$V_3 = 0 \tag{25}$$

2.2.3. Lagrangian

After substituting Expressions (18)–(25) in the Lagrangian expression, we obtain:

$$\begin{aligned} L = K - V \;=\; & \frac{1}{2}\left(J_1 C_\psi^2 + J_2 S_\psi^2 + J_3 + h^2\left(m_{T_1} + m_{T_2}\right)\right)\dot{\phi}^2 + \frac{1}{2}\left(J_1 + J_2\right)\dot{\psi}^2 \\ & + h\left(l_{T_2} m_{T_2} C_\psi - l_{T_1} m_{T_1} S_\psi\right)\dot{\phi}\dot{\psi} - g\left(l_{T_1} m_{T_1} S_\psi - l_{T_2} m_{T_2} C_\psi\right) \end{aligned} \tag{26}$$

2.2.4. Generalized Forces

The external forces in the mechanical system are owing to the following four physical effects: (a) aerodynamic forces created by the propellers; (b) the electromechanical forces generated by the propellers; (c) the viscous forces that model the dissipative effects that are present in the system and; (d) the elastic force created by the cable. After grouping the effect of these forces for each generalized coordinate, the following result is achieved for $\mathbf{Q}(t) = [Q_\psi(t), Q_\phi(t)]^T$:

$$Q_\psi(t) = C_{T_m}\omega_m\left|\omega_m\right| l_m - C_{R_t}\omega_t\left|\omega_t\right| - \left(f_{v_\psi}\dot{\psi} + f_{c_\psi} sign\left(\dot{\psi}\right)\right) + k_t\dot{\omega}_t \tag{27}$$

$$\begin{aligned} Q_\phi(t) &= C_{T_t}\omega_t\left|\omega_t\right| l_t C_\psi - C_{R_m}\omega_m\left|\omega_m\right| C_\psi - \left(f_{v_\phi}\dot{\phi} + f_{c_\phi} sign\left(\dot{\phi}\right)\right) - C_c\left(\phi - \phi_0\right) \\ &+ k_m\dot{\omega}_m C_\psi \end{aligned} \tag{28}$$

where $C_{T_m}\omega_m\left|\omega_m\right|l_m$ and $C_{T_t}\omega_t\left|\omega_t\right|l_tC_\psi$ represent the aerodynamic thrust torques acting along the ψ and ϕ angles, respectively; $C_{R_t}\omega_t\left|\omega_t\right|$ and $C_{R_m}\omega_m\left|\omega_m\right|C_\psi$ denote the aerodynamic cross-couplings effects generated by the propeller; the terms $\left(f_{v_\psi}\dot{\psi}+f_{c_\psi}sign\left(\dot{\psi}\right)\right)$ and $\left(f_{v_\phi}\dot{\phi}+f_{c_\phi}sign\left(\dot{\phi}\right)\right)$ define the magnitudes of friction torques for each generalized coordinate; $k_t\dot{\omega}_t$ and $k_m\dot{\omega}_mC_\psi$ express the inertial counter torques that are owing to the reaction produced by a change in the rotational speed of the rotor propellers; and the term $C_c\left(\phi-\phi_0\right)$ is the magnitude of the torque exerted by the cable (it has a certain stiffness that allows us to model it as a spring) on the ϕ angle.

Finally, it should be noted that the works of Tastermirov et al. [13] and Mullhaupt et al. [22] provide more details about the external forces in the TRMS and other laboratory platforms with similar dynamics.

2.2.5. Equations of Motion

Upon substituting Expressions (26)–(28) in Equation (14) and after some straightforward manipulations, we obtain the following equations of motion:

$$\begin{aligned}&\left(J_1+J_2\right)\ddot{\psi}+h\left(l_{T_2}m_{T_2}C_\psi-l_{T_1}m_{T_1}S_\psi\right)\ddot{\phi}+\left(\frac{\left(J_1-J_2\right)}{2}S_{2\psi}\right)\dot{\phi}^2+g\left(l_{T_1}m_{T_1}C_\psi+l_{T_2}m_{T_2}S_\psi\right)=\\&=C_{T_m}\omega_m\left|\omega_m\right|l_m-C_{R_t}\omega_t\left|\omega_t\right|-\left(f_{v_\psi}\dot{\psi}+f_{c_\psi}sign\left(\dot{\psi}\right)\right)+k_t\dot{\omega}_t\end{aligned}\tag{29}$$

$$\begin{aligned}&h\left(l_{T_2}m_{T_2}C_\psi-l_{T_1}m_{T_1}S_\psi\right)\ddot{\psi}+\left(J_1C_\psi^2+J_2S_\psi^2+J_3+h^2\left(m_{T_1}+m_{T_2}\right)\right)\ddot{\phi}\\&-h\left(l_{T_1}m_{T_1}C_\psi+l_{T_2}m_{T_2}S_\psi\right)\dot{\psi}^2+\left(\left(J_2-J_1\right)S_{2\psi}\right)\dot{\phi}\dot{\psi}=\\&=C_{T_t}\omega_t\left|\omega_t\right|l_tC_\psi-C_{R_m}\omega_m\left|\omega_m\right|C_\psi-\left(f_{v_\phi}\dot{\phi}+f_{c_\phi}sign\left(\dot{\phi}\right)\right)-C_c\left(\phi-\phi_0\right)+k_m\dot{\omega}_mC_\psi\end{aligned}\tag{30}$$

in which the value and units of all of the mechanical parameters are illustrated in Tables 2 and 3, respectively. Finally, we can express the motion equations of the system in a compact form by means of matrix notation, thus obtaining the complete dynamic model of the mechanical part of the TRMS in the following expression:

$$\mathbf{M}(\mathbf{q}(t))\ddot{\mathbf{q}}(t)+\mathbf{C}(\mathbf{q}(t),\dot{\mathbf{q}}(t))\dot{\mathbf{q}}(t)+\mathbf{G}(\mathbf{q}(t))+\mathbf{F}(\dot{\mathbf{q}}(t))+\mathbf{T}(\mathbf{q}(t),\dot{\boldsymbol{\omega}}(t))=\mathbf{E}(\mathbf{q}(t))\boldsymbol{\Omega}(t)\tag{31}$$

where:

$$\mathbf{M}(\mathbf{q}(t))=\begin{bmatrix}J_1+J_2 & h\left(l_{T_2}m_{T_2}C_\psi-l_{T_1}m_{T_1}S_\psi\right)\\ h\left(l_{T_2}m_{T_2}C_\psi-l_{T_1}m_{T_1}S_\psi\right) & J_1C_\psi^2+J_2S_\psi^2+J_3+h^2\left(m_{T_1}+m_{T_2}\right)\end{bmatrix}\tag{32}$$

$$\mathbf{C}(\mathbf{q}(t),\dot{\mathbf{q}}(t))=\begin{bmatrix}0 & \frac{1}{2}\left(J_1-J_2\right)S_{2\psi}\dot{\phi}\\ -h\left(l_{T_1}m_{T_1}C_\psi+l_{T_2}m_{T_2}S_\psi\right)\dot{\psi} & \left(J_2-J_1\right)S_{2\psi}\dot{\psi}\end{bmatrix}\tag{33}$$

$$\mathbf{G}(\mathbf{q}(t))=\begin{bmatrix}g\left(l_{T_1}m_{T_1}C_\psi+l_{T_2}m_{T_2}S_\psi\right)\\ 0\end{bmatrix}\tag{34}$$

$$\mathbf{F}(\dot{\mathbf{q}}(t))=\underbrace{\begin{bmatrix}f_{v_\psi} & 0\\ 0 & f_{v_\phi}\end{bmatrix}}_{\mathbf{F_v}}\dot{\mathbf{q}}(t)+\underbrace{\begin{bmatrix}f_{c_\psi}sgn\left(\dot{\psi}\right)\\ f_{c_\phi}sgn\left(\dot{\phi}\right)\end{bmatrix}}_{\mathbf{F_c}(\dot{\mathbf{q}}(t))}=\begin{bmatrix}f_{v_\psi}\dot{\psi}+f_{c_\psi}sgn\left(\dot{\psi}\right)\\ f_{v_\phi}\dot{\phi}+f_{c_\phi}sgn\left(\dot{\phi}\right)\end{bmatrix}\tag{35}$$

$$\mathbf{T}(\mathbf{q}(t),\dot{\boldsymbol{\omega}}(t))=\underbrace{\begin{bmatrix}0\\ C_c\left(\phi-\phi_0\right)\end{bmatrix}}_{\mathbf{M_c}(\mathbf{q}(t))}-\underbrace{\begin{bmatrix}0 & k_t\\ k_mC_\psi & 0\end{bmatrix}}_{\mathbf{M_i}(\mathbf{q}(t))}\dot{\boldsymbol{\omega}}(t)=\begin{bmatrix}-k_t\dot{\omega}_t\\ C_c\left(\phi-\phi_0\right)-k_m\dot{\omega}_mC_\psi\end{bmatrix}\tag{36}$$

$$\mathbf{E}(\mathbf{q}(t)) = \begin{bmatrix} C_{T_m} l_m & -C_{R_t} \\ -C_{R_m} C_\psi & C_{T_t} l_t C_\psi \end{bmatrix} \tag{37}$$

$$\mathbf{\Omega}(t) = \begin{bmatrix} \omega_m \, |\omega_m| \\ \omega_t \, |\omega_t| \end{bmatrix} \tag{38}$$

Table 2. Dynamic model of the TRMS: mechanical parameters.

Symbol	Parameter	Value	Units
l_t	Length of the tail part of the free-free beam	0.282	m
l_m	Length of the main part of the free-free beam	0.246	m
l_b	Length of the counterbalance beam	0.290	m
l_{cb}	Distance between the counterweight and the joint	0.276	m
r_{ms}	Radius of the main shield	0.155	m
r_{ts}	Radius of the tail shield	0.1	m
h	Length of the pivoted beam	0.06	m
m_{tr}	Mass of the tail DC motor and tail rotor	0.221	kg
m_{mr}	Mass of the main DC motor and main rotor	0.236	kg
m_{cb}	Mass of the counterweight	0.068	kg
m_t	Mass of the tail part of the free-free beam	0.015	kg
m_m	Mass of the main part of the free-free beam	0.014	kg
m_b	Mass of the counterbalance beam	0.022	kg
m_{ts}	Mass of the tail shield	0.119	kg
m_{ms}	Mass of the main shield	0.219	kg
m_h	Mass of the pivoted beam	0.01	kg

Table 3. Dynamic model of the TRMS: parameters of the pitch and yaw movements.

Symbol	Parameter	Value	Units
	Parameters of the Pitch movement		
$C^+_{T_m}$	Thrust torque coefficient of the main rotor ($\omega_m \geq 0$)	1.53×10^{-5}	$N \cdot s^2 \cdot rad^{-2}$
$C^-_{T_m}$	Thrust torque coefficient of the main rotor ($\omega_m < 0$)	8.8×10^{-6}	$N \cdot s^2 \cdot rad^{-2}$
C_{R_t}	Load torque coefficient of the tail rotor	9.7×10^{-8}	$N \cdot m \cdot s^2 \cdot rad^{-2}$
f_{v_ψ}	Viscous friction coefficient	0.0024	$N \cdot m \cdot s \cdot rad^{-1}$
f_{c_ψ}	Coulomb friction coefficient	5.69×10^{-4}	$N \cdot m$
k_t	Coefficient of the inertial counter torque due to change in ω_t	2.6×10^{-5}	$N \cdot m \cdot s^2 \cdot rad^{-1}$
	Parameters of the Yaw movement		
$C^+_{T_t}$	Thrust torque coefficient of the tail rotor ($\omega_t \geq 0$)	3.25×10^{-6}	$N \cdot s^2 \cdot rad^{-2}$
$C^-_{T_t}$	Thrust torque coefficient of the tail rotor ($\omega_t < 0$)	1.72×10^{-6}	$N \cdot s^2 \cdot rad^{-2}$
$C^+_{R_m}$	Load torque coefficient of the main rotor ($\omega_m \geq 0$)	4.9×10^{-7}	$N \cdot m \cdot s^2 \cdot rad^{-2}$
$C^-_{R_m}$	Load torque coefficient of the main rotor ($\omega_m < 0$)	4.1×10^{-7}	$N \cdot m \cdot s^2 \cdot rad^{-2}$
f_{v_ϕ}	Viscous friction coefficient	0.03	$N \cdot m \cdot s \cdot rad^{-1}$
f_{c_ϕ}	Coulomb friction coefficient	3×10^{-4}	$N \cdot m$
c_c	Coefficient of the elastic force torque created by the cable	0.016	$N \cdot m \cdot rad^{-1}$
ϕ_0	Constant for the calculation of the torque of the cable	0	rad
k_m	Coefficient of the inertial counter torque due to change in ω_m	2×10^{-4}	$N \cdot m \cdot s^2 \cdot rad^{-1}$

To conclude, the dynamic model of the mechanical part of the TRMS (31) can be summarized in a simplified form if we consider that the movement of the platform is sufficiently smooth. In this way,

the terms of the inertial counter torques, $k_t\dot{\omega}_t$ and $k_m\dot{\omega}_m C_\psi$, can be considered negligible in comparison with the other terms. Thereby, the dynamic model of the TRMS can be rewritten as:

$$\mathbf{M}(\mathbf{q}(t))\ddot{\mathbf{q}}(t) + \mathbf{D}(\mathbf{q}(t), \dot{\mathbf{q}}(t)) = \mathbf{E}(\mathbf{q}(t))\boldsymbol{\Omega}(t) \tag{39}$$

where the matrices $\mathbf{M}(\mathbf{q}(t))$, $\mathbf{E}(\mathbf{q}(t))$ and $\boldsymbol{\Omega}(t)$ have been defined in Equations (32), (37) and (38), respectively, and the new matrix $\mathbf{D}(\mathbf{q}(t), \dot{\mathbf{q}}(t)) = [D_\psi(t), D_\phi(t)]^T$ is given by:

$$D_\psi(t) = \frac{1}{2}(J_1 - J_2)\, S_{2\psi}\dot{\phi}^2 + g\left(l_{T_1} m_{T_1} C_\psi + l_{T_2} m_{T_2} S_\psi\right) + \left(f_{v_\psi}\dot{\psi} + f_{c_\psi} sgn(\dot{\psi})\right) \tag{40}$$

$$D_\phi(t) = -h\left(l_{T_1} m_{T_1} C_\psi + l_{T_2} m_{T_2} S_\psi\right)\dot{\psi}^2 + \left((J_2 - J_1)\, S_{2\psi}\right)\dot{\phi}\dot{\psi} + \left(f_{v_\phi}\dot{\phi} + f_{c_\phi} sgn(\dot{\phi})\right) + C_c(\phi - \phi_0) \tag{41}$$

3. Design of the Control System

The proposed decentralized nonlinear control scheme is based on decoupling the electrical dynamics from the mechanical dynamics. Once these dynamics have been decoupled, a nonlinear multivariate inner loop is closed in order to control the vector of the angular velocities of the propellers, $\boldsymbol{\omega}(t) = [\omega_m(t), \omega_t(t)]^T$, and then, a nonlinear multivariate outer loop is closed to control the vector of the generalized coordinates of the system, $\mathbf{q}(t) = [\psi(t), \phi(t)]^T$, in order to achieve stabilization and precise trajectory tracking tasks for the controlled position of the generalized coordinates of the TRMS. If we make the dynamics of the inner loop control much faster than the mechanical dynamics of the TRMS in Equation (39), the dynamics of the inner loop can be therefore made approximately equal to $\mathbf{I}^{2\times 2}$, (i.e., $\boldsymbol{\omega}^*(t) \approx \boldsymbol{\omega}(t)$), and the outer loop can be designed independently [23].

Among the advantages of this control scheme are: (a) the robust nonlinear controller design procedure is simplified to a great extent, since it allows one to design the multivariate inner loop in an independent manner from the multivariate outer loop, thus dividing the control design process into two much simpler design processes; (b) this scheme can be more easily and safely implemented than the standard controllers used in the control of the TRMS platform, which involve closing a single loop, because the nested control loops proposed in this work are sequentially implemented, first closing the inner loop, which exhibits a very high relative stability in the presence of system uncertainties, external disturbances and noisy corruptions, and later closing the outer loop, which is more prone to becoming unstable, but for which the risk of exhibiting unstable motions has been significantly reduced by previously having closed the inner loop; (c) the disturbances affecting the secondary or inner loop are effectively compensated before they affect the main process output, thereby improving the stability of the system; (d) the closing of the control loop around the secondary part of the process reduces the phase lag seen by the primary or outer controller, resulting in increased speed of response; (e) the cascade control scheme is not strongly sensitive to modeling errors, although large errors could lead to oscillations or instability in one of the feedback controllers; (f) any variation in the static gain of the secondary part of the process is compensated by its own tie; (g) the use of this scheme can dramatically improve the performance of control strategies, reducing both the maximum deviation and the integral error for disturbance responses. In the scheme shown in Figure 5, the outer loop controller generates an auxiliary command reference vector $\boldsymbol{\omega}^*(t) = [\omega_m^*(t), \omega_t^*(t)]^T$ for the velocities of the propellers on the basis of the tracking objective for the vector of generalized coordinates: $\mathbf{q}(t) = [\psi(t), \phi(t)]^T$. The inner loop controller takes the command vector signal generated by the outer loop $\boldsymbol{\omega}^*(t)$ as its reference for the inner loop propeller velocity control system. The different parts of the proposed control scheme are explained next.

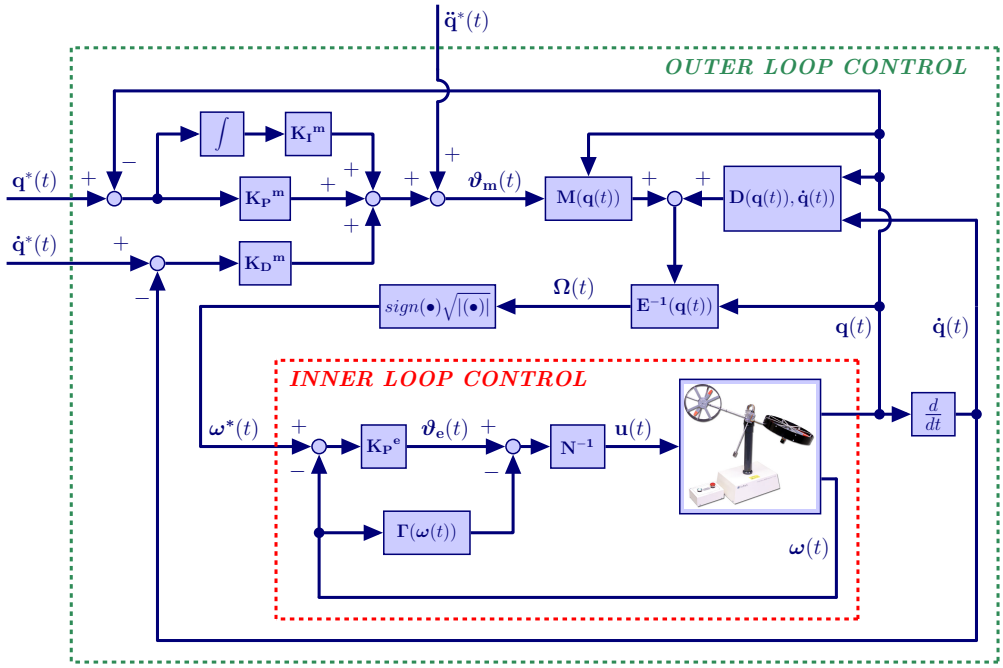

Figure 5. Robust decentralized nonlinear control scheme for the TRMS.

3.1. Inner Loop Control

The inner loop control is designed to calculate the required values for the input control voltages of the motors in the MATLAB/Simulink® environment, $\mathbf{u}(t) = [u_m(t), u_t(t)]^T$, in order to reduce and eliminate the difference between the vector of angular velocities of the propellers of the TRMS, $\boldsymbol{\omega}(t) = [\omega_m(t), \omega_t(t)]^T$, and the reference vector of these angular velocities, $\boldsymbol{\omega}^*(t) = [\omega_m^*(t), \omega_t^*(t)]^T$, which is the output of the outer loop. In this sense, the feedback multivariate control input, $\mathbf{u}(t) = [u_m(t), u_t(t)]^T$, is synthesized as a nonlinear input transformation and classical proportional controller with a nonlinear cancellation vector:

$$\mathbf{u}(t) = \mathbf{N}^{-1}[\boldsymbol{\vartheta}_\mathbf{e}(t) - \boldsymbol{\Gamma}(\boldsymbol{\omega}(t))] \tag{42}$$

in which $\mathbf{N}$ and $\boldsymbol{\Gamma}(\boldsymbol{\omega}(t))$ are defined in Equations (12) and (13), respectively, and $\boldsymbol{\vartheta}_\mathbf{e}(t) = [\vartheta_m(t), \vartheta_t(t)]^T$ represents a vector of auxiliary control inputs, given by:

$$\boldsymbol{\vartheta}_\mathbf{e}(t) = \dot{\boldsymbol{\omega}}(t) = -\mathbf{K}_\mathbf{P}^\mathbf{e}[\boldsymbol{\omega}(t) - \boldsymbol{\omega}^*(t)] \tag{43}$$

where $\mathbf{K}_\mathbf{P}^\mathbf{e} \in \mathbb{R}^{2\times 2}$ is a constant diagonal positive definitive matrix that represents the design elements of a vector-valued classical proportional controller.

The closed loop tracking error vector, $\mathbf{e}_\omega(t) = \boldsymbol{\omega}(t) - \boldsymbol{\omega}^*(t)$, for the electrical part is obtained after substituting Expression (42) in the dynamic model of the electrical part of the system in Equation (11), yielding the following expression:

$$\dot{\boldsymbol{\omega}}(t) + \mathbf{K}_\mathbf{P}^\mathbf{e}\mathbf{e}_\omega(t) = 0 \tag{44}$$

The controller design matrix $\mathbf{K}_\mathbf{P}^\mathbf{e}$ is designed so as to render the following 2×2 complex-valued diagonal matrix, $\mathbf{p}_\mathbf{c}^\mathbf{e}(s)$, defined as:

$$\mathbf{p}_\mathbf{c}^\mathbf{e}(s) = \mathbf{I}^{2\times 2}s + \mathbf{K}_\mathbf{P}^\mathbf{e} \tag{45}$$

as first degree Hurwitz polynomials with the desired roots located in the left half of the complex plane in order to achieve the convergence of the tracking error dynamics to a small vicinity around the origin of the error phase space. In particular, the constant controller gain matrix $\mathbf{K_P^e}$ of the closed loop characteristic polynomial is determined by means of a term by term comparison with the following desired Hurtwitz 2×2 diagonal matrix:

$$\mathbf{p_{c_d}^e}(s) = \mathbf{I}^{2\times 2}s + \mathbf{p_c^e} \tag{46}$$

where $\mathbf{p_c^e} \in \mathbb{R}^{2\times 2}$ is a diagonal positive definite matrix, which represents the desired position of the poles in closed loop. Therefore, the design controller gain is given by:

$$\mathbf{K_P^e} = \mathbf{p_c^e} \tag{47}$$

Finally, to conclude the description of the inner loop control, we highlight again that the design parameters are selected for the sake of making the dynamics of the inner loop control much faster than the outer loop dynamics, this way ensuring the functioning of the cascade controller [24]. The secondary controller must be relatively quick so that it attenuates a disturbance before the disturbance affects the primary controlled variable. A general guideline is that the secondary one should be three-times faster than the primary [25]. It should be noted that the cascade strategy has to be tuned in a sequential manner. In this procedure, the inner loop control should be tuned first, because the secondary controller or inner loop affects the open-loop dynamics of the primary or outer loop. Thereby, and in order to tune the parameters in the inner loop control, which are the gains of the proportional controller defined in matrix $\mathbf{K_P^e}$, the primary controller will be disconnected, i.e., the cascade should be open, and then, the electrical controller will be tuned in a conventional manner, which involves a plant experiment, initial tuning calculation and fine-tuning based on a closed-loop dynamic response.

3.2. Outer Loop Control

The objective of the outer loop control is to determine the required values for the angular velocities of the main and tail rotors, i.e., the reference vector for the angular velocities, which is the reference input of the inner loop, $\boldsymbol{\omega}^*(t) = [\omega_m^*(t), \omega_t^*(t)]^T$, in order to eliminate the difference between the generalized coordinates of the TRMS, $\mathbf{q}(t) = [\psi(t), \phi(t)]^T$, and the reference trajectories for these coordinates, $\mathbf{q}^*(t) = [\psi^*(t), \phi^*(t)]^T$. To achieve this goal, the following multivariate nonlinear feedback control input vector, $\boldsymbol{\Omega}(t)$, is synthesized as a nonlinear input transformation and a proportional-integral-derivative (PID) controller with a nonlinear cancellation vector:

$$\boldsymbol{\Omega}(t) = \mathbf{E^{-1}}(\mathbf{q}(t))[\mathbf{M}(\mathbf{q}(t))\boldsymbol{\vartheta}_\mathbf{m}(t) + \mathbf{D}(\mathbf{q}(t), \dot{\mathbf{q}}(t))] \tag{48}$$

where $\boldsymbol{\vartheta}_\mathbf{m}(t) = [\vartheta_\psi(t), \vartheta_\phi(t)]^T$ represents a vector of auxiliary control variables, given by:

$$\boldsymbol{\vartheta}_\mathbf{m}(t) = \ddot{\mathbf{q}}(t) = \ddot{\mathbf{q}}^*(t) - \mathbf{K_D^m}(\dot{\mathbf{q}}(t) - \dot{\mathbf{q}}^*(t)) - \mathbf{K_P^m}(\mathbf{q}(t) - \mathbf{q}^*(t)) - \mathbf{K_I^m}\int(\mathbf{q}(t) - \mathbf{q}^*(t)) \tag{49}$$

where $\mathbf{K_D^m}$, $\mathbf{K_P^m}$ and $\mathbf{K_I^m} \in \mathbb{R}^{2\times 2}$ are diagonal positive definitive matrices that represent the design elements of a vector-valued classical proportional-integral-derivative multivariate controller.

The closed loop tracking error vector, $\mathbf{e_q}(t) = \mathbf{q}(t) - \mathbf{q}^*(t)$, for the mechanical part is obtained after substituting Expression (48) in the simplified model of the mechanical part in Equation (39), yielding the following expression:

$$\mathbf{e_q^{(3)}}(t) + \mathbf{K_D^m}\ddot{\mathbf{e}}_\mathbf{q}(t) + \mathbf{K_P^m}\dot{\mathbf{e}}_\mathbf{q}(t) + \mathbf{K_I^m}\mathbf{e_q}(t) = 0 \tag{50}$$

In order to achieve the convergence of the tracking error dynamics to a small vicinity around the origin of the tracking error phase space, the controller design matrices $\mathbf{K_D^m}$, $\mathbf{K_P^m}$ and $\mathbf{K_I^m}$ are chosen

in such a manner that all non-zero components of the 2×2 complex valued diagonal matrix, $\mathbf{p_c^m}(s)$, defined as,

$$\mathbf{p_c^m}(s) = \mathbf{I}^{2\times 2}s^3 + \mathbf{K_D^m}s^2 + \mathbf{K_P^m}s + \mathbf{K_I^m} \tag{51}$$

are all third degree Hurwitz polynomials whose roots are located sufficiently far into the left half on the complex plane. The stability of Expression (51) can be studied by using the Routh–Hurwitz criterion. Bearing in mind that the set of design matrices $\mathbf{K_P^m}$, $\mathbf{K_D^m}$ and $\mathbf{K_I^m}$ are diagonal, the stability of each error variable $\mathbf{e_q}(t) = [e_\psi(t); e_\phi(t)]^T = [\psi(t) - \psi^*(t); \phi(t) - \phi^*(t)]^T$ can be studied in an independent manner. After applying the Routh–Hurwitz criterion, one obtains the following stability conditions: (i) $K_{D_i}^m, K_{P_i}^m > 0$; and (ii) $0 < K_{I_i}^m < K_{D_i}^m \cdot K_{P_i}^m$ for $i = \psi, \phi$. After considering the previous stability restrictions, the constant controller gains $\mathbf{K_D^m}$, $\mathbf{K_P^m}$ and $\mathbf{K_I^m}$ of the closed loop characteristic polynomial are determined by using a term by term comparison with the following desired Hurtwitz 2×2 complex-valued diagonal matrix:

$$\mathbf{p_{c_d}^m}(s) = \left(\mathbf{I}^{2\times 2}s + \mathbf{p_c^m}\right)\left(\mathbf{I}^{2\times 2}s^2 + 2\boldsymbol{\zeta}_\mathbf{c}^\mathbf{m}\boldsymbol{\omega}_\mathbf{c}^\mathbf{m}s + (\boldsymbol{\omega}_\mathbf{c}^\mathbf{m})^2\right) \tag{52}$$

where $\mathbf{p_c^m}$, $\boldsymbol{\zeta}_\mathbf{c}^\mathbf{m}$ and $\boldsymbol{\omega}_\mathbf{c}^\mathbf{m} \in \mathbb{R}^{2\times 2}$ are diagonal positive definite matrices. Therefore, the design controller gains are given by:

$$\mathbf{K_D^m} = 2\boldsymbol{\zeta}_\mathbf{c}^\mathbf{m}\boldsymbol{\omega}_\mathbf{c}^\mathbf{m} + \mathbf{p_c^m} \tag{53}$$

$$\mathbf{K_P^m} = (\boldsymbol{\omega}_\mathbf{c}^\mathbf{m})^2 + 2\boldsymbol{\zeta}_\mathbf{c}^\mathbf{m}\boldsymbol{\omega}_\mathbf{c}^\mathbf{m}\mathbf{p_c^m} \tag{54}$$

$$\mathbf{K_I^m} = \mathbf{p_c^m}(\boldsymbol{\omega}_\mathbf{c}^\mathbf{m})^2 \tag{55}$$

Finally, the necessary angular velocity vector values, $\boldsymbol{\omega}^*(t) = [\omega_m^*(t), \omega_t^*(t)]^T$, are obtained from the input control vector, $\boldsymbol{\Omega}(t) = [\omega_m \left|\omega_m\right|, \omega_t \left|\omega_t\right|]^T$, by performing the following operation:

$$\boldsymbol{\omega}^*(t) = \begin{bmatrix} \omega_m^*(t) \\ \omega_t^*(t) \end{bmatrix} = \begin{bmatrix} sign\left(\omega_m \left|\omega_m\right|\right)\sqrt{\left|\omega_m \left|\omega_m\right|\right|} \\ sign\left(\omega_t \left|\omega_t\right|\right)\sqrt{\left|\omega_t \left|\omega_t\right|\right|} \end{bmatrix} \tag{56}$$

4. Experimental Section

This section describes the experiments carried out to verify the effectiveness of the proposed control algorithm. In the following subsections, we briefly explain the experimental platform and the software tools, and after that, we illustrate the experimental results on the real platform, including a comparison with other control algorithms in terms of both stabilization and trajectory tracking task performance.

4.1. Experimental Setup

The implementation of the designed robust decentralized controller is carried out by using the following equipment:

- A twin rotor MIMO system provided by Feedback Instruments® (see Figure 1 and [9]).
- A PC operating in a Windows® environment using software tools from *MathWorks® Inc* (MATLAB®, Simulink, Control Toolbox, Real Time Workshop® (RTW), Real Time Windows Target® (RTWT)) and Visual C^{++} Professional®.
- The real TRMS is connected to the computer by means of an Advantech® PCI1711 card, which is accessible in the MATLAB/Simulink® environment through the Real-Time Toolbox®.
- The control signals in the MATLAB/Simulink® environment consist of two input voltages (in the range $[-2.5, 2.5]$ V) for the two DC motors A-max 26 provided by Maxon Motor®.
- The vector of generalized coordinates, $\mathbf{q}(t) = [\psi(t), \phi(t)]^T$, are measured by using two HCTL 2016 digital encoders provided by Agilent Technologies®, and the angular velocity vector $\boldsymbol{\omega}(t) = [\omega_m(t), \omega_t(t)]^T$ is measured by using two DC-Tacho DCT 22 provided by Maxon Motor®.

- The sampling rate for the controlled system is 0.002 s.

On the other hand, the executable file for the proposed control scheme is achieved by performing the following steps (see Figure 6): MATLAB® acts as the application host environment, in which the other MathWorks® products run, and Simulink® provides a well-structured graphical interface for the implementation of the proposed nonlinear control scheme. Real Time Workshop® automatically builds a C^{++} source program from the Simulink Model. The C^{++} Compiler® compiles and links the code created by Real Time Workshop® to produce an executable program. Real Time Windows Target® communicates with the executable program acting as the control program and interfaces with the TRMS through the PCI1711 card. Real Time Windows Target® controls the two-way data, or signal flow, to and from the model (which is now an executable program), and to and from the PCI1711 card. The advantage of this approach is that the designer only needs to model the process, using the graphical tools available in Simulink®, without having to worry about the mechanics of communication to and from the TRMS.

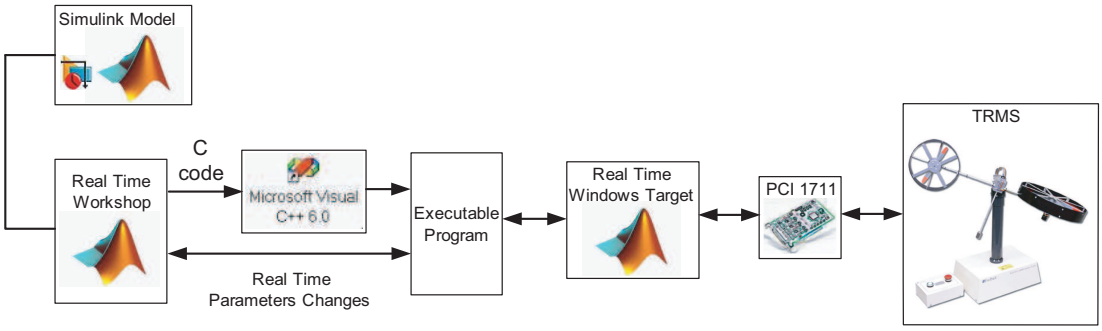

Figure 6. Control system development flow diagram.

4.2. Experimental Results

This subsection discusses the experiments carried out to verify the efficiency of the control strategy proposed in Section 3 in the following aspects: (a) robustness with regard to large initial errors; (b) quick convergence of the tracking errors to a small neighborhood of zero; (c) smooth transient responses; (d) low control effort; (e) robustness with regard to modeling errors. In the trials, the desired reference trajectories for the pitch (ψ) and the yaw (ϕ) angles have been selected in order to obtain a complex and challenging trajectory for the TRMS, which allows one to show the main characteristics and excellent performance of the proposed control scheme, but avoiding at the same time the saturation of the actuators of the laboratory platform. This reference trajectory is defined by the following expression:

$$\mathbf{q}^*(t) = \begin{bmatrix} \psi^*(t) \\ \phi^*(t) \end{bmatrix} = \begin{bmatrix} A_{0_\psi} + A_{1_\psi}\left(2sin(\omega_{1_\psi}t) + sin(\omega_{2_\psi}t)\right) \\ A_{1_\phi}sin(\omega_{1_\phi}t) + A_{2_\phi}\left(sin(\omega_{2_\phi}t) + sin(\omega_{3_\phi}t)\right) \end{bmatrix} \tag{57}$$

where $\mathbf{q}^*(t) = [\psi^*(t), \phi^*(t)]^T$ is the reference trajectory vector of the generalized coordinates, and the values of the above constants are given by:

$$\begin{aligned} A_{0_\psi} &= 0.4\ rad; & \omega_{1_\psi} &= 0.0785\ rad/s; \\ A_{1_\psi} &= 0.1\ rad; & \omega_{2_\psi} &= 0.0157\ rad/s; \\ A_{1_\phi} &= 0.8\ rad; & \omega_{1_\phi} &= 0.157\ rad/s; \\ A_{2_\phi} &= 0.3\ rad; & \omega_{2_\phi} &= 0.0785\ rad/s; \\ & & \omega_{3_\phi} &= 0.0157\ rad/s; \end{aligned} \tag{58}$$

In order to demonstrate the exponential convergence of the desired trajectories, and the robustness with respect to large initial errors, the initial position of the TRMS is defined as $\mathbf{q_0}(t) = [0,0]^T$, which represents a different value than the initial position of the reference trajectory vector $\mathbf{q}^*(t)$. With regard to the parameters of the plant used in the experimentation, the values of which are presented in Tables 1–3, we have to highlight that the discrepancies in the model due to modeling errors are around 5%, as a consequence of the difficulty involved in adequately modeling all of the dynamics terms. The small errors observed in the dynamics identification trials, which have been performed in our research, are compensated by the action of the proposed control scheme. With the use of an integral action on the outer loop, eliminating the possible steady state errors is achieved.

On the other hand, the design of the proposed nonlinear control scheme and the choice of the values of the gain vectors, which are tuned according to the procedure explained in Section 3, have been done in order to achieve a control as fast as possible, but avoiding possible saturations of the input voltages of the motors in the MATLAB/Simulink® environment, which occur at ± 2.5 V. The summary of the procedure carried out to tune the designer parameters is explained next. Firstly, the inner loop control has been tuned using the model of the electrical part of the TRMS by means of numerical simulations. In this first stage, the parameters of the proportional controller have been tuned in order to achieve the fast dynamics of the inner loop. In other words, the aim is to achieve a quick convergence of the closed loop tracking error vector, $\mathbf{e}_{\boldsymbol{\omega}}(t)$, to a small vicinity around the origin of the tracking error phase space. Secondly, we have assumed the dynamics of the inner loop to be equal to $\mathbf{I}^{2\times 2}$, and then, we have tuned, again by means of numerical simulations, the parameters of the PID controller in the outer loop. Finally, the values obtained in the simulations have been slightly adjusted in the experimental trials with the laboratory platform. Thereby, for the inner loop controller, the values of the desired Hurtwitz 2×2 complex diagonal matrix for the controller are $\mathbf{p_c^e}(s) = diag(12.0, 9.0)$, and for the outer loop controller, the values of the matrices of the desired Hurtwitz polynomial vector for the feedback controller are $\mathbf{p_c^m} = diag(1.0, 1.0)$, $\boldsymbol{\zeta}_\mathbf{c}^\mathbf{m} = diag(1.5, 1.5)$ and $\boldsymbol{\omega}_\mathbf{c}^\mathbf{m} = diag(2.0, 1.8)$. More details about how to tune controllers based on a cascade scheme can be consulted in some reference works [25–28].

In the following lines, we discuss the performance of the proposed decentralized control scheme, which is shown in the next graphs (Figures 7–11), where, in order to show the improvements of this design, we shall also compare the experimental results obtained using the proposed control (denoted in the graphs as decentralized nonlinear control (DEC NON)), a standard PID control [29] (denoted in the graphs as PID CLASSIC) and a PID control with a derivative filter coefficient [19] (denoted in the graphs as PID DFC). Figure 7 illustrates a comparison between the desired trajectory, $\mathbf{q}^*(t) = [\psi^*(t), \phi^*(t)]^T$, and the real trajectory of the TRMS, $\mathbf{q}(t) = [\psi(t), \phi(t)]^T$. This graph shows that the three algorithms are robust with regard to large initial errors. However, the proposed decentralized control scheme has the smoothest transient response and the best performance in trajectory tracking, as can also be observed in Figure 8, which shows, for each control, the closed loop tracking error vector, $\mathbf{e_q(t)} = \mathbf{q}(t) - \mathbf{q}^*(t) = [\psi(t) - \psi^*(t), \phi(t) - \phi^*(t)]^T$. The proposed decentralized controller has a closed loop tracking error vector that remains bounded within a vicinity of radius $[0.04, 0.10]^T$ *rad*, while the standard PID and the PID with derivative filter have error vectors bounded in $[0.02, 0.35]^T$ *rad* and $[0.02, 0.33]^T$ *rad*, respectively. Therefore, although the three control algorithms achieve a quick convergence of the tracking error to a small neighborhood of zero, the proposed control scheme presents the smallest error.

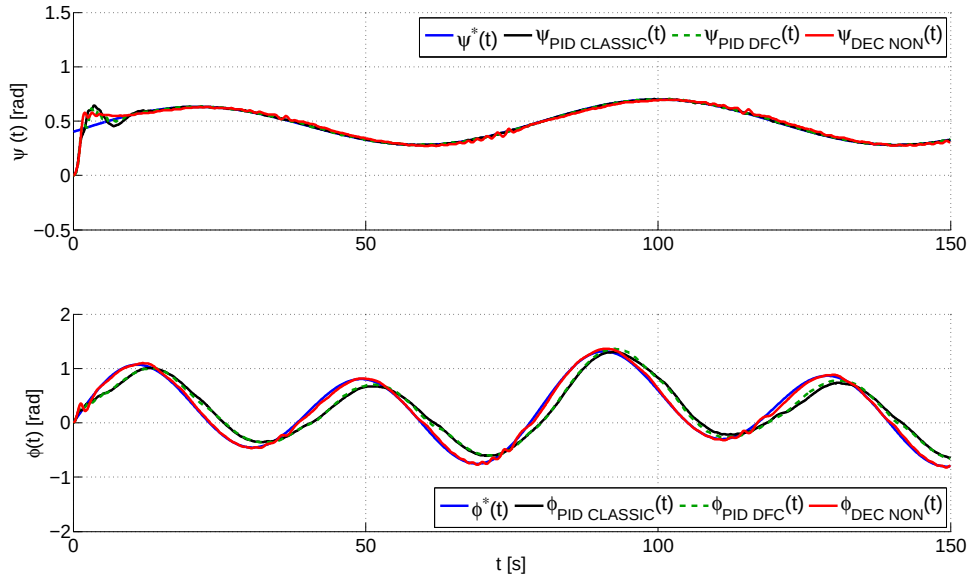

Figure 7. Real and desired evolution trajectories of the vector of the generalized coordinates of the TRMS, $\mathbf{q}(t) = [\psi(t), \phi(t)]^T$.

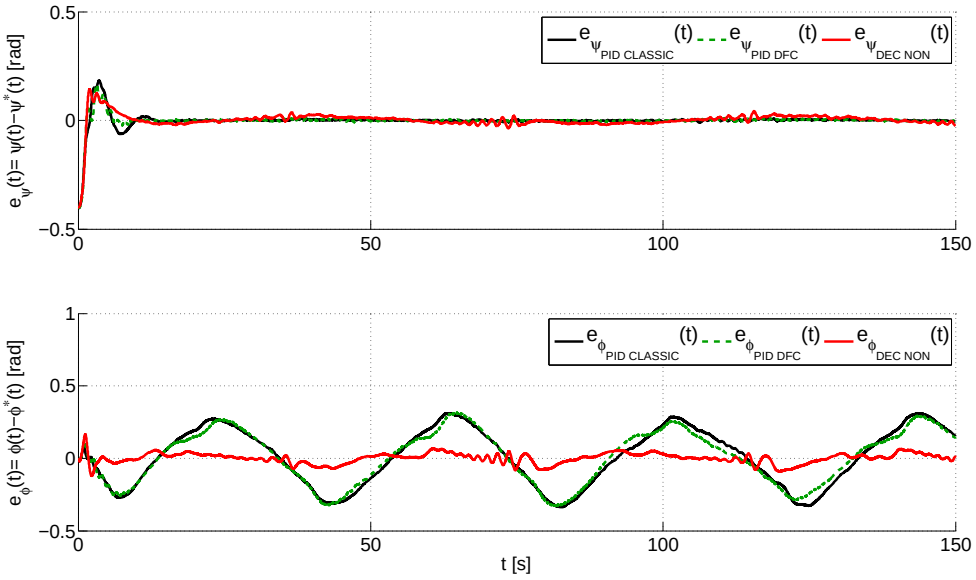

Figure 8. Evolution of the error vector of generalized coordinates of the TRMS, $\mathbf{e_q}(\mathbf{t}) = \mathbf{q}(t) - \mathbf{q}^*(t) = [\psi(t) - \psi^*(t), \phi(t) - \phi^*(t)]^T$.

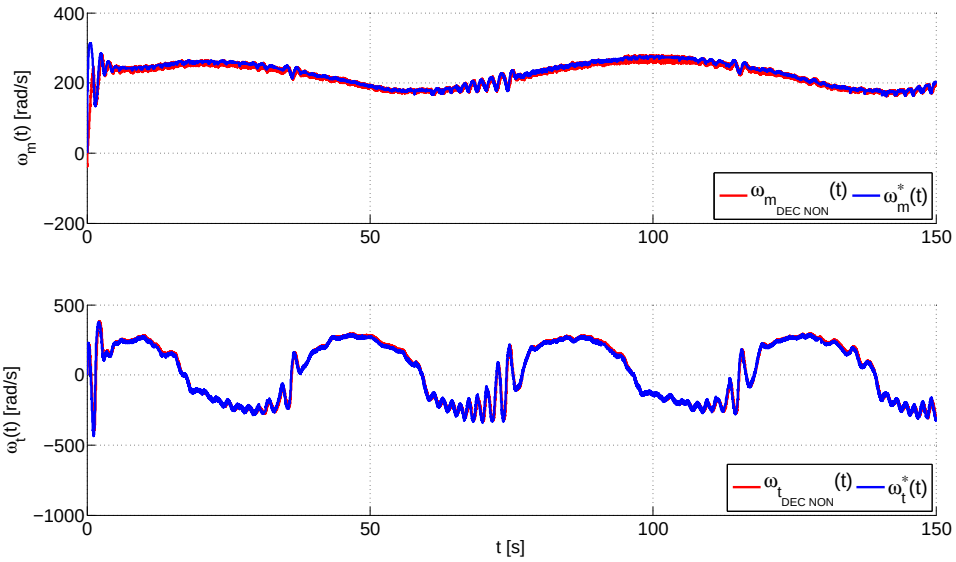

Figure 9. Real and desired evolution trajectories of the angular velocity vector, $\boldsymbol{\omega}^*(t) = [\omega_m^*(t), \omega_t^*(t)]^T$ and $\boldsymbol{\omega}(t) = [\omega_m(t), \omega_t(t)]^T$.

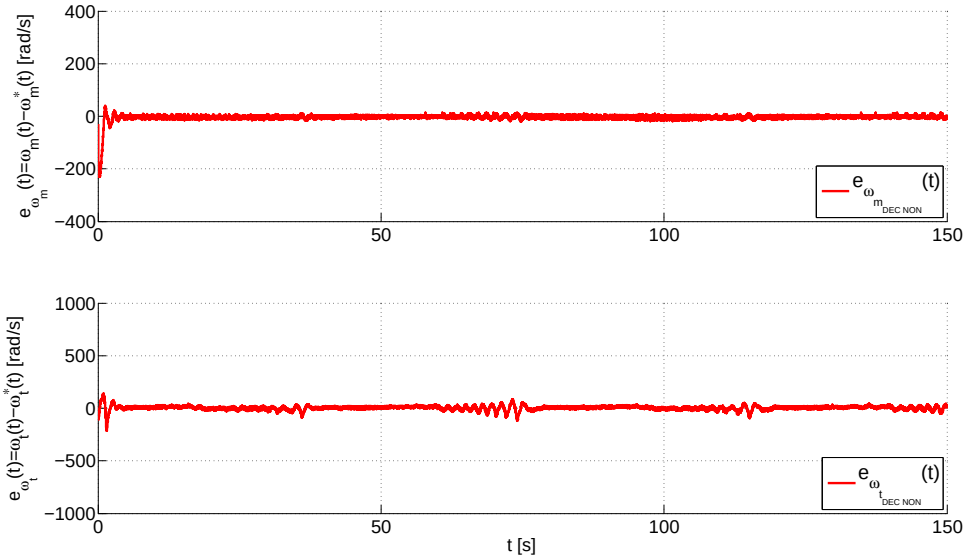

Figure 10. Evolution of the angular velocity error vector, $\mathbf{e}_{\boldsymbol{\omega}}(t) = \boldsymbol{\omega}(t) - \boldsymbol{\omega}^*(t) = [\omega_m(t) - \omega_m^*(t), \omega_t(t) - \omega_t^*(t)]^T$.

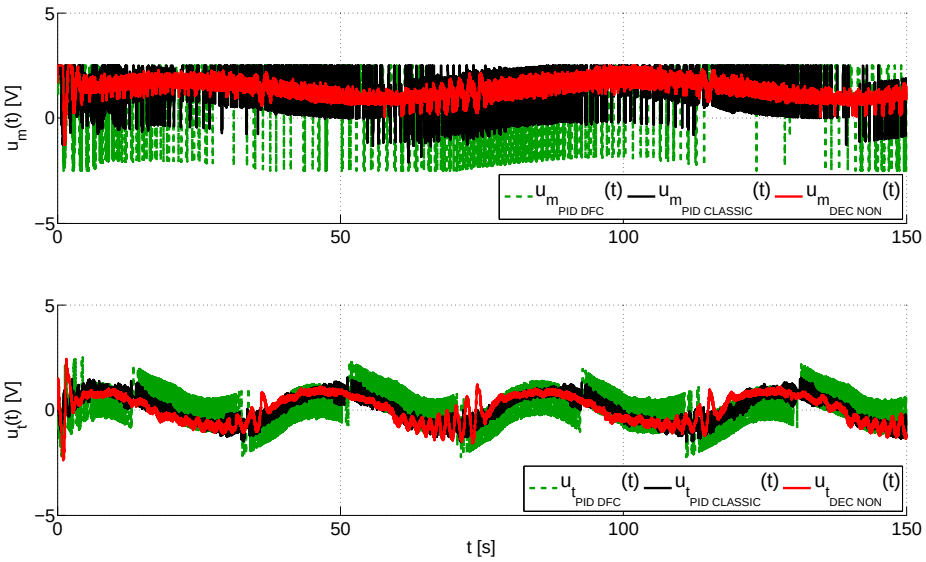

Figure 11. Evolution of the input voltage vector, $\mathbf{u}(t) = [u_m(t), u_t(t)]^T$, in the MATLAB/Simulink® environment.

On the other hand, the performance of the inner control loop is shown in Figure 9, which illustrates a comparison between the angular velocity vector, $\boldsymbol{\omega}^*(t) = [\omega_m^*(t), \omega_t^*(t)]^T$, obtained from the output of the outer loop, and the real magnitudes of the angular velocity vector, $\boldsymbol{\omega}(t) = [\omega_m(t), \omega_t(t)]^T$. Again, the proposed control has a smooth transient response and a fast convergence of the tracking error to a neighborhood near to zero as evidenced in Figure 10, which shows, for each control, that the angular velocity error vector, $\mathbf{e}_{\boldsymbol{\omega}}(t) = \boldsymbol{\omega}(t) - \boldsymbol{\omega}^*(t) = [\omega_m(t) - \omega_m^*(t), \omega_t(t) - \omega_t^*(t)]^T$, remains bounded in $[20, 120]^T$ rad/s. Finally, the input voltage vectors in the MATLAB/Simulink® environment, $\mathbf{u}(t) = [u_m(t), u_t(t)]^T$, are shown in Figure 11. This graph illustrates that the smallest control input effort is provided by the proposed control scheme, which furthermore presents a smooth evolution of the input voltage vector without saturations unlike both PID controls, the standard PID and the PID with derivative filter coefficient. As you may observe at the top of this figure, both PID controls cause the saturation of the control signal of the main rotor, which occurs at ± 2.5 V, for long periods of time during the trials. These saturations cause a worse performance of each one of these controllers in comparison with the proposed control scheme.

Additionally, the performances of the control methods have been measured in terms of the integral squared tracking error, $ISE = \int_{t_A}^{t_B} \mathbf{e_q}(t)^T \mathbf{e_q}(t) \mathrm{d}t = \int_{t_A}^{t_B} (e_\psi(t)^2 + e_\phi(t)^2) \mathrm{d}t$, the integral absolute tracking error, $IAE = \int_{t_A}^{t_B} (|e_\psi(t)| + |e_\phi(t)|) \mathrm{d}t$, and the integral time absolute tracking error, $ITAE = \int_{t_A}^{t_B} t(|e_\psi(t)| + |e_\phi(t)|) \mathrm{d}t$, where $t_A = 0$ s and $t_B = 150$ s denote the initial and final time of the simulation, and $\mathbf{e_q}(t) = [e_\psi(t), e_\phi(t)]^T = [\psi(t) - \psi^*(t), \phi(t) - \phi^*(t)]^T$ is the closed loop tracking error vector. The *ISE* and the *IAE* criteria will treat all of the tracking errors in a uniform manner. However, the *ITAE* criterion, as time appears as a factor, will heavily penalize errors that occur late in time, but ignore errors that occur early in time. The results achieved are illustrated in Table 4, showing the best performance of the proposed decentralized control scheme (DEC NON) in comparison to the other conventional controls (PID CLASSIC and PID DFC). Both PID controls show a similar behavior and have a worse performance when they are compared to the proposed control method.

Table 4. Performance of the control methods.

Control Method	*ISE*	*IAE*	*ITAE*
Robust Decentralized Nonlinear Control (DEC NON)	0.3956	6.6579	435.7
Standard PID control (PID CLASSIC)	5.8275	26.7591	2002.4
PID control with the derivative filter coefficient (PID DFC)	5.0814	24.8175	1834.4

To sum up, the experimental results show a better performance of the proposed decentralized control scheme against the other control laws. The proposed control law illustrates a better performance in the following aspects: (1) robustness in relation to large initial errors with a smooth transient response; (2) better tracking of the reference trajectories; (3) quick convergence of the tracking errors to the smallest neighborhood of zero; (4) less control effort; and (5) the absence of saturations in the input control voltages.

5. Conclusions

In this study, we have successfully designed a novel robust nonlinear multivariate decentralized control scheme for the underactuated and nonlinear twin rotor MIMO system (TRMS) laboratory platform. This control system is based on decoupling the electrical from the mechanical dynamics and the use of two nested nonlinear multivariate loops. The inner loop is designed as a nonlinear input transformation and classical proportional controller with a nonlinear cancellation vector and is responsible for the stabilization and tracking of the vector of angular velocities of the propellers of the TRMS. The outer loop control is designed as a nonlinear input transformation, a proportional-integral-derivative (PID) linear action and nonlinear compensation vector, which determines the required values for the reference velocities in order to achieve the elimination of the difference between the generalized coordinates of the TRMS and the reference trajectories for these. This independence in the design of the control loops is possible thanks to having made the dynamics of the inner loop much faster than the dynamics of the mechanical part. This control system is very simple and allows the platform to be perfectly stabilized and positioned in space. Additional advantages of this control approach are: (a) simplification of the control design procedure due to the design of two much simpler dynamics, which are controlled separately; (b) this scheme can be more easily and safely implemented than the standard controllers used in the control of the TRMS platform, which involve closing a single loop, because the nested control loops proposed in this work are sequentially implemented, first by closing the inner loop, which exhibits a very high relative stability in the presence of system uncertainties, external disturbances and noisy corruptions, and later through closing the outer loop, which is more prone to becoming unstable, but whose risk of exhibiting unstable motions has been significantly reduced by having previously closed the inner loop. The experimental tests carried out, in order to verify the performance of the proposed decentralized controller, show not only the accurate tracking of the reference trajectories, but also the better performance of the proposed control compared to the other two conventional controllers. The robustness in regards to large initial errors and possible modeling errors, the quick convergence to a small neighborhood of zero and the smooth transient response with a low control effort are the main features of the proposed design.

Acknowledgments: This work has been partially supported by the Spanish Ministerio de Economía y Competitividad/FEDER under the TEC2016-80986-R, DPI2016-80894-R, TIN2013-47074-C2-1-R and DPI2014-53499-R grants. Lidia M. Belmonte holds an Formación del Profesorado Universitario (FPU) Scholarship (FPU014/05283) from the Spanish Government.

Author Contributions: L.M.B., R.M, A. F.-C and J.A.S conceived, designed and performed the experiments. Additionally, L.M.B., R.M, A. F.-C and J.A.S analyzed the data and participated in writing the paper.

Conflicts of Interest: The authors declare no conflicts of interest.

References

1. Nonami, K.; Kendoul, F.; Suzuki, S.T. *Autonomous Flying Robots—Unmanned Aerial Vehicles and Micro Aerial Vehicles*; Springer: Heidelberg, Germany, 2010.
2. Espizona, T.; Dzul, A.; Llama, M. Linear and Nonlinear Controllers Applied to Fixed-Wing UAV. *Int. J. Adv. Robot. Syst.* **2013**, *10*, 33, doi:10.5772/53616.
3. Fernández-Caballero, A.; Belmonte, L.M.; Morales, R.; Somolinos, J.A. Generalized Proportional Integral Control for an Unmanned Quadrotor System. *Int. J. Adv. Robot. Syst.* **2015**, *12*, 85, doi:10.5772/60833.
4. Alvarenga, J.; Vitzilaios, N.I.; Valavanis, K.P.; Rutherford, M.J. Survey of Unmanned Helicopter Model-Based Navigation and Control Techniques. *J. Intell. Robot. Syst.* **2015**, *80*, 87–138.
5. Ali, Z.A.; Wang, D.; Aamir, M. Fuzzy-Based Hybrid Control Algorithm for the Stabilization of a Tri-Rotor UAV. *Sensors* **2016**, *16*, 652, doi:10.3390/s16050652.
6. Cabecinhas, D.; Naldi, R.; Silvestre, C.; Cunha, R.; Marconi, L. Robust Landing and Sliding Maneuver Hybrid Controller for a Quadrotor Vehicle. *IEEE Trans. Control Syst. Technol.* **2016**, *4*, 400–412.
7. Chen, F.; Wu, Q.; Jiang, B.; Tao, G. A Reconfiguration Scheme for Quadrotor Helicopter via Simple Adaptive Control and Quantum Logic. *IEEE Trans. Ind. Electron.* **2015**, *62*, 4328–4335.
8. Zheng, B.; Zhong, Y. Robust Attitude Regulation of a 3-DOF Helicopter Benchmark: Theory and Experiments. *IEEE Trans. Ind. Electron.* **2011**, *58*, 660–670.
9. Feedback Co. *Twin Rotor MIMO System 33-220 User Manual*; Feedback Co.: Crowborough, UK, 1998.
10. Rahideh, A.; Shaheed, M.H.; Huigberts, H.J.C. Dynamic Modelling of a TRMS Using Analytical and Empirical Approaches. *Control Eng. Pract.* **2008**, *16*, 241–259.
11. Toha, S.F.; Latiff, I.A.; Mohamad, M.; Tokhi, M.O. Parametric modelling of a TRMS using dynamic spread factor particle swarm optimisation. In Proceedings of the UKSim 2009: 11th International Conference on Computer Modelling and Simulation, Cambridge, UK, 25–27 March 2009; pp. 95–100.
12. Tanaka, H.; Ohta, Y.; Okimura, Y. A local approach to LPV-identification of a Twin Rotor MIMO System. *IFAC Proc. Vol.* **2011**, *44*, 7749–7754.
13. Tastemirov, A.; Lecchini-Visintini, A.; Morales, R.M. Complete Dynamic Model of the TWIN Rotor MIMO System (TRMS) with Experimental Validation. In Proceedings of the 39th European Rotorcraft Forum 2013 (ERF 2013), Moscow, Russia, 3–6 September 2013.
14. Chalupa, P.; Prikryl, J.; Novák, J. Modelling of Twin Rotor MIMO System. *Procedia Eng.* **2015**, *100*, 249–258.
15. Juang, J.-G.; Lin, R.-W.; Liu, W.-K. Comparison of classical control and intelligent control for a MIMO system. *Appl. Math. Comput.* **2008**, *25*, 778–791.
16. Wen, P.; Lu, T.W. Decoupling control of a twin rotor mimo system using robust deadbeat control technique. *IET Control Theory Appl.* **2008**, *2*, 999–1007.
17. Rahideh, A.; Shaheed, M.H. Constrained output feedback model predictive control for nonlinear systems. *Control Eng. Pract.* **2012**, *20*, 431–443.
18. Jahed, M.; Farrokhi, M. Robust adaptive fuzzy control of twin rotor MIMO system. *Soft Comput.* **2013**, *17*, 1847–1860.
19. Kumar-Pandey, S.; Laxmi, V. Control of Twin Rotor MIMO System using PID controller with derivative filter coefficient. In Proceedings of the 2014 IEEE Students' Conference on Electrical, Electronics and Computer Science, Bhopal, India, 1–2 March 2014.
20. Belmonte, L.M.; Morales, R.; Fernández-Caballero, A.; Somolinos, J.A. A Tandem Active Disturbance Rejection Control for a Laboratory Helicopter with Variable Speed Rotors. *IEEE Trans. Ind. Electron.* **2016**, doi:10.1109/TIE.2016.2587238.
21. Alagoz, B.B.; Ates, A.; Yeroglu, C. Auto-tuning of PID controller according to fractional-order reference model approximation for DC rotor control. *Mechatronics* **2013**, *23*, 789–797.
22. Mullhaupt, P.; Srinivasan, B.; Levine, J; Bonvin, D. Control of the Toycopter Using a Flat Approximation. *IEEE Trans. Control Syst. Technol.* **2008**, *16*, 882–896.
23. Morales, R.; Feliu, V.; Jaramillo, V. Position control of very lightweight single-link flexible arms with large payload variations by using disturbance observers. *Robot. Auton. Syst.* **2012**, *60*, 532–547.
24. Son, Y.I.; Kim, I.H.; Choi, D.S; Shim, D. Robust Cascade Control of Electric Motor Drives Using Dual Reduced-Order PI Observers. *IEEE Trans. Ind. Electron.* **2015**, *62*, 3672–3682.

25. Marlin, T.E.; *Process Control, Designing Processes and Control Systems for Dynamic Performance*, 2nd ed.; McGraw-Hill: New York, NY, USA, 2000.
26. Arrieta, O., Vilanova, R., Balaguer, P. Procedure for cascade control systems design: Choice of suitable PID tunings. *Int. J. Comput. Commun. Control* **2008**, *3*, 235–248.
27. Alfaro, V.M.; Vilanova, R.; Arrieta, O. Robust tuning of Two-Degree-of-Freedom (2-DoF) PI/PID based cascade control systems. *J. Process Control* **2009**, *19*, 1658–1670.
28. Veronesi, M., Visioli, A. Simultaneous closed-loop automatic tuning method for cascade controllers. *IET Control Theory Appl.* **2011**, *5*, 263–270.
29. Feedback Co. *Twin rotor MIMO system. Control Experiments*; Manual 33-949S Ed01; Feedback Co.: Crowborough, UK, 2008.

© 2016 by the authors; licensee MDPI, Basel, Switzerland. This article is an open access article distributed under the terms and conditions of the Creative Commons Attribution (CC-BY) license (http://creativecommons.org/licenses/by/4.0/).

2.4 Unmanned Aerial Vehicles based on Computer Vision for Assistance Robotics

To conclude the chapter dedicated to the results, this section presents the research works focused on the proposal of autonomous UAVs as aid systems for the home care of dependent persons. These works are briefly described below.

The first paper deals with the main aspects, both technical and human, that should be considered in the design and development of aerial robots based on computer vision to assist care-dependent people. In this regard, the validation system that has been deemed appropriate for the early stages of development is also introduced. This system is based on the use of virtual reality platforms for 3D simulation of UAV flight in conditions similar to domestic environments. The conclusions on these aspects are detailed in the document included in Subsection 2.4.1: "Assisting Dependent People at Home Through Autonomous Unmanned Aerial Vehicles".

The second work deals with the problem of planning the flight path of a quadrotor to carry out the monitoring of the person to be assisted. The objective is that the UAV performs an autonomous flight from its base to the person's position. In this flight, the UAV must be positioned in front of the person's face to take facial images that would be treated a posteriori for emotion analysis. The initial simulation results show the effectiveness of the proposed state-machine trajectory planner. Details of this work can be found in the document included in Subsection 2.4.2: "Trajectory Planning of a Quadrotor to Monitor Dependent People".

2.4.1 Assisting Dependent People at Home Through Autonomous Unmanned Aerial Vehicles

Publication Data

ABSTRACT:
This work describes a proposal of autonomous unmanned aerial vehicles (AUAVs) for home assistance of dependent people. AUAVs will monitor and recognize human activities during flight to improve their quality of life. However, before bringing such AUAV assistance to real homes, several challenges must be faced to make them viable and practical. Some challenges are technical and some others are related to human factors. In particular, several technical aspects are described for AUAV assistance: (1) flight control, based on our active disturbance rejection control algorithm, (2) flight planning (navigation in obstacle environments), and, (3) processing signals, acquired both from flight-control and monitoring sensors. From the assisted person's viewpoint, our research focuses on three cues: (1) the user's perception about AUAV assistance, (2) the influence on human acceptance of AUAV appearance and behavior at home, and (3) the human-robot interaction between assistant AUAV and assisted person. Finally, virtual reality platforms are proposed to carry out preliminary tests and user acceptance evaluations.

CITATION:
L.M. Belmonte; R. Morales; A.S. García; E. Segura; P. Novais; A. Fernández-Caballero. "Assisting Dependent People at Home Through Autonomous Unmanned Aerial Vehicles". *Ambient Intelligence – Software and Applications –, 10th International Symposium on Ambient Intelligence*. ISAmI 2019. AISC, vol. 1006, 216–223. Springer, 2020. ISBN 978-3-030-24096-7. DOI:10.1007/978-3-030-24097-4_26.

Reprinted by permission from Springer Nature: Springer, Ambient Intelligence – Software and Applications –, 10th International Symposium on Ambient Intelligence. ISAmI 2019. Advances in Intelligent Systems and Computing, by P. Novais, J. Lloret, P. Chamoso, D. Carneiro, E. Navarro, S. Omatu (eds), Copyright 2020.
License Number: 4620140503135. License Date: Jul 01, 2019.

Assisting Dependent People at Home Through Autonomous Unmanned Aerial Vehicles

Lidia M. Belmonte[1,2], Rafael Morales[1,2], Arturo S. García[1,2], Eva Segura[1,2], Paulo Novais[3], and Antonio Fernández-Caballero[1,2,4(✉)]

[1] Instituto de Investigación en Informática de Albacete, Universidad de Castilla-La Mancha, 02071 Albacete, Spain
{rafael.morales,arturosimon.garcia,eva.segura,Antonio.Fdez}@uclm.es
[2] Escuela Técnica Superior de Ingenieros Industriales, Universidad de Castilla-La Mancha, 02071 Albacete, Spain
lidiamaria.belmonte@uclm.es
[3] Escola de Engenharia, Universidade do Minho, Campus de Gualtar, 4710-057 Braga, Portugal
pjon@di.uminho.pt
[4] CIBERSAM (Biomedical Research Networking Centre in Mental Health), Madrid, Spain

Abstract. This work describes a proposal of autonomous unmanned aerial vehicles (AUAVs) for home assistance of dependent people. AUAVs will monitor and recognize human activities during flight to improve their quality of life. However, before bringing such AUAV assistance to real homes, several challenges must be faced to make them viable and practical. Some challenges are technical and some others are related to human factors. In particular, several technical aspects are described for AUAV assistance: (1) flight control, based on our active disturbance rejection control algorithm, (2) flight planning (navigation in obstacle environments), and, (3) processing signals, acquired both from flight-control and monitoring sensors. From the assisted person's viewpoint, our research focuses on three cues: (1) the user's perception about AUAV assistance, (2) the influence on human acceptance of AUAV appearance and behavior at home, and (3) the human-robot interaction between assistant AUAV and assisted person. Finally, virtual reality environments are proposed to carry out preliminary tests and user acceptance evaluations.

Keywords: Autonomous unmanned aerial vehicles · Home assistance · Dependent people

1 Introduction

The use of unmanned aerial vehicles (UAVs) has notably increased in the last years. Moreover, computer vision in UAVs plays a role beyond serving as mere recording and displaying of flight environments. By means of computer vision algorithms,

© Springer Nature Switzerland AG 2020
P. Novais et al. (Eds.): ISAmI 2019, AISC 1006, pp. 216–223, 2020.
https://doi.org/10.1007/978-3-030-24097-4_26

it is possible to extract useful information both of the aircraft's state and of its environment. This article proposes a framework for assisting dependent people at home through vision-based autonomous unmanned aerial vehicles (AUAVs) which do not require the presence of an operator and navigate indoor without contravening current laws for flying outdoors. Thus, the overall objective is to enhance dependent people's quality of life (QoL). QoL is the appreciation of well-being in daily human lives, including emotional, social and physical aspects. QoL of dependent people is usually reduced as a consequence of their functional incapacity for carrying normal daily activities. In addition, dependents often prefer to live in their own homes against other options, but it is difficult to provide the necessary security and home care without monitoring [1,2]. In this sense, the combination of information and communication technologies with mobile robotics provides intelligent and proactive actions to most problems that dependent people suffer at home. Thus, they facilitate the care of dependent people so that they improve their QoL in the comfort of their proper homes.

It is our conviction that aerial vehicles can complement other technologies in assisting dependents at home. Indeed, AUAVs act alone or in combination with other technologies like surveillance cameras and biometric bracelets. They also reach out where other solutions do not (for example, blind zones) through accompanying the person, positioning itself to observe his/her activities, evaluating his/her emotional state, and acting in accordance to each situation. For this sake, the main challenges for AUAVs to assist dependents within a family environment are described throughout this article. Explicitly, a double engineering solution to put in practice the above mentioned objective is described.

In first place, we have detected important technical challenges in terms of flight control, flight planning in environments with obstacles and signal processing. The solution for robust flight at home is active control by disturbance rejection, our proper algorithm recently introduced [3]. Signal processing is required for sensors that control the flight itself (e.g. inertial measurement unit sensors) and also those that observe the habitat. Obviously, the observed environment includes the dependent so that an on-board camera will capture the person's activities and facial expressions.

Secondly, human factors must consider the individual not just as an obstacle, but respecting his/her personal space when calculating the flight paths. In addition, the potential prejudices and doubts that a person has towards a flying robot, probably considered as an intruder or threat, have to be saved. Lastly, the most appropriate human-robot interaction between assisted and assistant must be defined to build a relationship of trust.

Finally, such proposal has to be evaluated. In this initial stage, the focus is put towards the acceptance of AUAVs as assistants, deepening in the user's response in immersive virtual reality environments to AUAV appearance and behavior, as well as the interaction between human and robot.

2 Technical Challenges

The development of AUAVs to serve as assistants for dependents at their own homes requires the design of a solution for autonomous and safe flight of the aircraft. The flight environment, that is the dependent person's home, is initially a place containing static obstacles from the viewpoint of navigation. However, the dependent person also moves around the environment as a dynamic obstacle that must be followed by the AUAV. In this context, the use of multi-rotor AUAVs has been considered appropriate due to their excellent maneuverability, agility, and versatility.

In addition, it is mandatory to reduce the AUAV's size in order not to interfere with people's daily routines in limited home space. However, such reduction makes difficult its control. Mainly, the sensitivity of an AUAV is highly affected both by exogenous (wind gusts) and endogenous (large non-linearities, uncertainties, dynamic couplings, etc.) disturbances that seriously affect its flight capacity and stability [4]. Several works have been developed to reduce the effects of wind gusts on the AUAV [13], but most of them are based on the assumption of persistent gusts of wind with a fixed speed, a fact that almost never occurs in reality. There are also enormous limitations on the available space, payload, and capacity of an AUAV's power supply system, leading to the use of small processors with low power consumption and limited memory [5].

On the other hand, the integration of AUAVs within the dependent person's home must be based on the principle that safety is not compromised during flight, exhibiting a level of safety equivalent to that of manned flight missions [7,8]. All this makes it necessary to design robust control algorithms that can be implemented in real small-size AUAVs [9]. Unfortunately, conventional control methods (*proportional integral derivative* (PID) and *linear quadratic* (LQR)) present serious performance problems when the size of AUAVs is reduced [10]. Therefore several methods have been developed to improve the control performance in multi-rotor AUAVs. These are non-linear type controllers based on mathematical models obtained through using complicated non-linear models and identification methods [11]. Many of them present highly complex problems, which complicates their use in real AUAVs with low consumption processors and limited memory. Another disadvantage is that the multi-rotor AUAV's dynamic model is an approximation to the real system, showing therefore problems due to parametric uncertainties and noise in sensors' measures.

In addition, robust algorithms of an adaptive nature have been developed in recent years to address the problem of parametric uncertainties in AUAVs. Unfortunately, they present problems when the multi-rotor AUAV navigates in outdoor environments (including indoors with open windows), as these control systems are affected by external wind disturbances [12]. In this sense, the development of controllers for multi-rotor AUAVs performing aggressive maneuvers under disturbances due to variable speed wind is now a completely open field.

In addition, the measurements from sensors have a high noise component, especially when the sensors are low cost [6]. In fact, signals can cause the control system to become unstable when used in feedback or compensation loops. The

search for methods to eliminate noise from signals through hardware and/or software is a field of current research in many application domains. In this way, a prevailing research field is to obtain signal filters that hardly present delays, have high robustness with respect to noise, do not need to presuppose statistical properties of noise, and can be implemented in low-cost hardware systems on-line and in real-time. Thus, a first major challenge for the development of our proposal is the design of innovative robust flight control and signal processing systems to be implemented on small processors with reduced energy consumption and limited memory.

We propose to improve the efficiency and robustness of the AUAV against significant uncertainties in its modeling and external disturbances to solve this first challenge. This has been done through the development of new algorithms based on the concept of active disturbance rejection control (ADRC) [3] and its experimentation with the Twin Rotor MIMO System (TRMS) (see Fig. 1).

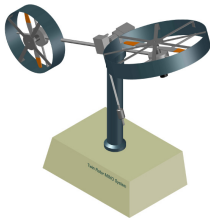

Fig. 1. TRMS system used in flight control simulations

ADRC handles the effects of disturbances (endogenous and exogenous) as an aggregate, global, purely time-dependent function without a particular structure. This concept allows the designer to avoid the use of an observer based on the non-linear structure of the (often non-existent) system and proposes a non-linear injection module of the inputs through their gain factors, instead of a merely linear observer. The arbitrarily close estimate of the aggregate disturbance allows its approximate cancellation through the appropriate control action. With this new concept it is intended to attain: (a) an improvement in the efficiency of the AUAV behavior, (b) a higher tolerance to large disturbances in the AUAV, (c) an easier adjustment and operation, and, (d) a drastic reduction of the AUAV probability to go into loss when performing home monitoring tasks.

3 Human Factor Challenges

Automated monitoring and identification of humans is a valuable tool in many areas such as rehabilitation, clinical psychology and gerontology for taking care in the family environment [14]. The availability of new static and mobile sensor types, and the consequent fusion of multi-sensory data in monitoring tasks offers novel solutions to model environments and diagnose situations based on the analysis of sensory data sequences [15].

Monitoring people physical activities and behaviors from computer vision is now well-established in our team [16]. For recognizing the emotional state of the human, a non-intrusive process is automatic detection of emotions based on the study of facial expressions [17]. The Facial Action Coding System encodes all possible facial expressions according to action units (AUs) that occur individually or in combination [18]. The exploitation of these context-aware emotional devices allows to deliver a highly personalized and dedicated collection of services designed to support users and improve their personal care.

Thus, the AUAV performs a capture of images of the dependent person's face. This requires the detection and focus on the principal parts of the face (eyes, nose, mouth, etc.). All this requires the positioning of the AUAV in front of the person's face from time to time. The captured information is sent to a base station responsible for the recognition of the dependent's emotions. In this way, the system evaluates the person's emotional state, together with his/her behavior, to determine the assistance needed for each situation.

Let us highlight that the ability of an UAV to fly autonomously is essential to carry out the proposed monitoring tasks. This ability is mandatory when considering that homes are closed environments composed of static and dynamic obstacles of different sizes and types, which endangers the safety of the monitored people. In the scientific literature, there are two approaches to autonomous navigation. (a) In deliberative motion planning the trajectories are obtained assuming a global knowledge of the environment, that is, a static environment [19]. In general, a deliberate trajectory planner is useful when the environment is known a priori, but may require too much computational effort when the environment is dynamic. (b) Reactive motion planning considers obstacle detection by means of a local sensory system (laser, optical flow sensors, stereo cameras or a single camera) and the consequent control of the trajectory to avoid the detected obstacles [20]. In this case, the information is incomplete and uncertain, and suffers from the additional problem of the difficult specification of direct movement plans.

In this sense, we propose to improve the navigation of the AUAV in environments with static and dynamic obstacles by developing a trajectory planner that takes into account the AUAV's dynamic and energetic constraints, and that contemplates the appearance of unexpected obstacles through computer vision and its corresponding integration in the AUAV control algorithm. In this respect, a navigation system composed of different stages is proposed. In the first stage it is assumed that the physical navigation environment is known (map of the home). Several methodologies for obtaining trajectories will be studied by means of optimization algorithms that result in AUAV trajectories free of obstacles. During the second stage new algorithms will be developed to provide the AUAV with the ability to adapt to dynamic environments by integrating the information coming from the sensory system to monitor the dependent person at home.

An interesting example on trajectory planning has been presented for autonomously monitoring wind turbine blades by means of a quadrotor following a hyperbolic path around the blade [21]. UAVs for monitoring large and

inaccessible structures have been also used by health, safety and environment inspectors in complex constructions such as power stations [22]. Recently, a novel framework has been developed to increment the ability of autonomous navigation, especially in cluttered environments [23]. Hence, robust and fast motion close to obstacles has been achieved, which demonstrates that a deeper integration of motion planning and perception improves robustness and computational efficiency. Future flight safety improvements will allow to extent the use of AUAVs in complex environments such as cities.

4 Virtual Reality Validation Process

The research work in AUAV assistance requires the validation of the technology and the acceptance of the dependent people. The obtained conclusions will allow to improve further developments. The validation should be carried out at homes of people willing to participate. Nevertheless, in this initial stage of development, it has been considered more appropriate to use simulations. This option saves costs, is more versatile and, most important, is much safer.

For this, we rely on virtual reality (VR) to perform evaluations, focused both on the flying robot assistant and on the assisted person. Thus, virtual worlds will be generated to process the sensor signals and evaluate the progress in flight control and planning. Virtual environments will recreate the dependent and his/her home (a closed environment with obstacles). The behavior of the AUAV will be simulated in different scenarios (see Fig. 2) using MATLAB and Unity 3D.

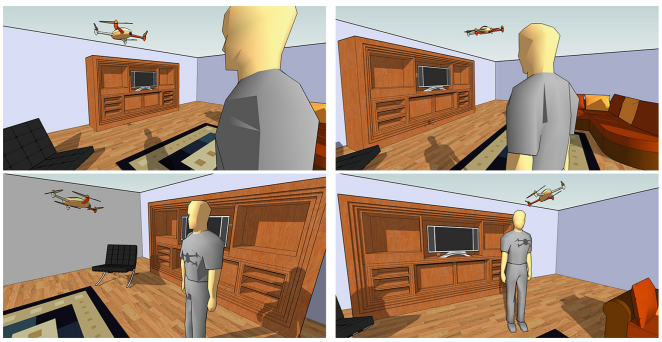

Fig. 2. VR environment to simulate AUAV assistance

Regarding a user validation of the proposal, the focus should be towards the acceptance of AUAVs as assistants, deepening in the users' responses to AUAV appearance and behavior, and human-robot interaction. Through the inclusion of immersive VR headsets and semi-immersive VR technologies, it is possible for real people to experience first hand sharing their space with AUAVs assistants. Even more, VR allow to observe the reaction of people to the flight of different virtual AUAVs around them and to investigate on several human-robot interaction techniques.

5 Conclusions

Personal dependency is defined as a functional incapacity for the development of daily-life activities, which requires assistance for their realization. However, dependent people usually prefer to live at their own homes, which implies care strategies in the family environment. This paper has proposed a solution for the development of indoor AUAV-based systems that allow home assistance of dependents with the aim of improving their quality of life.

Concretely, the use of AUAVs based on computer vision is proposed for the support and help of dependents. This proposal aims to develop UAVs capable of flying autonomously in a home to perform the task of monitoring and assisting dependents. However, this development process entails multiple challenges, both technical and human, that have to be addressed before making possible the use of AUAVs as assistants at home (e.g. a safety radius must be considered during the whole monitoring process to avoid collisions between UAV and person). In this article, we have introduced the bases for the development of solutions to advance in the line of research proposed. We have considered the aspects of AUAV control and navigation, as well as human monitoring. Lastly, virtual reality has been proposed as a key element in the validation of the robotic assistance system.

Acknowledgments. This work has been partially supported by Spanish Ministerio de Ciencia, Innovación y Universidades, Agencia Estatal de Investigación (AEI)/European Regional Development Fund (FEDER, UE) under DPI2016-80894-R grant, and by CIBERSAM of the Instituto de Salud Carlos III. Lidia M. Belmonte holds FPU014/05283 scholarship from Spanish Ministerio de Educación y Formación Profesional.

References

1. Fernández-Caballero, A., Martínez-Rodrigo, A., Pastor, J.M., Castillo, J.C., Lozano-Monasor, E., López, M.T., Zangróniz, R., Latorre, J.M., Fernández-Sotos, A.: Smart environment architecture for emotion recognition and regulation. J. Biomed. Inform. **64**, 55–73 (2016)
2. Castillo, J.C., Castro-González, Á., Fernández-Caballero, A., Latorre, J.M., Pastor, J.M., Fernández-Sotos, A., Salichs, M.A.: Software architecture for smart emotion recognition and regulation of the ageing adult. Cogn. Comput. **8**(2), 357–367 (2016)
3. Belmonte, L.M., Morales, R., Fernández-Caballero, A., Somolinos, J.A.: A tandem active disturbance rejection control for a laboratory helicopter with variable speed rotors. IEEE Trans. Ind. Electron. **63**(10), 6395–6406 (2016)
4. Mahony, R., Kumar, V., Corke, P.: Multirotor aerial vehicles: modeling, estimation, and control of quadrotor. IEEE Robot. Autom. Mag. **19**(3), 20–32 (2012)
5. Leishman, R.C., MacDonald, J.C., Beard, R.W., McLain, T.W.: Quadrotors and accelerometers: state estimation with an improved dynamic model. IEEE Control Syst. Mag. **34**(1), 28–41 (2014)
6. Tanveer, M.H., Ahmed, S.F., Hazry, D., Warsy, F.A., Joyo, M.K.: Stabilized controller design for attitude and altitude controlling of quad-rotor under disturbance and noisy conditions. Am. J. Appl. Sci. **10**(8), 819–831 (2013)

7. Belmonte, L.M., Morales, R., Fernández-Caballero, A., Somolinos, J.A.: Robust decentralized nonlinear control for a twin rotor MIMO system. Sensors **16**(8), 1160 (2016)
8. Yu, Y., Lu, G., Sun, C., Liu, H.: Robust backstepping decentralized tracking control for a 3-DOF helicopter. Nonlinear Dynam. **82**(1–2), 947–960 (2015)
9. Fernández-Caballero, A., Belmonte, L.M., Morales, R., Somolinos, J.A.: Generalized proportional integral control for an unmanned quadrotor system. Int. J. Adv. Robot. Syst. **12**, 85 (2015)
10. Bouabdallah, S., Noth, A., Siegwart, R.: PID vs LQ control techniques applied to an indoor micro quadrotor. In: Proceedings of the 2004 IEEE/RSJ International Conference on Intelligent Robotic Systems, Senday, Japan, pp. 2451–2456 (2004)
11. Bertrand, S., Guenard, N., Hamel, T., Piet-Lahanier, H., Eck, L.: A hierarchical controller for miniature VTOL UAVs: design and stability analysis using singular perturbation theory. Cont. Eng. Pract. **19**(10), 1099–1108 (2011)
12. Dydek, Z.T., Annaswamy, A.M., Lavretsky, E.: Adaptive control of quadrotor UAVs: a design trade study with flight evaluations. IEEE Trans. Cont. Syst. Tech. **21**(4), 1400–1406 (2013)
13. Sun, L., Zuo, Z.: Nonlinear adaptive trajectory tracking control for a quad-rotor with parametric uncertainty. Proc. Inst. Mech. Eng. G **229**(9), 1–13 (2014)
14. Castillo, J.C., Castro-González, Á., Alonso-Martín, F., Fernández-Caballero, A., Salichs, M.A.: Emotion detection and regulation from personal assistant robot in smart environment. In: Costa, A., Julián, V., Novais, P. (eds.) Personal Assistants: Emerging Computational Technologies, pp. 179–195. Springer, New York (2018)
15. Morales, R., Fernández-Caballero, A., Somolinos, J.A., Sira-Ramírez, H.: Integration of sensors in control and automation systems. J. Sensors **2017**, 6415876 (2017)
16. Castillo, J.C., Fernández-Caballero, A., Serrano-Cuerda, J., López, M.T., Martínez-Rodrigo, A.: Smart environment architecture for robust people detection by infrared and visible video fusion. J. Ambient. Intell. Humaniz. Comput. **8**(2), 223–237 (2017)
17. Lozano-Monasor, E., López, M.T., Vigo-Bustos, F., Fernández-Caballero, A.: Facial expression recognition in ageing adults: from lab to ambient assisted living. J. Ambient. Intell. Humaniz. Comput. **8**(4), 567–578 (2017)
18. Ekman, P., Friesen, W.V., Hager, J.C.: Facial Action Coding System. Manual and Investigator's Guide. Research Nexus, Salt Lake City (2002)
19. Lamiraux, F., Sekhavat, S., Laumond, J.P.: Motion planning and control for Hilare pulling a trailer. IEEE Trans. Robot. Autom. **15**(4), 640–652 (1999)
20. Balch, T., Arkin, R.C.: Behavior-based information control for multirobot teams. IEEE Trans. Robot. Autom **14**(6), 926–939 (1998)
21. Shivaram, S.: Structural Health Monitoring of Wind Turbine Blades using Unmanned Air Vehicles. Master's Dissertation, University of Dublin (2015)
22. Whitemore, H.: Koweit: how a drone is being used to monitor Health & Safety at the construction site, ENGIE Innovation (2015). https://innovation.engie.com/en/news/news/smart-buildings/koweit-how-a-drone-is-being-used-to-monitor-health-safety-at-the-construction-site-1/1112
23. Florence, P.R., Carter, J., Ware, J., Tedrake, R.: NanoMap: fast, uncertainty-aware proximity queries with lazy search over local 3D data. In: International Conference on Robotics and Automation (ICRA), Brisbane, Australia (2018)

2.4.2 Trajectory Planning of a Quadrotor to Monitor Dependent People

Publication Data

ABSTRACT:
This article introduces a framework for assisting dependent people at home through a vision-based autonomous unmanned aerial vehicle (UAV). Such an aircraft equipped with onboard cameras can be useful for monitoring and recognizing a dependent's activity. This work is focused on the problem of planning the flight path of a quadrotor to perform monitoring tasks. The objective is to design a trajectory planning algorithm that allows the UAV to position itself for the sake of capturing images of the dependent person's face. These images will be later treated by a base station to evaluate the persons emotional state, together with his/her behavior, this way determining the assistance needed in each situation. Numerical simulations have been carried out to validate the proposed algorithms. The results show the effectiveness of the trajectory planner to generate smooth references to our previously designed GPI (generalized proportional integral) controller. This demonstrates that a quadrotor is able to perform monitoring flights with a high motion precision.

CITATION:
L.M. Belmonte; R. Morales; A.S. García; E. Segura; P. Novais; A. Fernández-Caballero. "Trajectory Planning of a Quadrotor to Monitor Dependent People". *Understanding the Brain Function and Emotions*. IWINAC 2019, LNCS, vol. 11486, 212–221. Springer, 2019. ISBN 978-3-030-19591-5. DOI:10.1007/978-3-030-19591-5_22.

Reprinted by permission from Springer Nature: Springer, Understanding the Brain Function and Emotions. IWINAC 2019. Lecture Notes in Computer Science, by J. Ferrández Vicente, J. Álvarez-Sánchez, F. de la Paz López, J. Toledo Moreo, H. Adeli (eds), Copyright 2019.
License Number: 4597121446632. License Date: May 27, 2019.

Trajectory Planning of a Quadrotor to Monitor Dependent People

Lidia M. Belmonte[1,2], Rafael Morales[1,2], Arturo S. García[1,2], Eva Segura[1,2], Paulo Novais[3], and Antonio Fernández-Caballero[1,2(✉)]

[1] Instituto de Investigación en Informática de Albacete, Universidad de Castilla-La Mancha, 02071 Albacete, Spain
antonio.fdez@uclm.es
[2] Escuela Técnica Superior de Ingenieros Industriales, Universidad de Castilla-La Mancha, 02071 Albacete, Spain
[3] Escola de Engenharia, Universidade do Minho, Campus de Gualtar, 4710-057 Braga, Portugal

Abstract. This article introduces a framework for assisting dependent people at home through a vision-based autonomous unmanned aerial vehicle (UAV). Such an aircraft equipped with onboard cameras can be useful for monitoring and recognizing a dependent's activity. This work is focused on the problem of planning the flight path of a quadrotor to perform monitoring tasks. The objective is to design a trajectory planning algorithm that allows the UAV to position itself for the sake of capturing images of the dependent person's face. These images will be later treated by a base station to evaluate the persons emotional state, together with his/her behavior, this way determining the assistance needed in each situation. Numerical simulations have been carried out to validate the proposed algorithms. The results show the effectiveness of the trajectory planner to generate smooth references to our previously designed GPI (generalized proportional integral) controller. This demonstrates that a quadrotor is able to perform monitoring flights with a high motion precision.

Keywords: Home assistance · Dependent people · Unmanned aerial vehicles · Quadrotor · Trajectory planning · Generalized proportional integrated controller

1 Introduction

Inability to perform daily tasks reduces the autonomy and quality of life of dependent people. These people require daily help that has traditionally been provided by health personnel in specialized care centers. However, this kind of care forces dependents to leave their homes, which is an additional problem, since this is not usually the habitual preference. To counteract this situation, family members are usually those who dedicate their time to assist the dependent person. But, in many cases, this is not the ideal solution either. Family

© Springer Nature Switzerland AG 2019
J. M. Ferrández Vicente et al. (Eds.): IWINAC 2019, LNCS 11486, pp. 212–221, 2019.
https://doi.org/10.1007/978-3-030-19591-5_22

caregivers, who cope with a lack of resources and preparation, are sometimes overwhelmed by the situation. Consequently, their quality of life is also affected. In addition, every day the number of cases of dependent people living alone is more frequent. Therefore, they must obligatory move to specialized centers to receive the necessary care.

Hence, it is necessary to focus research on the development of home care strategies that allow assistance to dependents. In this way, their personal autonomy is increased. They can stay at home as long as possible and improve their quality of life. In this sense, new technologies provide novel solutions for the care and support of dependents [11,16,23,25]. Assistance robotics is fundamental at this point. However, it is essential to work with methods that allow the correct monitoring and identification of the dependent's condition for designing systems that respond to their needs [21,28]. One of them is automatic recognition of emotions, a non-invasive method in which our research group has extensive experience [6,7,13,18]. This approach requires taking photographs of the person's face for further analyzing the information collected. Thus, the person's mood is detected and the necessary assistance is determined under each situation.

In this context, unmanned aerial vehicles (UAVs) may suppose a new model of home care [17,20,30]. Indeed, an UAV equipped with an on-board camera [1,2], can be very useful in home monitoring. This type of vision-based aircraft allows, unlike other static vision systems, access to remote points, avoid dead angles, and position itself in front of the person [14,15]. The taking of snapshots allows a subsequent recognition of emotions [22]. For this purpose, this article describes a trajectory planner for the flight of a quadrocopter equipped with a camera to capture snapshots of the person's face. The aim is to generate smoothed reference trajectories for a generalized proportional integral (GPI) control algorithm [12], so that the UAV performs the simulation of a flight aimed at monitoring the person. The proposed approach is validated by numerical simulations in MALTAB/Simulink environment [3–5]. This work is part of an ongoing research to design autonomous UAVs for their future use as home assistance for dependent people.

2 Quadrotor Dynamics

A quadrotor [12,31] is a rotatory-wing UAV formed by four rotors arranged in the shape of a cross and equidistant from the center of mass of the aircraft, as shown in Fig. 1. Such a vehicle allows vertical take-off and landing, and is characterized by high maneuverability, agility, and versatility. In addition, it can move at low speed, reducing the risk of collision in flight, and improving the quality of the image recorded by a camera aboard. For all these reasons, it has been considered suitable for the proposed approach.

The quadrotor's thrust is generated by the four fixed-angle propellers of the rotors. The lift forces are modified by changing the propellers rotation speed, thus achieving the three possible movements, namely, pitch, roll, and yaw. As shown in Fig. 1, by increasing (reducing) the speed of the propeller [1] while reducing (increasing) the speed of the propeller [3] the pitch movement is obtained. In

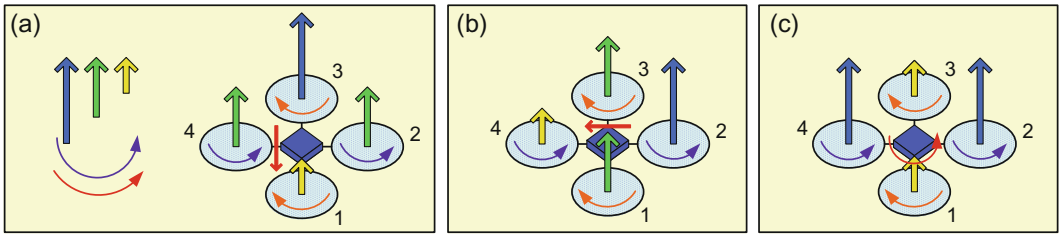

Fig. 1. Quadrotor's motion principles.

the case of increasing (reducing) the speed of the propeller [2] while reducing (increasing) the speed of the propeller [4], the roll movement is produced. And finally, by increasing (decreasing) the speed between each pair of propellers, it is possible to modify the yaw angle. The system of equations that model this dynamic behavior has been obtained through the Euler-Lagrange approach [8, 19], resulting in:

$$\begin{aligned} m\ddot{x} &= -u\sin\theta & \ddot{\psi} &= \tau_\psi \\ m\ddot{y} &= u\cos\theta\sin\phi & \ddot{\theta} &= \tau_\theta \\ m\ddot{z} &= u\cos\theta\cos\phi & \ddot{\phi} &= \tau_\phi \end{aligned}$$

where m is the mass, g is the gravity acceleration, x and y are coordinates in the horizontal plane, z is the vertical position, the angles ϕ, θ and ψ express the independent orientation angles, u is defined as the total thrust and τ_ψ, τ_θ and τ_ϕ denote the angular moments (yawing moment, pitching moment and rolling moment, respectively). Moreover, the following assumption has been considered: orientation angles θ and ϕ are upper and lower bounded in intervals $-\frac{\pi}{2} < \phi < \frac{\pi}{2}$ and $-\frac{\pi}{2} < \theta < \frac{\pi}{2}$.

3 Control Algorithm

A control scheme is necessary for regulating and tracking the trajectory that will be generated by the planner (which will be detailed in the next section) to perform a precise flight that allows monitoring a dependent in the proposed assistance system. For this purpose, we have selected a generalized proportional integral (GPI) controller, which is based on the theory of differential flatness, and which has demonstrated good performance in the control of nonlinear systems, which is the case od a quadrotor. GPI control sidesteps the need for traditional asymptotic state observers and proceeds directly to use structural state estimates in place of the actual state variables [26,27]. The effect of such structural estimates in the controller is neglected in the feedback control law by means of suitable integral output tracking error feedback control actions.

The complete design of the GPI controller can be consulted in detail in our previous work [12]. The results of this research demonstrated the effectiveness of the proposed approach in comparison with the classical PID control in the

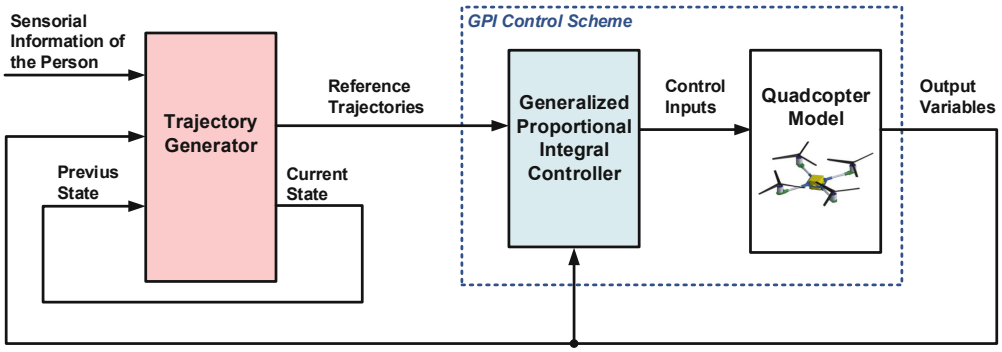

Fig. 2. General control scheme.

following terms: (a) stabilization and trajectory tracking tasks; (b) performance when the measured signals are corrupted by noise; and (c) dynamic response when atmospheric disturbances such as gusty wind affect the quadrotor.

4 Trajectory Planning

Planning trajectories is one of the problems to necessarily resolve when designing autonomous mechatronic systems and mobile robots. For this reason, it is a field that has attracted the interest of the research community in recent years [9,10, 24,29]. Thus, this section describes the trajectory planning algorithm designed for the quadrotor. The overall goal is to make a flight for monitoring a dependent person. To do this, the UAV, which will initially be in a base position on the ground, must take off, approach the person and surround him/her until finding the face. Then, the UAV will take a photograph of the face that will be sent to a base station for analysis. Finally, the UAV must conclude the circular motion around the person and return to its base.

During the planner's development, the following considerations have been considered. (i) The sensors provide the information of the person's position defined by the face's center coordinates (x_p, y_p, z_p); (ii) the person remains static during the monitoring process; (iii) there are not obstacles at the monitoring height at which the UAV works; (iv) a safety radius, R, is defined during the whole monitoring process to avoid collisions between the UAV and the person; and, (v) when the UAV does not perform any monitoring task, it remains in the base position whose coordinates are (x_b, y_b, z_b).

The trajectory planner is based on a state machine. The states define the maneuvers to be performed by the UAV during the monitoring process. For each state, the planner generates smoothed reference trajectories for the position (coordinates x, y, z) and the yaw angle (ψ) of the UAV. These references are the inputs to the GPI algorithm, which determines the required inputs to control the UAV's flight. The general control scheme of the quadrotor is illustrated in Fig. 2.

As shown in the figure, the trajectory generator depends on the person's information provided by the sensors (x_p, y_p, z_p), the UAV's output variables (x, y, z, ψ), and the previous machine state. The planner defines the references trajectories during the monitoring process so that the UAV's camera focus points towards the UAV's forward direction or the person. The considered states for the trajectory planner are the following.

- **State 0: Home.** It defines the initial state of the UAV located on its base. When it receives the instruction to start the monitoring process, it transits to state 1.
- **State 1: Takeoff.** Generation of the trajectory for the take-off of the UAV. When the quadrotor reaches the face's height defined by z_p coordinate, it transits to state 2.
- **State 2: Person Search.** The UAV is requested to rotate its position, that is, to vary its yaw angle to find the person. When the cameras center is aligned with the person, it transits to state 3.
- **State 3: Approximation.** The UAV performs an approach maneuver advancing in a straight line towards the person. The objective is to reach the Safety Position located in the circumference of radius R defined around the person. When this position is reached, it transits to state 4.
- **State 4: Waiting in Safety Position.** Intermediate state in which the UAV stops before starting the circular movement around the person in order to search his/her face. Once the programmed timeout has elapsed, it transits to state 5.
- **State 5: Face Search.** The UAV is requested to perform a circular movement around the person while varying the yaw angle so that the camera on board points towards the person. When the UAV is in front of the face, it transits to state 6.
- **State 6: Data Capture.** The UAV stops for a while to take a picture of the person's face. This image is transmitted to a base station for analysis. After the time required for data capture elapses, it transits to state 7.
- **State 7: Motion to Safety Position.** Continuation of the circular movement until the turn is completed and the previously defined safety position has been reached. In that position, it transits to state 8.
- **State 8: Base Search.** Keeping the position, the UAV is requested to modify its yaw angle until the camera is focused towards the base; then, it transits to state 9.
- **State 9: Return to Base.** The UAV must advance in a straight line until it is positioned on the base. When the UAV is on position (x_b, y_b, z_p), it transits to state 9.
- **State 10: Yaw Angle Adjustment.** The UAV is requested to modify its yaw angle so that it can subsequently land on the base correctly and be ready for the next monitoring process.
- **State 11: Landing.** The UAV lands at the base position and transits to the initial state (0) for the next monitoring process.

5 Numerical Simulations

The numerical simulations carried out to evaluate the trajectory planning for the quadrotor are detailed in this section. These simulations were performed within the MATLAB/Simulink environment. The parameters used are defined in Table 1.

Table 1. Parameters defined in the MATLAB/Simulink trials.

Planner's parameters
Safety radius, $R = 2$ [m]
Base position, $(x_b, y_b, z_b) = (0, 0, 0)$ [m]
Velocity in Z axis, $v_z = 6.8 \cdot 10^{-2}$ [m/s]
Velocity in diagonal motion (x, y), $v_d = 7 \cdot 10^{-2}$ [m/s]
Angular velocity for yaw adjustment, $\omega_\psi = 3 \cdot \pi/100$ [rad/s]
Angular velocity for circular motion, $\omega_{circle} = 3 \cdot \pi/100$ [rad/s]
Period of time for State 4 (waiting in safety position), $t_{s4} = 15$ [s]
Period of time for State 6 (data capture), $t_{s6} = 30$ [s]
Person's parameters
Face's position, $(x_p, y_p, z_p) = (4, -4, 1.7)$ [m]
Face's orientation, $\alpha_p = \pi/4$ [rad]
UAV's parameters
Initial position, $(x(0), y(0), z(0)) = (x_b, y_b, z_b)$ [m]
Initial yaw angle, $\psi(0) = 0$ [rad]
Camera's angle, $\alpha_{camera} = \pi/4$ [rad]
Controller's parameters
The same design parameters used in our previous work [12]
Simulation parameters
Sample time, $Ts = 0.01$ [s]
Simulation time, $t = 300$ [s]

Figure 3 illustrates the reference trajectory generated by the planner and the trajectory performed by the UAV, both in a 3D representation. In this picture, the planner's highlight points are detailed. Firstly, there is the base position in which the UAV remains between each monitoring process. Second, we have the person's face position and the direction (where he/she is looking at), which is represented by an arrow. In third place, there is the safety position reached by the UAV in the approximation maneuver and the same position where the UAV returns after taking the photo. Finally, we have the position where the UAV stops to capture that data.

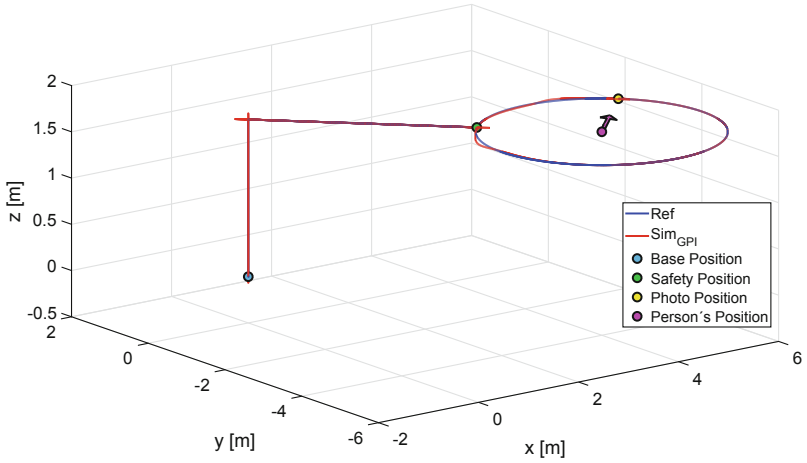

Fig. 3. 3D center of mass of the quadrotor trajectory.

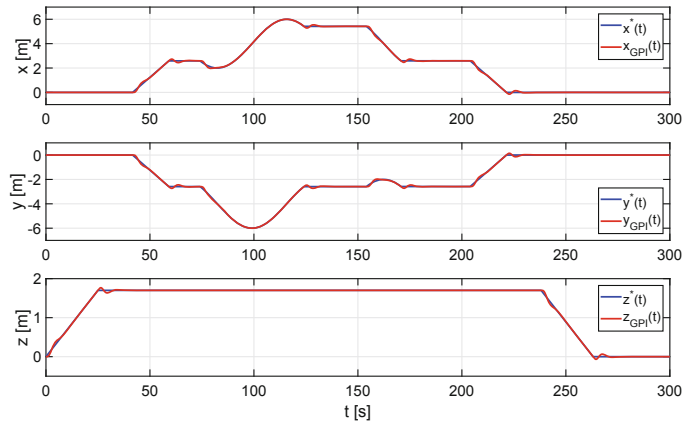

Fig. 4. Position and reference variables of the center of mass of the quadrotor.

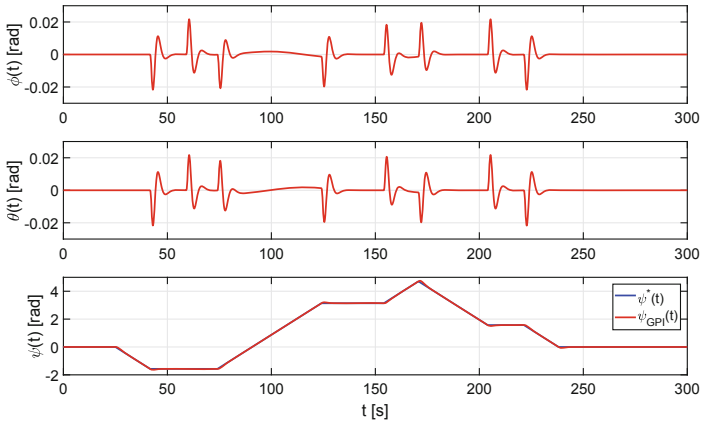

Fig. 5. Attitude variables of the quadrotor.

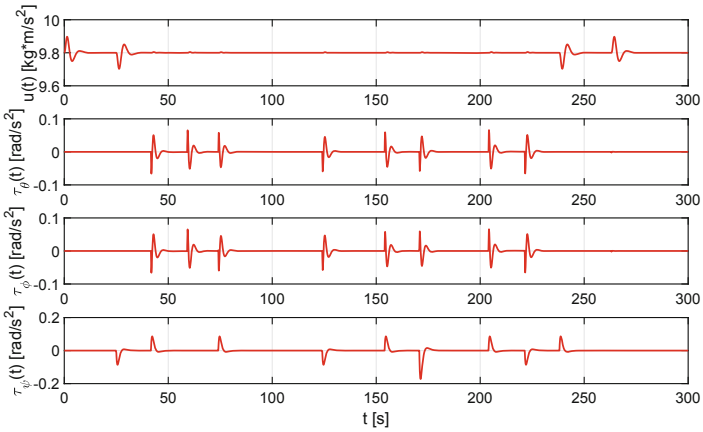

Fig. 6. Applied control inputs.

In Figs. 4 and 5 it is possible to appreciate the precision of the GPI controller for trajectory tracking of the quadrotor's position and orientation. And, finally, the control inputs applied to the UAV model are detailed in Fig. 6.

6 Conclusions

The need of novel home care strategies for dependent people has motivated this work. We have designed a trajectory planner for a quadrotor aimed to monitor dependents. The final aim is to perform an autonomous flight to observe the person and take a photo of his/her face that will be later analyzed to determine the person's mood. That information will allow providing the assistance required at each moment.

Despite being the first development of the trajectory planner, the results of the simulations are positive. The planner is able to generate smoothed reference trajectories that allow performing precise flights of the UAV governed by a GPI controller. In future works, it will be necessary to improve the planner in the following aspects: (a) to increase the planner's detail to consider the transitions between states as a consequence of the movement of the person during the monitoring process; (b) to develop a strategy for detecting obstacles and avoiding collisions in the flight environment; (c) to perform an experimentation of the proposed approach in virtual reality environments before moving to real scenarios.

Acknowledgments. This work has been partially supported by Spanish Ministerio de Ciencia, Innovación y Universidades, Agencia Estatal de Investigación (AEI)/European Regional Development Fund (FEDER, UE) under DPI2016-80894-R grant. Lidia M. Belmonte holds FPU014/05283 scholarship from Spanish Ministerio de Educación y Formación Profesional.

220 L. M. Belmonte et al.

References

1. Almansa-Valverde, S., Castillo, J.C., Fernndez-Caballero, A.: Mobile robot map building from time-of-flight camera. Expert Syst. Appl. **39**(10), 8835–8843 (2012)
2. Belmonte, L.M., Castillo, J.C., Fernández-Caballero, A., Almansa-Valverde, S., Morales, R.: Flying depth camera for indoor mapping and localization. In: Mohamed, A., Novais, P., Pereira, A., Villarrubia González, G., Fernández-Caballero, A. (eds.) Ambient Intelligence - Software and Applications. AISC, vol. 376, pp. 243–251. Springer, Cham (2015). https://doi.org/10.1007/978-3-319-19695-4_25
3. Belmonte, L.M., Morales, R., Fernández-Caballero, A., Somolinos, J.A.: A tandem active disturbance rejection control for a laboratory helicopter with variable speed rotors. IEEE Trans. Ind. Electron. **63**(10), 6395–6406 (2016)
4. Belmonte, L.M., Morales, R., Fernández-Caballero, A., Somolinos, J.A.: Robust decentralized nonlinear control for a twin rotor MIMO system. Sensors **16**(8) (2016). Article 1160
5. Belmonte, L.M., Morales, R., Fernández-Caballero, A., Somolinos, J.A.: Nonlinear cascade-based control for a twin rotor MIMO system. In: Nonlinear Systems - Design, Analysis, Estimation and Control, pp. 265–292. In-Tech (2016)
6. Castillo, J.C., Castro-González, Á., Alonso-Martín, F., Fernández-Caballero, A., Salichs, M.Á.: Emotion detection and regulation from personal assistant robot in smart environment. In: Costa, A., Julian, V., Novais, P. (eds.) Personal Assistants: Emerging Computational Technologies. ISRL, vol. 132, pp. 179–195. Springer, Cham (2018). https://doi.org/10.1007/978-3-319-62530-0_10
7. Castillo, J.C., et al.: Software architecture for smart emotion recognition and regulation of the ageing adult. Cogn. Comput. **8**(2), 357–367 (2016)
8. Castillo, P., Dzul, A., Lozano, R.: Real-time stabilization and tracking of a four rotor mini rotorcraft. IEEE Trans. Control Syst. **12**(4), 510–516 (2004)
9. Chocoteco, J., Morales, R., Feliu, V.: Enhancing the trajectory generation of a stair-climbing mobility system. Sensors **17**(1), 1–31 (2017)
10. Chocoteco, J., Morales, R., Feliu, V., Sánchez, L.: Trajectory planning for a stair-climbing mobility system using laser distance sensors. IEEE Sens. J. **10**(3), 944–956 (2016)
11. Chocoteco, J., Morales, R., Feliu, V.: Improving the climbing/descent performance of stair-climbing systems confronting architectural barriers with geometric disturbances. Mechatronics **30**, 11–26 (2015)
12. Fernández-Caballero, A., Belmonte, L.M., Morales, R., Somolinos, J.A.: Generalized proportional integral control for an unmanned quadrotor system. Int. J. Adv. Robot. Syst. **12** (2015). Article 85
13. Fernández-Caballero, A., et al.: Smart environment architecture for emotion recognition and regulation. J. Biomed. Inform. **64**, 55–73 (2016)
14. Gascueña, J.M., Fernández-Caballero, A.: Agent-oriented modeling and development of a person-following mobile robot. Expert Syst. Appl. **38**(4), 4280–4290 (2011)
15. Gascueña, J.M., Fernández-Caballero, A.: Agent-based modeling of a mobile robot to detect and follow humans. In: Håkansson, A., Nguyen, N.T., Hartung, R.L., Howlett, R.J., Jain, L.C. (eds.) KES-AMSTA 2009. LNCS (LNAI), vol. 5559, pp. 80–89. Springer, Heidelberg (2009). https://doi.org/10.1007/978-3-642-01665-3_9
16. Igual, R., Plaza, I., Medrano, C., Rubio, M.A.: Personalizable smartphone-based system adapted to assist dependent people. J. Ambient. Intell. Smart Environ. **6**(6), 569–593 (2014)

17. Kim, S.J., Lim, G.J., Cho, J., Côté, M.J.: Drone-aided healthcare services for patients with chronic diseases in rural areas. J. Intell. Robot. Syst. **88**(1), 163–180 (2017)
18. Lozano-Monasor, E., López, M.T., Vigo-Bustos, F., Fernández-Caballero, A.: Facial expression recognition in ageing adults: from lab to ambient assisted living. J. Ambient. Intell. Humaniz. Comput. **8**(4), 567–578 (2017)
19. Lozano, R.: Unmanned Aerial Vehicles-Embedded Control. Wiley, Hoboken (2010)
20. Todd, C., et al.: Towards an autonomous UAV for indoor flight in healthcare: a review of research challenges and approaches. Int. J. Emerging Technol. Adv. Eng. **5**(8), 21–28 (2015)
21. Maglogiannis, I., Ioannou, C., Tsanakas, P.: Fall detection and activity identification using wearable and hand-held devices. Integr. Comput. Aided Eng. **23**(2), 161–172 (2016)
22. Martínez-Gómez, J., Fernández-Caballero, A., García-Varea, I., Rodríguez, L., Romero-González, C.: A taxonomy of vision systems for ground mobile robots. Int. J. Adv. Robot. Syst. **11**, 111 (2014)
23. Morales, R., Chocoteco, J., Feliu, V., Sira-Ramrez, H.: Obstacle surpassing and posture control of a stair-climbing robotic mechanism. Control Eng. Pract. **21**, 604–621 (2013)
24. Morales, R., Feliu, V., González, A.: Optimized obstacle avoidance trajectory generation for a reconfigurable staircase climbing wheelchair. Robot. Auton. Syst. **58**, 97–114 (2010)
25. Morales, R., González, A., Feliu, V., Pintado, P.: Environment adaptation of a new staircase climbing wheelchair. Auton. Robot. **23**, 275–292 (2007)
26. Morales, R., Sira-Ramírez, H.: Trajectory tracking for the magnetic ball levitation system via exact feedforward linearization and GPI control. Int. J. Control **83**, 1155–1166 (2010)
27. Morales, R., Sira-Ramírez, H., Feliu, V., González, A.: Adaptive control based on fast online algebraic identification and GPI control for magnetic levitation systems with time-varying input gain. Int. J. Control **87**, 1604–1621 (2014)
28. Rodriguez, F.J., Rico, F.M., Olivera, V.M.: Neural networks for recognizing human activities in home-like environments. Integr. Comput. Aided Eng. **26**(1), 37–47 (2019)
29. Solea, R., Nunes, U.: Trajectory planning and sliding-mode control based trajectory-tracking for cybercars. Integr. Comput. Aided Eng. **14**(1), 33–47 (2007)
30. Todd, C., et al.: A proposed UAV for indoor patient care. Technol. Health Care (2015). https://doi.org/10.3233/THC1046
31. Zemalache, K.M., Beji, L., Maaref, H.: Two inertial models of X4-flyers dynamics, motion planning and control. Integr. Comput. Aided Eng. **14**(2), 107–119 (2007)

CHAPTER 3

Closure

The closure of the doctoral dissertation is detailed in this chapter. Section 3.1 presents the discussion on the research carried out. After an introduction on the suitability of UAVs as a means to monitor people for assistance purposes, three blocks are introduced to summarize the main contributions regarding the study on computer vision in autonomous UAVs, the development of robust control algorithms, and the proposal of vision-based UAVs to assist dependent persons, respectively. Finally, Section 3.2 is dedicated to recapitulating the main conclusions of this thesis, and to presenting the ongoing and future research.

3.1 Discussion

Based on robotics and computer vision, the thesis project has proposed the use of small unmanned aerial vehicles to improve the quality of life and care of people in situation of dependency.

The concept of *dependency* or *care dependency* refers to the situation in which people, for different reasons, such as illness or disability, need help to perform daily tasks [26]. One of the sectors of the population that suffers most from this situation is the aging adults, who often live alone at home. The changes in today's society have led to a demographic panorama that until a few decades ago was unusual. Nowadays, the number of elderly people has increased and the proportion with respect to the rest of the population has also increased. As a consequence, the aging of the population is a reality.

The World Health Organization (WHO) has been aware of this new reality and has performed studies and reports in order to adapt the public health systems and the response

of communities to this new paradigm. Among the different options proposed by WHO, the role of technology should be highlighted. It has to provide solutions to improve aspects such as personal autonomy, mobility, participation, and communication of people. The objective is to promote and maintain the level of functional ability that allows well-being, considering physical, mental and social aspects, during aging. This goal is included in the concept of *healthy aging* [29].

In the face of the loss of intrinsic capacity, help must be given to maintain the level of functional ability. This may entail the need for adapting the dependent's home and even the obligation to leave it in order to receive the precise attention in specialized centers. This decision is usually not voluntary and undermines the dependent's quality of life. WHO insists on the importance of providing solutions that do not involve the abandonment of the person's usual environment. This is also reflected in the Spanish law on the *Promotion of Personal Autonomy and Care for Dependent Persons* [11]. Article 13 indicates that care for dependent persons and the promotion of their personal autonomy should be oriented towards the attainment of improvement in personal quality and autonomy, in order to facilitate an autonomous existence in their habitual environment as long as they wish.

Faced with this situation, the family members themselves often provide help for the care and attention of the dependent person. However, this situation, together with the lack of means and preparation, results in an additional problem. The family members themselves also suffer a reduction in their quality of life [8, 9]. In addition, it must be considered that this solution is sometimes not possible either. Family members, mainly for work reasons, do not have the time necessary for the proper care of the dependent. On the other hand, more and more often the number of elderly people who live alone, either by their own decision or by situations such as the loss of the closest family members, increases. These people, even more, see drastically reduced the possibilities of continuing living at home whilst receiving the necessary attention. Therefore, it is mandatory to focus research on solutions to counteract this situation.

In this sense, this doctoral thesis focuses on the problem of care for dependent persons and approaches it from a technological point of view. It is true that other solutions such as home care provided by qualified people or providing support and training to family members are alternatives in these cases [12, 24]. Likewise, improving conditions in health centers, in such a way that they approach and resemble domestic environments, may be useful to reduce the feeling of abandonment of the home. However, given the demographic trend of recent years, these solutions may not be feasible in the future. Therefore, it is necessary to bet on new technologies to solve the problems of elderly people and dependents in general. *Assistance robotics* can and must play an important role in this matter.

Among the different options for the implementation of assistance robotics, this research has focused on *unmanned aerial vehicles* (UAVs). These aircraft allow access to remote and/or hard-to-reach points without the intervention of an on-board operator. Equipped with vision cameras, they also allow capturing images of the environment for later analysis or even in real time. These features have allowed their use in fields such as surveillance, infrastructure inspection, fire control, transport of goods and medical equipment, among

others. In all these applications, the UAV is usually controlled or at least supervised by an operator on the ground. However, the technological advance is aimed at suppressing this human control by a totally autonomous mode of control.

Autonomous UAVs, equipped with vision cameras, represent a novel technological solution that allows going all over the person's home, overcoming possible obstacles and barriers, such as stairs and blind zones (where static cameras are not useful). Alone or complemented with other technologies, such as biometric wristbands, these vehicles are a means for monitoring the activity of the dependent. In this way, it is possible to collect images that can be treated to analyze the mood and behavior of the person and determine the assistance needed. Based on this premise, the topic and main objective of the thesis has been the control and navigation of UAVs based on computer vision for assistance purposes.

In order to address the proposed research, three partial goals (sub-objectives) were established: (a) to study the integration of computer vision for the navigation and control of the UAV; (b) to increase and improve the movement capacity and stability of the UAV in the face of disturbances of different nature, and (c) to develop the proposal for UAVs as home assistance systems to aid dependent persons. These goals defined the three thematic blocks in which the work plan was divided (computer vision in UAVs, control algorithms for UAVs, and proposal of assistant UAVs). The research works on these topics were published in journals of notable impact and books of international relevance, thus constituting the results of this doctoral thesis per compendium of publications (see Chapter 2). Below is a summary of the main contributions regarding the three topics.

3.1.1 Study on the Computer Vision in Autonomous UAVs

One of the main issues addressed in this doctoral thesis is the study on how computer vision is integrated into the flight operations in autonomous UAVs.

The initial idea was to perform a state of the art study on the issue, but given the great number of works published in this area, it was decided to approach the task from a systematic point of view. This way, a systematic mapping study was carried out to review, classify and structure papers focused on computer vision in autonomous air vehicles. This is, to the best of our knowledge, the first systematic mapping study conducted on this topic.

This study has made it possible to identify and analyze (a) the flight operations for which computer vision has been used, (b) for which types of UAVs the proposals have been designed and/or validated, (c) the configuration and features of the used vision systems, and (d) the tests carried out in the validation process. The main conclusions of the study are briefly summarized below:

- The research on navigation and control solutions integrating computer vision for autonomous UAVs is an area of great interest to the scientific community. The number of papers published on this topic shows an outstanding annual growth trend.

- Most of the works analyzed focus on a solution for a specific operation and not to achieve a fully autonomous UAV based on computer vision. However, the trend shows how the research focus has shifted, from relatively less complex operations, such localization or stabilization towards missions closer to the autonomous concept, such as tracking of paths and objectives, and the avoidance of obstacles.

- Unmanned rotary-wing aerial vehicles have been the principal focus of the researchers' interest. Within this class, the quadrotor is the vehicle for which most solutions have been presented, followed at a distance by helicopters.

- The most widely used vision system is monocamera installed on board the aircraft. Most works analyzed use this configuration. About the camera's orientation, it usually depends on the flight operation. Stereo systems have also been used in a non-depreciable number of publications.

- A significant number of the works analyzed, more than 50%, were validated by flight tests. However, experimentation and especially simulation are still frequently used.

It is important to note at this point that the systematic mapping study was carried out considering the particular focus of this thesis, the UAVs as robots to assist dependent persons. In this sense, the criteria for inclusion and exclusion of the articles were written in relation to this, and the results of the study were analyzed, not only from a general point of view but also from the particular perspective of this research project. Among the conclusions obtained in this respect, the following should be highlighted:

- It is necessary to focus future studies principally on vision-based target tracking and obstacle avoidance, so that the UAV follows the person in monitoring tasks, meeting the safety conditions to make it possible to use such assistant UAVs in real environments.

- The main features of quadrotors, vertical take-off and landing, hovering flight, and greater maneuverability and its relative simpler flight control, makes them a suitable model for complex indoor (and outdoor) environments where the assistant could be used.

- Regarding the vision system, the best solution seems to use a monocular system aboard the UAV. This solution is easier to install, allows reducing the payload for the UAV and the vision algorithms are simpler. However, the use of a stereo system is not discarded in the future if depth information is needed. The vision system's localization should be on-board the UAV to perform the tracking of the person.

- Finally, virtual reality will be essential in the first stages of development of flying assistant robots. This tool allows testing the UAV's operation in a safe environment and conducting studies on the user acceptance of such technology. After that, real flight tests in controlled conditions should be performed before bringing these novel assistants to real homes.

As part of the research carried out on the integration of computer vision in UAVs, a solution was designed based on the use of a depth camera for navigation in indoor environments. This approach considers two phases, the first phase of mapping in which the camera is used as a range sensor. And a second, in which it is used as a gray-scale camera for localization purposes within the flight environment. The flight environment is represented by a modular collection of occupancy grids that are added to the map as new objects are found. This approach can, therefore, be extended for its use in obstacle detection and avoidance solutions.

3.1.2 Design of Robust Control Algorithms for UAVs

In relation to the second goal, improvement of the UAV's movement capacity and stability, the study has focused on the development of several robust control schemes for different aircraft unmanned models. These aerial vehicles are generally characterized by nonlinear, multivariable and coupled dynamics. In addition, most of them are underactuated systems, i.e., the number of control inputs is lower than the number of degrees of freedom (DoF) of the system. All these features complicate the modeling and control process.

At this point, it is important to consider another relevant issue that may difficult the control. For the use of UAVs in assistance robotics, and mainly in the proposal of UAVs as assistants in real homes, it is necessary to reduce the UAV's size in order to disturb as less as possible the routine of person to be assisted. This reduction implies two additional disadvantages: (a) the flight capacity and stability is more affected by disturbances, both exogenous (wind gusts) and endogenous (non-linearities, uncertainties, dynamic couplings,...); (b) the space, payload and power's system capacity are limited, which derivative in the need of small processors with low power consumption and limited memory.

All these conditions undermine the effectiveness of traditional control methods. Therefore, it is necessary to focus the study on robust control schemes, which should be implemented in small-size processors in order to ensure the UAV's stability and control. In all applications flight safety must be maximum, even more in those designed to help people, where the UAV flies close to them.

At this respect, the research carried out during the doctoral thesis has focused on three kinds of robust control schemes which have been designed and implemented for several platforms: two differential flat systems (quadrotor and flapping-wing models) and a laboratory helicopter (TRMS). Below, a summary of the results in this area is presented:

- Generalized Proportional Integer (GPI) Control (Based on Flatness Theory):

  A robust GPI control scheme has been applied in a nonlinear, multivariable and underactuated quadrotor model. The controller design is based on the flatness property (the quadrotor model is differentially flat because all the system variables can be parameterized solely in terms of the flat outputs and a finite number of

their time derivatives). GPI control uses structural state estimates based on integral reconstructors in place of the actual state variables, and only requires inputs, outputs and iterated integrals of such available signals. The effect of the neglected initial states is suitably compensated by means of a sufficiently large number of additional iterated integral output errors, integral input errors and control actions. Numerical simulations demonstrated the effectiveness of the proposed approach in comparison with a classical PID control in the following terms: (a) stabilization and trajectory tracking tasks; (b) performance when the measured signals are corrupted by noise; and (c) dynamic response when atmospheric disturbances, such as gusty wind, affect the quadrotor.

- GPI-Observer-Based Active Disturbance Rejection Control
  - Based on Flatness:

    A robust observer-based linear output feedback control scheme has been designed for a miniature flapping-wing aerial vehicle (FMAV). In the design of the controller, two theories have shown to be fundamental. Firstly, the development relies on a model simplified by the time-average theory, and secondly, the flatness property is used again to obtain a simplified-perturbed model from the previous one. This way, an active disturbance rejection scheme based on linear GPI observers has been proposed for trajectory tracking. The numerical simulations carried out in the MATLAB/Simulink® environment proof the efficiency of the design regarding quick convergence of the tracking errors to a small neighborhood of zero and smooth transient responses.

  - Two-Stage Control Scheme:

    In this case, the study platform has been the TRMS. At this point, it is necessary to highlight the role of this system in the research carried out. The characteristics of this laboratory helicopter, marked by a non-linear and strongly coupled behavior, make it a challenging platform. In this sense, the results obtained have been published in high impact journals and books of relevance in the field of control. Our article published in the IEEE Transactions on Industrial Electronics journal stands out here. In this work, the excellent performance of the application of the ADRC algorithm based on GPI observers in the design of decentralized strategies in hierarchical systems is demonstrated. It is proposed a linearizing, global, approach for the robust output feedback controller design for output trajectory tracking tasks on the perturbed hierarchical systems of which the TRMS system is composed. The key idea is that each individual feedback loop is based on the use of a classical feedback controller and a suitably extended high gain linear observer; thus aiding the feedback controller in two important tasks: (1) the accurate estimation of the input-output system model nonlinearities; and (2) the accurate estimation of the unmeasured phase variables associated with each of the linearizing output variables. These two key pieces of information are used in the proposed feedback controller to (a) cancel the influence of the nonlinearities

as a lumped unstructured time-varying term, and (b) design an output feedback control law based on the approximate estimates of the output associated phase variables. The effectiveness of the proposed approach is demonstrated by means of the real experiments performed in the laboratory platform.

- Nonlinear-Cascade Control Scheme

A cascade-based nonlinear, multivariable and robust control scheme has been designed for the TRMS. The controller, composed of two nested loops, is based on the division of the dynamics of the TRMS into the electrical and mechanical part. Firstly, the electrical controller or inner loop was designed for controlling the angular velocity of each propeller, and then the outer loop or mechanical controller used for determining the necessary velocities to control the spatial position of the TRMS. Some of the advantages of the proposed configuration is the following: (a) the controller design procedure is simplified to a great extent; (b) this scheme can be more easily and safely implemented than the standard controllers; (c) the disturbances affecting the inner loop are effectively compensated before they affect the main process output, thereby improving the stability of the system; (d) the response speed is increased; e) the cascade control scheme is not strongly sensitive to not too large modeling errors. The proposed control scheme has been validated by numerical simulations and experimental tests in which the controller has shown an excellent performance in both stabilization and trajectory tracking tasks.

3.1.3 Proposal of Vision-Based UAVs to Assist Dependent Persons

Finally, the discourse is focused on the last stage of the predoctoral research. This phase has dealt with the proposal of UAVs as a system of assistance, from a theoretical and practical approach. Thus, the final objective of this proposal is the development of a UAV capable of flying autonomously, in a home, to perform the task of monitoring and assistance to dependent persons. However, this development process involves multiple challenges that must be addressed to make possible, viable, and practical the concept of assistant UAVs. The study of these challenges was one of the main developments carried out.

At this point, it is necessary to highlight the collaboration with Professor Paulo Novais, and his research group at the Synthetic Intelligence Lab (ISLab), as a result of the predoctoral stay at Universidade do Minho (Braga, Portugal). The work of the ISLab is framed in the field of Ambient Intelligence and is focused on conducting studies on the behavior of people in specific scenarios for efficient integration as a means of interaction with technology. This research experience made it possible to highlight the importance and need to consider human factors and the role of the proper assisted person. In this sense, it is important to emphasize that the design of UAVs, which can be used in tasks to aid elderly people, and dependents in general, requires not only approaching the problem from a technical point of view to ensure the autonomous and safe flight of the aircraft, but also the need to consider the person himself/herself, respect his/her personal space, study how to improve the acceptance of the

presence of an assistant robot and, thus, work on building a relationship of trust between the UAV-assistant and the person-assisted.

In addition to this preliminary study on the challenges, both technical and human, the work carried out in relation to the proposal of assistant UAVs, has focused on two issues of a more practical nature: the development of a validation system, and the design of a trajectory planner for the UAV flight.

The following lines summarize the main contributions and conclusions in relation to the four topics discussed: (1) definition of the technical aspects to be considered for the development of autonomous UAVs for assistance in the home of dependent persons; (2) definition of the human level challenges that must be faced in order for the proposal to be accepted by the persons who are to be helped; (3) development of a virtual reality-based validation system that allows both the technical evaluation of the proposal and future studies on the acceptance of UAVs as assistants by dependent persons; and (4) development of a flight path planner for a quadrotor in monitoring tasks.

Technical Challenges

From a technical point of view, the main challenge to achieve is the autonomous and safe flight of the aircraft within the assistance environment, in this case, the home of the dependent person. It has been considered appropriate to use rotary wing UAVs due to their excellent maneuverability, agility and versatility. However, given the conditions it is necessary to reduce their size to a minimum, which leads to problems that make them difficult to control. After the analysis of these factors, and of the possible solutions, the use of a robust control scheme based on the active rejection of disturbances has been proposed. On the other hand, it is necessary to deal with the noise problems that may appear in the measurements coming from the sensors.

For the autonomous navigation of the UAV, a two-stage navigation system has been proposed to determine the path free of static obstacles (assuming the existence of a home map) and its adaptation to the dynamic environment through the integration of information from the sensors (mainly the on-board vision system).

Human Factor Challenges

From the point of view of the assisted person, the objective to achieve is the capture by the UAV of facial photographs of the person to be sent to an emotional detection system that should evaluate the emotional state of the person and determine the task of assistance needed. For this monitoring task, it is essential to have the autonomous navigation capacity of the UAV indicated above, as well as to consider the needs of the person, respect their personal space, hinder as little as possible their daily work, and therefore contribute to the acceptance of the assistant system by the user.

Virtual Reality Validation Process

One of the main topics considered has been the design of a virtual reality (VR) platform for the flight simulation of the assistant UAV in a 3D environment that recreates the home of a dependent person. In this way, through the inclusion of immersive and semi-immersive VR technology, real people will be able to experience the monitoring process performed by a virtual UAV flying around them within a safe environment. This tool will make it possible to carry out studies and analysis centered on the assisted person, and not only on the assistant robot. The conclusions of these tests will allow modifications and improvements, mainly related to the physical characteristics of the UAV, and the design parameters of the flight planner.

In the development of this tool, two software programs have been essential: *MATLAB/Simulink®* and *Unity 3D*. The first software simulates the control system of the UAV, including its dynamic modeling (which defines the behavior of the UAV) and control algorithms (determine the control input to apply in order to achieve the desired movement of the UAV, for example, to follow the person at a certain distance). The output of the simulation, i.e. the status of the UAV (position and orientation), is sent to the second program, Unity 3D, in charge of recreating the UAV within the virtual environment. The movement of the (virtual) UAV is achieved by periodically updating its position and orientation, according to the values received from MATLAB/Simulink®. At the same time, it is necessary to provide as feedback the information of the virtual environment (for instance the distance from the UAV to the person) to the control scheme, that is, from Unity 3D to MATLAB/Simulink®. The bidirectional communication system between both programs has been developed using the Message Queue Telemetry Transport (MQTT) protocol, based on a subscription model and topic publication. The first 3D designs of the UAV and virtual environment have also been made. The ongoing research aims to improve and complete the development by adding, among other things, configuration options to select flight control parameters or different scenarios in Unity 3D, and integrating RV technology to perform immersive tests.

Trajectory Planning

The last issue addressed within the framework of assistant UAVs has been flight planning. The objective has been to design a trajectory planning algorithm for the positioning of the UAV during the monitoring process, considering the person's position, and keeping a safety distance that respects the personal space and avoids collision risks. The first development is based on a state machine and has been tested through simulation tests. The results demonstrate the effectiveness of the planner in generating smooth reference trajectories that allow the precise flight of a quadrotor controlled by the previously designed GPI scheme. Extending the planner's details to consider the person's movement and the integration of a solution to avoid obstacles are the main points of improvement for future evaluations using the virtual reality platform.

3.2 Conclusions and Future Work

This thesis has addressed the control and navigation of UAVs based on computer vision for their application in assistance robotics. In particular, the focus has been on the problematic of home care of dependents. The objective and motivation to address this issue have been the search for technology solutions that would provide greater autonomy to dependent people, so that they can continue to live at their homes for as long as they wish, receiving the care they need.

The work carried out during the predoctoral investigation has been divided into two main phases. The first phase has dealt with technical issues, of a more general nature, such as the integration of computer vision for navigation and flight control of autonomous UAVs, as well as the development of robust control algorithms for different aircraft models and platforms. At this point, it is important to note that the research results in this area are applicable to the design of autonomous UAVs for any other purpose, not just assistance robotics. The second phase has specifically focused on the development of the proposal of UAVs to assist dependent persons. To this end, a study has been carried out on the different aspects, both technical and human, to be considered for the design and development of these UAVs for home assistance. In addition, two fundamental issues for this development have been addressed: the design of a virtual reality platform, and the development of a trajectory planner for the monitoring process. The virtual reality platform will make it possible to carry out evaluations centered on the assistant UAV, mainly in questions relating to the flight planning, as well as on the person assisted by means of studies on the perception and acceptance of the technology. This tool may also be suitable in the simulation of other robots, not only aerial, and again for other purposes.

The future lines of work concerning the proposal of assistant UAVs are: (i) to advance in the design of the trajectory planner, (ii) to carry out tests using the virtual reality platform (in its most advanced version), (iii) to verify the proposal through experimental and flight tests, (iv) to extend the functionality of the assistance system. The ongoing research focuses on the first two points, while experimentation and especially real flight trials should be addressed later (once possible faults in the previous stages are corrected). The last point concerns long-term improvements to extend the present proposal. Below, the main tasks and suggestions for this future research are briefly detailed:

1. Trajectory Planner

   1.1. Increasing the planner's detail in order to consider the transitions between states that allow adapting the UAV's flight to the person's motion during the monitoring process.

   1.2. Integration of the information relative to the map of the environment and sensors of the UAV to calculate an obstacle-free path with dynamic adaptation to avoid unexpected obstacles in the flight trajectory.

2. Virtual Reality Platform

   2.1. Increasing the configuration options of the 3D simulation platform to, among others, select and configure the flight control parameters, as well as choosing among different models of home scenarios.

   2.2. Carrying out tests using immersive VR technology by the people for which the UAV assistants are conceived. Performing studies on the acceptance of the technology and on possible improvements.

3. Experimental and Flight Tests

   3.1. Design and set-up of a quadrotor (or adaptation of a commercial model), including the installation of an embedded vision system and the sensors required for control.

   3.2. Validation of the navigation and control solutions previously designed in real flight trials. Implementation and test of a novel ADRC control scheme for the quadrotor.

   3.3. Verification of the performance of the quadrotor in monitoring a person within a laboratory or controlled environment that ensures safety measures.

4. Long-Term Improvements: Extending the Functionality

   The research line of the thesis has been based on the premise of the suitability of UAVs to technologically contribute to the care of dependent people, usually elderly people who live alone. In the proposal of UAVs as personal assistants, a computer system will analyze the person's mood, to determine the assistance needed, by processing the information grabbed by the aircraft's camera. The analysis and response capacities of this computer system are key points to improve and extend the proposal made. Algorithms can be included for the detection of circumstances that imply a risk for the dependent person. For example, the UAV could conduct an inspection flight throughout the house, verifying rooms and facilities such as the kitchen and gas plate. Another suggestion regarding the computer system is the ability to automatically communicate with the medical services in case of an emergency such as a fall.

   Providing new help models would significantly enhance the proposal of the assistant UAVs, thus improving the viability and acceptance of these new models of care robots on the part of the dependent people as well as for the rest of society. All this would contribute to a greater deployment of this type of assistance in real homes, thus improving the quality of life of a greater number of dependent people. It would also be possible to extend the target population of these UAV-based aid systems. Personal assistants of general purpose for help and support tasks may be interesting solutions in a world each time more and more connected to new technologies in the era of the Internet of Things.

Bibliography

[1] ATIA. What is AT? URL `https://www.atia.org/at-resources/what-is-at/`. Assistive Technology Industry Association (ATIA) [Web; accessed on 11 June 2019].

[2] L. M. Belmonte, R. Morales, A. Fernández-Caballero, and J. A. Somolinos. Nonlinear cascade-based control for a twin rotor mimo system. *Nonlinear Systems-Design, Analysis, Estimation and Control*, pages 265–292, 2016. doi: 10.5772/64875.

[3] A. Bertomeu-Motos, S. Ezquerro, J. A. Barios, L. D. Lledó, S. Domingo, M. Nann, S. Martin, S. R. Soekadar, and N. Garcia-Aracil. User activity recognition system to improve the performance of environmental control interfaces: a pilot study with patients. *Journal of NeuroEngineering and Rehabilitation*, 16(1), Jan. 2019. doi: 10.1186/s12984-018-0477-5.

[4] S. Blackman, C. Matlo, C. Bobrovitskiy, A. Waldoch, M. L. Fang, P. Jackson, A. Mihailidis, L. Nygård, A. Astell, and A. Sixsmith. Ambient assisted living technologies for aging well: A scoping review. *Journal of Intelligent Systems*, 25(1), Jan. 2016. doi: 10.1515/jisys-2014-0136.

[5] J. Broekens, M. Heerink, H. Rosendal, et al. Assistive social robots in elderly care: a review. *Gerontechnology*, 8(2):94–103, 2009.

[6] A. Costa, V. Julian, and P. Novais. *Personal Assistants: Emerging Computational Technologies. Intelligent Systems Reference Library*, volume 132. Springer, 2017.

[7] J. Costa-Font, D. Elvira, and O. Mascarilla-Miró. 'Ageing in place'? exploring elderly people's housing preferences in spain. *Urban Studies*, 46(2):295–316, 2009. doi: 10.1177/0042098008099356.

[8] M. V. Delicado Useros, A. Alfaro Espín, E. Candel Parra, and A. Barnés Martínez. Family caregivers: Nurses' perception and attitudes. *Social Medicine*, 6(3):151–161, 2012.

[9] K. F. dos Anjos, R. N. S. de Oliveira Boery, and R. Pereira. Quality of life of relative caregivers of elderly dependents at home. *Texto & Contexto - Enfermagem*, 23(3): 600–608, Sept. 2014. doi: 10.1590/0104-07072014002230013.

[10] S. Dupuis-Blanchard, O. N. Gould, C. Gibbons, M. Simard, S. Éthier, and L. Villalon. Strategies for aging in place. *Global Qualitative Nursing Research*, 2:2333393614565187, Feb. 2015. doi: 10.1177/2333393614565187.

[11] España. Ley 39/2006, de 14 de diciembre, de Promoción de la Autonomía Personal y Atención a las personas en situación de dependencia. *Boletín Oficial del Estado*, 2006. URL `https://www.boe.es/eli/es/l/2006/12/14/39/con`.

[12] M. C. Fernández-Gallego, J. M. M. Asencio, F. J. M. Santos, R. C. Arándiga, E. C. Fernández, J. P. B. Sicilia, F. J. N. Moya, I. L. Abajo, M. C. Mañas, and C. B. de las Nieves. Effect of the act on promotion of personal autonomy and care for dependent persons on their family caregivers. *BMC Health Services Research*, 12(1), Dec. 2012. doi: 10.1186/1472-6963-12-462.

[13] F. Gomez-Donoso, F. Escalona, F. M. Rivas, J. M. Cañas, and M. Cazorla. Enhancing the ambient assisted living capabilities with a mobile robot. *Computational Intelligence and Neuroscience*, 2019:1–15, Apr. 2019. doi: 10.1155/2019/9412384.

[14] E. Iecovich. Aging in place: From theory to practice. *Anthropological notebooks*, 20 (1):21–33, 2014. ISSN 1408-032X.

[15] E. Ivorra, M. Ortega, J. Catalán, S. Ezquerro, L. Lledó, N. Garcia-Aracil, and M. Alcañiz. Intelligent multimodal framework for human assistive robotics based on computer vision algorithms. *Sensors*, 18(8):2408, July 2018. doi: 10.3390/s18082408.

[16] R. Kachouie, S. Sedighadeli, R. Khosla, and M.-T. Chu. Socially assistive robots in elderly care: a mixed-method systematic literature review. *International Journal of Human-Computer Interaction*, 30(5):369–393, 2014.

[17] P. Lansley. Can adapting the homes of older people and providing assistive technology pay its way? *Age and Ageing*, 33(6):571–576, Sept. 2004. doi: 10.1093/ageing/afh190.

[18] E. Martinez-Martin and A. P. del Pobil. Personal robot assistants for elderly care: An overview. In *Personal Assistants: Emerging Computational Technologies*, pages 77–91. Springer, Sept. 2017. doi: 10.1007/978-3-319-62530-0_5.

[19] M. Memon, S. Wagner, C. Pedersen, F. Beevi, and F. Hansen. Ambient assisted living healthcare frameworks, platforms, standards, and quality attributes. *Sensors*, 14(3): 4312–4341, Mar. 2014. doi: 10.3390/s140304312.

[20] J. Meyer, M. Brell, A. Hein, and S. Gessler. Personal assistive robots for AAL services at home. The Florence point of view. In *Proceedings of the 3rd. IoPTS workshop*, Brussels, 2009.

[21] A. E. murabet, A. Abtoy, A. Touhafi, and A. Tahiri. Ambient assisted living system's models and architectures: A survey of the state of the art. *Journal of King Saud University - Computer and Information Sciences*, 2018. ISSN 1319-1578. doi: 10.1016/j.jksuci.2018.04.009.

[22] F. Oswald, H.-W. Wahl, O. Schilling, C. Nygren, A. Fänge, A. Sixsmith, J. Sixsmith, Z. Széman, S. Tomsone, and S. Iwarsson. Relationships Between Housing and Healthy Aging in Very Old Age. *The Gerontologist*, 47(1):96–107, feb 2007. doi: 10.1093/geront/47.1.96.

[23] M. Post. Definitions of quality of life: What has happened and how to move on. *Topics in Spinal Cord Injury Rehabilitation*, 20(3):167–180, July 2014. doi: 10.1310/sci2003-167.

[24] M. Rodríguez-Pérez, A. Abreu-Sánchez, M. J. Rojas-Ocaña, and R. del Pino-Casado. Coping strategies and quality of life in caregivers of dependent elderly relatives. *Health and Quality of Life Outcomes*, 15(1), Jan. 2017. doi: 10.1186/s12955-017-0634-8.

[25] P. Sabine, W. Franz, and W. Katharina. AAL robotics: State of the field and challenges. *Studies in Health Technology and Informatics*, page 117–124, 2015. doi: 10.3233/978-1-61499-524-1-117.

[26] L. Salvador-Carulla and V. I. Gasca. Defining disability, functioning, autonomy and dependency in person-centered medicine and integrated care. *International journal of integrated care*, 10(5), 2010. doi: 10.5334/ijic.495.

[27] P. Theofilou. Quality of life: Definition and measurement. *Europe's Journal of Psychology*, 9(1):150–162, Feb. 2013. doi: 10.5964/ejop.v9i1.337.

[28] WHO. Disability and rehabilitation: Assistive devices and technologies, . URL `https://www.who.int/disabilities/technology/en/`. World Health Organization [Web; accessed on 11 June 2019].

[29] WHO. Ageing and life-course: What is healthy ageing?, . URL `https://www.who.int/ageing/healthy-ageing/en/`. World Health Organization [Web; accessed on 18 June 2019].

[30] WHO. Assistive technology: Fact sheet, 18 May 2018. URL `https://www.who.int/news-room/fact-sheets/detail/assistive-technology`. World Health Organization [Web; accessed on 11 June 2019].

[31] WHO. *Active ageing: a policy framework*. World Health Organization, Geneva, 2002. URL `http://www.who.int/iris/handle/10665/67215`.

[32] WHO. *World report on ageing and health*. World Health Organization, Geneva, 2015. ISBN 978-92-4-156504-2. URL `http://www.who.int/iris/handle/10665/186463`.

[33] WHO. *Integrated care for older people: guidelines on community-level interventions to manage declines in intrinsic capacity*. World Health Organization, Geneva, 2017. ISBN 978-92-4-155010-9. URL `http://www.who.int/iris/handle/10665/258981`.

[34] WHOQOL Group. The World Health Organization quality of life assessment (WHOQOL): development and general psychometric properties. *Social science & medicine*, 46(12):1569–1585, 1998.

[35] J. L. Wiles, A. Leibing, N. Guberman, J. Reeve, and R. E. S. Allen. The meaning of "aging in place" to older people. *The Gerontologist*, 52(3):357–366, Oct. 2011. doi: 10.1093/geront/gnr098.